Università degli studi di Trieste

XXXIII Ciclo del dottorato di ricerca in Fisica

Black holes and star formation in galaxy clusters: a view from simulations

Settore scientifico-disciplinare:
FIS/05

Coordinatore:
Prof. Francesco Longo

Dottorando:
Luigi Bassini

Supervisore:
Prof. Stefano Borgani
Dr. Elena Rasia
Dr. Giuliano Taffoni

Anno Accademico 2019/2020

"Is this real? Or has this been happening
inside my head?"

"Of course it is happening inside your head, but
why on earth should that mean that
it is not real?"

Abstract

Galaxy clusters are the most massive objects in the universe; they are located at the nodes of the cosmic web from which they continuously accrete matter. In the recent years, observations at different wavelengths from ground-based and space-borne telescopes have provided a wealth of information on the cluster bright components: the cluster galaxies which are visible in the optical bands, and the intra-cluster medium, which is observable through its X-ray emission and in the microwave wavelengths through the Sunyaev–Zeldovich effect. All these observations have contributed to enlarge the sample of known clusters (at low and high redshifts), increasing at the same time our knowledge on the astrophysical processes that take place within these massive objects. Today, galaxy clusters represent an important tool from both a cosmological point of view (through their number counts) and galaxy formation models. Indeed, given their particular location at the nodes of the cosmic web, galaxy clusters coincide with the densest regions of the universe, where the evolution of galaxies experience the impact of an extreme environment.

The galaxies within clusters are mainly red massive ellipticals or bulge dominated, with little ongoing star formation, especially close to the cluster core. Among them, a relevant role is occupied by the brightest cluster galaxy (BCG), the most luminous and massive cluster galaxy typically located at the cluster center. In the BCGs, the low values of star formation rates are related to a hampering of the cooling rate by the feedback from the active galactic nuclei (AGN), as highlighted by the frequent presence of radio-loud AGNs. This feedback is generated by the gas accretion around the central supermassive black hole (SMBH), whose mass is known to strongly correlate with a number of BCG properties, like its stellar mass and its stellar velocity dispersion. Very recently, other correlations involving SMBHs masses and global cluster properties (like cluster mass and temperature) were found. Interestingly, these correlations showed a lower scatter with respect to the correlations involving BCGs properties, suggesting that the physical processes that drive SMBH mass growth might be closely related to the large scale properties of the hosting galaxy cluster.

Motivated by these observational works, in the first part of my thesis I used the Dianoga simulations, a set of 29 zoom-in cosmological hydrodynamical simulations centred on massive galaxy clusters, to study the symbiotic growth of galaxy clusters and the SMBHs at their center. In particular, in Bassini et al. (2019) we investigated the correlations between SMBH mass and cluster mass and temperature, their establishment and evolution. Moreover, we studied how gas accretion and BH-BH mergers contribute to SMBH growth across cosmic time. The results show that the observed correlations derive from two processes that take place at different times. In particular, at $z \gtrsim 2$, SMBHs grow rapidly by gas accretion, until they are massive enough to regulate gas cooling in the inner part of the galaxy (proto)cluster. At this stage, a correlation between SMBH masses and cluster mass is already in place. At later times ($z \lesssim 1$), SMBHs increase their mass through BH-BH mergers, which at $z = 0$ become the largest contributor to the total SMBH mass ($\sim 60\%$). During this last process, substructures hosting the merging SMBHs are disrupted and the unbound stars enrich the diffuse stellar component rather than increase the BCG mass. However, even though mergers play an important role for the growth of these central massive SMBHs, the same is not true when considering the whole population of SMBHs within our simulations. Indeed, in the analysis published in Gaspari et al. (2019), I showed that for SMBHs with $M_{\rm BH} < 10^9\ \rm M_{\odot}$, BH-BH mergers represent a sub-dominant process with respect to gas accretion. Given this last result, we conclude that simulations suggest a SMBH-galaxy co-evolution mediated by AGN feedback.

Even though AGN feedback is fundamental in regulating the star formation in low-redshift galaxy clusters, by the time it starts to be effective galaxy clusters are already populated by the most massive galaxies in the universe. Given their large mass and their low star formation rates, it is thought that most of the stars are produced at high redshift during brief and intense burst of star formation. This view has numerous indirect evidences, both observational and theoretical. For example, astroarchaeology analysis of massive ellipticals shows a direct proportionality between the mass of a galaxy and

its age. Moreover, numerical simulations and semi-analytical models predict that most of the stars within the BCGs ($> 50\%$) are already formed by $z \sim 3$ during the proto-cluster stage, i.e. the infancy stage of clusters of galaxies, and are later assembled through galaxy mergers. This is also confirmed by observations, which find that the most massive BCGs show multiple nuclei indicative of recent mergers. However, it is still difficult to draw a complete picture of galaxy cluster evolution using available data. Indeed, even though the number of detected protoclusters is rapidly increasing, the resulting sample is still fairly heterogenous being based on different detection methods, each having its own limitations and bias.

In this context, cosmological hydrodynamical simulations represent the most advanced theoretical tool to provide a coherent interpretative framework of all such observations on proto-clusters. However, before obtaining a meaningful interpretation of observational data on cluster evolution, it is important to study whether theoretical models match the available high redshift observational constraints. Therefore, in the second part of my thesis I studied the star formation rate (SFR) within galaxy clusters and protoclusters over the redshift range $0 < z < 4$. This analysis, published in Bassini et al. (2020), finds that state-of-the-art cosmological simulations have difficulties in reproducing the very high star formation rates measured from recent observations. To better understand the physical reasons for the difference between theory and observations, I also studied galaxy properties in protocluster environment in a more statistical approach. In particular, I compared the main sequence of star forming galaxies as predicted by cosmological simulations and semi-analytical models to the observed one at $z \sim 2$. This analysis highlighted that theoretical models do not reproduce both the normalization of such correlation and its distribution at fixed stellar mass, meaning that the highest values of SFRs are missed. Interestingly, these results are consistent within a wide range of values for the parameters of the subgrid star formation model, including the elimination of any feedback due to AGNs.

This analysis hints that the sub-grid models included in simulations are reductive and do not correctly reproduce the star formation history of galaxy (proto)clusters. Therefore, an effort to extend the modelization of the astrophysical processes relevant for star formation is needed. Indeed, given the results obtained in this thesis, it seems unfeasible to reach an agreement with

observations without a modification of the models currently implemented. This task, which need to be addressed in future works, will benefit from the increasing number of multi-wavelength observations of highly star forming galaxies, whose properties can be used to put constraints on the subgrid models implemented in modern cosmological simulations.

Contents

Chapter 1

What is a Galaxy Cluster?

The history of galaxy clusters goes back to the XVIII century, when Charles Messier and F. Wilhelm Herschel independently produced the first catalogs of astronomical objects, generically referred to as nebulæ. These are the first catalogs of objects different from stars and were fairly heterogeneous, with only two common characteristics: their diffuse aspect and their high brightness. Even though their origin (galactic or extragalctic) was not known yet, it was already noted that some of them were clustered on the sky. It was not until 1923, when Edwin P. Hubble observations of Cepheids in one of Messeier's nebulæ, that the extragalactic nature of some of those objects was proved. Between these, there were two galaxy overdensities near the Virgo and Coma Berenices constellations, that given their enormous distance have been identified as physically related clumps of galaxies, which are now known as Virgo and Coma clusters. Interestingly, only few years later Zwicky, studying the rotational velocity of galaxies within the Coma cluster, concluded that there must be a 'Dunkle Materi′, now known as dark matter, dominating the gravitational potential within the cluster (Zwicky, 1933). Indeed, he estimated a total mass of the cluster through the virial theorem at least 400 times the mass estimated through galaxies luminosity.

Around 20 years later the presence of a diffuse gas within clusters of galaxies was theoretically expected, for two main reasons: (i) galaxies and stars within clusters were expected to form out of gas condensation, a process that likely is not 100% efficient; (ii) collisions between galaxies were supposed to be relatively common in such environment, with interstellar matter swept out as a result of such encounters (Limber, 1959). However, the properties of the intracluster gas (e.g., if it was hot or cold) were still unclear. Moreover, even though Zwicky (1933) deduced a large amount of dark matter from his computation, this view was still largely refused and the presence of diffuse gas was thought to play an important role to solve the missing mass problem. Boldt et al. (1966) was the first to claim a detection of extended X-ray emission from cluster of galaxies at $25\ \mathrm{keV}$. Even though this measurement turned out to be a spurious detection, it influenced both theoretical and observational works. Felten et al. (1966), in addition to show that it was unlikely that the detected flux was coming from the galaxies within the cluster, computed a temperature for the diffuse gas component of $7 \times 10^7\ \mathrm{K}$ assuming the gas is thermalized, a value very near to what is found in recent observations (7-9 keV, e.g. Sato et al. 2011). Finally, Meekins et al. (1971) and Gursky et al. (1971) independently detected X-ray emission from the Coma cluster. This measurement not only confirmed the presence of a hot diffuse gas component, but also constrained the total gas mass to be $1 - 2\%$[1] the mass required for gravitational binding. Around ten years later, the presence of a diffuse plasma has been corroborated by the detection of the Sunyaev–Zeldovich effect (SZ, Sunyaev & Zeldovich 1972) from three galaxy clusters (Birkinshaw et al. 1984), which proved in a complementary fashion the conclusions reached with X-ray observations. Therefore, the emerging picture confirmed in the following years, was of galaxy clusters defined as overdensity of galaxies surrounded by a diffuse plasma not associated with individual galaxies both in equilibrium within a common gravitational potential well dominated by dark matter. These three components are shown in Fig. 1.1 and Fig. 1.2. Fig 1.1 is a composite image from Hubble[2], Chandra[3], and Spitzer[4] of the massive galaxy cluster J1426.5+3508. In the image are clearly visible both the galaxies (red) and the ICM (blue). Even though the DM component can not be directly observed, its effects are visible through the distortions of galaxy shapes in the neighbourhood of the cluster center due to gravitational lensing. An example of this effect is shown in Fig. 1.2.

In the more recent years, the introduction of ground and space based telescopes working at different wavelengths has enabled to expand the sample

---

[1] This fraction is now fixed to $\sim 15\%$ from more recent measurements.

[2] https://hubblesite.org/

[3] https://chandra.si.edu/

[4] https://www.nasa.gov/mission_pages/spitzer/main/index.html

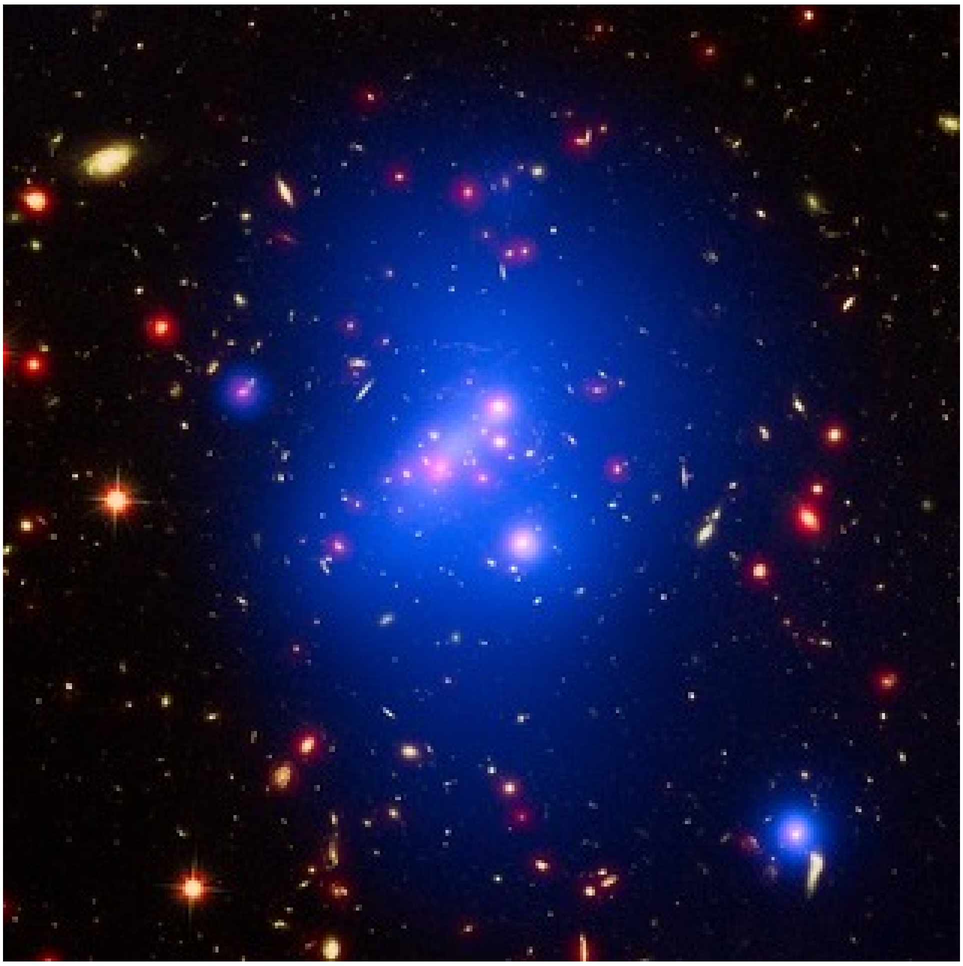

Fig. 1.1: Hubble, Chandra, and Spitzer composite image of the massive galaxy cluster J1426.5+3508. Credits: https://hubblesite.org/image/3690/news/15-galaxy-clusters.

of known galaxy clusters and a deeper understanding of their astrophysical properties. Therefore, today galaxy clusters represent an important tool from both a cosmological point of view (through their number counts, e.g. Allen et al. 2011, Kravtsov & Borgani 2012) and galaxy formation models. Indeed, given that they are located at the nodes of the cosmic web (see Fig. 1.3), galaxy clusters coincide with the most dense regions of the universe, where the evolution of galaxies and thus their resulting properties depend on a range of environmental effects.

In the following sections of this chapter I will review the main astrophysical properties of galaxy clusters on which the main results of my work are

Fig. 1.2: Hubble image of the galaxy cluster Abell S1063. In the image are clearly visible the distortion on galaxy shapes due to gravitational lensing. Credits: https://hubblesite.org/image/4293/news/15-galaxy-clusters.

based (Chapters 3 and 4).

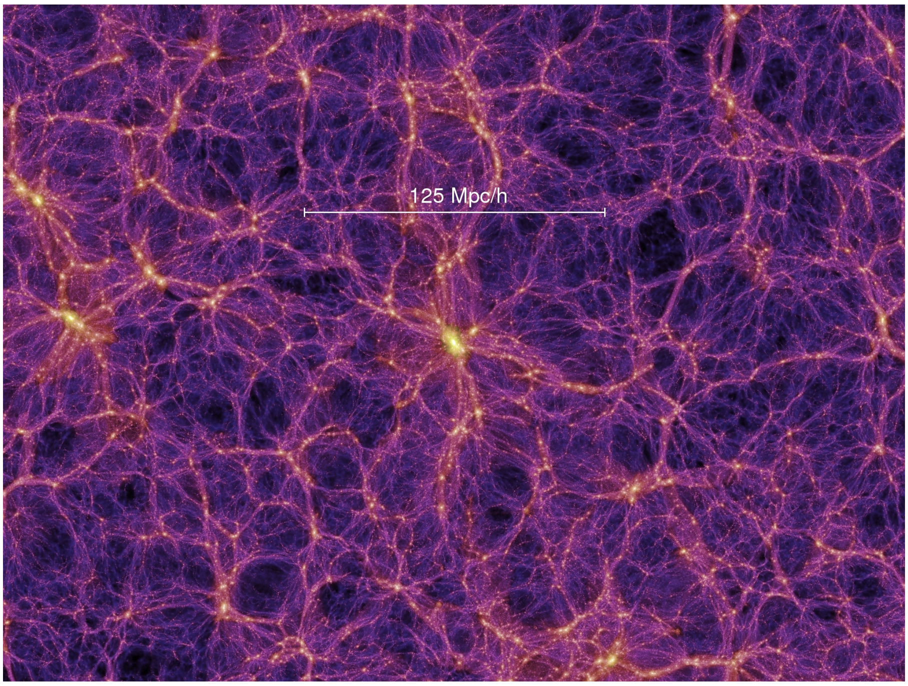

Fig. 1.3: Projected density field for a 15 Mpc/h thick slice at redshift $z = 0$ for the dark matter only Millenium simulation. The densest regions are showed in yellow and orange and corresponds to clusters and groups of galaxies. Credits: https://wwwmpa.mpa-garching.mpg.de/galform/virgo/millennium/

1.1 Galaxy clusters in the local universe

I start the description of galaxy clusters by their properties at $z = 0$ in the optical bands, which map their stellar content. Even though stars are the only component which is visible at optical wavelengths, they comprise only few percent of the total mass of galaxy clusters. In Fig. 1.4 I show the ratio between the total stellar mass within R_{500}[5] and the total cluster mass within the same aperture, derived both from simulations and observations. The results show that stars within massive clusters ($M_{500} \approx 10^{15}$ M$_\odot$) account for only $\sim 1\%$ of the total mass, while the percentage increases to few percent at decreasing cluster mass. Most of the stars within galaxy clusters are locked in galaxies, with a non-negligible fraction composed by unbound stars which is commonly referred as intra-cluster light (ICL) and can account up to $20\% -$

---

[5] I define R_Δ as the radius of the sphere encompassing an average density Δ times the critical density of the universe at that redshift, $\rho_{\rm cr} = 3H^2(z)/8\pi G$. M_Δ will be the mass within R_Δ. See also Sect. A.3 of the Appendix.

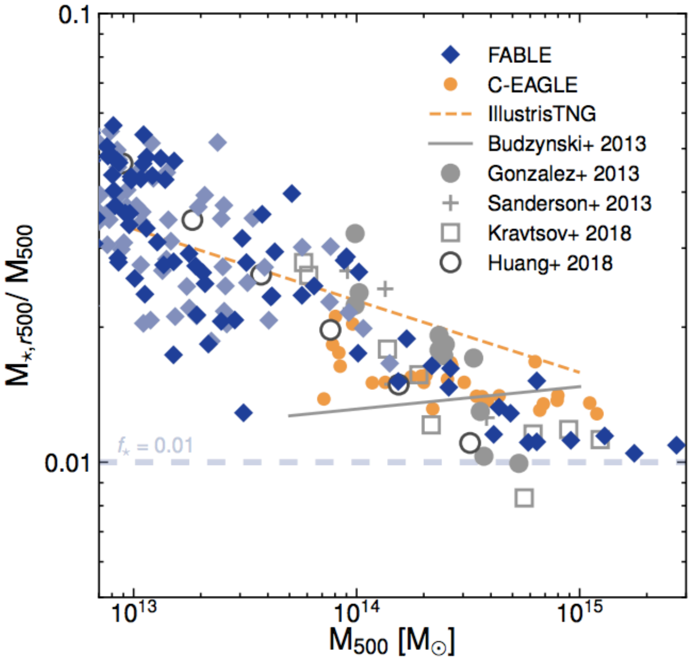

Fig. 1.4: Ratio between stellar and total mass in clusters within R_{500}. Both observational results and results from few numerical simulations are shown. Credits: Henden et al. (2019).

40% of the total stellar mass within the virial radius (e.g., Gonzalez et al. 2013, Kravtsov et al. 2018).

Galaxies within clusters are typically massive ellipticals or bulge dominated, with little ongoing star formation, especially near the cluster core. This is a manifestation of the well known morphology-density relation: early type galaxies (ETGs) are preferentially located in dense environments, while star forming galaxies (SFGs) are more common in the field. An example of this environmental effect is shown in Fig. 1.5, where the rest frame color distribution is plotted against galaxy number density[6] and absolute magnitude. From the figure it is clear that more luminous (and more massive) galaxies are mainly red galaxies. The peak of the distribution at $2 < (u - r) < 3$ identify the so called 'red sequence' (e.g., Bell et al. 2004) and is clearly more prominent at the higher densities. For this reason, as I will show later in this Chapter, the red-sequence galaxies are a very important tool to iden-

---

[6] Σ_N, used in Fig. 1.5, is a frequently used sky surface density estimator, defined as the inverse of the volume centred on a galaxy and encompassing the N nearest neighbours within a given redshift interval.

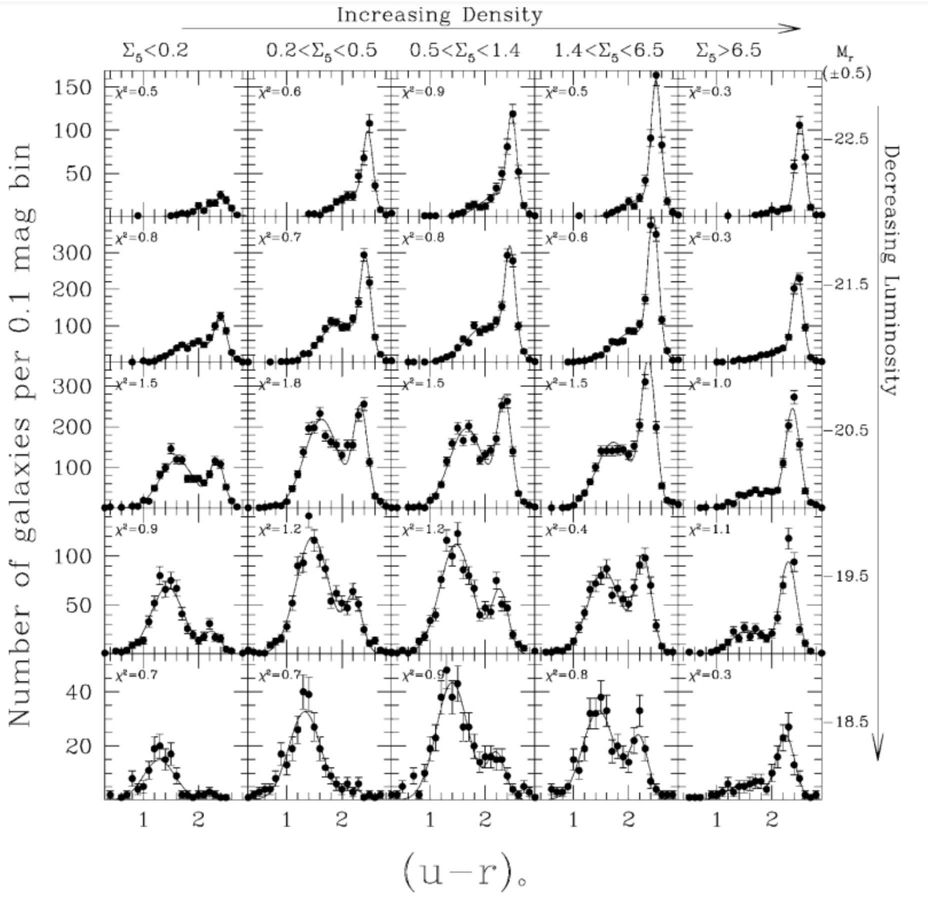

Fig. 1.5: Rest frame colour distribution as a function of galaxy number density (top x-axis) and absolute magnitude (M_r, right y-axis). Solid lines represent double Gaussians fit to the data. Credits: Balogh et al. (2004).

tify clusters. On the contrary, at lower galaxy number densities and absolute magnitudes, a second peak becomes clearly visible at $1 < (u - r) < 2$. This, usually referred as blue sequence, is associated to the SFGs commonly found in the field. The morphology-density relation hints that the environment plays a key role in the evolution of galaxies, with the dense environments of galaxy clusters representing one extreme of this process.

Important clues on the origin of the massive galaxies which are found within galaxy clusters, and thus on the formation of galaxy cluster itself, come from astroarchaeology. Using the luminosity weighted age of the stars within the galaxy and the ratio between α-elements (O, Ne, Mg, Si, Ca, Ti) and iron (α/Fe) it is possible to derive the star formation history (SFH) of

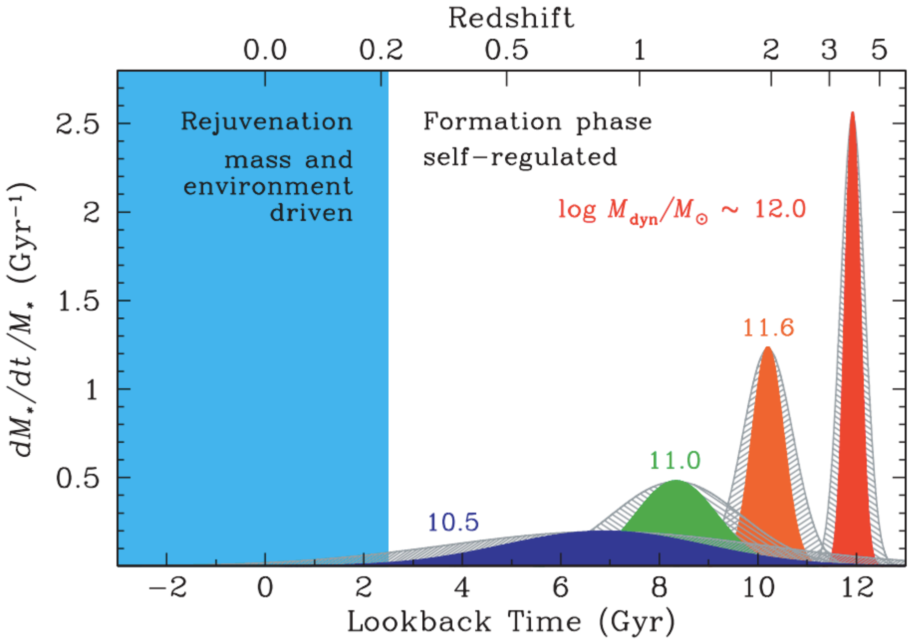

Fig. 1.6: Specific star formation rate as function of look-back time for early-type galaxies of various masses as indicated by the labels. The grey hatched curves indicate the range of possible variation in the formation time-scales that are allowed within the intrinsic scatter of the α/Fe ratios derived. Intermediate- and low-mass galaxies in low-density environments get rejuvenated via minor star formation events below redshift z $\sim$ 0.2. This suggests a phase transition from a self-regulated formation phase without environmental dependence to a rejuvenation phase, in which the environment plays a decisive role possibly through galaxy mergers and interactions. Credits to Thomas et al. (2010).

elliptical galaxies. The results obtained from this analysis suggest that more massive ellipticals (independently of their environment) formed at earlier times, a feature that is known as downsizing. At the same time, the values of α/Fe show that the higher the mass, the shorter the time scale of star formation (e.g., Thomas et al. 2010, Conroy et al. 2014). These well studied phenomena are shown in Fig. 1.6. In particular, the figure shows the SFH of elliptical galaxies in different mass bins, with the grey hatched curves indicating the possible variations due to the scatter in the derived values of α/Fe. From the figure it is clear how more massive galaxies form earlier, reaching higher values of SFR. Therefore, since galaxy clusters are formed by the most massive ellipticals in the universe, it is expected that they form most of their stellar mass during a brief and intense burst of star formation

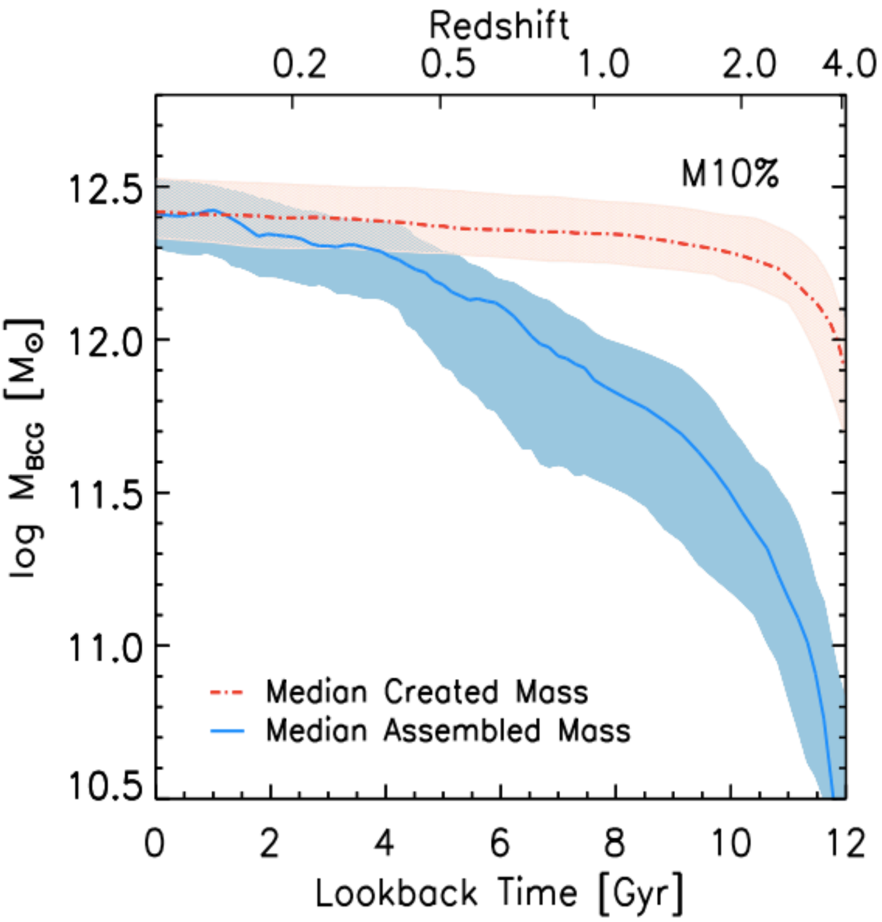

Fig. 1.7: BCG mass evolution in cosmological simulations of galaxy clusters. The mass of the BCG is defined as the total stellar mass within $0.1 \times R_{500}$. The red line shows the stellar mass, which at $z = 0$ is within the BCG, already formed at a given lookback time. The blue line shows the stellar mass that is already assembled within the main progenitor of the BCG at a given lookback time. Shaded regions encompass the 16% and 84% percentiles for the sample of simulated clusters. Credits: Ragone-Figueroa et al. (2018).

at redshifts $z \gtrsim 2$.

Among all the galaxies within the cluster, a relevant role is covered by the brightest cluster galaxy (BCG). This is the brightest, most massive galaxy and is usually located at the center of the cluster[7] (e.g., Lin & Mohr 2004). From a morphological point of view, BCGs are massive red ellipticals, with

---

[7] During the thesis, we are going to identify the brightest cluster galaxy as the central one.

very little ongoing star formation. In the local universe, observations find residual SFR of the order of $\sim 0.1\ \mathrm{M_\odot yr^{-1}}$ (e.g., Fraser-McKelvie et al. 2014, McDonald et al. 2018). As discussed in Sect. 1.2.3, these low values of SFR are the result of the balance between radiative cooling and AGN heating, as highlighted by the frequent presence of radio-loud AGNs within BCGs (e.g., Von Der Linden et al. 2007, Best et al. 2007). The stellar mass of the BCG is found to correlate with the total mass of the cluster (e.g., DeMaio et al. 2018, Kravtsov et al. 2018), and given its particular location resemble the formation history of the cluster itself. It is generally accepted that BCGs are primarily assembled through mergers rather than from in situ star formation. Indeed, observations find that the most massive BCGs (often called 'cD' in literature) show multiple nuclei indicative of recent mergers (e.g., Tonry 1987). These merger events are also thought to be at the origin of the ICL (e.g., Lin & Mohr 2004, Murante et al. 2007). A similar evolutionary pattern is also suggested by both semi-analytical models (e.g., De Lucia & Blaizot 2007) and cosmological simulations (e.g., Ragone-Figueroa et al. 2018), which predict that most of the stars ($\gtrsim 50\%$) are formed by $z \sim 3$, and are later assembled through galaxy mergers. This is shown in Fig. 1.7, where the BCG mass already formed at a given lookback time (dashed red line) is compared to the BCG mass that is already assembled within the main BCG progenitor (solid blue line). From the figure it is clear how the mass is formed much earlier then it is assembled within the BCG. Therefore, also the formation history of the BCG, much like the other massive ellipticals within clusters, suggests that most of the stars within galaxy clusters are formed at high redshift within a short period of time.

1.2 Intra-cluster medium

The other luminous component of galaxy clusters is the diffuse hot gas within the potential well of the cluster, the ICM. This component accounts for $\sim 15\%$ of the total cluster mass (see Fig. 1.8), and it is accreted during the process of structure formation, as the diffuse gas (consisting mostly of hydrogen and helium) follows the collapse of the dynamically dominant dark matter. During this process the kinetic energy of the gas is transformed into thermal energy through adiabatic compression and shocks, reaching temperatures of $T \sim 10^7 - 10^8$ K. At this high temperatures the gas is in the form of a

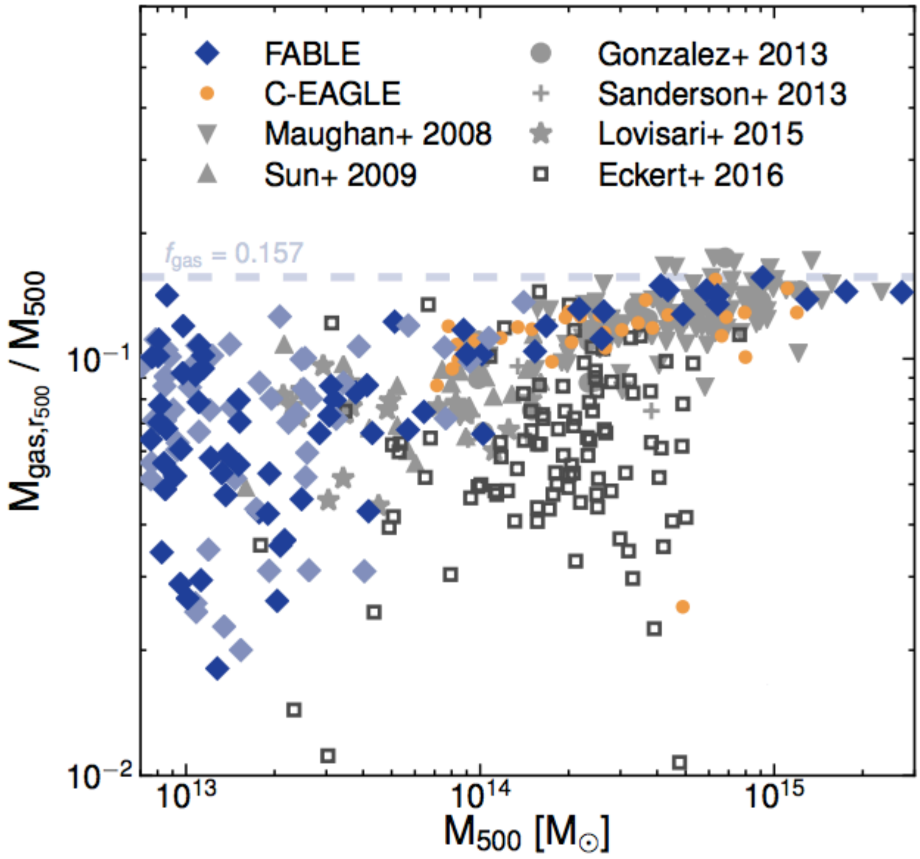

Fig. 1.8: Gas fraction within galaxy clusters both in simulations (FABLE and C-EAGLE) and observations (grey points). Horizontal dashed line represents the cosmic baryon fraction in the used cosmology. Credits: Henden et al. (2019).

fully ionized plasma, emitting in the X-ray band via two physical processes: Bremsstrahlung and emission lines of heavy elements (e.g., Sarazin 1988). The former entails the scattering of electrons to ionized atoms. The radiative power due to this process depends both on temperature ($\propto T^{1/2}$) and ions and electron densities ($\propto n_i n_e$) and enables to recover important pieces of information on the thermodynamic properties of the ICM. The emission lines of heavy elements encodes information on the metallicity content of the ICM, and becomes progressively more relevant at temperatures $\lesssim 1-2$ keV. We will not study in detail the metals in galaxy clusters in this thesis, even though chemical evolution studies are very important in order to obtain information about clusters evolution. For example, theoretical studies demonstrated that most of the gas within the ICM is not stripped or expelled by galaxies within the cluster, but must have a cosmological origin (Matteucci & Vettolani 1988). Moreover, numerical simulations studying metallicity profiles of clusters showed the need of a strong feedback mechanism, now adopted as active galactic nuclei (AGN) feedback, to match the observed metallicity profiles (e.g., Tornatore et al. 2004, Biffi et al. 2018). Apart from the X-ray emission, the ICM can also be detected and studied through the SZ effect. At first order, this effect is due to the CMB photons which are scattered upwards in energy by the encounters with the high energy electrons within the ICM through inverse Compton scattering. The amplitude of the intensity change in the CMB is proportional to the integral of the electron pressure along the line of sight and does not depend on redshift (e.g., Birkinshaw 1999). Therefore, the SZ effect can be used to identify distant clusters in maps of the CMB (e.g., Carlstrom et al. 2002), and with high enough angular resolution the pressure profile of nearby clusters can be reconstructed (e.g., Planck Collaboration et al. 2013).

In the following I review some key information that can be obtained through the study of the ICM.

1.2.1 Hydrostatic masses

As most of the mass within galaxy clusters is in the form of dark matter, it is not possible to directly measure its total mass. The most direct way is to use gravitational lensing, which is only sensitive to the gravity independently of the nature of the dark matter or the dynamical state of the system of interest (see, e.g., Hoekstra et al. 2013 for a review). However, the two gravitational lensing regimes have both some drawbacks. The strong gravitational lensing gives information about the total mass only within the inner part of the cluster, where the gravitational potential is stronger, while the weak lensing mass derivation can be affected by large errors unless the galaxy shapes and source redshifts are accurately known. Without the possibility of directly measuring the total mass, different observable probes indirectly related to the total mass are used.

One possibility is to use the profiles of thermodynamic properties (temperature and density) under the assumption of hydrostatic equilibrium. This is a strong hypothesis, even though observations show that galaxy clusters

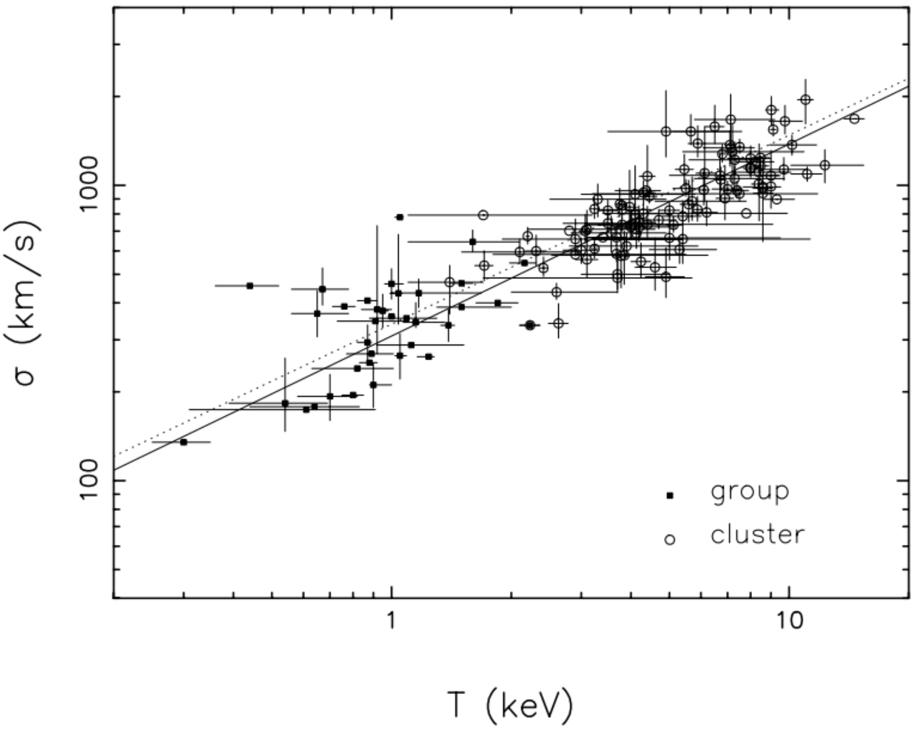

Fig. 1.9: Correlation between temperature and galaxy velocity dispersion within galaxy groups and clusters. The best fit relation is $\sigma \propto T^{0.65\pm0.03}$ for clusters and $\sigma \propto T^{0.64\pm0.038}$ and groups. The relation is very near to the theoretical expectation ($\sigma \propto T^{0.5}$) derived assuming that both the ICM and galaxies are in equilibrium within the common gravitational well of the cluster. Credits: Xue & Wu (2000).

are nearly relaxed in the local universe (see Fig. 1.9). Under the hydrostatic equilibrium assumption, the repulsive force due to the pressure gradient is balanced by the gravitational potential force, i.e. $\nabla\phi(\mathbf{x}) = -\nabla p(\mathbf{x})/\rho_g(\mathbf{x})$, where $\phi(\mathbf{x})$, $p(\mathbf{x})$, and $\rho_g(\mathbf{x})$ are the gravitational potential, the pressure, and the gas density respectively. Assuming the equation of state for an ideal gas and spherical simmetry the previous equation can be written as

$$M_{\mathrm{HE}}(<r) = -\frac{rk_BT(r)}{G\mu m_p}\left[\frac{d\ln\rho_g(r)}{d\ln r} + \frac{d\ln T(r)}{d\ln r}\right], \qquad (1.1)$$

where $M_{\mathrm{HE}}(<r)$ is the total mass within the radius r, k_B is the Boltzmann constant, m_p is the proton mass, μ the mean molecular weight, and $T(r)$ is the temperature profile. The gas density can be directly extracted from the X-

ray surface brightness profiles due to the dependence of the Bremsstrahlung to the density square. The temperature instead is recovered through a spectral analysis.

Of course, deviations from hydrostatic equilibrium can be expected. Indeed, astrophysical processes within the cluster can lead to non-thermal pressure support in form of turbulence, bulk motion, cosmic rays or other phenomena. Moreover, the time-scale for relaxation is of the order of the Gyr, and, since clusters are located at the nodes of the cosmic web, merger events are not rare and a cluster may still not have had enough time to completely relax after its last major merger or series of minor mergers. In these cases, the mass measured through the hydrostatic equilibrium hypothesis will be under-estimated. The bias introduced by assuming hydrostatic equilibrium can be accounted for by using a control sample and comparing the estimated mass with the mass obtained through gravitational lensing, or using numerical simulations. The former analysis shows that the hydrostatic mass is, on average, biased low by $\sim 30\%$ (e.g., Eckert et al. 2016). A similar result is also found using numerical simulations, which show that the mass estimated from X-ray analysis is sistematically lower that the true mass (e.g., Rasia et al. 2006, Nagai et al. 2007, Rasia et al. 2012, Ansarifard et al. 2020, and Pratt et al. 2019 for a review).

1.2.2 Self similarity

Another widely used method to derive the cluster mass is by resorting to scaling relations with other observables, such as its temperature, X-ray bolometric luminosity, or gas mass. These relations are usually defined as power laws, and can be predicted from simplified models like the self-similar model of Kaiser (1986). This model is based on three assumptions: (i) the underlying model is an Einstein-de Sitter universe with $\Omega_m = 1$; (ii) the initial density fluctuations are scale free; (iii) the processes that shape cluster properties do not introduce characteristic scales in the problem. Under these assumptions, and considering the hydrostatic equilibrium approximation, from Eq. 1.1 it follows:

$$T \propto \frac{M}{R} \propto (\Delta\rho_{\rm cr})^{1/3} M^{2/3}, \tag{1.2}$$

where T is computed at the virial radius R, and $\rho_{\rm cr}$ is the critical density of the universe at a given redshift, $\rho_{\rm cr} = 3H(z)^2/8\pi G$. The virial radius is defined assuming the definition of cluster mass derived from the spherical collapse model, i.e. a spherical region of space encompassing an average density Δ times the critical density of the universe, where Δ depends on the assumed cosmological model. Using the expression for the critical density and for the Hubble parameter, $H(z) = H_0 \times E(z)$ (Eq. A.7), it is also possible to enlighten the redshift dependence of the scaling relation:

$$T \propto \frac{M}{R} \propto E(z)^{2/3} M^{2/3}. \tag{1.3}$$

Under the same assumptions a relation between the gas and the total mass can be obtained (e.g., Kravtsov & Borgani 2012):

$$M(< R) \propto M_g(< R). \tag{1.4}$$

The combination of the previous two expressions leads to the relations with other properties, like the bolometric X-ray luminosity. Assuming that the emission is dominated by Bremsstrahlung radiation:

$$L_{\rm bol} \propto \rho_g^2 \sqrt{T} R^3 \propto M_g^2 \frac{\sqrt{T}}{R^3} \propto M^{4/3} E(z)^{7/3}, \tag{1.5}$$

where in the last passage Eq. 1.3 and Eq. 1.4 have been used.

However, while it is remarkable how this model based on simplistic assumptions works in predicting some scaling relations, it was also realized that real clusters follow slightly different scaling relations when quantities linked to the gas density are involved, e.g. the luminosity. For example, using Eq. 1.3 and Eq. 1.5 it is possible to derive the relation between X-ray bolometric luminosity and temperature, $L_{\rm bol} \propto T^2$. Observationally, this relation is steeper with an exponent typically > 2.5 (e.g., Markevitch 1998). The departure of scaling relations from the theoretical prediction of self-similarity is justified by the fact that scale-dependent astrophysical processes are in place. I briefly review these processes in the next section.

1.2.3 AGN feedback

The first scale-dependent process is radiative cooling, which is especially relevant in the core region of galaxy clusters given the dependence of the radiative power on $\propto \rho^2$ (assuming that radiative cooling is dominated by Bremsstrahlung radiation). However, if radiative cooling would be the only process active within cluster cores it would cause a rapid condensation of cold gas with predicted cooling rate within the inner part of the cluster of $100{-}1000\ M_\odot\,\mathrm{yr}^{-1}$ (e.g, White et al. 1997, Peres et al. 1998, Allen et al. 2001, Hudson et al. 2010). Such high cooling rates would imply blue and highly star forming BCGs, while current observations suggest star formation rates of $\sim 0.1\ M_\odot\ \mathrm{yr}^{-1}$ for massive clusters (e.g., Fraser-McKelvie et al. 2014). The absence of such high SFR is explained invoking a heating feedback mechanism, now identified as the feedback by the super massive black holes (SMBHs) at the center of galaxy groups and clusters. This feedback prevents catastrophic cooling, injecting energy in the ICM in a self-regulated fashion, such that cooling and heating energies balance each other within 10% (see Fabian 2012 for a review). Observationally, the presence of an AGN at the center of clusters can be inferred from the detection of X-ray cavities around the cluster core, which are commonly interpreted as the effect of energetic outflows of radio plasma from the central AGN that displaces the hot X-ray emitting gas (e.g, Best et al. 2007, Mittal et al. 2009, Bîrzan et al. 2012). One exceptional example is shown in Fig. 1.10, which shows the inner 700 kpc region of the MS0735.6+7421 cluster, superimposing the X-ray (blue), I-band (white), and radio (red) wavelengths. In the figure two radio jets emerging from the nucleus are clearly visible, extending for tens of kpc. The jets extend then in radio lobes, corresponding to the presence of X-ray cavities, with diameter size of ~ 200 kpc.

The estimated mechanical energy exchange between the bubbles and the ambient gas is linearly correlated to the X-ray luminosity (which corresponds to the energy loss) inside the cooling region (e.g., Fabian 2012, Bîrzan et al. 2012). An example of this correlation by Hlavacek-Larrondo et al. (2015) is shown in Fig. 1.11. Here the cavity power (P_{cav}) is computed considering the work done by a relativistic fluid to inflate the radio bubbles, while the cooling luminosities correspond to the bolometric X-ray luminosity ($0.01 - 100$ keV) within the radius at which the cooling time is 7.7 Gyrs. This strong correlation

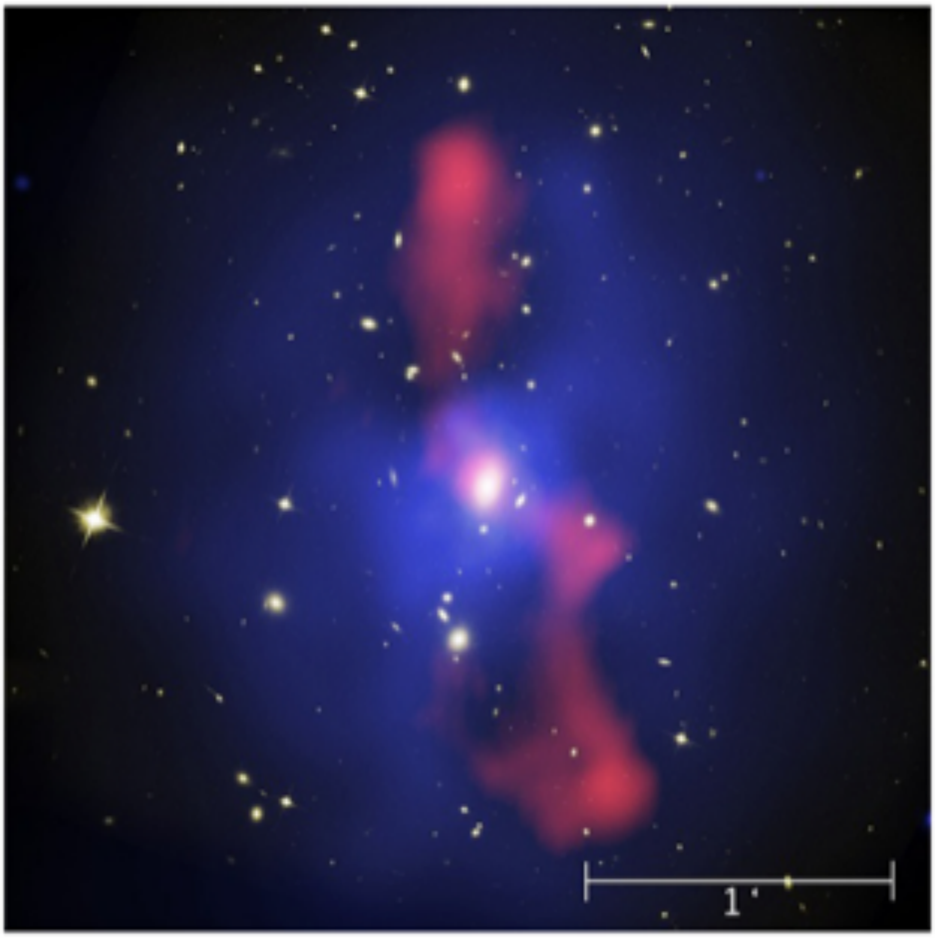

Fig. 1.10: Image of the inner ~ 700 kpc of the MS0735.6+7421 cluster combining the X-ray (blue), I-band (white), and radio wavelengths (red). Credits: McNamara et al. 2009.

between the bubble power and cooling rate supports the theoretical view of self regulation between heating and cooling in the central regions of galaxy clusters and is one of the few direct evidences of AGN feedback. Besides the X-ray cavity, AGN activity is also manifest through radio emission from the central source. However, the radio power weakly correlates with the energy deposited in the ICM by the radio cavities and is up to a factor of few thousand smaller, suggesting that most of the feedback is mechanical and is characterized by high efficiencies (e.g., McNamara & Nulsen 2007). Since the presence and the role of AGN feedback in the cluster environment is well established, it is not surprising that the mass of the SMBHs at the

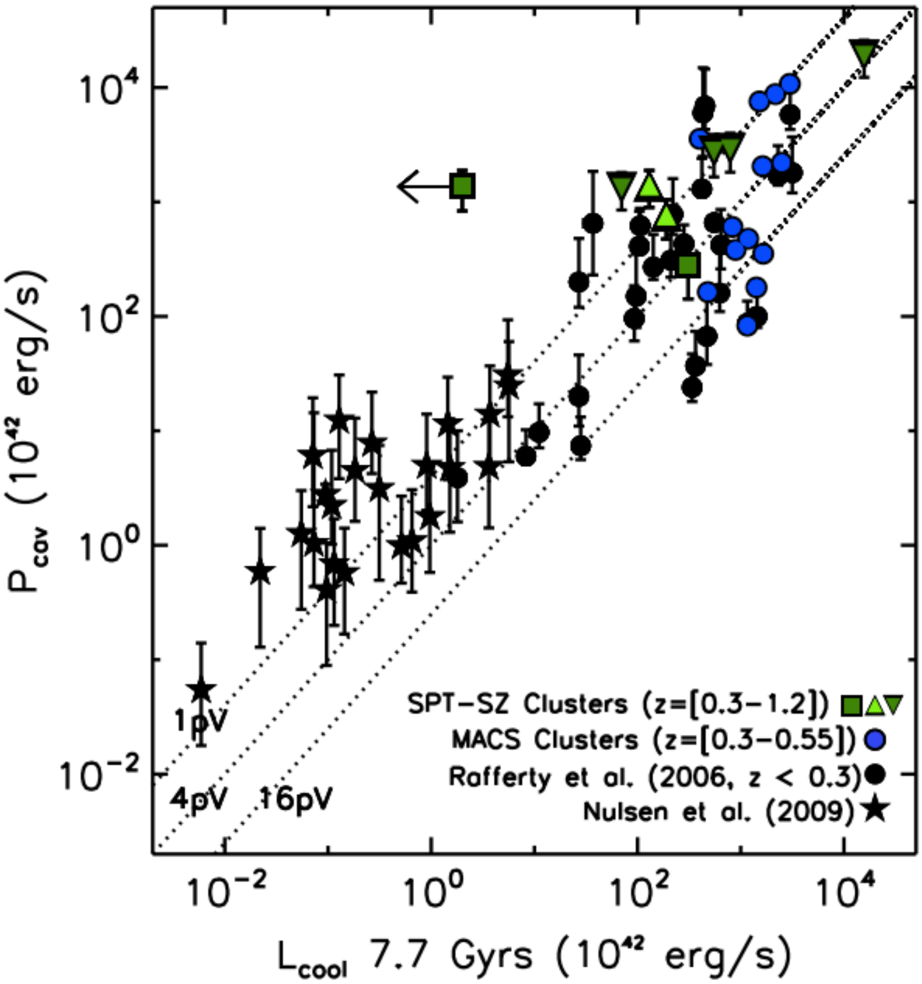

Fig. 1.11: Comparison between the mechanical power being injected by the AGN in the BCG ($P_{\rm cav}$) and the cooling luminosity (L_{cool}) of the cluster at 7.7 Gyrs. Different symbols are from different samples and redshift (see legend and Hlavacek-Larrondo et al. 2015 for further details). The diagonal lines indicate $P_{\rm cav} = L_X$ assuming pV, $4pV$ or $16pV$ as the energy deposited, where p is the thermal pressure of the ICM at the radius of the bubble and V is the volume of the cavity. Credits: Hlavacek-Larrondo et al. (2015).

clusters center also correlate with BCGs and galaxy clusters properties. These correlations are reviewed in Sect. 1.4.

From a theoretical point of view, the inclusion of AGN feedback in numerical simulations of galaxy clusters enabled to reach a better agreement with a number of observations such as the correlation between cluster temperature and bolometric X-ray luminosity (e.g., Puchwein et al. 2008, Truong et al. 2018) and radial metallicity profiles (e.g., Biffi et al. 2017). The inclusion of AGN feedback also successfully offset cooling at low redshift, producing BCG masses that are roughly in agreement with recent observations (e.g., Martizzi et al. 2012). However, I will show in Chapter 4 that it is still challenging for numerical simulations (e.g., Ragone-Figueroa et al. 2018, Henden et al. 2019) and semi-analityical models (e.g., Hirschmann et al. 2016) to reproduce the low specific star formation rates observed in massive galaxies ($M_\star > 10^{11}$ $\mathrm{M}_\odot$), which are typically overestimated by an order of magnitude.

1.3 Protoclusters in the distant Universe

In Sect. 1.1 we discussed how the astro-archeology studies of massive elliptical galaxies and the formation history of BCGs suggest that most of the stars which end up in massive clusters by $z = 0$ are formed at high redshifts, $z \gtrsim 3$, and are assembled within the main halo only at later times. Therefore, studying the protocluster stage of cluster evolution is of fundamental importance since the properties of $z = 0$ galaxy clusters strongly depend on the physical processes operating at $2 \lesssim z \lesssim 4$, epoch at which the SFR, the SMBH accretion rate, and ensuing feedback processes peak. In this section I will briefly review the available observational constraints and techniques used to identify galaxy clusters, together with the theoretical expectations about the evolution of (proto)cluster regions. This section is mainly based on the theoretical works by Chiang et al. (2013), Muldrew et al. (2015), Contini et al. (2016), Muldrew et al. (2018), and the review by Overzier (2016).

First of all, it is important to define a protocluster: a structure that at some point of its evolution will collapse into a galaxy cluster, i.e. a virialized halo with $M > 10^{14}$ $\mathrm{M}_\odot$. Even though this is straightforward theoretically and readily usable in numerical simulations, it can not be adopted in observations, as it requires to know *a priori* the evolution of the system. Therefore, it is useful to resort to simulations to link the *putative* protoclusters that are observed at high redshift with their local descendants.

Numerical simulations show that the volume occupied by a protocluster is fairly large, covering up to 45 h^{-1} comoving Mpc (cMpc) in size at $z = 2$ for a $z = 0$ Coma-like cluster (see Fig. 1.12). Given their large spa-

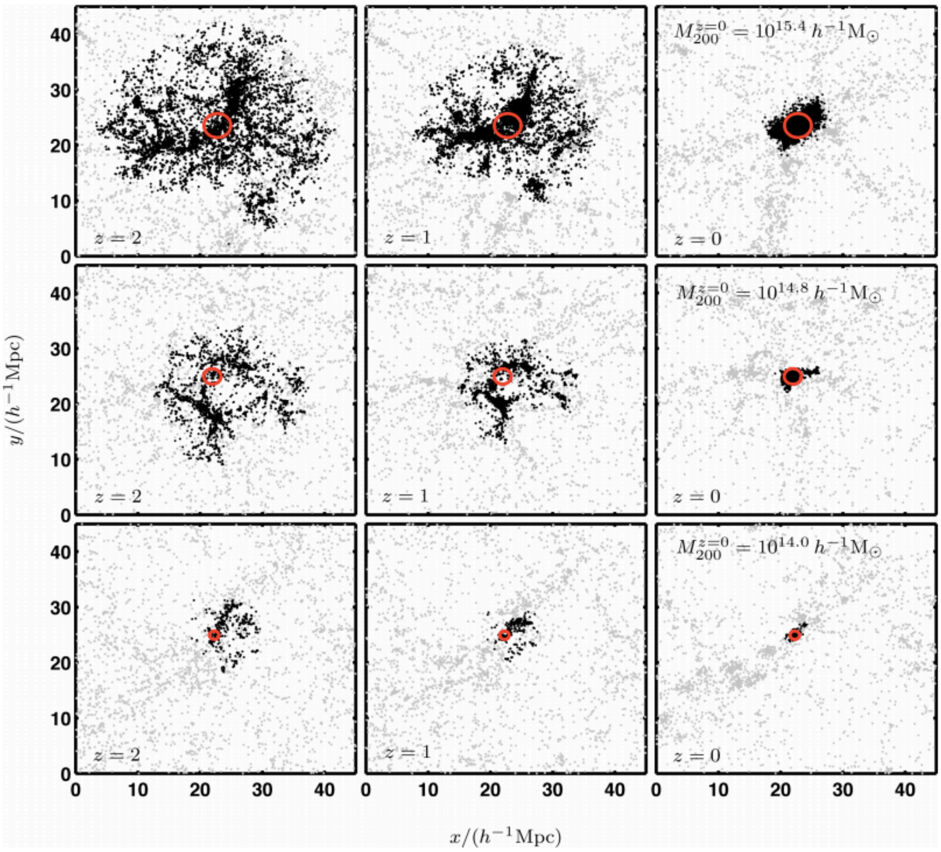

Fig. 1.12: Spatial extent of protoclusters at $z = 2$ (left panel), $z = 1$ (centre panel), and $z = 0$ (right panel), with different final masses as indicated in the Figure. All distances are comoving. Black points represent a galaxy of stellar mass greater than $10^8\ h^{-1}\ \mathrm{M}_\odot$ that will end up in the cluster while grey points represent those that will not. The red circle corresponds to the $z = 0$ centre and comoving viral radius of the cluster. Credits: Muldrew et al. (2015).

tial extent, protoclusters at high redshift are expected to be characterized by a large number of relatively small halos, which given their still reduced gravitational potential wells usually lack the presence of a virialized gas component and are not detectable through techniques based on ICM properties. Indeed, Contini et al. (2016) showed that at $z \gtrsim 2$ around 70% of protoclusters galaxies are centrals. However, numerical simulations also show that the mass of the *main progenitor* of Coma-like structures can reach masses of $\sim 10^{14}\ \mathrm{M}_\odot$ at $z \sim 2$ (see Fig. 1.13). These rare objects can be observationally detected as high redshift clusters. Since the main progenitor of a galaxy clus-

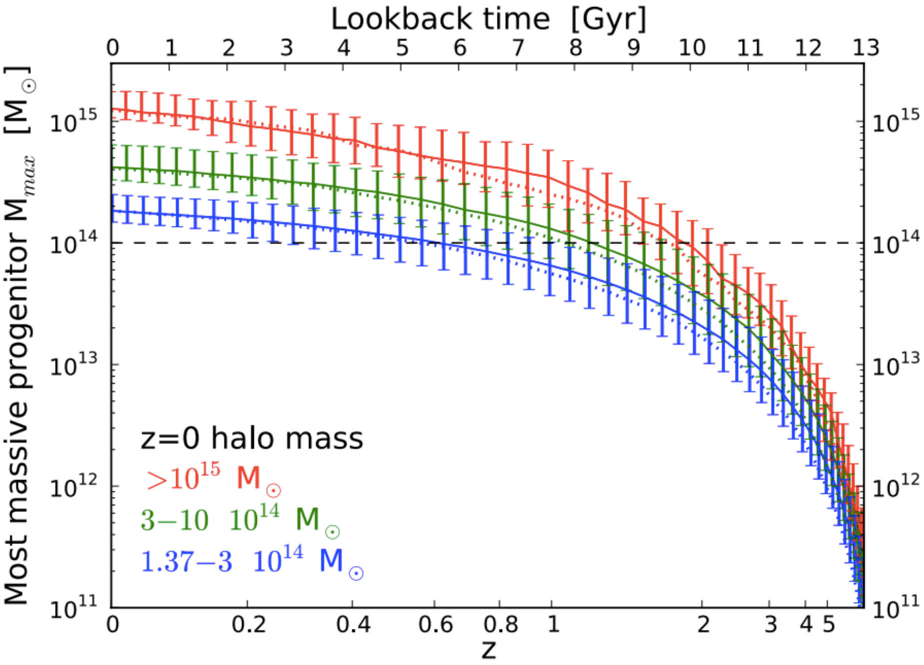

Fig. 1.13: Evolution of the mass of the main progenitor for clusters of different final masses in numerical simulations. The lines and errorbars show median values with $1-\sigma$ scatter. Credits: Chiang et al. (2013).

ter is generally easier to be observed and studied, it is useful to investigate through numerical simulations to which extent its mass is a good proxy of the cluster mass at $z = 0$. The results of this analysis, carried out by Muldrew et al. (2015), are shown in Fig. 1.14. As it can be seen from the figure, the scatter on the $M_{z=2} - M_{z=0}$ plane is large (0.54 dex RMS deviation from the true mass). This is also in line with the results of Chiang et al. (2013) shown in Fig. 1.13, where it can be seen that main progenitors with similar masses at $z \gtrsim 2$ can have descendants (clusters at $z = 0$) with quite different masses. As it is clear from Fig. 1.14, a better estimate of the final mass can be obtained considering the ratio between the most massive and the second most massive halos within the protocluster. Of course, this procedure can be difficult to be applied in observations for the challenges of identifying the second most massive halo and estimate its mass.

Since the protocluster regions are spread over such large distances, and most of the mass is not within a single halo, the most accurate estimate of the final mass of the cluster might be obtained by the exploitation of the

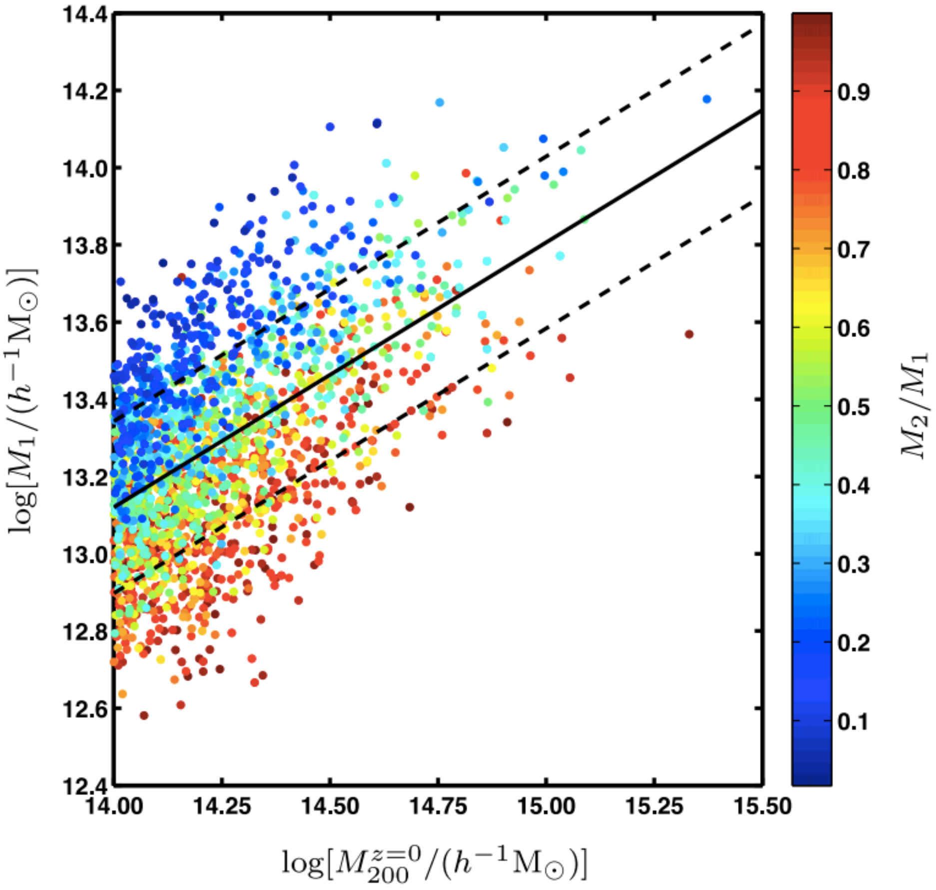

Fig. 1.14: Correlation between the mass of the most massive progenitor of a galaxy cluster at $z = 2$ and the $z = 0$ cluster mass. Points are color-coded according to the ratio between the most massive and the second most massive progenitors of the cluster at $z = 2$. Credits: Muldrew et al. (2015).

large scale information of the protocluster region. In particular, Chiang et al. (2013) showed that there is a clear correlation between the final cluster mass and the galaxy overdensity computed over a large enough region ($\gtrsim 15$ cMpc, see Fig. 1.15). The drawback of this analysis is that it requires spectroscopic identification of galaxies spread over a relatively large volume.

1.3.1 Observations of protoclusters

Observationally, different techniques can be used to search for clusters and protoclusters. At $z \lesssim 1.4$ the same properties of galaxy clusters used to identify objects in the local universe can be exploited. In particular, since

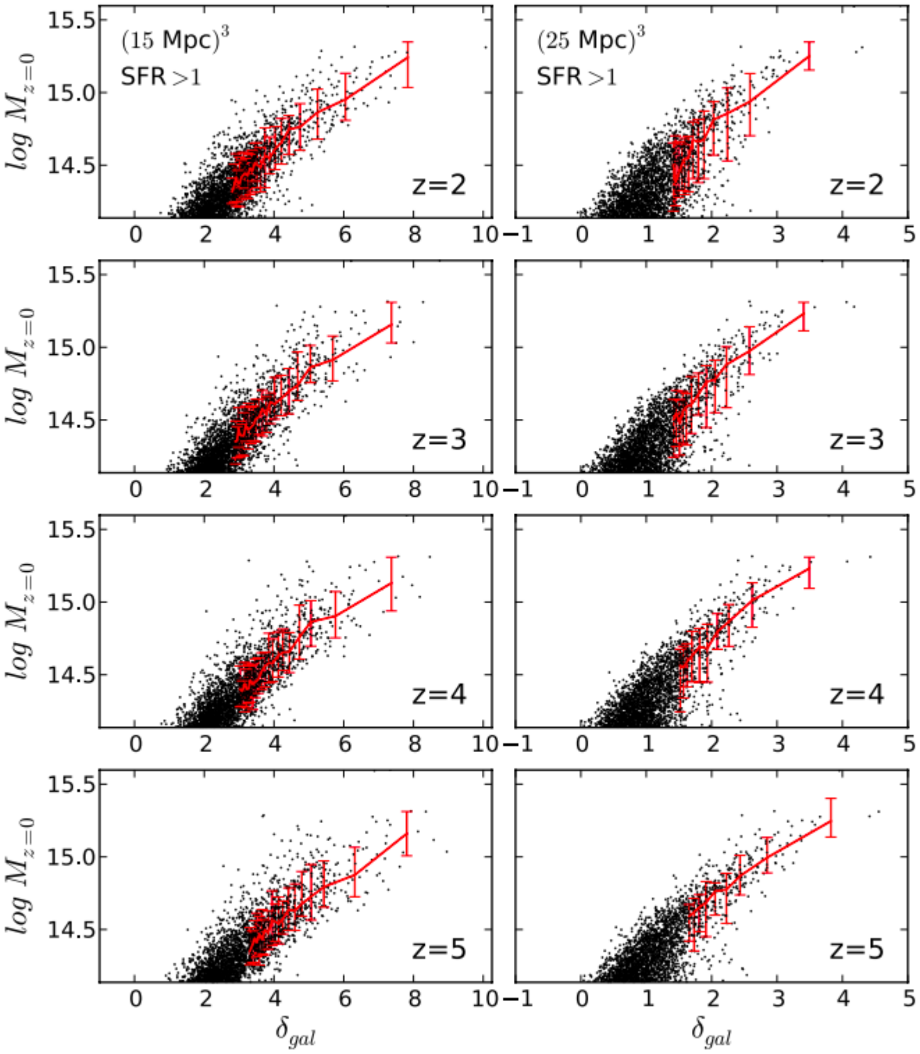

Fig. 1.15: Correlation between galaxy overdensity $\delta_{\rm gal}$ at $z = 2, 3, 4, 5$ and final cluster mass in numerical simulations. $\delta_{\rm gal}$ is computed considering two windows of 15 cMpc (left panel) and 25 cMpc (right panel). In both cases only galaxies with SFR > 1 M$_\odot$ yr^{-1} have been considered. Credits: Chiang et al. (2013).

the galaxy population is dominated by quiescent ellipticals, it is reasonable to look for concentrations of red sequence and other massive galaxies (e.g., Gladders & Yee 2000, Gladders & Yee 2005, Gilbank et al. 2011). Another possibility relies on the properties of the ICM, which can be detected through X-ray emission (Rosati et al. 2002, Mullis et al. 2005, Stanford et al. 2006) and especially through the SZ signal which does not decrease with the cluster redshift (e.g., Bleem et al. 2015). The redshift limit $z \sim 1.4$ is indicative; indeed, these techniques have been able to identify few clusters up to $z = 2$ (see Overzier 2016 for a review).

While clusters at $z \lesssim 1.4$ show characteristics very similar to local systems, at higher redshift they could be very different among them. Some observations report the discovery of already mature clusters, with an enhanced fraction of red and quenched galaxies with respect to the field, at least in the core (Papovich et al. 2010, Strazzullo et al. 2010, Gobat et al. 2011, Strazzullo et al. 2013, Strazzullo et al. 2013, Tanaka et al. 2013b, Newman et al. 2014, Andreon et al. 2014, Cooke et al. 2016), while other observations clearly show a mixed population of quenched and star forming galaxies (Tanaka et al. 2013a, Brodwin et al. 2013, Gobat et al. 2013, Strazzullo et al. 2016, Hatch et al. 2017). Interestingly, few observations also suggest a reversal in the SFR-density relation with an increasing sSFR toward the core of the cluster (Tran et al. 2010, Santos et al. 2014, Santos et al. 2015, Smith et al. 2019). This view is also supported by different observations. For example, the SFR density computed within clusters and protoclusters increases with redshift, reaching values $10^3 - 10^4$ times higher that what is found in the field around $z \sim 2$ (e.g., Clements et al. 2014, Kato et al. 2016). A similar conclusion is found considering the SFR within a (proto)cluster normalized by its total mass. This quantity is shown in Fig. 1.16, where data of known clusters and protoclusters are plotted. Much like the SFR density, Also this quantity is an increasing function of redshift, with an empirical parametrization $\propto (1+z)^7$ (Cowie et al. 2004, Geach et al. 2006), suggesting an enhancement of the SFR within (proto)clusters at high redshift (e.g., Popesso et al. 2012, Smail et al. 2014, Ma et al. 2015, Santos et al. 2015, Smith et al. 2019, Cooke et al. 2019). In fig. 1.16 is also shown as a black dashed line the equivalent quantity as computed for the field. Following Popesso et al. (2012), this is computed dividing the cosmic SFR density by Madau & Dickinson (2014) by the mean comoving matter density ($\Omega_M \times \rho_c$, being ρ_c the critical density). The comparison between field and protoclusters highlights the presence of a reversal in the SF-density relation at $z \gtrsim 1$.

At $z \gtrsim 2$, as the search for specific morphological galaxy types or ICM related properties became unfeasible, the search for protoclusters rely on the detection of galaxy overdensities in projection and redshift space. The clear limitation of this technique is that it relies on large survey of galaxies where

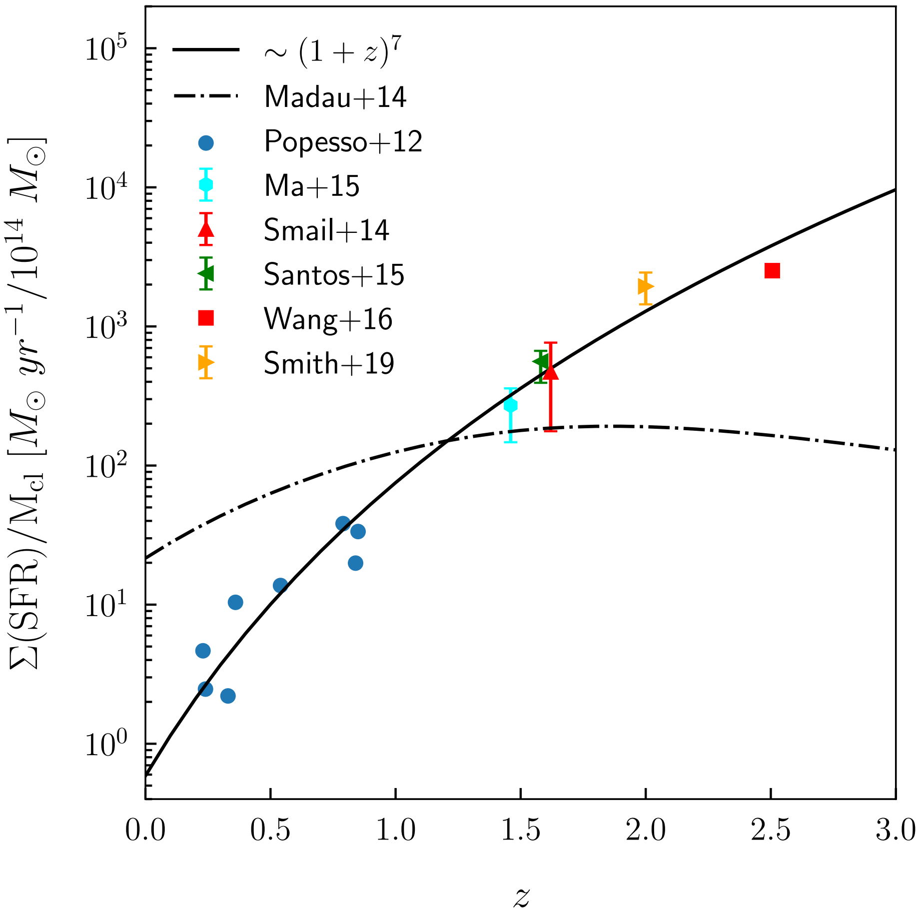

Fig. 1.16: SFR normalised by cluster mass as a function of redshift. Coloured points are observational data from Popesso et al. (2012), Ma et al. (2015), Smail et al. (2014), Santos et al. (2015), Wang et al. (2016), and Smith et al. (2019). The solid black line $\sim (1+z)^7$ shows an empirical fit to data suggested by Cowie et al. (2004) and Geach et al. (2006). The dashed black line is the evolution of the same quantity computed for the field from Madau & Dickinson (2014) data (see main text for further details).

spectroscopic redshift estimates are needed. There are mainly two ways to overcome these limitations. First, it is possible to first identify galaxy overdensities on the sky, and then followup the densest regions by computing the spectroscopic redshift for the galaxies of interest. The second method consists to look for a particular class of galaxies that are believed to be good tracers of dense environments. Few examples are high redshift radio galaxies that have many characteristic that make them potential progenitors of local

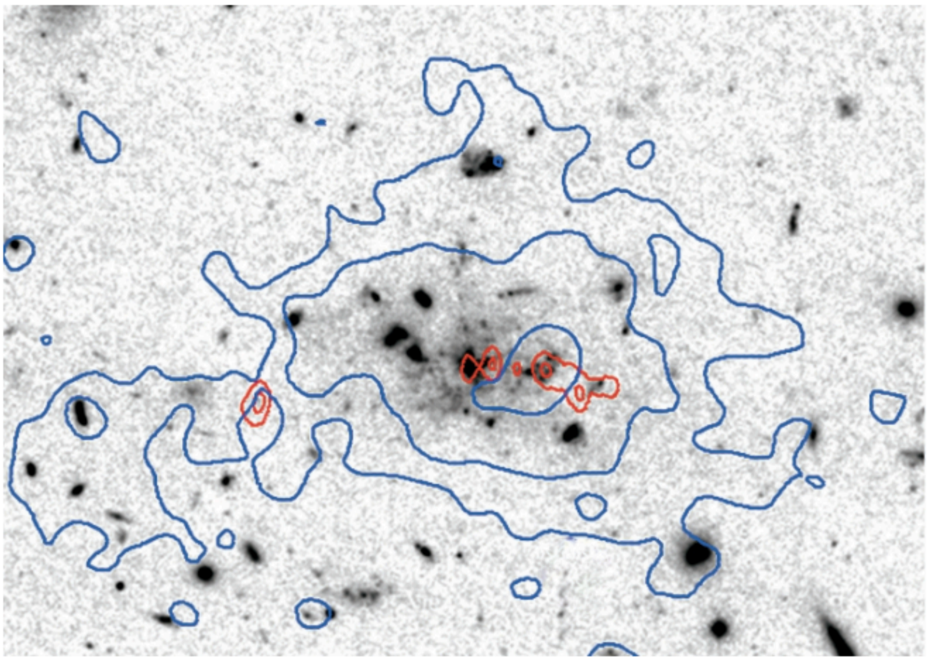

Fig. 1.17: VLT Lyα contours (blue) delineating the gaseous nebula and the VLA 8 GHz contours (red) delineating the non-thermal radio emission are superimposed on the composite ($g_{475} + I_{814}$) ACS image. The size of the region showed is 33" $\times$ 23" (25" $\sim$ 200 kpc). Credits: Miley et al. (2006).

BCGs (e.g., Best et al. 1998, Miley & De Breuck 2008, Collet et al. 2015). A well known example of a protocluster detected through this method is the structure surrounding the so-called Spiderweb Galaxy at $z = 2.16$ (e.g., Pentericci et al. 2000, Miley et al. 2006, Dannerbauer et al. 2014), which is shown in Fig. 1.17. In the figure are clearly visible multiple clumps which are presumably satellite galaxies that are still merging with the central radio galaxy. These galaxies are surrounded by a giant gaseous halo which extends by at least ~ 200 kpc. This structure has also been extensively studied through numerical simulations, concluding that this object is likely the progenitor of a massive galaxy cluster ($M_{z=0} \sim 10^{15}$ M$_{\odot}$, Saro et al. 2009).

Other tracers are QSO, and Lyα blobs which trace large reservoirs of cool intergalactic gas associated with dense locations in the cosmic web, where the gas is ionized and illuminated by a powerful AGN or starbursts. In this context, an important population of galaxies are dusty star forming galaxies (DSFGs, see Casey et al. 2014), highly star forming and heavily obscured by dust, emitting in the far infrared (FIR) and sub-millimetric bands.

These galaxies represent the strongest starbursts and are expected to be the progenitors of local massive ellipticals (Cimatti et al. 2008, Ricciardelli et al. 2010, Fu et al. 2013, Ivison et al. 2013, Toft et al. 2014, Gómez-Guijarro et al. 2018). They trace the dusty star-forming phase of protoclusters, and their expected short star-burst phase of few hundreds of Myrs (e.g., Granato et al. 2004, Thomas et al. 2010) makes them relatively rare objects. Albeit their rareness they have been successfully used to identify dense and highly star forming enviroments up to redshift $z \sim 4$ (Clements et al. 2014, Oteo et al. 2018, Miller et al. 2018) and have been observed in a number of already known high reshift protoclusters (Chapman & Casey 2009, Dannerbauer et al. 2014, Umehata et al. 2015, Coogan et al. 2018, Lacaille et al. 2019, Smith et al. 2019).

Even if all the aforementioned techniques have enabled to detect a number of protoclusters at different evolutionary stages, the resulting sample is still fairly heterogeneous being based on different methods, each having its own limitation and bias. Therefore, it is still currently difficult to draw a complete picture of galaxy cluster evolution using the available data set. A useful tool to interpret all the observations are cosmological simulations. However, before obtaining a meaningful interpretation of observational data on cluster evolution, it is important to study whether theoretical models match the already available high redshift observational constraints.

This will be the aim of the second part of this Thesis. In particular, in Chapter 4 I make use of 12 simulations out of the set of 29 hydrodynamical zoom-in simulations of galaxy clusters named Dianoga, presented in Chapter 2, to investigate the predictive power of state of the art cosmological simulations around the peak of the SFR in the protocluster stage of structure formation. The aim of this Chapter is:

- to test if cosmological simulations can reproduce the integrated values of SFRs which are observed within protocluster regions;
- to study if cosmological simulations reproduce protocluster galaxies properties, like their SFRs, gas fractions, and star formation efficiencies.

1.3.2 Theoretical models of protoclusters evolution

The study of galaxy evolution within protoclusters with semi-analytical models and numerical simulations is relatively recent. Both semi-analytical mod-

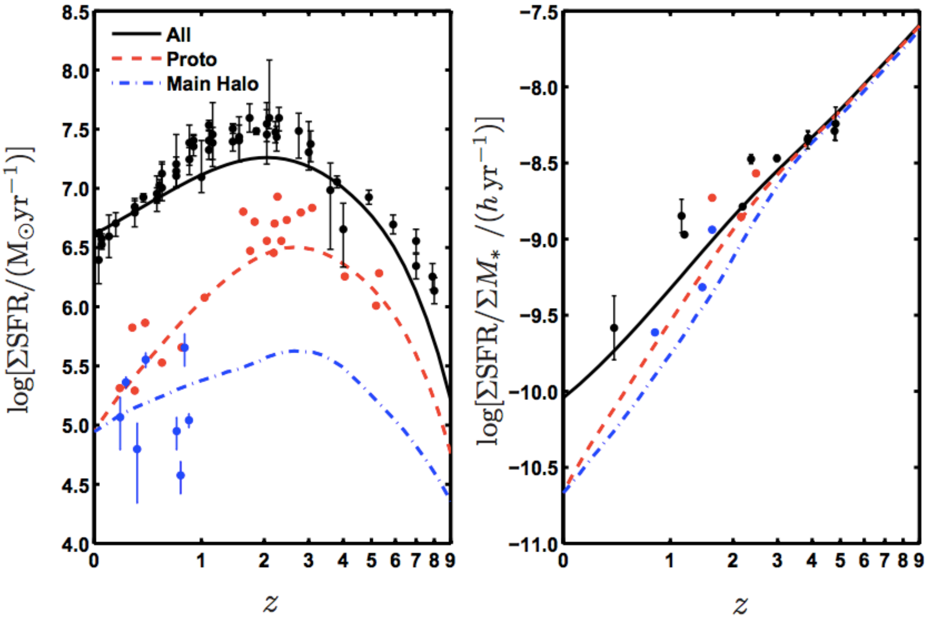

Fig. 1.18: *Left panel:* total SFR as contributed by all galaxies within the simulation (black line), the galaxies within protocluster regions (red dashed line), and galaxies within the main halo of each protocluster (blue dashed line). Colored points are observational data (see Muldrew et al. 2018 for further details). *Right panel:* specific SFR (i.e., SFR per unit of stellar mass) color-coded as in the left panel. Credits: Muldrew et al. (2018).

els and numerical simulations are based on models for baryonic physics that depend on a range of parameters (see Chapter 2). These are typically tuned in order to reproduce a few observational constraints in the local universe, such as the galaxy stellar mass function, but they are not typically constrained against measurements at higher redshift. Therefore, even though galaxy and galaxy cluster properties are well reproduced at $z = 0$, there is no guarantee that their formation history ought to be correct. Only recently, also due to the availability of observational data, constraints for theoretical models at $z > 0$ have started to be used.

One of these models, the semi-analytical model developed by Henriques et al. (2015), was used by Chiang et al. (2017) and Muldrew et al. (2018) to study the evolution of the SFR within protocluster regions, comparing it with the one derived for the field. The results by Muldrew et al. (2018) are shown in Fig. 1.18. The authors show that at $z > 4$ the gradients of the SFHs in all the environments are similar, meaning that the rate at which the

SFR changes does not depend on the density. This is also confirmed by the fact that the specific SFR (sSFR) as computed in protocluster regions and the field does not show relevant differences at $z > 4$. These results suggest that there is no reversal in the morphology-density relation at high redshift, even though few observational evidences suggest otherwise (see previous section). However, we note that a complete agreement about this result is not reached between different theoretical works, as the results obtained by Hwang et al. (2019) using the IllustrisTNG simulation (Pillepich et al. 2018) show that the SFR is an increasing function of the local density at $z > 1$, with this dependence becoming stronger at higher redshift.

The second feature that can be noted from Fig. 1.18 is that at $z < 4$ the SFR decreases more rapidly within protocluster regions, such that the SFH peaks earlier ($z \sim 2.64$) compared to the field ($z \sim 2.07$). After that, the SFR continues to decrease more rapidly in the higher density regions. The net effect is that the SFR of the field is broader than in protoclusters, with this difference not driven by an enhancement of the star formation in dense environment at high redshift, but by the suppression of the star formation in protocluster regions at $z \lesssim 3$. Contini et al. (2016) used the semi-analytical model presented in Contini et al. (2014) applied to 27 N-body simulations of galaxy clusters and studied how the passive-galaxy sequence forms. In particular, the authors showed that most of passive galaxies are quenched in the process of becoming satellites. During the accretion, the hot halo gas is stripped from the galaxy so that new material for star formation will not be available through gas cooling.

While the properties of galaxies at relatively low redshift and the processes that drive their quenching within galaxy clusters are roughly understood, the discrepancies shown by theoretical models for the inversion of the star formation rate-density relation at high redshift hint that something is missing in our understanding of galaxy evolution. In this respect Granato et al. (2015) used a set of zoom-in cosmological simulations to compare the predicted FIR fluxes to the observations of the few putative protocluster regions observed by Clements et al. (2014). The results showed that numerical simulations do not to reproduce the high SFRs observed in protoclusters characterised by overdensities of DSFGs, as simulations miss to predict sufficiently high peaks of star formation activity at early epochs.

More recently, Hayward et al. (2020) compared the submillimetre galaxies (SMG) number counts as predicted by the Illustris and IllustrisTNG cosmological simulations with observations. In accordance with the results by Granato et al. (2015), they found that numerical simulations underpredict the number of SMGs by ~ 1 dex at $S_{850} \gtrsim 4$ mJy. A similar analysis has been carried out by Lovell et al. (2020), using the SIMBA cosmological simulations (Davé et al. 2019). Differently from Hayward et al. (2020), Lovell et al. (2020) find a good agreement between the predicted and observed SMG number counts at $S_{850} \gtrsim 1$ mJy, suggesting that the agreement between numerical simulations and observations can be achieved without resorting to exotic solutions, like a top-heavy initial mass function (IMF). However, the authors also find that the galaxy SFR function is underpredicted by 0.7 dex at SFR $< 10\ \mathrm{M}_{\odot}\ \mathrm{yr}^{-1}$. This adds to known problems for both semi-analytical models and numerical simulations, which struggle to reproduce the right normalization of the main sequence of star forming galaxies, i.e. the correlation between galaxy stellar mass and SFR, around the peak of the cosmic star formation rate density. Indeed, all semi-analytical models and numerical simulations underpredict the normalization of the main sequence by a factor of $\sim 2-3$ (Hirschmann et al. 2016, Davé et al. 2016, McCarthy et al. 2017, Donnari et al. 2019, Davé et al. 2019). This feature will be discussed in Chapter 4.

1.4 SMBH in galaxy clusters

The feedback processes related to the SMBHs hosted in the BCGs at the center of galaxy clusters represent the most clear evidence of the role of AGN feedback in regulating the cooling flow and the closely related star formation.The idea of co-evolution between SMBHs and galaxies is widely accepted also in galaxy evolution regardless of the environment. One of the main indirect observational evidences are the correlations between SMBH mass (M_{BH}) and the properties of the hosting galaxy, which have been known, and studied, since the first measurements of M_{BH}.

The first analysis presenting a large sample of galaxies (32) was published more than 20 years ago by Magorrian et al. (1998), and showed a clear correlation between M_{BH} and the bulge luminosity of the hosting galaxy, which is directly related to the bulge stellar mass assuming a mass to light ratio. This first discovery led to a large number of works, that con-

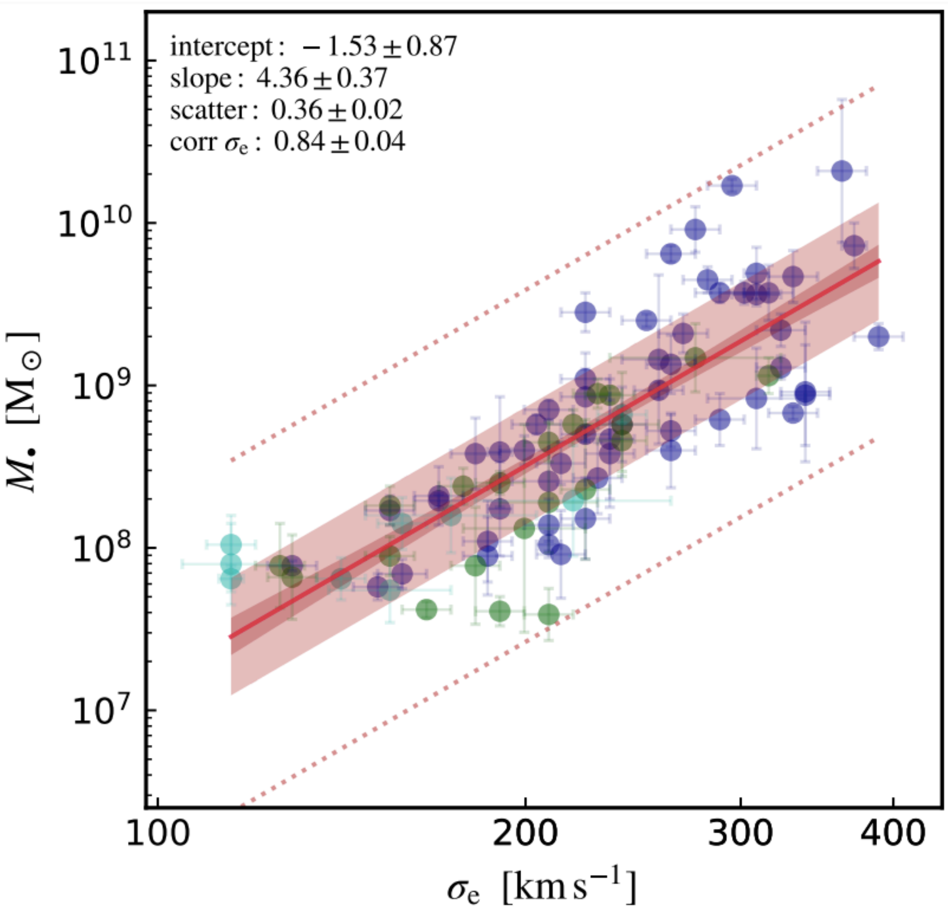

Fig. 1.19: Correlation between SMBHs masses and 1D stellar velocity dispersion of galaxies. The inset shows the mean and errors of all the posteriors from the Bayesian linear fitting *linmix* (https://github.com/jmeyers314/linmix), including the intercept, slope, intrinsic scatter ($1-\sigma$ interval plotted as a light red band, $3-\sigma$ as dotted lines). Red line and dark band are the mean fit and related $15.87-84.13$ percentile interval. Galaxies are plotted with different colors given their morphology: blue are ellipticals, green are intermediate lenticulars, and cyan are non-barred/barred spiral LTGs. From our work published in Gaspari et al. (2019).

firmed the observed correlation (e. g., Ho 1999, Merritt & Ferrarese 2001, Laor 2001, Kormendy & Gebhardt 2001, McLure & Dunlop 2002, Marconi & Hunt 2003, Ferrarese & Ford 2005, Graham 2007, Gültekin et al. 2009, Sani et al. 2011,Graham & Scott 2013, McConnell & Ma 2013), and also proposed other correlations with different quantities. Indeed, in the same year Gebhardt et al. (2000) and Ferrarese & Merritt (2000) reported the discovery of a very tight correlation between $M_{\rm BH}$ and the 1D stellar velocity dispersion, σ_e. In these works the authors claimed that this relation is in fact the fundamental one, as the associated scatter is only 0.30 dex, mostly ascribed to observational errors rather than to an intrinsic diversity between velocity dispersion and $M_{\rm BH}$. An updated version of the $M_{\rm BH} - \sigma$ correlation is shown in Fig. 1.19. After the first papers of 20 years ago the two relations ($M_{\rm BH} - M_\star$ and $M - \sigma_e$) have been diffusely studied and even if at times arguments in favor of one relation or the other (e.g., Kormendy & Ho 2013, McConnell & Ma 2013) were advanced more recent analyses still suggest that the stellar velocity dispersion is more fundamental than the stellar mass (e.g., Shankar et al. 2016).

Ferrarese (2002) also suggested that the total gravitational mass, traced by the circular velocity, is the real driver of the observed correlations. However, this seems not to be the case as it is known that $M_{\rm BH}$ do not correlate with galaxy disks, while galaxy disks show a close correlation with DM (e.g., Kormendy & Bender 2011, Sabra et al. 2015).

1.4.1 Causal or non-causal origin

The study of the correlations involving $M_{\rm BH}$ is important, as the dependence on different galaxy components provides useful insights on the growth of the SMBH at the galaxy center and consequently on putting constrains on galaxy evolution models. At first order the theoretical models explaining such correlations can be divided into two categories. The first do not assume any causal connection between the growth of the SMBH and the galaxy stellar component, with the correlation formed as a consequence of a large enough number of merger events. These models, to which I will refer as *non-causal*, forecast a strong and linear $M_{\rm BH} - M_\star$ correlation with a decreasing scatter at increasing galaxy stellar mass. The second category of models has its foundation on the idea of co-evolution between SMBH and hosting galaxy, which usually resort to AGN feedback as the process mediating both gas accretion into the central SMBH and star formation. These models, to which I will refer as *causal*, foresee a strong correlation with thermodynamic quantities like the stellar velocity dispersion or the X-ray temperature of the halo. In the following I will describe few examples from both the aformentioned categories.

The first experiment toward a non-causal origin of the observed correlations has been proposed by Peng (2007). In a statistical experiment the authors started from a distribution of galaxies with stellar masses drew from a Schechter mass function (Schechter 1976), to which a SMBH was associated with masses drew from a random distribution. From these initial conditions, they showed that after a sufficiently high number of mergers, the systems will eventually end up to a linear relation with a scatter that is inversely proportional to the number of mergers. Jahnke & Macciò (2011) used a semi-analytical model and showed that the number of mergers that a typical halo undergoes in a cosmological environment is enough to completely ascribe the observed correlation to galaxy mergers. The results by Jahnke & Macciò (2011) are shown in Fig. 1.20. In particular, they considered a merger tree constructed from the Lagrangian code PINOCCHIO (Monaco et al. 2002). To each DM halo with $M_{\rm halo} > 10^8$ $\rm M_\odot$ they assigned a stellar mass and a BH mass drew from two distributions centered at $M_\star/M_{\rm DM} = 10^{-3}$ and $M_{\rm BH}/M_{\rm DM} = 10^{-7}$ respectively with a scatter taken from a log-uniform distribution of 3 dex. Following the merger tree, whenever two DM halos merge their stellar and BH masses are summed. From Fig. 1.20 it is clear that even starting from an uncorrelated distribution (blue points), at the end of the simulation the system lie on a linear correlation (red points).

However, even if mergers can theoretically explain the observed correlations with the galaxy stellar mass, it is not obvious what would happen to other quantities like the stellar velocity dispersion. Moreover, the other important consequences of mergers besides the linear correlation between $M_{\rm BH}$ and $M_\star$ is that the scatter scales as $\sim 1/\sqrt{N}$, N being the number of mergers the systems undergo. Thus, it is expected the scatter on the relation to be a decreasing function of the mass, as more massive systems are expected to undergo more mergers. However, from an observational point of view this evidence is still lacking (e.g., McConnell & Ma 2013, Gaspari et al. 2019).

Besides the models by Peng (2007) and Jahnke & Macciò (2011), there is a variety of models based on AGN feedback that might explain the observed correlations. Among them, in the following I will describe the models by Churazov et al. (2005) and Gaspari & Sadowski (2017). The first is a simple toy model, which however is based on the same assumptions as the AGN feedback mechanism that is implemented in our cosmological simula-

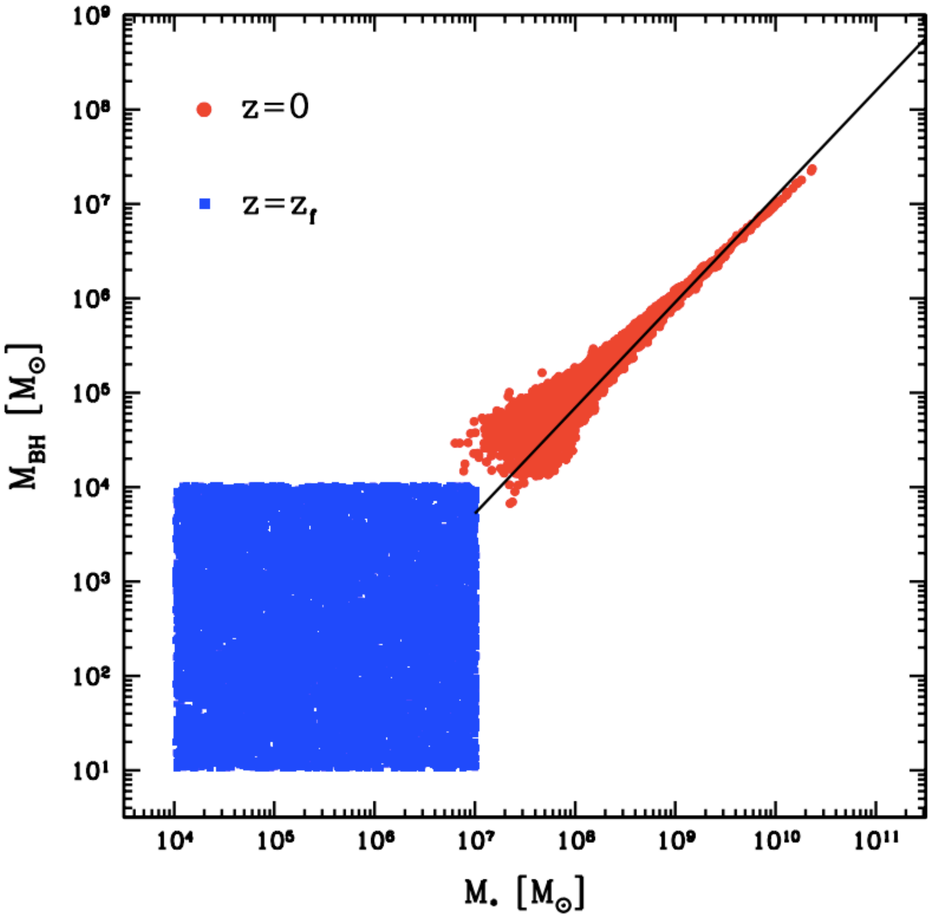

Fig. 1.20: Changes in the correlation between M_{BH} and $M_\star$ from an initially uncorrelated (within 4 dex in each parameter, blue points) distribution at high z to $z = 0$ purely by mass assembly along the merger trees, i.e., without the inclusion of star formation and SMBH gas accretion. The final distribution is characterized by near unity slope, with a decreasing scatter at higher masses. The solid black line shows the observational results by Häring & Rix (2004). Credits: Jahnke & Macciò (2011).

tions (see Chapter 2). In this model two modes for the AGN feedback are assumed. At low accretion rates, it is assumed that $\sim 10\%$ of the accreted mass is transformed into energy. As we have seen in Sect. 1.2.3, there are observational evidences that at low accretion rates the AGN feedback is mainly kinetic. The energy carried by these outflows is efficiently transferred to the surrounding cold gas, resulting in a high gas heating efficiency. For this reason in the model it is assumed that all the energy released at low accretion rates is used to heat the surrounding gas. On the contrary, at high accretion rates the heating efficiency decreases. Therefore, in the model the heating energy reaches a maximum value at $\dot{M} \sim 0.01 \times \dot{M}_{\rm Edd}$, where $M_{\rm Edd}$ is the Eddington accretion rate, i.e., the value of accretion rate at which radiation pressure overcome the gravitational pull. A sketch of the heating power as

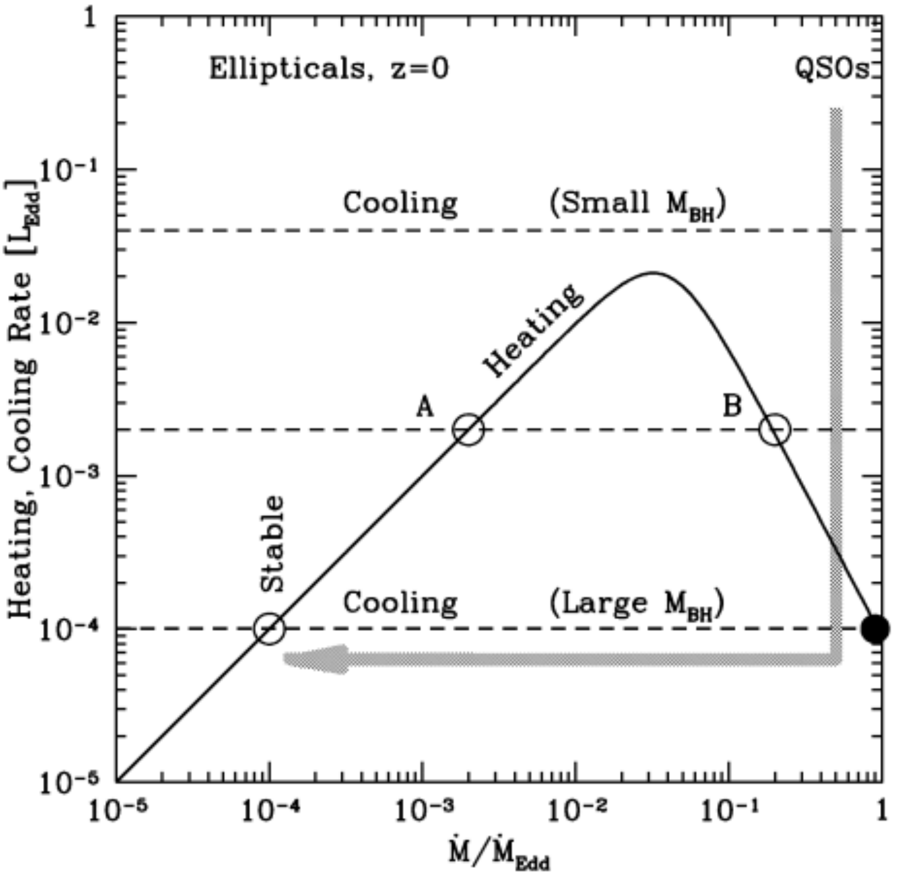

Fig. 1.21: Illustration of gas heating and cooling in elliptical galaxies. The thick solid line shows, as a function of the SMBH accretion rate, the heating rate due to outflow, which is complemented/dominated by radiative heating near the Eddington limit. Horizontal dashed lines show the gas cooling rate. Credits: Churazov et al. (2005)

a function of the accretion rate (in units of the Eddington accretion rate) is shown in Fig. 1.21 as a solid line. In the same plot, horizontal dashed lines represent possible values for the cooling rate. The higher dashed line represent the case of a young galaxy, with lot of gas and a relatively low mass central SMBH. In this situation the BH will grow by gas accretion near the Eddington limit, until it is massive enough to balance the cooling rate. The system will then be in the position pointed as B in the figure. In this state, if the heating power slightly overcomes the cooling rate, the amount of cold gas will decrease, implying both lower cooling and accretion rates. However, at lower accretion rates the heating power is higher, causing a runaway process that will find a stable solution in the points at which the heating power (solid line) intercepts the value of the cooling rate (dashed line) on the left of the peak of the heating power. In Fig. 1.21 this happens either at the point labelled as A or as *stable*. This points represent, for example, today galaxy clusters where intermittent radio lobes maintains a self-regulated cycle of cooling and heating. In this framework and under the assumption of Bondi accretion (Bondi 1952), Churazov showed that the observed correlation between M_{BH} and σ_e naturally arises in massive ellipticals[8] ($\sigma_e > 200$ km/s) from the balance between cooling rate and gas heating by AGN feedback.

The second model has been developed by Gaspari & Sadowski (2017), by relaxing the hypothesis of an accretion rate described by the Bondi formula. This model is based on numerical simulations focused on different scales, together with the observational evidence of the balance between heating and cooling within the core of galaxy clusters. The key process for the condensation of the cold gas that will eventually feed the central BH is described in Gaspari et al. (2013). In this work the authors used numerical simulations on the galactic scale to probe the physical process that eventually fuel the central BH. In particular, they showed that non-linear evolution of thermal instabilities in the hot halo form when $t_{\mathrm{cool}}/t_{\mathrm{ff}} \lesssim 10$, leading to the formation of cold clouds and filaments. This result is also in agreement with other idealized theoretical experiments (e.g., Meece et al. 2015). The cold structures inelastically collide, loosing angular momentum and moving toward the center of the galaxy. This model takes the name of chaotic cold accretion (CCA). Given the feeding process, Sadowski & Gaspari (2017) used magnetohydrodynamical simulations down to the Schwarzschild radius (r_{S}) to study the details of the feedback concluding that at accretion rates ranging in the interval $10^{-6} - 10^{-2}\ \dot{M}_{\mathrm{Edd}}$ the relevant process is the mechanical feedback, with an efficiency that accounts to $\approx 3\%$ of the accreted rest mass energy flux. The resulting self-regulated cycle is described in Fig. 1.22. In the core region ($r \lesssim 0.1\ r_{\mathrm{vir}}$) thermal instabilities lead to the formation of warm and cold clouds, which inelastically collide loosing angular momentum and moving

---

[8] The model is limited to massive ellipticals as stellar feedback is not considered.

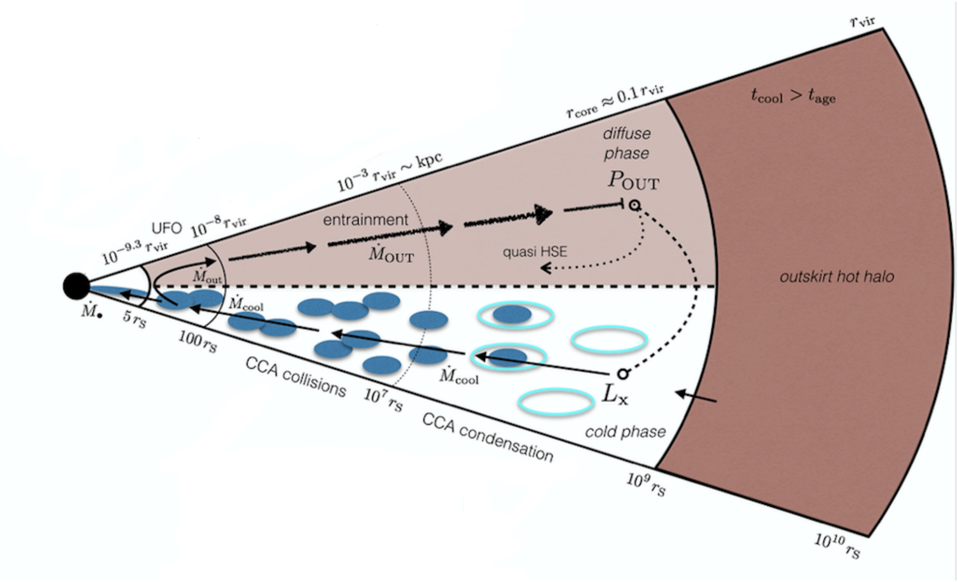

Fig. 1.22: Diagram of the multiphase accretion inflow and outflow. The self-regulated AGN feedback loop works as follows. The turbulent gaseous halo condenses in localized, large-scale, high-density peaks (cyan), leading to the drop out of cold clouds and warm filaments (blue). The clouds rain down and recurrently collide in a chaotic and inelastic way (CCA), canceling angular momentum and flowing toward the SMBH. Within $\sim 100\ r_S$, the gravitational accretion process releases ultrafast outflows (UFOs), while only a small gas fraction is sinked through the horizon. The outflows slow down at larger radii, entraining the gas of the background profile. The energy is thermalized in the core, balancing the X-ray luminosity. Credits: Gaspari & Sadowski (2017).

toward the inner regions. Within the inner region ($r < 100\ r_{\rm S}$) the gravitational accretion process releases ultrafast outflows (UFOs), that move in the outer regions entraining more gas. Therefore, the feedback is the result of the thermalization of the UFOs, that balance the radiative lost energy.

Within this framework, Gaspari & Sadowski (2017) related the gas accretion onto the central BH to the thermodynamical properties of the halo within the core region ($r \lesssim 0.1 r_{\rm vir}$), under the observationally suggested assumption that AGN feedback exactly balance radiative cooling. They found that the fundamental quantity is the X-ray temperature measured within the core region, with a scaling $M_{\rm BH} \propto T_X^2$, which therefore is expected to be the correlation with the lower scatter. The secondary correlation with the stellar velocity dispersion arises since, assuming virialization, it is possible to relate T_X to σ_e, obtaining a scaling $M_{\rm BH} \propto \sigma_e^4$, very similar to the values found in literature (e.g., Kormendy & Ho 2013, McConnell & Ma 2013, Gaspari et al. 2019).

1.4.2 Correlation between $M_{\rm BH}$ and galaxy cluster properties

Among all the SMBHs, the ones residing at the center of galaxy groups and clusters occupy a special place in the correlations reviewed in the previous section. Indeed, some observations suggest that these BHs are over-massive with respect to the $M_{\rm BH} - M_\star$ or $M_{\rm BH} - \sigma_e$ relations (e.g., Gebhardt et al. 2011, Hlavacek-Larrondo et al. 2012, Thomas et al. 2016). This feature is present also in Fig. 1.19, where the high mass end of the $M_{\rm BH} - \sigma_e$ is a significant source of scatter with increasingly over-massive BHs (five objects are approaching the top $3-\sigma$ channel), in conjunction with the increased presence of BCGs. A similar conclusion has been pointed out by other authors, which found that the $M_{\rm BH} - \sigma_e$ correlation saturates at high stellar velocity dispersion (e.g., Sect. 6.7.2 of Kormendy & Ho 2013 and references there in).

Since their hosting galaxies are the BCG and not ordinary galaxies, Bogdán et al. (2018) suggested that they may undergo a different evolutionary path with respect to BHs at the center of satellite galaxies, and that their growth might be indirectly driven by the large scale properties of the entire cluster. To test this hypothesis they studied all the BHs within BGGs and BCGs whose mass was known by dynamical measurements. For the final sample of 17 objects they computed the ICM temperature for the groups and clusters within an aperture $\lesssim R_{500}$, without any core exclusion. In their analysis, the cluster temperature is used as a proxy for the cluster mass through the scaling relations defined in Sect. 1.2.2. Since the luminosity or mass of the BCGs have been found to correlate well with the hosting halo both in observational (e.g, Lin & Mohr 2004; Brough et al. 2008) and numerical (e.g., Ragone-Figueroa et al. 2018) studies, a correlation between $M_{\rm BH}$ and cluster mass (temperature) is expected (e.g., Mittal et al. 2009), although $M_{\rm BH}$ and cluster global properties ought not be necessarily connected. Interestingly, Bogdán et al. (2018) found a tight correlation between $M_{\rm BH}$ and T_X (see Fig. 1.23) with a scatter in the $M_{\rm BH} - T_X$ relation that is lower than that of the $M_{\rm BH} - M_\star$ relation ($\sigma = 0.38$ and $\sigma = 0.61$ respectively).

Other observational works followed, which expanded the sample of clus-

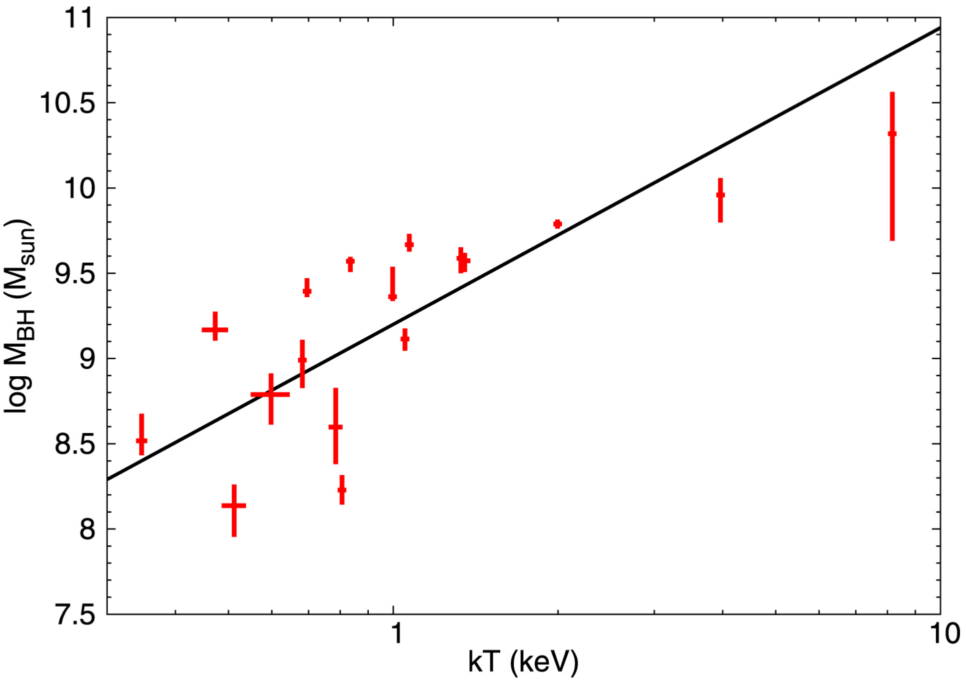

Fig. 1.23: Correlation between the BH mass and the best-fit gas temperature of the group/clusters. The red crosses are observational data, while the solid black line shows the best-fit power-law relation. The Pearson and Spearman correlation coefficients of the relation are 0.97 and 0.83, respectively, showing a strong correlation. Credit Bogdán et al. (2018).

ters studied (Phipps et al. 2019) and tried to constrain the physical processes that drive the correlation (Lakhchaura et al. 2019, Gaspari et al. 2019). Lakhchaura et al. (2019) analyzed a sample of 47 galaxies, including 18 BGGs/BCGs, 16 non-BCG elliptical galaxies, and 13 lenticular galaxies, and studied the correlations between the central BH and galaxy properties (temperature, σ_e, bulge luminosity, and total gravitational mass) using different apertures. The largest aperture used is $5 \times r_e \approx 0.1 \times R_{500}$. Therefore, all the quantities refer to the core of the cluster. In this respect we also note that Bogdán et al. (2018) used a median aperture of $0.3 \times R_{500}$ and with a sample of 6 galaxy clusters they showed that the temperature does not change more than 10% using apertures within the range $[0.1 - 0.4] \times R_{500}$. Therefore, the values of temperature computed by Lakhchaura et al. (2019) can also be regarded as a good proxy of the clusters virial temperature. The results by Lakhchaura et al. (2019) are shown in Fig. 1.24, where the correlations between $M_{\rm BH}$ and temperature (left panel), X-ray luminosity (central panel),

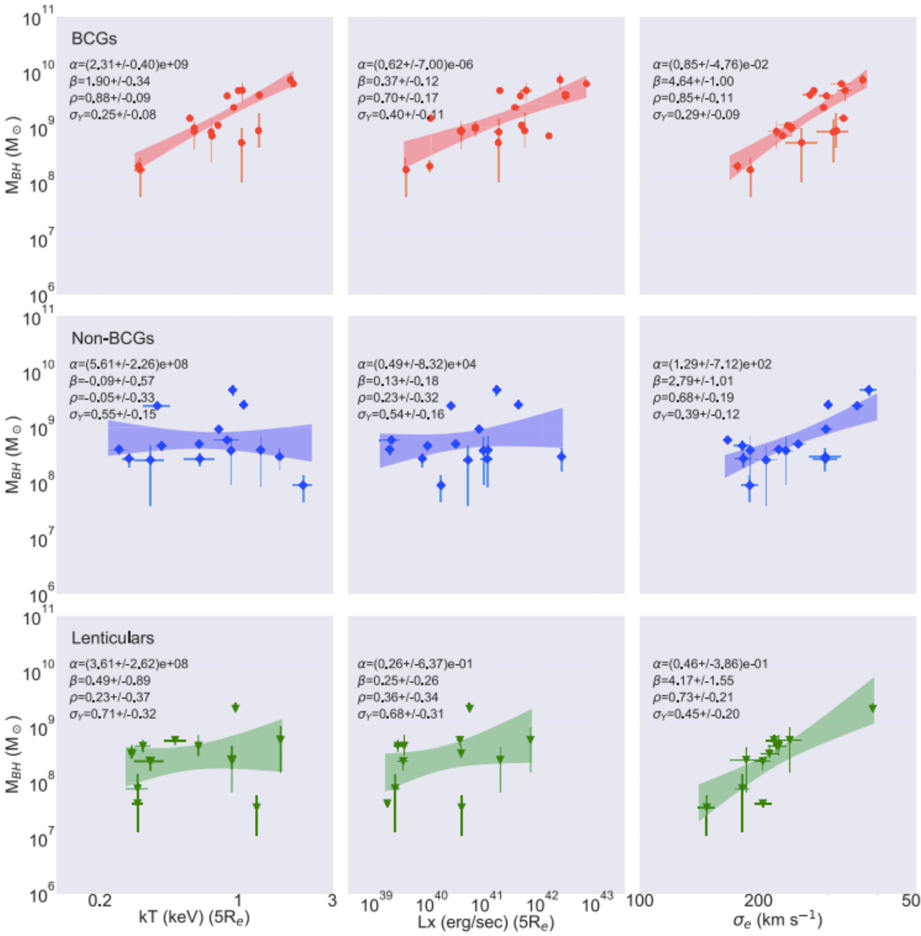

Fig. 1.24: Correlation between SMBH mass and hot atmosphere temperature (left panel), X-ray luminosity (central panel), and stellar velocity dispersion (right panel). Both temperature and luminosity are computed within an aperture of 5 effective radii. The intercept α, slope β, correlation coefficient ρ, and intrinsic scatter (σ_Y; in dex units), obtained from the log-log correlation analyses ($Y = \alpha X^{\beta}$), and their 68 per cent uncertainties are given in the insets. The shaded areas show the 68 per cent confidence regions for the correlations. Credits: Lakhchaura et al. (2019)

and stellar velocity dispersion are studied for different galaxy morphologies and environments. Lakhchaura et al. (2019) found that the BH mass strongly correlate with the temperature only for BHs within central galaxies (left panels of Fig. 1.24), while for non-central galaxies the correlation is essentially null (correlation coefficient equal to -0.05 ± 0.33). Since BCGs undergo a large number of mergers (see also the discussion in Sect. 1.1), this result has been interpreted as an evidence of a non-causal origin for the observed correlations. This conclusion is strengthen by the fact that the correlation between BH mass and the total gravitational mass within $5r_e$ (estimated assuming hydrostatic equilibrium) is consistent with a linear relation, which is the key consequence of a large number of merger events.

In Gaspari et al. (2019) we made a similar analysis, using 85 supermassive BHs with mass obtained by means of dynamical methods and derived a large number of correlations with thermodynamic properties in addition to the X-ray luminosity and temperature over different extraction radii (galactic, core, R_{500}). Our results confirmed a tight correlation between BH mass at the center of BGGs/BCGs, much tighter than the one with $M_\star$ or σ_e, confirming the results of Bogdán et al. (2018). Moreover, we found that also non-central galaxies lie on the same relation, a result in contrast with the findings of Lakhchaura et al. (2019). We interpreted the observed low scatter on the $M_{\rm BH} - T_X$ relation as a proof in favor of the CCA model, which foresee a direct correlation between BHs and the hot halo temperature, independently of the galaxy environmental position.

To summarize, by one side all these recent works suggest that the growth of BHs in BGGs/BCGs is regulated by physical processes that also influence the thermodynamical properties of the ICM. At the same time, the physical processes that lead to the observed correlations are still debated. Therefore, in the work presented in Chapter 3 I investigate the correlation between the mass of BHs in BCGs and the global properties of the hosting cluster, such as temperature and mass measured within R_{500} by employing the set of cosmological hydrodynamical simulations to be described in Chapter 2, with the aim of answering the following questions:

- Do numerical simulations reproduce the observed $T_{500} - M_{\rm BH}$ and $M_{500} - M_{\rm BH}$ relations?
- Which are the processes that lead to the observed relations and through which channels (e.g., gas accretion or BH-BH mergers) do SMBHs grow in time?
- Is M_{500} as appropriate as $M_{\rm BCG}$ to probe $M_{\rm BH}$?

Moreover, Besides the study of SMBHs at the center of galaxy clusters, I will also show the typical number of merger events that BHs undergo in our numerical simulations, as this result can be used to put constraints to the possibility of completely explain the observed correlations by means of BH-BH mergers.

Chapter 2

Numerical Simulations

In this Chapter I introduce the general properties of the cosmological codes used in theoretical cosmology and astrophysics (see Vogelsberger et al. 2020 for a recent review). After a first introduction on the aims of cosmological codes in Sect. 2.1, in Sect. 2.2 and Sect. 2.3 I briefly present the most used gravity and hydro solvers. In Sect. 2.4 I introduce GADGET-3, the code used to run our simulations, on which Chapter 3 and Chapter 4 are based. In Sect. 2.5 I describe how the initial conditions (ICs) for our zoom in simulations are generated, and I list the main properties of the simulated clusters. Finally, in Sect. 2.6 I describe the software used for the post-processing of the simulations.

2.1 Cosmological simulations

In order to fully describe the evolution of structures in a cosmological environment it is necessary to simulate both the collisionless components, like DM and stars within galaxies, and the collisional baryonic component. The former can be statistically described by a distribution function $f(\mathbf{x}, \mathbf{v}, t)$ in the phase space, i.e. the number of particles within the position interval $[\mathbf{x}, \mathbf{x} + d\mathbf{x}]$ and velocity interval $[\mathbf{v}, \mathbf{v} + d\mathbf{v}]$ at fixed time t. The function f satisfies the collisionless Boltzmann equation (also called Vlasov equation)

$$\frac{\mathrm{d}f}{\mathrm{d}t} = \frac{\partial f}{\partial t} + \mathbf{v} \cdot \frac{\partial f}{\partial \mathbf{x}} - \nabla\Phi \frac{\partial f}{\partial \mathbf{v}} = 0, \tag{2.1}$$

where Φ is related to the distribution function via the Poisson equation

$$\nabla^2\Phi(\mathbf{x},t) = 4\pi G \int f(\mathbf{x},\mathbf{v},t)\mathrm{d}\mathbf{v}. \tag{2.2}$$

Solving this equation requires to solve a partial differential equation on a six dimensional domain, which is computational prohibitive at a reasonable resolution. Therefore, Eq. 2.1 is usually solved by sampling the initial distribution with particles, and evolving the resulting N-body system computing gravitational forces between particles and weakening 2-body interactions at small scales. The codes used for this computation are usually referred as N-body codes and have nowadays reached full maturity (e.g., Springel 2016).

The collisonal baryonic component, i.e. the gas, is more complex to simulate. In the most simple scenario, the gas can be considered as non-radiative and can be described by the Euler equations for an ideal fluid, which represent conservation of mass, momentum and energy:

$$\frac{\partial\rho}{\partial t} + \nabla(\rho\mathbf{v}) = 0 \tag{2.3}$$

$$\frac{\partial}{\partial t}(\rho\mathbf{v}) + \nabla\cdot(\rho\mathbf{v}\otimes\mathbf{v} + \mathcal{I}P) = 0 \tag{2.4}$$

$$\frac{\partial(\rho e)}{\partial t} + \nabla(\rho e\mathbf{v} + P\mathbf{v}) = 0, \tag{2.5}$$

where ρ, P, $\mathbf{v}$, and e are the density, pressure, velocity, and total specific energy, and $\otimes$ and $\mathcal{I}$ are the outer product and the identity matrix. Even in this simple case, however, results can differ depending on the particular method employed to discretize and integrate the fluid equations (e.g., Sembolini et al. 2016). On top of fluid dynamics, for a realistic description of the evolution of astrophysical objects other physical processes are needed. These include radiative cooling, star formation, chemical evolution, stellar feedback, SMBH growth, and AGN feedback. All these processes take place on small scales compared to the numerical resolution that modern cosmological simulations can achieve. For example, star formation takes place within molecular clouds which have diameter sizes of $\sim 20-200$ pc, while the sphere of influence of a SMBH of mass 10^8 $\mathrm{M}_\odot$ is around 10 pc. On the contrary, modern cosmological simulations achieve resolutions that range from few hundreds of pc to few kpc. To encompass this issue, effective subgrid models are used to describe the effects that unresolved astrophysical processes have on scales resolved by the simulations. Since these processes are not described starting from first principles, results can strongly depend on their particular implementation.

I introduce the subgrid models implemented in our code in Sect. 2.4, after reviewing the main schemes used to integrate the equations of motion for a collisionless N-body system and the fluid equations used for the description of the gas component in Sect. 2.2 and Sect. 2.3.

2.2 N-body simulation

Once the initial distribution function (see Eq. 2.1) has been discretized by means of particles, the evolution of the system is determined by gravitational interaction. As already said, in a cosmological context N-body codes have reached full maturity, meaning that different schemes differ mainly in terms of computational costs rather than the goodness of the solution. A particularly recent example of this is the comparison carried out by Sembolini et al. (2016), in which the authors compared the results of a cosmological simulation of a galaxy cluster using 12 different state-of-the-art codes. In the DM only run, Sembolini et al. (2016) showed that all the investigated quantities were in agreement well within 10 per cent of each other.

In the following I briefly review the main schemes used to solve a N-body problem.

2.2.1 Particle-Particle, PP

The most obvious way to evolve a N-body system is to directly compute the the force acting on each particle as:

$$\vec{F}_i = -\sum_j \frac{G m_i m_j (\vec{r}_i - \vec{r}_j)}{|\vec{r}_i - \vec{r}_j|^3}. \tag{2.6}$$

This scheme has the evident advantage of integrating the exact equation of motion. However, the divergence that arises in Eq. 2.6 whenever two particles come close enough can greatly slows down the computation, since to correctly integrate particles orbits the distance travelled during a time-step must be smaller than inter-particle distance. For this reason, Eq. 2.6 is usually modified introducing a parameter $\epsilon > 0$:

$$\vec{F}_i = -\sum_j \frac{G m_i m_j (\vec{r}_i - \vec{r}_j)}{(|\vec{r}_i - \vec{r}_j|^2 + \epsilon^2)^{3/2}}, \tag{2.7}$$

which is commonly referred as *gravitational softening*. The introduction of the gravitational softening solves the problems related to the singularity at 0, at the price of deviating from Newtonian forces at scales $\sim \epsilon$. Therefore, the amplitude of the gravitational softening is a scale under which simulations results are not reliable. Moreover, the introduction of the gravitational softening also reduces two-body interactions, preserving the collisionless property of the system. Indeed, as the resolution of the simulations is relatively coarse, the particles used to sample the density field have to be considered as a population rather then a single object. Therefore, two-body interactions may not be physical. Finally, the drawback of this scheme is that it scales with the square of the number of particles and it is, thus, computationally expensive.

2.2.2 Particle-Mesh, PM

The particle-mesh (PM) scheme is based on the decomposition of the computational domain into a grid. Starting from the position of the particles within the simulation, it is then possible to associate to each cell a density

$$\rho_m = \frac{1}{l^3} \sum_i m_i W(\mathbf{x}_i - \mathbf{x}^c_m), \tag{2.8}$$

being l and $\mathbf{x}^c_m$ the size and center coordinates of a cell, and $\mathbf{x}_i$ and m_i the position and mass of each particle. W determines the weight of each particle and its choice differentiate different PM flavors. Given the discrete form of the density field, it is possible to compute its Fourier transform $\tilde{\rho}_k$ and the gravitational potential through the Poisson equation

$$\tilde{\phi}(\vec{k}) = -4\pi G \frac{\tilde{\rho}_k}{|\vec{k}|^2}, \tag{2.9}$$

which is subsequently transformed back in real space. The force $\mathbf{F}_m$ acting at the position of the center of the cell is then obtained as the gradient of the gravitational potential through a finite-difference method. Finally, the force is interpolated at the position of each particle using the same kernel

W employed in Eq. 2.9:

$$\mathbf{F}(\mathbf{x}_i) = \sum_m W(\mathbf{x}_i - \mathbf{x}^c_m)\mathbf{F}_m. \tag{2.10}$$

The advantage of this scheme over the PP is that it is computationally cheaper as it scales as $\propto N_c \log N_c$, being N_c the number of cells in which the computational domain is subdivided. Moreover, as two body interactions are suppressed, this scheme naturally preserve the collisionless property of the system. However, the PM is not precise at small scales as the force deviates from Newtonian interactions at scales comparable to l. A possible solution is to use adaptive cells, where the initial cell is subdivided in smaller units (for example dividing each side by two) until some condition is reached (e.g., by imposing the mass within each sub-cell to remain roughly constant). These schemes take the name of adaptive mesh refinement (AMR) schemes (Couchman 1991).

2.2.3 Treecode

The Treecode (Barnes & Hut 1986) is constructed in order to maintain a coarse-grained representation of the system at large scales, while reaching higher resolution on small scales with respect to the PM scheme. In particular, the initial domain (also called root node) is iteratively subdivided in smaller cells (defined as nodes of the tree) until each single cell contains no more than a particle (an example of this process is illustrated in Fig. 2.1). To compute the force acting on a particle, the tree is walked starting from the root node. If a node is viewed under an angle smaller than a given parameter θ_c (usually referred as critical opening angle), i.e. the condition

$$\theta = \frac{l}{r} \leq \theta_c \tag{2.11}$$

is satisfied, then the node is treated as a single particle, with total mass given by the sum of the mass of all the particles within the node and position given by their center of mass. Otherwise, the tree is walked through until Eq. 2.11 is satisfied. The accuracy of this scheme relies on the choice of θ_c: large values mean a very coarse-grained representation of the system, while smaller and smaller values effectively converge to a PP scheme. Typical values for this parameter are around ~ 0.5. In this formulation, a better resolution is

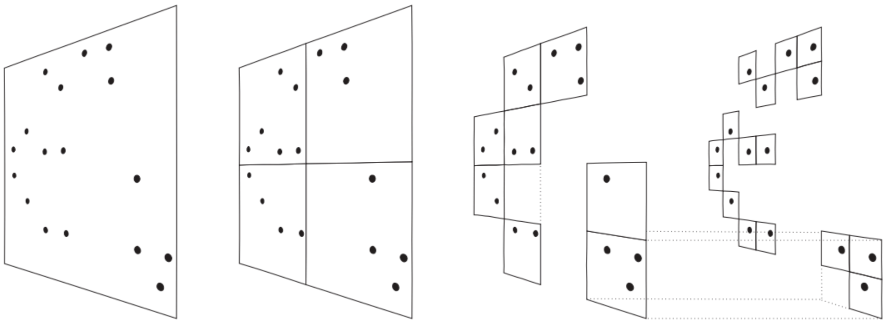

Fig. 2.1: Illustration of the construction of a tree. The initial domain is iteratively subdivided in smaller cells, until only one particle per cell is left. Each intermediate cell is defined as a *node* of the tree. Credits: Springel et al. (2001b).

achieved on small scales while maintaining the same computational scaling ($\propto N \log N$) of the PM scheme. The drawback of this scheme is that a large amount of memory is needed to store the tree.

2.2.4 TreePM

The TreePM scheme is a combination of the PM and the Treecode. The basic idea is to split the Fourier transform of the gravitational potential into two components corresponding to long (ϕ_l) and short (ϕ_s) range forces:

$$\begin{aligned}
\tilde{\phi}_k &= -\frac{4\pi G\tilde{\rho}_k}{k^2} \\
&= -\frac{4\pi G\tilde{\rho}_k}{k^2}\exp\left(-k^2r_s^2\right) - \frac{4\pi G\tilde{\rho}_k}{k^2}\left(1-\exp\left(-k^2r_s^2\right)\right) \\
&= \tilde{\phi}_k^l + \tilde{\phi}_k^s \qquad (2.12) \\
\tilde{\phi}_k^l &= -\frac{4\pi G\tilde{\rho}_k}{k^2}\exp\left(-k^2r_s^2\right) \\
\tilde{\phi}_k^s &= -\frac{4\pi G\tilde{\rho}_k}{k^2}\left(1-\exp\left(-k^2r_s^2\right)\right),
\end{aligned}$$

where r_s is the parameter that defines long and short range. For the long range, the forces are computed using a PM scheme and $\tilde{\phi}_k^l$ is used in Eq. 2.9. For the short range, the forces can be analytically transformed in real space

$$\mathbf{f}^s(\mathbf{r}) = -\frac{Gm\mathbf{r}}{r^3}\left(\mathrm{erfc}\left(\frac{r}{2r_s}\right) + \frac{r}{r_s\sqrt{\pi}}\exp\left(-\frac{r^2}{4r_s^2}\right)\right), \qquad (2.13)$$

where erfc is the complementary error function. Given Eq. 2.13, the force acting on each particle is then computed using a Treecode scheme.

The resulting TreePM scheme is significantly more efficient in terms of computational cost with respect to a pure treecode, even though it is even more memory consuming.

2.2.5 P3M

This scheme is very similar to the TreePM, with the difference that short range forces are not computed with a Treecode, but via a PP scheme. The advantage over the TreePM is that there is no need to store the Tree. However, the PP part can be computationally very expensive in cosmological simulations as the matter is highly clustered.

2.3 Hydrodynamic schemes

As already mentioned, modeling gravitational interaction can describe the evolution of cosmological structures only at a first approximation. Indeed, about 15 percent of the universe matter is collisional and the evolution of the gas needs to be accounted. The first step to simulate the evolution of the gas in a cosmological context is to solve the Euler equations for an ideal fluid (Eqs. 2.3, 2.4, 2.5). The codes used to solve these equations can be in first approximation divided in two families: Eulerian and Lagrangian. In the following I briefly review the main idea behind both approaches.

2.3.1 Eulerian schemes

In this approach the computational domain is divided on a fixed grid with thermodynamic properties associated to each cell. The evolution of the system is then given by the computation of the fluxes between neighbouring cells.

As an example, consider a 1 dimensional problem. In 1D the equations 2.3, 2.4, and 2.5 can be written as

$$\frac{\partial \mathbf{U}}{\partial t} + \frac{\partial \mathbf{F}(\mathbf{U})}{\partial x} = 0, \tag{2.14}$$

where $\mathbf{U} = (\rho, \rho v, \rho e)$ is the vector of the conserved quantities and $\mathbf{F} =$

$(\rho v, \rho v^2 + p, v(\rho e + p))$ is the relative flux vector. After discretizing the initial domain in intervals $I_i = [x_{i-1/2}, x_{i+1/2}]$, integrating Eq. 2.14 over I_i results in:

$$\frac{d}{dt}\int_{x_{i-1/2}}^{x_{i+1/2}} \mathbf{U}(x,t)dx = \mathbf{F}(\mathbf{U}(x_{i-1/2},t)) - \mathbf{F}(\mathbf{U}(x_{i+1/2},t)). \tag{2.15}$$

Integrating over the time interval $[t^{n+1}, t^n]$ gives:

$$\begin{aligned}\int_{x_{i-1/2}}^{x_{i+1/2}} \mathbf{U}(x,t^{n+1})dx = &\int_{x_{i-1/2}}^{x_{i+1/2}} \mathbf{U}(x,t^n)dx + \\ &\int_{t^n}^{t^{n+1}} \mathbf{F}(\mathbf{U}(x_{i-1/2},t)) - \int_{t^n}^{t^{n+1}} \mathbf{F}(\mathbf{U}(x_{i+1/2},t)).\end{aligned} \tag{2.16}$$

At first order all the conserved quantities can be considered as constant within each cell. Under this assumption, the fluxes at the interfaces between neighbouring cells are computed solving a Riemann problem (e.g., Toro 2009), that is two constant states divided by a discontinuity. Since the solution to this problem is self-similar, i.e. it depends only on the ratio x/t, the fluxes computed at cells interfaces are constant over a time interval Δt, and Eq. 2.16 can be rewritten as

$$\mathbf{U}_i^{n+1} = \mathbf{U}_i^n + \frac{\Delta t}{\Delta x}\left(\widetilde{\mathbf{F}}_{i-1/2} - \widetilde{\mathbf{F}}_{i+1/2}\right), \tag{2.17}$$

where $\widetilde{\mathbf{F}}_{i\pm1/2}$ are the fluxes computed at the interfaces using an exact or approximate Riemann solver.

The first and more important implication of using a Riemann solver is that these schemes automatically include the dissipative terms necessary to describe discontinuities, across which the entropy is not conserved. However, since the domain is discretized in cells, discontinuites are also introduced where the exact flux is continuous, resulting in spurious dissipation. This spurious effect can be reduced using different reconstruction methods for the states at the interfaces, instead of a constant approximation. Examples of zero (piecewise constant), first (piecewise linear), and second (piecewise parabolic) order approximations are shown in Fig. 2.2 respectively with red, blue, and green dashed lines. Note, however, that using higher than zero order approximations can lead to oscillations in the numerical solution. Indeed,

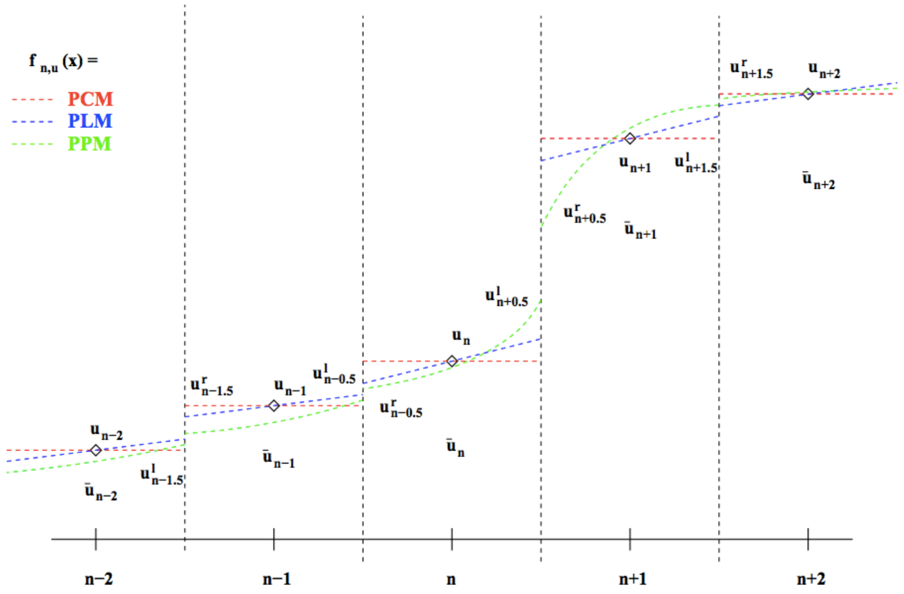

Fig. 2.2: Reconstruction of the variable u on a grid using different methods: piecewise constant (PCM), piecewise linear (PLM) or piecewise parabolic (PPM). The reconstruction allows both to estimate di average value ($\bar{u}_n$) and the values at the cells interfaces ($\bar{u}^r_{n-0.5}$, $\bar{u}^l_{n+0.5}$) which are used as initial conditions for the Riemann problem. Credits: Dolag et al. (2008).

when a reconstruction is applied in the presence of a discontinuity, the spatial derivative of the reconstructed variable within a cell can be unrealistically high. To prevent such oscillations, slope limiters (which limit the derivative of the reconstructed variable to realistic values) have to be employed (see, e.g., Springel 2010b). The second implication arising from Eq. 2.17 is that since the fluxes $\widetilde{\mathbf{F}}_{i\pm1/2}$ at contiguous cells are the same but with opposite signs, mass, momentum, and energy are exactly conserved. However, angular momentum is not conserved and even the energy is not conserved anymore once gravity is taken into account. Since the internal energy in this approach is computed as the difference between the total and kinetic energy, this can impact also thermodynamic properties (e.g., Springel 2010b).

In this formulation Eulerian codes are not highly performing in cosmological simulations, as they lack natural adaptivity, i.e. the capability of increasing the resolution in high density environment. A possible solution is to adopt an AMR scheme, similarly to what is done in a PM scheme. The downsize of this approach is that errors can be generated at the interfaces within cells with different sizes, which can suppress the formation of gravitational instabilities (e.g., O'Shea et al. 2005, Heitmann et al. 2008).

These schemes have been implemented in astrophysical codes like ENZO (Bryan et al. 2014) and RAMSES (Teyssier 2002), used to perform cosmological simulations like the Horizon-AGN[1].

2.3.2 Lagrangian schemes

The basic idea behind the Lagrangian approach is to follow the trajectories of single fluid elements, instead of evolving thermodynamic quantities within a fixed grid. The most famous and used scheme is the smoothed particle hydrodynamics (SPH; for recent reviews see Price 2008, Springel 2010a, Price 2012), which I describe in this section. However, other Lagrangian schemes exist. I will briefly describe them in the next section.

The basic idea behind the SPH schemes is the definition of a smoothed version of a generic field $\mathbf{F}$ through the convolution with a Kernel W:

$$\mathbf{F}_s(\mathbf{r}) = \int \mathbf{F}(\mathbf{r}')W(\mathbf{r}-\mathbf{r}', h)d\mathbf{r}', \tag{2.18}$$

where h is the characteristic length of the kernel. W is normalized to 1 and converges to the Dirac δ function for $h \to 0$. The kernel is also symmetric, twice differentiable, non-negative, and monotonically decreasing. These conditions ensure that the error relative to the smoothed field are of the order of $\sim h^2$ (e.g., Price 2012). The most obvious kernel to be used is a Gaussian. However, a Gaussian does not have a compact support and is therefore not computationally efficient. For this reason in practice a Gaussian-like kernel with compact support (which goes to 0 after few smoothing lengths) is used.

Knowing the value of the field $\mathbf{F}$ on a set of discretized points with positions $\mathbf{r}_j$, to which a constant mass m_j is associated, it is then possible to write Eq. 2.18 in the discretized form:

$$\mathbf{F}_s \simeq \sum_j \frac{m_j}{\rho_j}\mathbf{F}_j W(\mathbf{r}-\mathbf{r}_j, h), \tag{2.19}$$

where ρ_j is the density computed at $\mathbf{r}_j$ and $\mathbf{F}_j = \mathbf{F}(\mathbf{r}_j)$. The goodness of the approximation in Eq. 2.19 depends on the number of points within the

---

[1] https://www.horizon-simulation.org

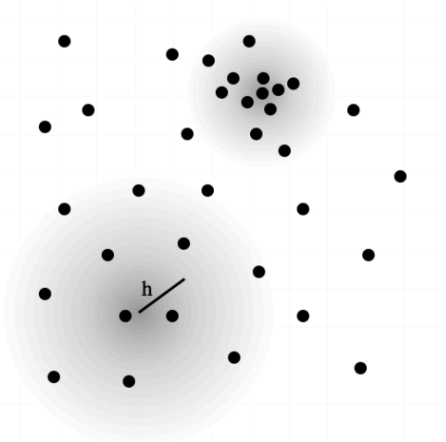

Fig. 2.3: Illustration of density reconstruction from Eq. 2.20. The value of h is not constant at each point and changes in order to take into consideration the same number of particles. The estimate of the density can be interpreted as the sum of the mass of the particles within the compact support of the kernel divided by the volume, with the difference that the masses of the particles are weighted via the Kernel, which has decreasing values at larger distances. This limits numerical noise due to particles at the boundary of the compact support of the Kernel. Credits: Price (2012)

compact support of the kernel. For this reason, a constant value of h perform poorly in cosmological simulations, where the density span various orders of magnitude. Therefore, h is usually taken to be adaptive, by forcing the number of particles within the compact support to be roughly constant. A particular case of Eq. 2.19 is obtained considering the density field

$$\rho_s(\mathbf{r}_i) = \sum_j m_j W(\mathbf{r}_i - \mathbf{r}_j, h_i), \tag{2.20}$$

where this time the value of the field is computed at the position of the $i-th$ particle. Note that since h is adapative, it will be different for each particle (see Fig. 2.3). Eq. 2.20 is one of the fundamental equations at the base of the SPH scheme.

In the modern derivation, the SPH equations of motion are obtained from Eq. 2.20 and by applying the Euler-Lagrange equations to the discretized Lagrangian of an inviscid fluid:

$$L = \sum_b m_b \left[\frac{1}{2} v_b^2 - u_b(\rho_b, s_b) \right], \tag{2.21}$$

where v_b, u_b and s_b are respectively the velocity, internal energy, and the entropy associated to each particle. The resulting equation of motion can be written as

$$\begin{aligned}
m_i \frac{d\mathbf{v}_i}{dt} &= -m_i \sum_j m_j \left[\frac{P_i}{\Omega_i \rho_i^2} \nabla_i W_{ij}(h_i) + \frac{P_j}{\Omega_j \rho_j^2} \nabla_i W_{ij}(h_j) \right], \\
\Omega_j &\equiv \left[1 - \frac{h_j}{3\rho_j} \sum_k m_k \frac{\partial W_{jk}(h_j)}{\partial h_j} \right], \qquad (2.22) \\
W_{jk}(h_j) &\equiv W(\mathbf{r}_j - \mathbf{r}_k, h_j),
\end{aligned}$$

where P_i is the pressure associated to each particle, and Ω_j are correction terms arising from the fact that the smoothing length is adaptive. Using the equation of state for a perfect gas

$$P = A(s)\rho^\gamma = (\gamma - 1)\rho u, \qquad (2.23)$$

where γ is the polytropic index and $A(s)$ the entropic function, together with the first principle of thermodynamics it is possible to compute the evolution of the thermodynamic quantities as

$$\frac{du_i}{dt} = \frac{\rho_i}{\Omega_i \rho_i^2} \sum_j m_j (\mathbf{v}_i - \mathbf{v}_j) \cdot \nabla_i W_{ij}(h_i). \qquad (2.24)$$

Of course, this is not the only possible choice. Alternatively, the entropy can be evolved through the equation

$$\frac{dA}{dt} = \frac{\gamma - 1}{\rho^{\gamma - 1}} \left(\frac{du}{dt} - \frac{P}{\rho^2} \frac{d\rho}{dt} \right) = \frac{\gamma - 1}{\rho^{\gamma - 1}} \left(\frac{du}{dt} \right)_{diss}, \qquad (2.25)$$

where the subscript $diss$ stands for any dissipative term. This choice has the practical advantage of avoiding errors due to the numerical integration, as for an adiabatic flow the entropy is conserved.

The SPH scheme is naturally adaptive, as higher density regions are sampled by a higher number of particles. As already highlighted in the previous section, this feature is extremely important when dealing with cosmological simulations. Moreover, given the expression of the Lagrangian (Eq. 2.21), it is possible to understand all the pros and cons of this scheme. First of all, the starting Lagrangian is invariant under translations, rotations, and does not explicitly depend on time. Therefore, the SPH scheme naturally conserve momentum, angular momentum, and energy. On the other side, the Euler-Lagrange equations imply the continuity of all thermodynamical quantities. For this reason SPH schemes do not correctly describe discontinuities (such as shocks and gas mixing) without the inclusion of ad hoc dissipative terms. These terms are introduced as an artificial viscosity, to describe shocks, and an artificial thermal conduction, to enable mixing between different gas phases which will be otherwise prevented by the SPH solutions to the fluid equations (see, e.g., Price 2008). The effect of the artificial conduction is shown in Fig. 2.4, which display the solution to a Riemann problem. The zoom on the contact discontinuity, i.e. a discontinuity in the density field but not in the pressure, clearly shows that without any artificial conduction term a 'blip' in the pressure is present (blue points). This gradient in the pressure, which is eliminated by the introduction of the artificial conduction term (red points), prevent gas mixing and has profound implications also in more complex cosmological simulations (see, e.g., Frenk et al. 1999, Sembolini et al. 2016). Finally, being the fields discretized using particles, the coupling with gravity is straightforward.

SPH schemes have been successfully implemented and used in cosmological simulations. A few examples are the EAGLE simulations (Schaye et al. 2015), BAHAMAS (McCarthy et al. 2017), Magneticum (Hirschmann et al. 2014), Romulus (Tremmel et al. 2017), and also our simulations, the DIANOGA set.

2.3.3 Meshless and moving mesh schemes

A third group of schemes has also been introduced in the recent years. These schemes are constructed with the aim of achieving the natural adaptivity of an SPH scheme, while avoiding the introduction of artificial dissipative terms by using a Riemann solver to integrate the Euler equations. This result has been obtained in two different ways, and the resulting schemes have been implemented in the codes AREPO (Springel 2010b) and GIZMO (Hopkins 2015). In the following I will provide only the basic ideas and I refer to the aforementioned papers for more details.

AREPO is based on a moving mesh scheme. In particular, a set of points is used to define a mesh through a Voronoi tessellation. The natural adaptivity

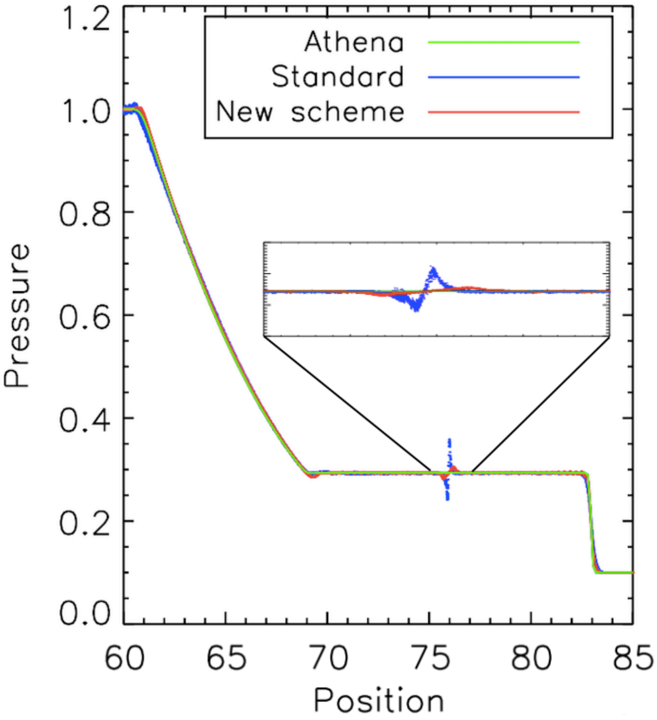

Fig. 2.4: Numerical solution to a Riemann problem with different hydro-dynamical schemes. Blue points (standard) refers to a SPH scheme without an artificial conduction term. Red points (new scheme) refers to the SPH scheme implemented in GADGET-3, while the green line refer to the grid-based code Athena (Stone et al. 2008). Without the introduction of an artificial conduction term a spurious discontinuity in the pressure at the contact discontinuity is clearly visible. Credits: Beck et al. (2016).

of this scheme arises as at each time step the points used to construct the mesh move with same velocity of the local flow. Once the mesh is constructed the evolution of thermodynamic quantities is computed evaluating the fluxes between neighouring cells as in an Eulerian scheme. This scheme has been used for a few state-of-the-art cosmological simulations, like Illustris (Genel et al. 2014), IllustrisTNG (Pillepich et al. 2018), and FABLE (Henden et al. 2018).

GIZMO works with a similar strategy with respect to AREPO, with the difference that there is not an actual mesh and the volume is discretized between particles using the same family of kernels that is used for the SPH density estimation. In this way each particle, which also in this case follows the local flow of the fluid, interacts not only with adjacent cells, but also with all the particles within the compact support of the kernel (usually between 32 and 64 particles). The other important difference with respect to AREPO is that in the meshless finite mass implementation of this scheme, the position and velocity of the interfaces where the fluxes are computed are chosen in order to have a zero net mass flux, such that each particle mass is effectively conserved. This also enable to achieve better energy conservation properties with respect to a pure Eulerian scheme. This scheme has been used in recent cosmological simulations, such as MUFASA (Davé et al. 2016), SIMBA (Davé et al. 2019), and also for zoom-in simulations focused on galaxy evolution such as the FIRE-2 project (Hopkins et al. 2018).

2.4 GADGET-3

The simulations used for our works are performed with the developer version of GADGET-3, which is based on the public code GADGET-2 (Springel et al. 2001a, Springel 2005). This code implements a TreePM scheme for gravity, where the PM part is adaptive (i.e., an AMR scheme). The scheme used to integrate fluid equations is a density-entropy SPH (i.e., Eq. 2.25 is used to evolve thermodynamic properties), with a number of improvement with respect to the standard scheme (see Beck et al. 2016). The modifications include: (i) a higher order interpolation kernel (Wendland C4 kernel with 200 neighbours); (ii) a time dependent artificial viscosity to correctly describe shock waves and a time dependent artificial conduction to correctly describe gas mixing that will be otherwise suppressed by the SPH solution to fluid equations; (iii) gravity corrections to the artificial conduction term which are needed since this term is proportional to pressure and internal energy gradients, which naturally arise in the presence of gravity and would in this case lead to unwanted conduction.

As already mentioned, besides hydrodynamics other physical processes are needed to fully describe the evolution of cosmic structures. Since a broad overview of these subgrid models will require a dedicated work, in the following sections I only focus on the models implemented in GADGET-3 that will be extensively discussed in Chapter 3 and Chapter 4, with particular attention on the model for star formation and AGN feedback.

2.4.1 Star formation model

The model for star formation strictly follows the model by Springel & Hernquist (2003), to which I refer for a more exhaustive description. In the following I only review the main aspects, which will be discussed more in depth in Chapter 4.

In this prescription each SPH particle samples a region of the interstellar medium (ISM), and is subdivided in a cold phase and a hot phase characterized by densities ρ_c and ρ_h, in pressure equilibrium one with each other. The total density associated to a particle will be the sum of the two: $\rho = \rho_c + \rho_h$. A SPH particle has a non null fraction of cold gas (i.e., $\rho_c > 0$), and thus becames multiphase, whenever some conditions on its thermodynamical properties are fulfilled. The condition is typically imposed on the density, which has to be higher than a given threshold $\rho_{\rm thr}$. However, a further condition on the temperature can be used. We will define the particular model employed when describing the set of simulations used in Chapter 3 and Chapter 4.

Given the cold fraction, a numerical instantaneous SFR is associated to each multiphase particle[2]:

$$\frac{\mathrm{d}\rho_\star}{\mathrm{d}t} = \dot{\rho}_\star = (1-\beta)\,\frac{\rho_c}{t_\star}, \tag{2.26}$$

where $t_\star$ is the characteristic timescale for star formation, while β is the fraction of massive stars (i.e., $M > 8\ \mathrm{M}_\odot$) that are expected to instantly explode as type-II supernovae (SNII) and depends on the chosen IMF, which in our simulations is always a Chabrier IMF (Chabrier 2003). The parameter $t_\star$ follows the expression:

$$t_\star(\rho) = t_0^\star \left(\frac{\rho}{\rho_{\rm thr}}\right)^{-1/2}. \tag{2.27}$$

$t_0^\star$ is set to $1.5\ \mathrm{Gyr}$ in order to match the observed Kennicutt relation (Kennicutt 1998). In practice, varying this parameter directly reflects into a variation of the numerical star formation efficiency (SFE). Indeed, using eq. 2.26 and eq. 2.27:

---

[2] By numerical SFR has to be intended the rate at which the mass in SPH gas particles should be transformed into stellar particles. The actual physical SFR of the model is $\rho_c/t_\star$

$$\mathrm{SFE} = \frac{\dot{\rho}_\star}{\rho_c} = \frac{1-\beta}{t_0^\star}\left(\frac{\rho}{\rho_{\rm thr}}\right)^{1/2}. \tag{2.28}$$

Given the SFR, part of the cold clouds is evaporated by means of supernovae feedback:

$$\frac{\mathrm{d}\rho_c}{\mathrm{d}t} = -A\beta\frac{\rho_c}{t_\star}, \tag{2.29}$$

where A is the efficiency of evaporation that determines the efficiency of thermal supernovae feedback and is taken to be a function of the local gas density, $A \propto \rho^{-4/5}$. These equations give rise to the self-regulated cycle of star formation: high cold cloud density leads to a high SFR, that in turn means more feedback and cloud evaporation. When cloud evaporates, the SFR decreases and material is returned to the hot phase, increasing ρ_h. Finally, a higher density means a higher cooling rate (see next section), which causes more gas to condense in cold clouds, so that the cycle restarts.

Besides the thermal feedback, simulations also implement galactic winds associated to star formation. The total mass entrained in the winds is taken to be proportional to the star formation rate

$$\dot{M}_{\rm wind} = \eta\dot{M}_\star, \tag{2.30}$$

where η is usually referred as mass loading factor and is fixed equal to 2 in all of our simulations. Note, however, that recent theoretical works suggest that the mass loading factor is not constant and depends on the mass of the galaxy, as well as on redshift (e.g., Muratov et al. 2015). The effect of a variable mass loading factor on our simulations will be tested in future works. Together with the total mass in galactic wind, the other parameter to be specified is its velocity, which we assume to be $350\ \mathrm{km\ s^{-1}}$. This wind velocity is equivalent to assuming that the wind carries around 50% of supernova energy.

2.4.2 Radiative cooling and chemical enrichment

The physical process that enables the gas to cool down and form stars is radiative cooling, which in turn is related to the chemical enrichment of the gas particles. The production of metals in the simulations is computed following the formulation presented in Tornatore et al. (2007). Briefly, each stellar particle produces chemical elements (we specifically follow He, C, Ca, O, N, Ne, Mg, S, Si, Fe, Na, Al, and Ar in addition to keep track of H) through three different channels: type-Ia supernovae (SNIa), SNII and asymptotic giant branch (AGB) stars. The amount of metals produced is computed considering a Chabrier IMF, the mass-dependent life times by Padovani & Matteucci (1993), and the stellar yields from SNIa (Thielemann et al. 2003), SNII (Woosley & Weaver 1995 and Romano et al. 2010), and AGB (Karakas 2010). Once the amount of metals produced by a stellar particle is computed, these are spread between neighbouring gas particles using the same kernel function used for the SPH computations (Eq. 2.20).

The amount of metals for each gas particle is then used to compute the energy loss by radiative cooling, through a metal dependent cooling function. As it will be important for the discussion of Chapter 4, we note that this is the step in which the choice of the IMF may affects the SFR in numerical simulations. Indeed, the IMF determines the fraction of massive stars and the subsequent chemical pollution and cooling of the gas particles.

2.4.3 AGN feedback

The AGN feedback model is inspired to the original model developed by Springel et al. (2005). Briefly, during run time we identify groups of particles using the Friends of Friends (FoF) algorithm (Huchra & Geller 1982, see Sect. 2.6). BHs in our simulations are spawned at the center of each FoF group (defined as the position of the most bound particle), whenever conditions on total group stellar mass, stellar to DM mass ratio, and gas fraction are simultaneously fulfilled. The exact values, together with the BH seed mass, depend on the numerical resolution, and will therefore be specified when describing each simulations set in Chapters 3 and 4.

Once BHs are seeded, they are allowed to grow by two different channels: accretion of the surrounding gas and BH-BH mergers. The former follows the Eddington-limited alpha-enhanced Bondi accretion rate (Bondi 1952) formula:

$$\dot{M}_{\mathrm{Bondi},\alpha} = \alpha \frac{4\pi G^2 M_{\mathrm{BH}}^2 \rho}{(c_s^2 + v_{\mathrm{BH}}^2)^{3/2}}, \tag{2.31}$$

with α equal to 10 and 100 for hot ($T > 5 \times 10^5\ K$) and cold ($T < 5 \times 10^5\ K$) gas respectively (Steinborn et al. 2015). In eq. 2.31 all gas-related quantities (sound speed, c_s, bulk gas velocity relative to BH velocity, v_{BH}, and gas density, ρ) are smoothed over 200 gas particles with the kernel function centered at the position of the BH. The boosting factor α is needed as the Bondi formula has been derived under quite simplistic assumptions like spherical symmetry, and unperturbed and steady initial conditions. In a more realistic scenario, the accretion proceed in a chaotic way, with the overall effect of boosting the accretion by up a factor of 100 (e.g., Gaspari et al. 2013).

Given the gas accretion onto the BH particle, AGN energy feedback is given by

$$\dot{E} = \epsilon_r \epsilon_f \dot{M} c^2 \tag{2.32}$$

where $\dot{M}$ is the minimum between the Bondi (Eq. 2.31) and the Eddington accretion rate, $\dot{M} = \min(\dot{M}_{\text{Bondi},\alpha}, \dot{M}_{\text{Eddington}})$, and the energy is distributed and thermally coupled to the nearest 200 gas particles. In eq. 2.32, ϵ_r is the fraction of mass transformed in radiation energy and ϵ_f is the fraction of radiated energy thermally coupled to the gas particles. As it is done for the star formation subgrid model, also in this case the model parameters ϵ_r and ϵ_f are tuned so as to reproduce specifics observational constraints. In particular, we set the parameters in order to match the observed normalization of the $M_{\text{BH}} - M_\star$ correlation.

Besides gas accretion, BH particles can also grow by BH-BH mergers. In our implementation of the subgrid model two BHs are allowed to merge whenever they are near enough in the phase space. The particular values of the relative distance and velocity depend on the resolution and will be specified in Chapters 3 and 4.

2.5 Initial conditions

So far I have described the main ingredients used by cosmological codes to describe the growth of structures in the universe. However, the other important piece of information is the generation of the initial conditions (ICs) to be used together with a cosmological code. The ICs define the initial density and velocity fields which represent a realization of a random field with a given power spectrum and multi-variate distribution (which is assumed to be Gaussian). In this section I briefly describe how the ICs for cosmological simulations are produced, and I focus then to the particular case of the ICs used for our simulations.

The ICs for N-body numerical simulations are generated following the Lagrangian perturbation theory (e.g., Bouchet et al. 1995, Bernardeau et al. 2002). As has been already said in Sect. 2.3, differently from the Eulerian approach, where the evolution of the system is described by the fluxes between neighbouring cells defined on a fixed grid, in the Lagrangian framework the trajectories and velocities of single fluid elements (or particles) are followed. In particular, the position of a particle at each conformal time τ ($d\tau = dt/a$) can be expressed as

$$\mathbf{x}(\mathbf{q},\tau) = \mathbf{q} + \Psi(\mathbf{q},\tau), \tag{2.33}$$

where $\mathbf{q}$ is the Lagrangian coordinate of the particle, i.e. its initial position, and $\Psi(\mathbf{q},\tau)$ is the Lagrangian displacement field. Therefore, to generate the initial conditions starting from a lattice where the particles of the N-body simulation are placed[3], it is necessary to estimate $\Psi(\mathbf{q},\tau)$ for each initial position $\mathbf{q}$. In linear theory, the displacement field can be written as (e.g., Bernardeau et al. 2002)

$$\nabla_q \Psi = -D_{\rm L}(\tau)\delta(\mathbf{q}), \tag{2.34}$$

where $D_{\rm L}(\tau)$ is the linear growth factor (see Eq. A.12) and $\delta(\mathbf{q})$ is the density contrast. The latter is considered to be a Gaussian random field and therefore in the momentum space its statistic is completely defined by its second moment $P(k)$ (i.e., the power spectrum). Given $P(k)$, it is possible to define the density field at a scale k with its real and imaginary part ($\delta(\mathbf{k}) = \delta_r + i\delta_i$) defined by a Gaussian distribution with mean value at 0 and variance $\propto \sqrt{P(k)}$. In practice, $\delta(\mathbf{k})$ is written in its exponential form $\delta(\mathbf{k}) = |\delta(\mathbf{k})|e^{i\theta}$ with $|\delta(\mathbf{k})|$ drawn from the Rayleigh distribution

$$\mathcal{P}(|\delta(\mathbf{k})|) = \frac{|\delta(\mathbf{k})|}{P(k)} \exp\left[-\frac{|\delta(\mathbf{k})|^2}{2P(k)}\right], \tag{2.35}$$

and θ drawn from a uniform distribution in the range $[0, 2\pi)$. The random modulus and phases for each $\delta(\mathbf{k})$ define the particular realization of the density field given its statistic.

---

[3] The grid method is one of the most popular choice to generate pre-initial conditions. However there exist also more sophisticated schemes. For the generation of our initial conditions a glass-like particle distribution has been used.

With $\delta(\mathbf{k})$ at hand, it is then possible to compute the displacement field through Eq. 2.34 and Eq. 2.33. Following a similar procedure, it is also possible to compute the initial particles velocity. Since the displacement field is computed in linear theory, the starting redshift has to be high enough, such that the resolved scales are still in the linear regime. Therefore, the initial conditions are often generated in the redshift range $100 \lesssim z \lesssim 50$. In our simulations, the initial conditions are generated at $z = 70$.

2.5.1 DIANOGA zoom-in simulations

The procedure described in the previous section refers to the production of the ICs for a cosmological box, while our simulations are zoom-in simulation. Indeed, the dimension of a box is limited by the computational capabilities and the chosen numerical resolution. For example, to be able to resolve galaxies down to $M_\star \sim 10^9$ $\mathrm{M}_\odot$, the needed computational resources limit the dimension of the box to ~ 100 Mpc. A cosmological box of this size will be useful to study galaxy evolution but not the evolution of rare objects such as the most massive clusters with $M_{\rm vir} \sim 10^{15}$ $\mathrm{M}_\odot$. Since our primary interest is in these extreme objects, we rely on the zoom-in technique. As I will describe in the following paragraph, this technique enables to reach higher resolutions while keeping information on the cosmological environment. The complete procedure is described in Bonafede et al. (2011), and is based on the Zoomed Initial Conditions (ZIC) technique described in Tormen et al. (1997). I remand to these two works for a full explanation of the zoom-in ICs generation.

In order to generate the ICs for zoom-in simulations extra steps are needed, as the resolution is not constant over the whole box. The first step consists in the generation of a DM only cosmological box at a relatively low mass resolution. In particular in our case it was a box of $1\ h^{-1}$ Gpc side produced with the public code GADGET-2 (Springel 2005), in a ΛCDM cosmology with parameters $\Omega_\Lambda = 0.76$, $\Omega_M = 0.24$, $h = 0.72$, and $\sigma_8 = 0.8$ (consistent with WMAP-7 constraints; Komatsu et al. 2011). From this box, the standard FoF algorithm was used to select at $z = 0$ the 24 most massive clusters ($M_{200} > 8 \times 10^{14} h^{-1}$ $\mathrm{M}_\odot$) together with 5 less massive objects ($M_{200} \in [1-4] \times 10^{14}\ h^{-1}$ $\mathrm{M}_\odot$) randomly chosen. The density projection of the parent box from which the clusters have been selected is shown in

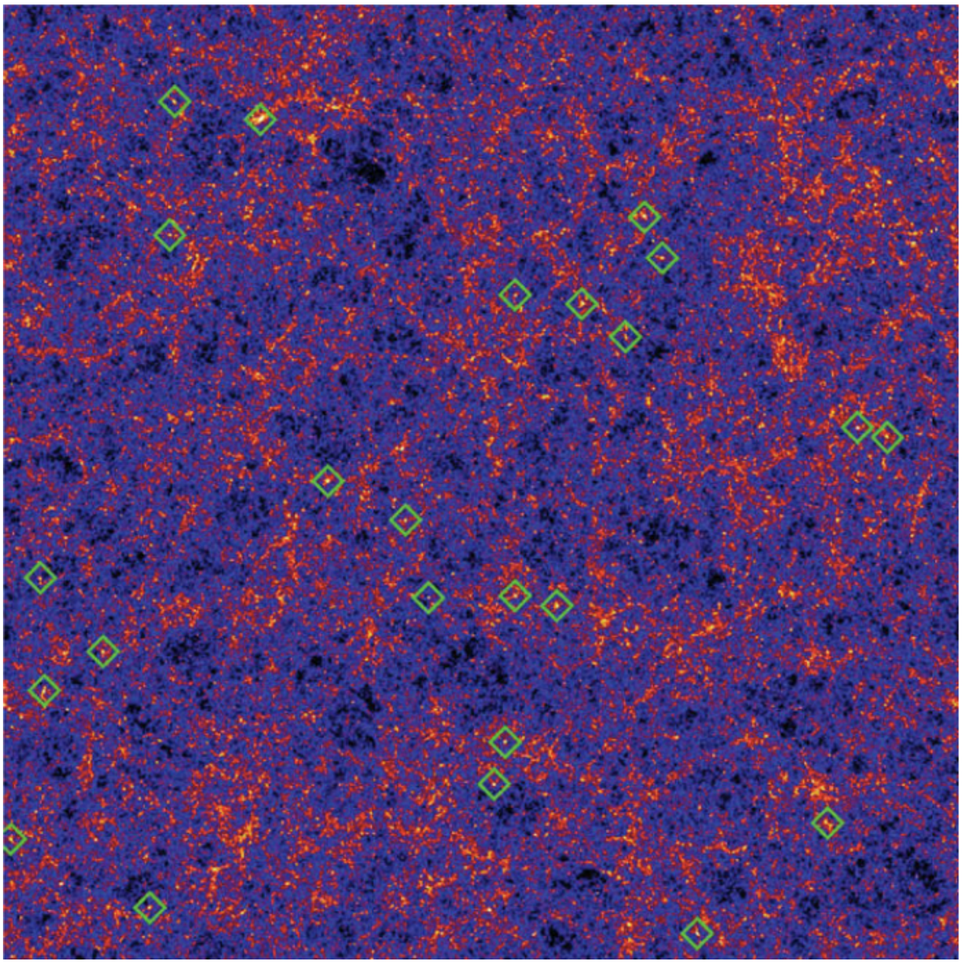

Fig. 2.5: Density projection over the $1\ h^{-1}$ Gpc side DM only simulations from which our clusters are extracted. Green diamonds represent the 24 most massive clusters. Credits: Bonafede et al. (2011).

Fig. 2.5, with the 24 most massive clusters shown as green diamonds.

To create the ICs for each zoom-in simulation, all the particles within $5-7\times R_{\rm vir}$[4] at $z=0$ were traced back to their position at the beginning of the simulation. The size of the region was chosen to guarantee a HR spherical volume around each cluster with a radius of $\sim 5-6$ virial radii. Since this region is quite large, the HR regions also contain secondary objects (groups and clusters). Indeed, in the 29 HR regions we find a total of 135 groups and clusters with $M_{500}>3\times10^{13}$ $\rm M_{\odot}$. Then, the box (with side $L_{\rm HR}$) containing all the particles that will end up in the selected region at

---

[4] In the used Cosmology, $R_{\rm vir}=R_{95}$

$z = 0$ was subdivided in 64^3 cells. All the cells containing at least one of the selected particles were then re-sampled with higher resolution DM particles. To displace the particles within the HR region, the same power spectrum of the parent simulation has been used, with the same amplitudes and phases. Shorter wavelengths were also added, to account for the smaller scales now resolved by the high resolution particles. Note that this step does not strictly rely on the initial resolution of the parent DM simulation; therefore, the resolution can be varied continuously without the need of re-simulate the parent simulation. To minimize the discontinuities between the low resolution and the HR zones, a third region has been added around the HR zone, with the same mass resolution of the parent simulation. Outside the high and medium resolution regions, the parent simulation was re-sampled at lower resolution using a spherical grid centered on the cluster with constant angular resolution $d\theta$. The height of each cell was then chosen in order to obtain an almost cubic cell, i.e. imposing $\mathrm{d}r \sim r\mathrm{d}\theta$, obtaining a decreasing resolution with increasing distance from the cluster. This LR regions is needed in order to keep track of the cosmological environment. A representation of the final grid with the HR region (blue and red zone), medium resolution region (green zone, with the same resolution of the parent simulation), and low resolution region (black grid) on which the initial conditions are created is shown in Fig. 2.6.

Once the ICs for the DM simulations were ready, baryons were added. To add baryons, the DM particles within the HR region were splitted with the mass ratio given by the cosmic baryon fraction. Gas particles were then displaced from DM by half the mean intra-particle distance, imposing conservation of mass and momentum.

The radius, mass, and temperature of the final sample of our simulated cluster are listed in Table 2.1, while I show a visual representation of the 24 most massive clusters in Fig. 2.7.

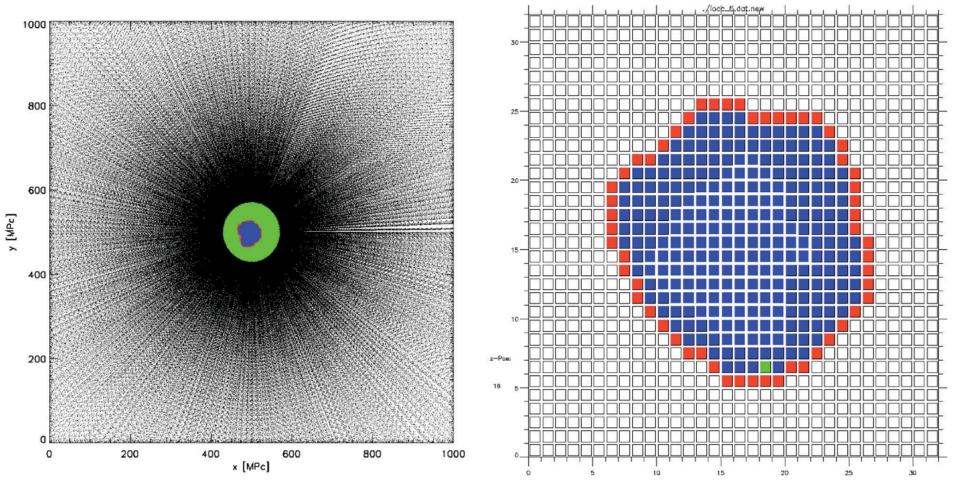

Fig. 2.6: Representation of the ICs for one zoom-in simulation. *Right*: HR region. Blue squares represent all the cells containing at least one DM particle which end up in the $5-7\times R_{\rm vir}$ region around the cluster. Green squares are added to the blue ones to avoid holes in the HR region, while red boxes are included to obtain a concave region. *Left*: The black cells represent the lowest resolution region, with decreasing mass resolution toward the outer region of the box. Green region is the one at intermediate resolution, with a mass resolution equal to the one of the parent simulation. Credits: Bonafede et al. (2011).

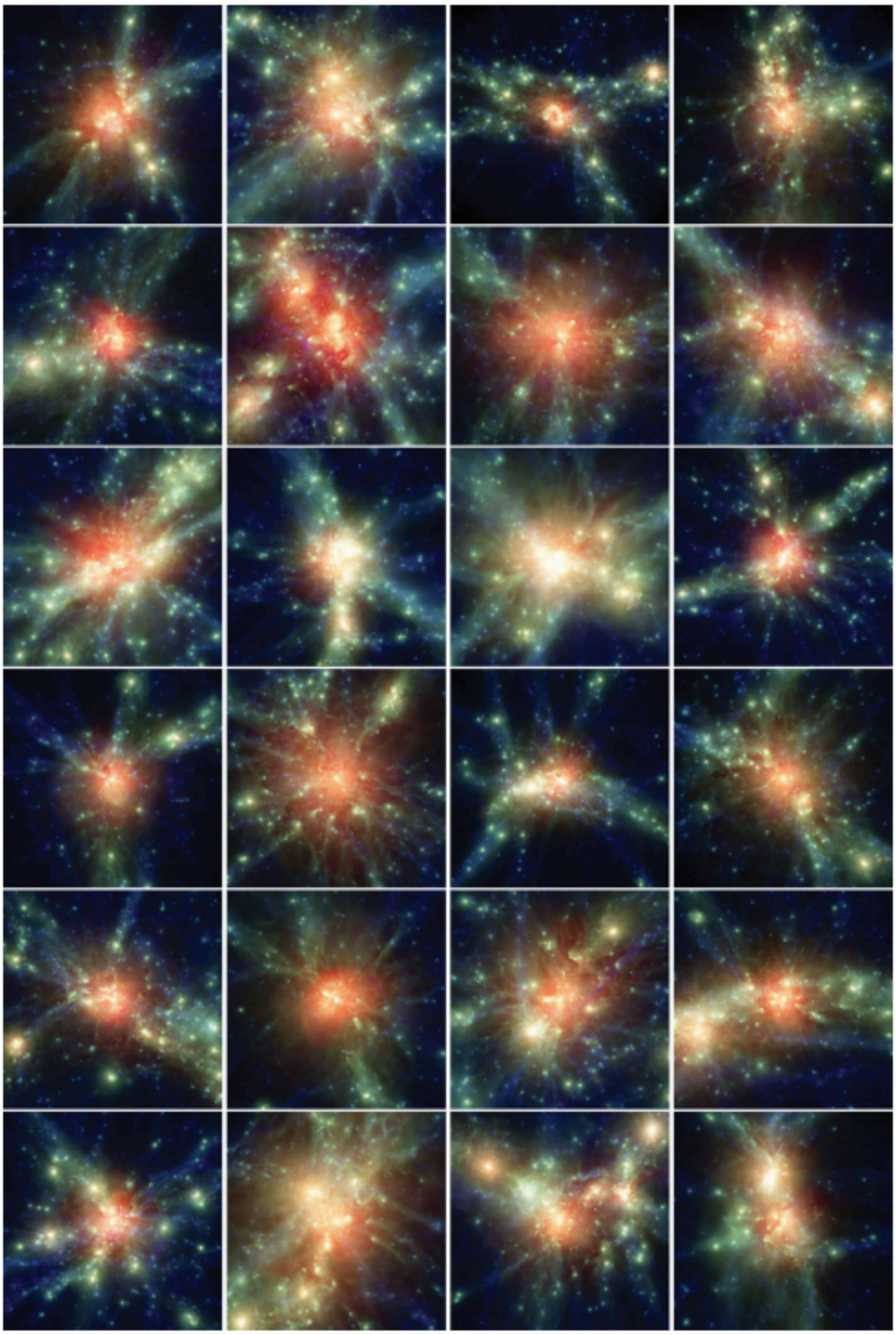

Fig. 2.7: Ray-tracing images of 15 Mpc h^{-1} regions around the centre of the individual 24 most massive clusters. Colour coded is the temperature of the gas. Credits: Bonafede et al. (2011).

	R_{200} [Mpc h^{-1}]	M_{200} [10^{15} h^{-1} M$_{\odot}$]	$T_{\rm sp}$ keV
D1	1.764	1.27	7.88
D2	1.188	0.39	3.30
D3	1.284	0.49	4.45
D4	1.175	0.38	3.28
D5	0.839	0.14	1.82
D6	1.693	1.12	6.23
D7	1.686	1.11	7.14
D8	1.752	1.24	4.64
D9	0.756	0.10	1.67
D10	1.653	1.04	6.78
D11	1.552	0.86	5.44
D12	1.889	1.58	7.39
D13	1.664	1.06	8.52
D14	1.832	1.43	7.97
D15	1.804	1.36	7.43
D16	2.241	2.72	7.95
D17	1.835	1.43	5.28
D18	1.547	0.85	6.12
D19	1.709	1.15	6.25
D20	1.832	1.43	7.62
D21	1.727	1.19	8.62
D22	1.882	1.56	10.58
D23	1.663	1.06	7.98
D24	1.680	1.09	7.92
D25	1.513	0.80	3.94
D26	1.763	1.26	7.34
D27	1.793	1.33	5.89
D28	1.877	1.55	8.76
D29	1.755	1.25	5.71

Table 2.1: Col. 1: cluster name. Col. 2: R_{200}. Col. 3: total mass within R_{200}. Col. 4: spectroscopic like temperature within R_{200}.

2.6 Halo finders

To analyze the output of the simulations it is necessary to use a halo (and sub-halo) finder, which is essential to define halos and subhalos. In our simulations, we use the FoF algorithm and Subfind (i.e., subhalo finder, Springel et al. 2001b, Dolag et al. 2009). The former is used at run-time only on DM particles. In practice, two DM particles are considered to be part of the same group if their distance is less than a fixed value, referred as linking length, which is commonly defined as a fraction of the mean inter-particle distance. We fix this parameter to 0.16. The information on the FoF groups is used, for example, for the subgrid model of AGN feedback at the seeding step.

Subfind is more sophisticated and time-consuming, and is run in post-processing. In particular, Subfind enables to define gravitationally bound structures. For a detailed description of this algorithm I refer to the original paper by Springel et al. (2001b). Briefly, the scheme identify local maximum in the density field, which is estimated at the position of each particle following the SPH density interpolation (i.e., Eq. 2.20). The position corresponding to the particle with the highest density is used as center of the putative substructure, and the neighbouring particles with decreasing density are added to the structure. The boundary of the structure correspond to the position where a saddle point in the density field is found. After this first selection, only gravitationally bound particles (i.e., with negative energy) are assigned to the final structure. The position of all halos and subhalos from Subfind will then be given by the position of the most bound particle within the structure.

Regarding our cluster simulations, it is important to note that Subfind is able to assign particles (DM, BHs, gas, and stars) to a cluster, and to find the substructures within it. However, in the version of Subfind implemented in GADGET-3 (Dolag et al. 2009), the BCG, ICL and ICM will all be assigned to the same structure: the main halo. Therefore, a definition of the BCG in our simulations will be only possible through a cut in the radial distance from the center of the cluster. A different version of Subfind exists, which employ the velocity distribution of the stellar particles in order to disentangle BCG and ICL (Dolag et al. 2010). However, this last version is not currently implemented in our code.

Chapter 3

Super massive BHs - galaxy clusters correlations

In this Chapter I investigate the correlations of central SMBH mass with cluster mass and temperature by employing the set of cosmological hydrodynamical simulations centered on massive clusters described in Chapter 2. I compare their scatter to that of the classical $M_{\rm BH} - M_{\rm BCG}$ relation. Moreover, I study how gas accretion and BH-BH mergers contribute to SMBH growth across cosmic time.

The specific aim is to answer the following questions: 1) Do numerical simulations reproduce the observed $T_{500} - M_{\rm BH}$ and M_{500}-$M_{\rm BH}$ relations? 2) Which are the processes that lead to the observed relations? 3) Do the relations evolve with redshift? 4) Through which channels (e.g., gas accretion or BH-BH mergers) do SMBHs grow in time? 5) Is M_{500} as good as $M_{\rm BCG}$ as a proxy for $M_{\rm BH}$?

The chapter is structured as follows: after a brief introduction in Sect. 3.1, in Sect. 3.2 I add specific details of the numerical simulations used in this work that were not described in Sect. 2.4. In Sect. 3.3 I detail how the quantities of interest are computed from simulations and the method employed for linear fitting. In Sect. 3.4 I present the results, that I discuss in Sect. 3.5. Finally, in Sect. 3.6 I sum up the main conclusions.

The work presented in this Chapter is based on two papers that we published on Astronomy & Astrophysics (Bassini et al. 2019) and on the Astrophysical Journal (Gaspari et al. 2019):

- **Bassini, L.**; Rasia, E.; Borgani, S.; Ragone-Figueroa, C.; Biffi, V.; Dolag, K.; Gaspari, M.; Granato, G. L.; Murante, G.; Taffoni, G.; Tornatore, L.: *Black hole mass of central galaxies and cluster mass correlation in cosmological hydro-dynamical simulations*,
  Astronomy & Astrophysics, Volume 630, October 2019, id.A144, 16 pp.

- Gaspari, M.; Eckert, D.; Ettori, S.; Tozzi, P.; **Bassini, L.**; Rasia, E.; Brighenti, F.; Sun, M.; Borgani, S.; Johnson, S. D.; Tremblay, G. R.; Stone, J. M.; Temi, P.; Yang, H. -Y. K.; Tombesi, F.; Cappi, M.:
  The X-Ray Halo Scaling Relations of Supermassive Black Holes,
  The Astrophysical Journal, Volume 884, October 2019, Issue 2, article id. 169, 41 pp.

3.1 Scientific context

In Chapter 1 we have seen that galaxies of every morphology host at their center a SMBH, whose mass correlates well with the bulge properties of the hosting galaxy and that the properties of the observed correlations might help to discern the physical processes that drive them (see Sect. 1.4.1). In particular, we discussed two possible explanations for the origin of such relations: the first is based on the fact that the mass of both galaxies and their SMBHs is regulated by AGN feedback and the second is a non-causal connection driven by mergers.

For what concerns the former category, in Sect. 1.4.1 I described two theoretical models (Churazov et al. 2005, Gaspari & Sadowski 2017), which show how a self-regulated feedback loop naturally leads to a tight correlation between SMBHs masses and hot atmospheric temperatures (or stellar velocity dispersion). These theoretical expectations have been later observationally probed by Bogdán et al. (2018) on cluster scales (see Fig. 1.23) and in Gaspari et al. (2019), where we showed that these correlations (particularly the one regarding the X-ray temperature) hold also for non-central galaxies. The model by Churazov et al. (2005) and the observations by Bogdán et al. (2018) and Gaspari et al. (2019) will be used in this Chapter as a reference to which compare our numerical results at $z = 0$.

I recall that the argument on the origin of the correlations is not settled yet (see Sect. 1.4.1). Indeed, Lakhchaura et al. (2019) confirmed the tight correlation between the SMBH mass and the X-ray temperature measured within few effective radii, but only when BCGs are considered (see Fig. 1.24). This result has been interpreted by the authors as a signature of a non-causal origin to the observed correlations. We will look at this argument in Sect. 3.4.4, where I also study correlations involving non-central galaxies, and in Sect. 3.4.7, where I study the typical number of mergers that SMBHs undergo to put constraints on the origin of the observed correlations.

3.2 Simulations

The analysis presented in this Chapter is based on the simulations presented in Sect. 2.5.1, the Dianoga set. In this section I will provide information on the numerical resolution of this particular run, and the choice of the parameters of the subgrid model for AGN feedback presented in Sect. 2.4.3. In particular, these simulations are run at a mass resolution of $m_{\rm DM} = 8.47 \times 10^8\ h^{-1}$ and $m_{\rm gas} = 1.53 \times 10^8\ h^{-1}$ for DM and initial gas particles. The Plummer equivalent gravitational softening for DM particles is set to $\epsilon = 5.6\ h^{-1}{\rm kpc}$ in comoving units at redshift higher than $z = 2$ and in physical units afterward. The gravitational softening lengths of gas, stars, and black hole particles are fixed in comoving coordinates to $5.6\ h^{-1}$ kpc, $3\ h^{-1}$ kpc, and $3\ h^{-1}$ kpc, respectively. In the next two sections I describe the particular model used for the AGN feedback, while in Sect. 3.2.3 I show the results regarding the BCG masses and the galaxy stellar mass function (GSMF) at $z = 0$.

3.2.1 SMBHs positioning and feeding

SMBHs of mass $3.2 \times 10^5\ h^{-1}\ {\rm M}_\odot$ are seeded at the position of the most bound particle of the structures identified by the FoF algorithm (see Sect. 2.6) that simultaneously satisfy all the following conditions: (i) the mass of the FoF group is higher than $8 \times 10^{11}\ h^{-1}\ {\rm M}_\odot$; (ii) the stellar mass of the structure is greater than $1.5 \times 10^{10}\ h^{-1}\ {\rm M}_\odot$; (iii) the ratio between the gas mass and the stellar mass is higher than 0.1; (iv) no other central SMBH is already present. The mass of the seeding is consistent with the expectation of the direct collapse. Under these conditions, the seeding of the SMBH happens in galaxies that have enough gas to promptly feed it.

A particularly tricky task is to ensure that SMBHs remain at the centre of their structure once they are seeded, as most of the time their mass at the current resolution is lower than the mass of DM particles. In order to avoid wandering black holes, they are re-positioned at each time step on the position of the most bound particle within the SMBH softening length. This calculation is restricted to particles with relative velocity with respect to the SMBH below $300\ \mathrm{km\ s^{-1}}$. This condition avoids that the SMBH particle ”jumps” into a close flyby structure that would displace it from the cluster center.

Once the SMBHs are seeded, they can grow by accretion of the surrounding gas or by BH-BH mergers. The former is determined by the alpha enhanced Bondi accretion rate (Eq. 2.31), while two SMBH particles merge whenever their relative velocity v_{rev} is smaller than $0.5 \times c_s$ and their distance r is less than twice the SMBH softening length. When a BH-BH merger happens, the SMBH particle of the most massive SMBH gains the mass of the merged one.

3.2.2 AGN feedback and model calibration

From the gas accretion into the SMBHs particles given by the Bondi accretion rate, it is then possible to derive the energy released by AGN feedback through Eq. 2.32. This energy is then distributed and thermally coupled to the nearest 200 gas particles. At this point, it is important to note that the effect of AGN feedback is strongly related to the particular implementation of the effective model for star formation presented in Sect. 2.4.1. Indeed, when a particle is multi-phase, its temperature evolves to an equilibrium temperature of $\sim 10^6$ K (see Springel & Hernquist 2003, Sect. 2). Once an external energy input is given to the particle, as it is the case for AGN feedback, deviations from the equilibrium temperature decay on time-scales that are smaller then a typical time-step. As a result, the energy released by AGN feedback is promptly lost if the effective model of star formation is active (see the discussion in Appendix A4 by Ragone-Figueroa et al. 2013). In order to avoid it, when AGN feedback deposits thermal energy to a particle, we compute the temperature that the cold phase would have if all this energy was deposited to the cold phase of the particle. If this temperature is higher than the average temperature of the particle before receiving energy from AGN feedback, then the particle exits its multiphase state. Moreover, in order to avoid that the particles that just received the energy re-enter the multiphase structure a few time-steps after, we also set a temperature threshold ($T_{\rm thre} = 2.5 \times 10^5$ K) above which a particle can not become multiphase. Note, however, that the temperature threshold only applies when we need to decide if a particle becomes multiphase. If the particle is already multiphase, the temperature threshold is not applied. Finally, in this model the energy released by the feedback is coupled with both the hot and cold phases of gas particles, with a proportion given by the masses in the two phases.

In Fig. 3.1 I show the calibration of the AGN feedback model used in the simulations, which involve to find the best values of the parameters ϵ_r and ϵ_f of Eq. 2.32. The calibration is based on the correlation between the stellar mass of galaxies, $M_\star$, and the mass of their central SMBHs, $M_{\rm BH}$. In the figure the small light-blue points represent non-central simulated galaxies identified by Subfind (see Sect. 2.6), while dark-blue dots represent simulated BCGs. The stellar masses of the BCGs are defined as the mass enclosed in a sphere of radius $0.1 \times R_{500}$ around the position of the central SMBH, while total stellar masses of non-BCGs are given as an output by Subfind.

To calibrate the parameters for the AGN-feedback model we aimed at reproducing the entire $M_{\rm BH} - M_\star$ relation thus including the overall distribution of galaxies and not only BCG. These are, in particular, compared with the observational data from McConnell & Ma (2013) represented in the figure by the dashed line. The value of ϵ_r is fixed to 0.07 independently of $\dot{M}_{\rm Bondi,\alpha}$, while ϵ_f depends on the mode of the AGN: during the quasar mode, meaning for $\dot{M}_{\rm Bondi,\alpha}/\dot{M}_{\rm Eddington} > 0.01$, $\epsilon_f = 0.1$, while during the radio mode ϵ_f is increased to 0.7.

In the plot I also include other observational data, namely the BCGs from McConnell & Ma (2013) and the samples from Savorgnan et al. (2016), Main et al. (2017), Bogdán et al. (2018), and Gaspari et al. (2019). In Main et al. (2017) SMBH masses are computed from K-band luminosities using the relation $\log(M_{\rm BH}/{\rm M}_\odot) = -0.38(\pm 0.06)(M_{\rm K} + 24) + 8.26(\pm 0.11)$ suggested by Graham (2007) and extracted from a sample of elliptical but not BCGs. In all the other works the mass of the SMBHs are derived from dynamical

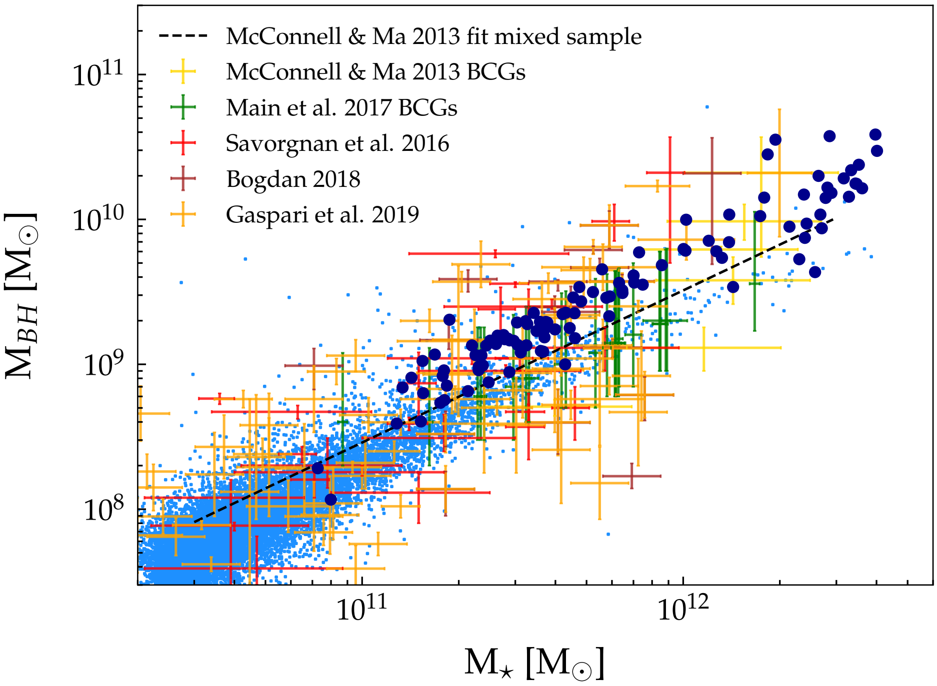

Fig. 3.1: Correlation between stellar mass and SMBH mass in observations and simulations. Small light-blue points represent non-BCG simulated galaxies, large black dots represent simulated BCGs. Yellow, green, red, brown, and orange crosses represent the observational data with their error bars taken from McConnell & Ma (2013), Main et al. (2017), Savorgnan et al. (2016), Bogdán et al. (2018), and Gaspari et al. (2019) respectively. The dashed black line is a linear best-fit of the sample of different type of galaxies by McConnell & Ma (2013). See text for details about $M_{\rm BH}$ and $M_\star$ definition and measurement.

measurements. The BCG masses in McConnell & Ma (2013) and Bogdán et al. (2018) are part of a compilation from previous literature and we refer to the original papers and references therein for further information on the methods employed to infer the stellar masses. In Savorgnan et al. (2016) the stellar masses are computed from bulge luminosities assuming a constant mass-to-light ratio, while in Gaspari et al. (2019) it is assumed a variable $M_\star/L_K$ scaling as a function of the stellar velocity dispersion (see Gaspari et al. 2019 for details). It should be noted that from Savorgnan et al. (2016) only ellipticals are used, that are not necessarily BCGs. In Main et al. (2017) the stellar masses are computed from K-band luminosity using the relation $\log(M/L_{\rm K}) = -0.206 + 0.135(B-V)$ given by Bell et al. (2003).

Our main constraint during the calibration is that the observed correlation between SMBHs mass and non-BCG galaxies (McConnell & Ma 2013, dashed line) passes through the bulk of the simulated galaxies (small blue points). We also care for an overall agreement at the BCG scales but with less emphasis because of the scatter of the observed sample (McConnell & Ma 2013) is high at the high mass end. Regarding the BCGs, we find that the simulated BCGs are in a good agreement with observational data at both ends of the mass range, but that the simulated points tend to stay above observational data at $M_\star > 10^{12}\ \mathrm{M}_\odot$, although still inside their error bars. This discrepancy does not necessarily highlight a poor description of the simulations since several factors need to be considered for a proper comparison. First, the SMBH masses are computed by adopting different methods. For example, those extracted by Main et al. (2017) are calibrated using a relation that does not include BCGs and, indeed, they are more aligned with the non-BCG sample. Second, BCG stellar masses are computed using different apertures in simulations and in the various observational samples. Furthermore, measurements of stellar mass from different works can disagree due to the different assumptions made during the data analysis, such as the assumed initial mass function, the adopted stellar mass-to-light ratio, distances, and beam aperture. Dynamical measurements can significantly disagree in particular when considering different tracers, such as stars versus circumnuclear gas, including different gas phases as warm and ionized versus cold and molecular gas. The resulting differences among catalogs can be comparable to the separation between simulated and observed data points. An example is clearly represented in the figure by NGC 4889, the galaxy with the most massive SMBH. This object is present in the Savorgnan et al. (2016), McConnell & Ma (2013), and Bogdán et al. (2018) samples and, while M_{BH} is identical because taken from the same source in the literature, the estimated BCG mass can be different even by a factor of ~ 2. This emphasizes the intrinsic difficulty in defining the BCG stellar masses and, at the same time, it quantifies a possible level of stellar mass difference among different works.

3.2.3 Galaxy mass properties

In our simulations the only tuning on the parameters of the subgrid models concerning baryonic physics is done in order to reproduce two constraints:

the Kennicutt-Schmidt relation for the star formation model and the Magorrian correlation for the AGN feedback model. It is then useful to see how the predictions from the simulations compare to other observational constraints, and in particular with the GSMF and the mass of the BCGs.

Since the stellar mass of the BCG will be extensively used in this Chapter, we start from the correlation between the BCG stellar mass and the total mass of the group/cluster. The results of the comparison are shown in Fig. 3.2. In numerical simulations, the BCG stellar mass is computed considering all the particles bounded to the main halo by Subfind and considering a 2D aperture of 50 physical kpc (pkpc). Therefore, the mass comprises the BCG mass plus the ICL along the line of sight. Simulations are in very good agreement with the observations by Kravtsov et al. (2018) and DeMaio et al. (2018). This is an important result, as in general simulations overshoot the stellar mass of the BCGs (e.g., Bahé et al. 2017, Henden et al. 2019).

In addition to BCGs stellar mass, we compare with the observed galaxy stellar mass function. For this comparison we first need to take into account the fact that our simulations are centered on galaxy clusters, while the data refers to the field[1]. Hence we expect to have in simulations a significant higher normalization of the GSMF. Operatively, we define galaxy clusters as spherical regions enclosing a mean matter density Δ times the critical density, $\rho_{\rm crit}$. Using the relation between $\rho_{\rm crit}$ and the mean cosmic matter density $\bar{\rho}$:

$$\rho_{\rm crit}(z) = \bar{\rho}(z) \times [\Omega_{\rm M}(1+z)^3 + \Omega_\Lambda]/\Omega_{\rm M}(1+z)^3, \tag{3.1}$$

and assuming that galaxies follow the DM distribution, it is necessary to normalize our GSMF by

$$N_{\rm norm} = \Delta \times [\Omega_M(1+z)^3 + \Omega_\Lambda]/\Omega_M(1+z)^3, \tag{3.2}$$

(see Vulcani et al. 2014, appendix B). In practice, I consider the most massive cluster in each of our simulated regions and all its galaxies within R_{100} (i.e., $\Delta = 100$) with the exclusion of the BCG, and then I normalize each mass bin by $N_{\rm norm}$.

The stellar mass of each galaxy is computed using three different defini-

---

[1] The same conclusions are reached also when comparing to a GSMF measured in galaxy clusters.

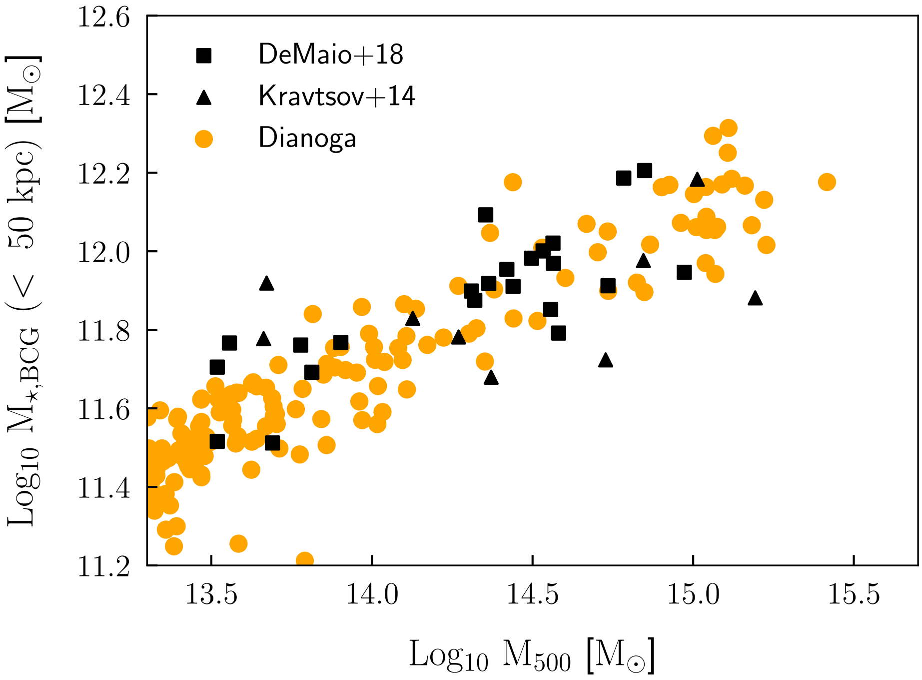

Fig. 3.2: Correlation between BCGs stellar mass and M_{500} at $z = 0$. Observations are taken from DeMaio et al. (2018) (blacks quares) and Kravtsov et al. (2018) (black triangles). The simulated values are shown as orange points. BCGs masses are obtained summing over all stellar particles bound to the main sub-halo of a group/cluster by Subfind (BCG+ICL) and within a 2D aperture of 50 pkpc.

tions: the sum of all stellar particles that Subfind associates to a substructure and the same sum limited to stellar particles within 30 pkpc and 50 pkpc from the center. The different definitions are used since it is not feasible to replicate the procedure used in observations. Indeed, in the observations used for this comparison, the stellar mass is derived by fitting the surface brightness profile which is then integrated to infinity and translated to a stellar mass through a mass-to-light ratio. The results are shown in Fig. 3.3, where I plot the GSMF obtained with the three definitions of stellar mass. First of all, we can see that the GSMF obtained considering all the stellar particles associated by Subfind to the substructures is larger than the one obtained via the other definitions, as Subfind likely associate to massive galaxies also a fraction of the intra-cluster light (ICL). Secondly, once a fixed aperture is used, the simulated GSMF is below observations by a factor of

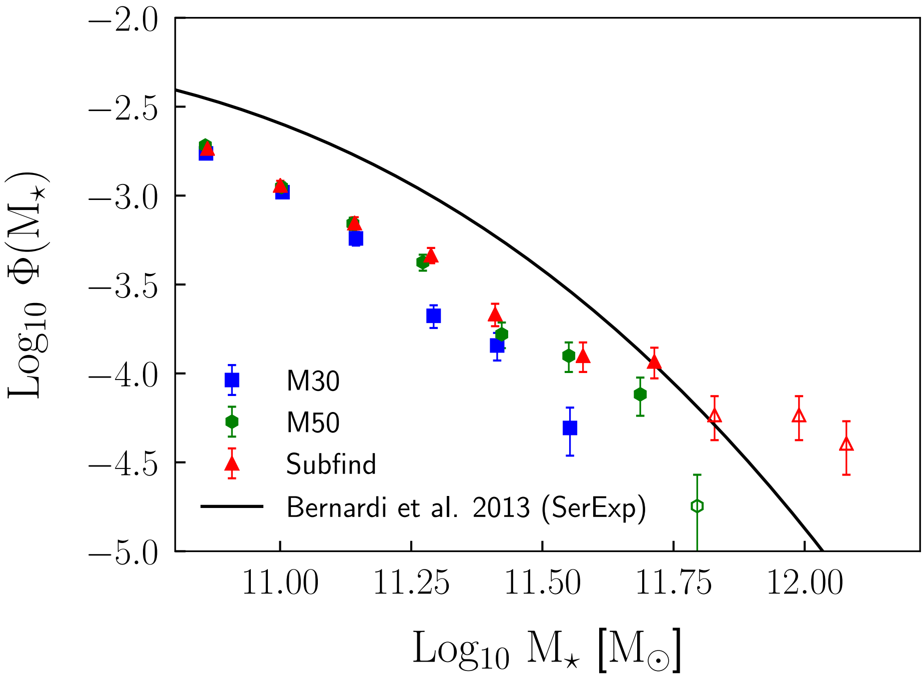

Fig. 3.3: GSMF at z = 0. Observational data are taken from Bernardi et al. (2013) (black solid line). Simulations data are derived considering as stellar mass the sum of all stellar particles bound to the galaxy by Subfind (red triangles), and the same sum restricted to particles within 50 pkpc (green hexagon) and 30 pkpc (blue squares). Error bars are computed assuming Poissonian errors. The simulated GSMF is normalized following Eq. 8. Filled and empty marks represent the mass bins with respectively more than and less than 10 galaxies.

two. As I will better show and discuss in the next Chapter, this is due to the implementation of the AGN feedback. I anticipate, however, that even though a better agreement in the GSMF normalization can be achieved through a different AGN feedback implementation, this comes at the cost of increasing the normalization of the $M_{\star,\mathrm{BCG}} - M_{500}$ correlation.

3.3 Method and samples

To investigate possible correlations between the central SMBHs and the global cluster properties it is necessary to extract the cluster masses and temperatures from the simulated regions. In addition, we need to calculate the SMBH mass and the two contributions to its growth: the accretion of the surrounding gas and the merger with other SMBHs. In the following, after specifying the definition of the cluster center, I describe how all these quantities are computed.

Cluster center. As mentioned in the previous section, the SMBHs are always positioned at the location of the most bound particle that should identify the center of the host halo. Therefore, the SMBHs are followed back in time to identify the position of the hosting halo center. For this goal, I saved at z=0 the unique identification number of the most massive SMBH particle which is within 10 kpc from the cluster minimum of the potential well, as identified by Subfind. Subsequently, I tracked it back in time to the epoch of its seeding. At each time, I checked that the SMBH is, as expected, at the minimum of the potential well of the hosting halo and not in a local minimum generated by merging substructures. With this approach, a merger tree of the central SMBHs is built rather than a merger tree of the clusters. It might be expected that the two trees differ especially at early epochs (similarly to the small differences between the BCG and the cluster merger trees pointed out in Ragone-Figueroa et al. 2018, which used the same set of simulations presented in this Chapter). However, I verified that for 80% of our systems the main progenitor of the SMBH is at the center of the main progenitor of the cluster up to $z = 2$ and for half of these the two trees coincide till the time when the SMBH is seeded.

Cluster masses. Once the center is defined as above, I considered the total gravitational mass of the cluster within an aperture radius $R \leq R_{500}$ computed by summing over all the species of particles: dark matter, cold and hot gas, stars, and black holes. At any redshift I considered only clusters with $M_{\rm cluster} = M_{500} \geq 1.4 \times 10^{13}$ $\mathrm{M}_{\odot}$ or, equivalently, with at least 20 thousands particles within R_{500}. The properties of the mass-selected sample are summarized in the top part of Table 3.1.

BCG stellar mass. The mass of the BCG, $M_{\rm BCG}$, is defined as the stellar mass enclosed in a sphere of radius $0.1 \times R_{500}$ around the cluster center.

SMBH mass. Given the identification number of a SMBH particle, the mass of the SMBH, $M_{\rm BH}$, at every redshift is quite easily retrieved from the simulation as it is the mass associated to that particle. The total mass of SMBH particles grows in time because of two separate phenomena: through the accretion of the diffuse gas or via BH-BH mergers. In our simulations, these are the only possible channels for the SMBH to increase its mass. The accretion mass ($M_{\rm BH}^{\rm acc}$) is obtained by integrating the accretion rate, information that is saved at each time step. The merged mass ($M_{\rm BH}^{\rm mer}$) is simply calculated as a difference between the total mass and the accretion mass. As discussed later in the chapter, the contribution to the SMBH mass by mergers is negligible at $z \geq 1.5$. Therefore the analysis of this component is restricted to lower redshifts.

Temperature. In order to compare the results obtained in this chapter to those from *XMM-Newton* observations I considered the spectroscopic-like temperature (Mazzotta et al. 2004):

$$T_{500} = \sum_i \left(\rho_i m_i T_i^{0.25}\right) \Big/ \sum_i \left(\rho_i m_i T_i^{-0.75}\right), \tag{3.3}$$

where ρ_i, m_i, and T_i are the density, mass, and temperature of the $i^{\rm th}$ gas particle within R_{500} emitting in the X-ray band, that is with $T_i > 0.3$ keV and a cold fraction lower than 10 per cent. In order to have a reliable estimation of the temperature inside R_{500} I imposed two conditions: a minimum of 10^4 hot gas particles and a maximum fraction of 5 per cent of gas particles discarded because too cold. All clusters satisfying these requirements have also $M_{500} > 1.4 \times 10^{13}$ $\rm M_{\odot}$, thus whenever I consider measurements of temperature I refer to a subsample of the mass selected-sample. The properties of the temperature-selected subsample are summarized in the bottom part of Table 3.1 and the analysis of this subsample is restricted to $z \leq 1$ because at the highest redshift bins, $z = 1.5$ and $z = 2$, we do not have enough statistics to apply a meaningful analysis.

Best-fitting procedure. For all the considered relations, I search for the best-fit power law in the form:

$$\log(Y/Y_0) = a + b \times \log(X/X_0), \tag{3.4}$$

where $\log$ always indicates the decimal logarithm. Temperature, cluster mass,

Table 3.1: Number of clusters, range of mass or temperature covered and their mean values for the mass samples (in the first half) and temperature subsamples (in the second half).

		M samples	
z	N	M_{500} [10^{14}M$_\odot$]	$< M >$ [10^{14}M$_\odot$]
0.0	135	0.14-25.83	2.94
0.5	114	0.14-14.11	1.65
1.0	85	0.14-5.15	0.99
1.5	59	0.14-2.48	0.69
2.0	37	0.15-1.59	0.52
		T subsamples	
z	N	T_{500} [keV]	$< T >$ [keV]
0.0	93	0.80-10.81	3.27
0.5	62	0.80-8.89	2.97
1.0	35	0.95-5.84	3.01

BCG stellar mass, and SMBH mass are always normalized by the same factors, expressed above as X_0 or Y_0 and respectively equal to 2 keV, 10^{14} M$_\odot$, 10^{11} M$_\odot$, and 10^{9} M$_\odot$.

To find the best-fit curve, I employed an IDL routine that is resistant with respect to outliers: ROBUST_LINEFIT[2]. For the simulated data, I always considered the BISECT option, recommended when the errors on X and Y are comparable so that there is no true independent variable. This is particularly appropriate in the case of numerical simulations where no errors are linked to measurements. To estimate the error associated with the parameters of the best-fitting relation, ten thousand bootstrap samples has been generated by randomly replacing the data. From the resulting distributions I derived the mean values and the standard deviations to be associated, respectively, with the parameters and their errors. All relevant best-fitting coefficients of the linear regressions are reported in Table 3.2 and will be discussed in the next two sections.

3.4 Results

---

[2] https://idlastro.gsfc.nasa.gov/ftp/pro/robust/robust_linefit.pro

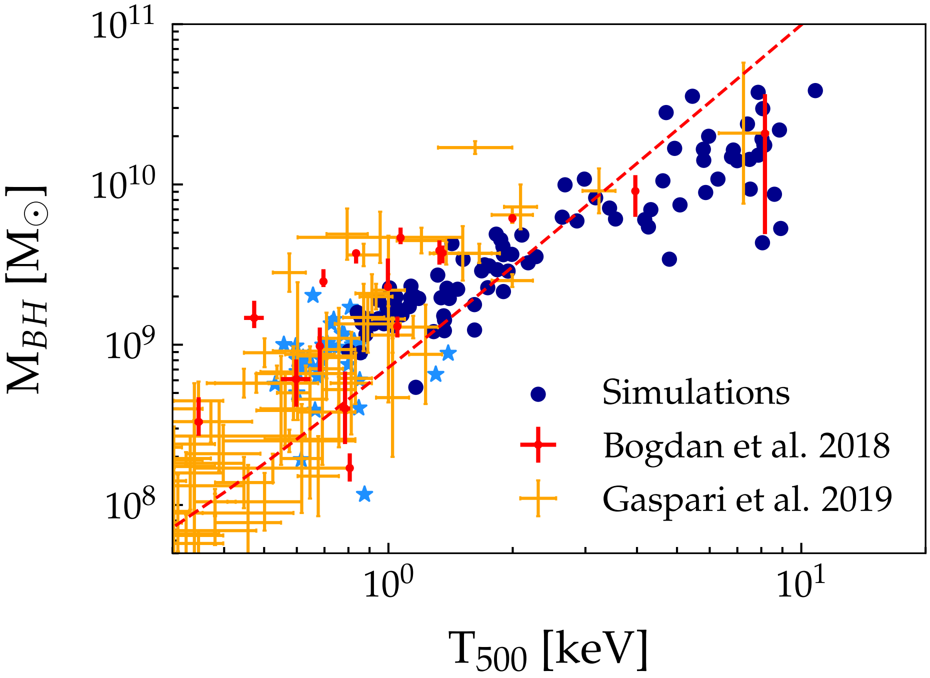

Fig. 3.4: Correlation between SMBH mass, $M_{\rm BH}$, and the clusters temperature, T_{500}. Red and orange crosses refer to observational data from Bogdán et al. (2018) and Gaspari et al. (2019) respectively. Dark-blue dots represent simulated clusters in the temperature subsample while cyan stars show the remaining objects of the mass sample. Dashed red line is the prediction of the toy model by Churazov et al. (2005).

3.4.1 Comparison with observational data

In this section I compare the numerical results to the observations presented in Bogdán et al. (2018), where the correlation between the mass of the SMBHs in BCG and the global temperature of clusters and groups of galaxies is presented. I also complement this analysis with the more recent data of Gaspari et al. (2019)[3]. Bogdán et al. (2018) derived the temperature from *XMM-Newton* observations of the hot gas; In Gaspari et al. (2019) we used published data of Chandra and wide-field *ROSAT/XMM Newton*. The extraction region for both is on average $\sim 0.2\,R_{500}$ (core included; As shown by Bogdán et al. (2018), such temperature is a good proxy for T_{500}) .

In Fig. 3.4 I show the correlation between $M_{\rm BH}$ and T_{500} for both sim-

---

[3] This sample includes not only massive galaxies in groups and clusters, but also isolated and spiral galaxies.

ulations and observations. In the figure I also show as a dashed red line the results of the simple toy model by Churazov et al. (2005) [4], which even under simplified assumptions reproduces the observed correlation. Results from simulations agree overall well with observations. Nevertheless, a more quantitative comparison between the two samples is difficult for an under-representation of clusters with $T_{500} > 2$ keV in the observational sample that, however, has a good number of systems below 1 keV.

In order to better populate the colder and less massive tail of the simulated cluster distribution I compare the correlation between $M_{\rm BH}$ and M_{500} by using the mass sample rather than the less-numerous temperature sub-sample (Table 1). In Bogdán et al. (2018) the total mass was not measured directly from their data but was derived from the temperature via the scaling relation by Lovisari et al. (2015):

$$M_{500} = 1.11 \times 10^{14} (kT/2\ \text{keV})^{1.65} \text{M}_{\odot}. \tag{3.5}$$

For this reason, before analyzing the $M_{\rm BH}$-M_{500} relation, it is helpful to compare the observed and simulated T_{500}-M_{500} relations. The observed and simulated data sets are shown in Fig. 3.5 together with the best-fitting linear relations. In case of the observed sample it has been verified that our fitting procedure, without the BISECT option, returned the same parameters of Eq. 3.5. In particular the value of the slope reported in Lovisari et al. (2015) ($b = 1.65 \pm 0.07$), is confirmed.

By looking at Fig. 3.5, a good agreement between simulated and observed clusters is found in the temperature range covered by Lovisari et al. (2015). However, the extrapolation of their best-fit line suggests a possible difference in the hottest-clusters regime. The two slopes agree within 1σ, but the observed clusters have on average slightly higher temperature with respect to simulated clusters at fixed mass. For example, the temperature of observed clusters is 9 per cent higher at $M_{500} = 10^{14}$ $\text{M}_{\odot}$. This feature is not new and has been already noted in Truong et al. (2018), where a similar set of numerical simulations is employed, and, more interestingly, in other numerical analysis, such as Henden et al. (2018). In particular, in their work the authors show that numerical results are in agreement with observations if are considered only cluster masses derived via weak lensing. This suggests that

---

[4] Equation 7 of Churazov et al. (2005) with $\delta_E = 10^{-4}$, $t_9 = 1$, $\Lambda(T)$ as defined in Tozzi & Norman (2001) with $Z = 0.3\ Z_{\odot}$, and $T = 3 \times 10^6\ \sigma_{200}\ K$

Table 3.2: Parameters of all best-fitting lines derived with the procedure described at the end of Sect. 3.3. For each (X,Y) pair of data, I fit the formula: $\log(Y/Y_0) = a + b \times \log(X/X_0)$ where the normalizations, X_0 or Y_0, are equal to 2 keV, $10^{14}M_\odot$,$10^{11}M_\odot$ and $10^9M_\odot$, respectively, for $T, M_{500}, M_{\rm BCG}$, and all SMBH masses: $M_{\rm BH}, M_{\rm BH}^{\rm mer}$, and $M_{\rm BH}^{\rm acc}$. The parameters a, b, and σ and their errors are the mean and standard deviation values of the distributions obtained by applying the procedure to ten thousand bootstrapping samples. The asterisks indicate that the analysis is performed to the temperature subsample.

(X, Y)	a	b	$\sigma_{Y\|X}$
$z = 0$			
M_{500}, T^*	0.10 ± 0.01	1.71 ± 0.03	0.07 ± 0.01
$T, M_{\rm BH}^*$	0.52 ± 0.02	1.28 ± 0.06	0.16 ± 0.02
$M_{500}, M_{\rm BCG}$	0.75 ± 0.01	0.66 ± 0.01	0.10 ± 0.01
$M_{\rm BCG}, M_{\rm BH}$	-0.42 ± 0.03	1.16 ± 0.04	0.14 ± 0.01
$M_{500}, M_{\rm BH}$	0.45 ± 0.02	0.76 ± 0.03	0.18 ± 0.02
$M_{500}, M_{\rm BH}^{\rm mer}$	0.20 ± 0.02	0.73 ± 0.04	0.23 ± 0.02
$M_{500}, M_{\rm BH}^{\rm acc}$	0.03 ± 0.02	0.83 ± 0.04	0.25 ± 0.02
$z = 0.5$			
M_{500}, T^*	0.05 ± 0.01	1.73 ± 0.04	0.08 ± 0.01
$T, M_{\rm BH}^*$	0.48 ± 0.03	1.49 ± 0.11	0.24 ± 0.03
$M_{500}, M_{\rm BCG}$	0.68 ± 0.01	0.69 ± 0.02	0.13 ± 0.01
$M_{\rm BCG}, M_{\rm BH}$	-0.42 ± 0.03	1.25 ± 0.05	0.16 ± 0.02
$M_{500}, M_{\rm BH}$	0.43 ± 0.02	0.86 ± 0.04	0.23 ± 0.02
$M_{500}, M_{\rm BH}^{\rm mer}$	0.06 ± 0.03	0.92 ± 0.06	0.34 ± 0.04
$M_{500}, M_{\rm BH}^{\rm acc}$	0.15 ± 0.03	0.90 ± 0.06	0.27 ± 0.03
$z = 1$			
M_{500}, T^*	-0.07 ± 0.01	1.72 ± 0.05	0.06 ± 0.01
$T, M_{\rm BH}^*$	0.46 ± 0.04	1.70 ± 0.22	0.22 ± 0.03
$M_{500}, M_{\rm BCG}$	0.67 ± 0.01	0.73 ± 0.03	0.11 ± 0.01
$M_{\rm BCG}, M_{\rm BH}$	-0.42 ± 0.04	1.45 ± 0.07	0.19 ± 0.02
$M_{500}, M_{\rm BH}$	0.56 ± 0.04	1.06 ± 0.08	0.27 ± 0.03
$M_{500}, M_{\rm BH}^{\rm mer}$	0.12 ± 0.04	1.21 ± 0.17	0.40 ± 0.09
$M_{500}, M_{\rm BH}^{\rm acc}$	0.35 ± 0.05	1.07 ± 0.09	0.30 ± 0.03
$z = 1.5$			
$M_{500}, M_{\rm BCG}$	0.69 ± 0.02	0.77 ± 0.05	0.12 ± 0.02
$M_{\rm BCG}, M_{\rm BH}$	-0.38 ± 0.05	1.58 ± 0.10	0.22 ± 0.02
$M_{500}, M_{\rm BH}$	0.71 ± 0.05	1.25 ± 0.11	0.30 ± 0.04
$M_{500}, M_{\rm BH}^{\rm acc}$	0.55 ± 0.06	1.27 ± 0.11	0.33 ± 0.05
$z = 2$			
$M_{500}, M_{\rm BCG}$	0.67 ± 0.02	0.75 ± 0.06	0.11 ± 0.03
$M_{\rm BCG}, M_{\rm BH}$	-0.33 ± 0.08	1.76 ± 0.20	0.26 ± 0.05
$M_{500}, M_{\rm BH}$	0.85 ± 0.08	1.35 ± 0.15	0.34 ± 0.04
$M_{500}, M_{\rm BH}^{\rm acc}$	0.72 ± 0.10	1.37 ± 0.16	0.36 ± 0.04

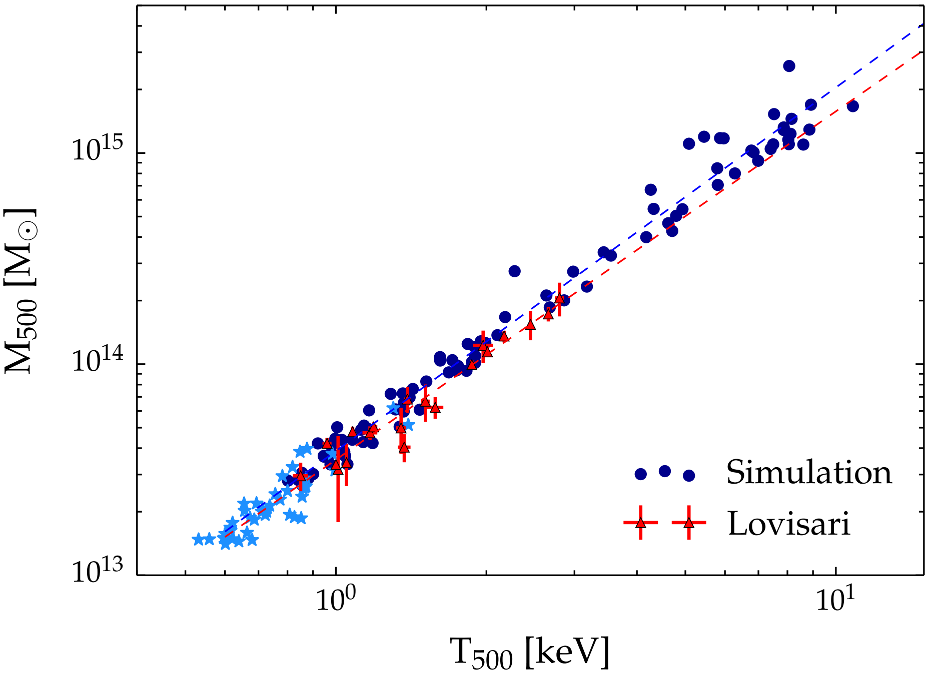

Fig. 3.5: Correlation between cluster mass, M_{500}, and cluster temperature, T_{500}. Symbols as in Fig.3.4, where the observational data are taken from Lovisari et al. (2015). Dashed lines are the best-fitting lines for both simulated and observed data.

the observed X-ray hydrostatic masses are biased low, as already described in Chapter 1 (see Sect. 1.2.1).

Finally, in Fig. 3.6 I compare the correlation between $M_{\rm BH}$ and the M_{500} as measured in simulations and as derived by Bogdán et al. (2018) and Gaspari et al. (2019). The results of the comparison are expected from the previous two figures: the simulated data points are in line with observations, especially at high ($M_{500} > 3 \times 10^{14}$ $M_\odot$) and low masses ($M_{500} < 3 \times 10^{13}$ $M_\odot$). In the intermediate mass range, the few observed data points tend to have slightly higher SMBH masses than the simulated objects. This apparent mis-match is presumably a consequence of the poor statistics of 10^{14} $M_\odot$ objects in the observational sample. More unlikely, this feature could suggest a broken power law to describe the $M_{\rm BH} - M_{500}$ relation, but such a drastic change in the slopes is difficult to justify.

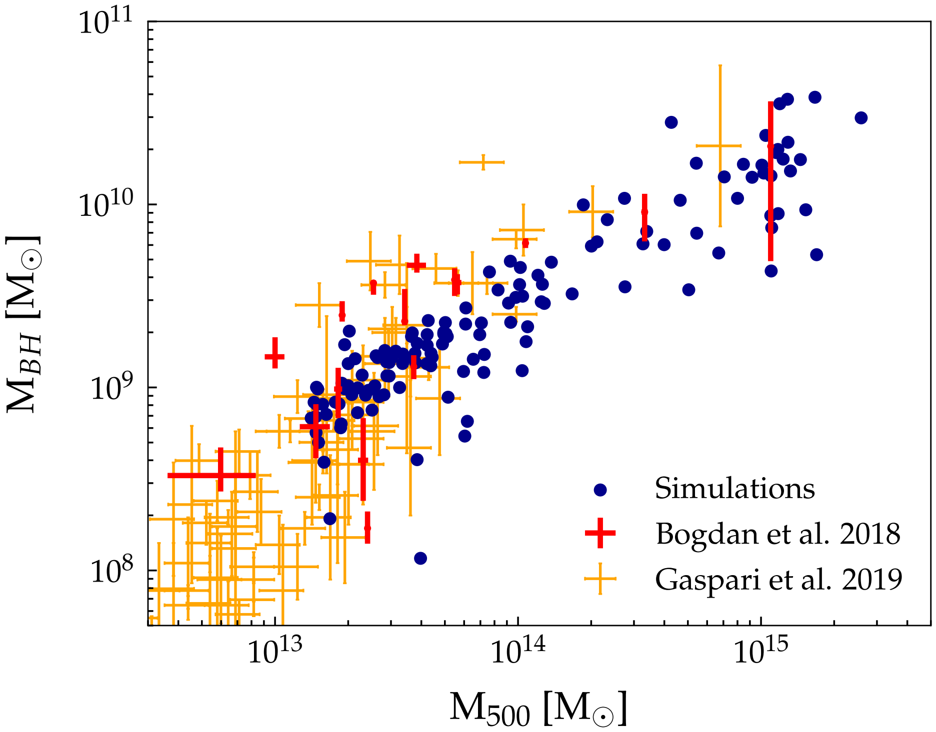

Fig. 3.6: Correlation between SMBH mass, $M_{\rm BH}$, and cluster mass, M_{500}. Symbols as in Fig.3.4.

3.4.2 The theoretical $M_{\rm BH}$-M_{500} relation

Since the simulated sample is in overall good agreement with the observed correlation between the mass of the central SMBHs and the mass of the clusters, I investigate here how single simulated systems evolve throughout time to form, by $z = 0$, the $M_{\rm BH} - M_{500}$ relation shown in Fig. 3.7. For this goal, three evolutionary tracks of representative SMBHs are over-plotted. These objects are chosen accordingly to their mass at $z = 0$; specifically, they refer to a small, a medium-mass, and a massive SMBH. To have some temporal reference I also indicated four specific times along each line: $z = 3$, $z = 2$, $z = 1$, and $z = 0$.

Despite the different final masses, the evolutionary tracks of the three systems have strong similarities which are common also in all the other objects analyzed (not shown for sake of clarity). Three phases are clearly distinguishable. At the highest redshifts, the mass of the SMBHs grows rapidly at almost constant M_{500}. This track begins instantaneously as the SMBHs are seeded

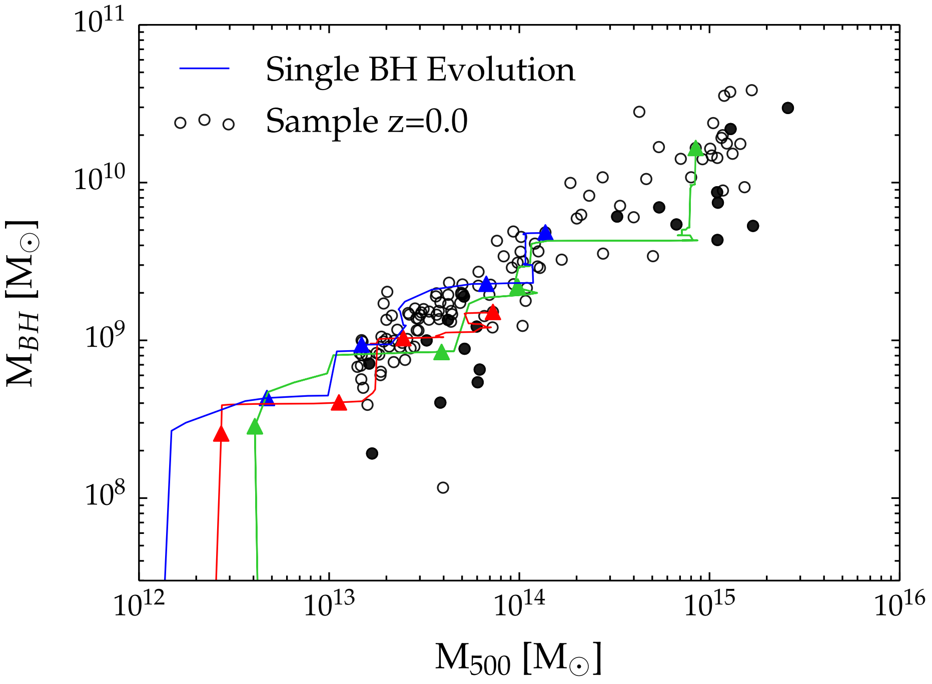

Fig. 3.7: Evolutionary tracks of three different systems on the $M_{\rm BH}$-M_{500} plane. Triangles over each line indicate the position of the systems on the plane at $z = 3$, $z = 2$, $z = 1$ and $z = 0$. Black circles represent our numerical sample at $z = 0$; the filled ones are systems for which M_{500} is increased by more than 40 percent in the last Gyr.

in a gas rich region. The SMBHs immediately gain mass at the Eddington limit by the accretion from the abundant surrounding gas, which is mostly cold and thus efficient at increasing the SMBH mass. This phase typically lasts half Gyr and can lead to the formation of SMBHs with a mass already of the order of $M_{\rm BH} \approx 10^8 - 10^9 {\rm M}_{\odot}$, in line with other hydrodynamical cosmological simulations (e.g., McAlpine et al. 2018). The fast SMBH growth ends when the $M_{\rm BH}$ is high enough to cause an intense feedback that leads to the ejection of part of the gas outside the shallow potential wells of the hosting galaxies. By then, all SMBHs in our sample are close to the $M_{\rm BH} - M_{500}$ relation. This happens before $z = 2$ and in some cases even at $z > 4$.

After this initial phase, the cluster and its central SMBH co-evolve, but not with a linear evolutionary track: the increase of the SMBH and cluster masses is not simultaneous. The shape of the tracks, instead, can be described as a stairway: the systems evolve in this plane either at almost constant $M_{\rm BH}$ or at almost constant M_{500}. The former situation occurs during cluster mergers. It starts when merging structures reach and cross R_{500} leading to a quick increment of the total cluster mass and finishes when the secondary objects are fully incorporated. These horizontal shifts in the $M_{\rm BH}$-M_{500} plane typically last 1 Gyr or less and only in the rare cases when multiple mergers are subsequently taking place they can last up to 2 Gyr. In the following period, spanning from 1 to 3 Gyr, the substructures move towards the center of the cluster and neither the SMBH mass nor the cluster mass change. Eventually, the merging objects reach the core and either feed the central SMBH with gas or induce a BH-BH merger or both. The event is captured by the vertical movement in the plot.

All these time-frames are clearly indicative as they depend on several parameters that characterize the merger events such as the mass ratio and the impact parameter. Nonetheless, it is always the case that the mass of the SMBH and of the cluster are for the largest majority of time at the connection between the horizontal and vertical steps rather than along their tracks. This behavior indicates that the scatter of the relation might differ when the sample is selected according to the dynamical status of the SMBH hosts. We expect that the points related to relaxed BCG in relaxed clusters will always be above the points linked to systems where either the BCG or the cluster are experiencing, or just experienced, a merger event. Indeed, we can expect that relaxed and perturbed systems are respectively located in the plot on the top and the bottom of the vertical segments. In favor of this picture, it is noticeable that the 20 clusters whose M_{500} grows by more than 40 per cent in the last Gyr (shown as black points in Fig. 3.7) have SMBHs that on median are 50 per cent smaller than those expected to follow the $\rm M_{500}$-$\rm M_{BH}$ relation.

3.4.3 Evolution of the $\rm M_{BH}$-$\rm M_{500}$ relation

After the inspection on the trajectory of individual objects I study here the evolution of the entire $\rm M_{500}$-$\rm M_{BH}$ relation. I start with the evaluation of the ratio between the mass gained by clusters and by central SMBHs between $z = 2$ and $z = 0$: $\Delta_M = M_{z=2}/M_{z=0}$, where M refers to either the total mass, M_{500}, or the SMBH mass, $M_{\rm BH}$. If these two ratios are constant, the slope of the relation will not change. The resulting ratios are shown in

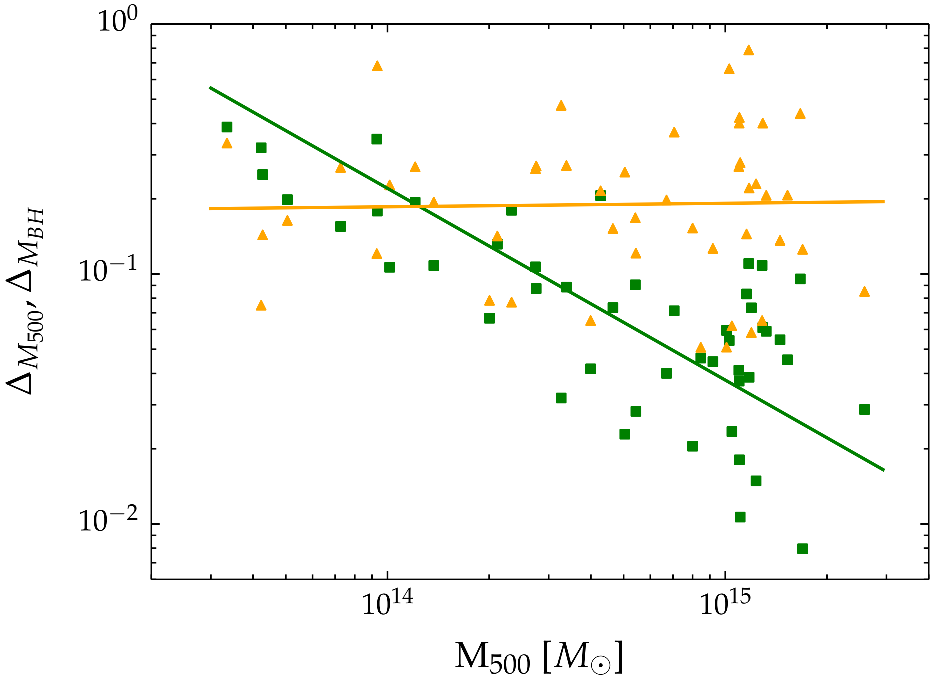

Fig. 3.8: Ratios between cluster (SMBH) masses at $z = 2$ and cluster (SMBH) masses at $z = 0$ as a function of the cluster masses at $z = 0$. Clusters are shown as green squares and SMBHs as yellow triangles. The sample used is the mass-selected sample identified at $z = 2$.

Fig. 3.8 as a function of the cluster total mass reached at $z = 0$ for the mass sample identified at $z = 2$. From the plot, it can be clearly inferred that the variation in total mass between the two epochs is strongly mass dependent. The absolute value of the slope of the best-fitting $\Delta_{M_{500}} - M_{500}$ relation is, indeed, greater than 0.75. Clusters with a final mass lower than 10^{14} M$_\odot$ increase their total masses by a factor between 3 and 6. Instead, massive clusters with final $M_{500} > 10^{15}$ M$_\odot$ increase their mass on average by a factor of about 30 with individual objects that can grow by more than two orders of magnitude. This feature is completely in line with the expectations of hierarchical clustering.

The high mass regime is particularly characterized by a large spread that is representative of what we might expect from a volume-limited sample because the most massive objects, $M_{500} > 10^{15}$ M$_\odot$ correspond to the most massive systems of the parent volume-limited cosmological box (see Sect 2.5.1). Vice versa, the scatter for the smallest systems is likely under-estimated.

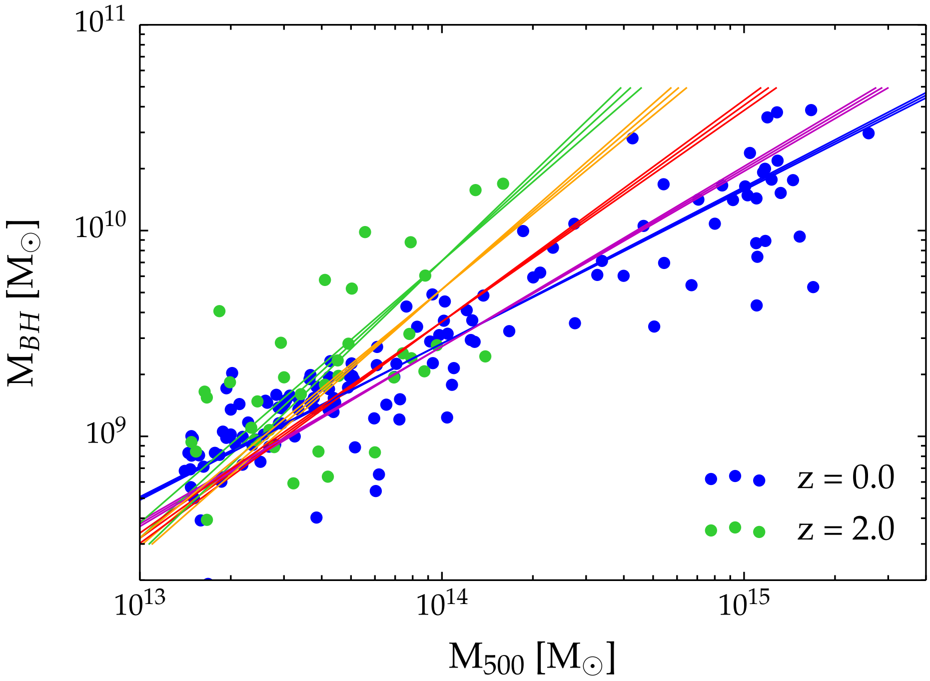

Fig. 3.9: Correlation between $\mathrm{M_{BH}}$ and $\mathrm{M_{500}}$ at different redshifts. At every redshift I show the best-fitting relation in the mass range of the respective samples. Namely, I show in green, orange, red, magenta, and blue the mass sample related to $z = 2, 1.5, 1, 0.5$ and $z = 0$, respectively.

Indeed, the linear trend is expected to flatten for the lowest masses to a constant growth rate value. On the other side, Fig. 3.8 also shows that the variation on the SMBHs mass is independent of the cluster mass and that SMBHs grow on average by a factor of about 5-6. As a consequence we expect a marked evolution of the slope of the $M_{\rm BH}$-M_{500} relation between $z = 2$ and $z = 0$.

This is confirmed in Fig. 3.9 where the best-fitting lines for our mass samples at all redshifts considered are plotted. The relations are steeper at higher redshifts: the value at $z = 2$, $b = 1.348$, is almost twice the value found at $z = 0$, $b = 0.753$. From Fig. 3.8 and Fig. 3.9 follows that the change in the slope is mainly driven by the different evolution rate of the most massive clusters with respect to the smallest objects, trend that is in line with the expectations from ΛCDM cosmology.

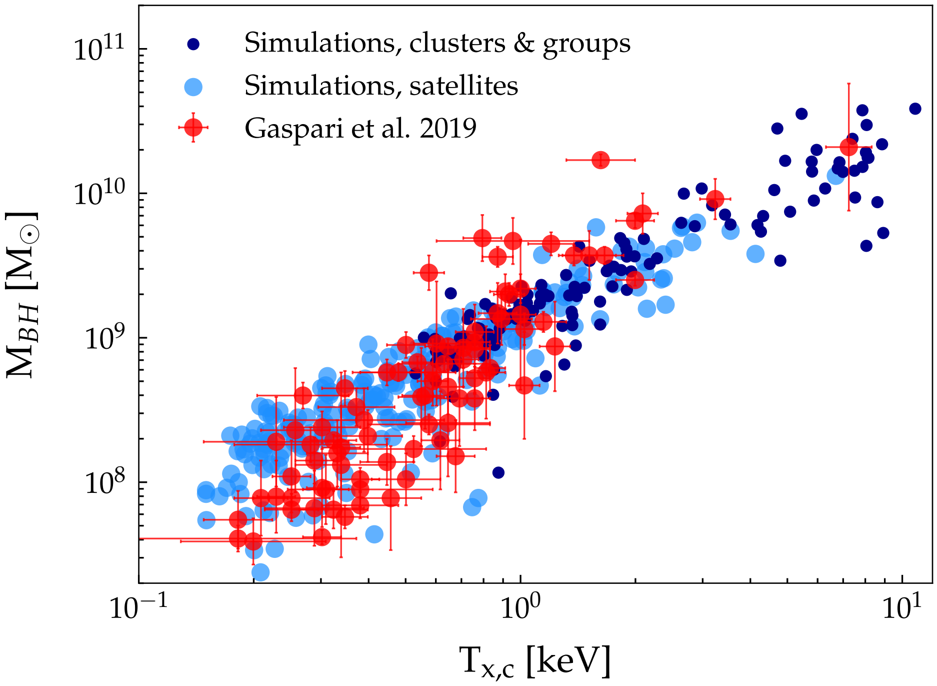

Fig. 3.10: Correlation between SMBH mass and atmospheric temperature in simulations and observations. Red points represent observations by Gaspari et al. (2019). Dark-blue points represent the 135 groups and clusters analyzed in our simulations, where T_X is computed within R_{500}. Cyan points are satellite galaxies in our simulations with at least 100 gas particles as associated by Subfind. For these galaxies T_X is computed from the gas particles associated by Subfind to the structure and with $T_X > 0.1$ keV.

3.4.4 $M_{\rm BH} - T_X$ correlation in non-central galaxies

In Fig. 3.4 I showed the correlation between central SMBH and cluster temperature. In this section I extend the analysis to SMBHs within satellite galaxies. The results are presented In Fig. 3.10, where I show the correlation between the X-ray temperature of galaxies and their central SMBH mass at $z = 0$. Red points refer to the observational sample of Gaspari et al. (2019), while the dark-blue points refer to the 135 groups and clusters already analyzed in the previous sections with the temperature computed as explained in Sect. 3.3 (i.e., considering X-ray emitting gas particles within R_{500}). Cyan points show satellite galaxies within our simulations. Since the gas temperature is involved, only galaxies with at least 100 gas particles (as associated to the galaxy by Subfind) are represented, in order to have a reliable value for T_X. The latter is computed considering only particles with $T_X > 0.1 \text{ keV}$ through Eq. 3.3. From the plot it is clear that SMBH mass exhibits a good correlation with X-ray temperature, also in numerical simulations. It is important to note that this result is not a genuine prediction, as AGN feedback is calibrated to reproduce the Magorrian relation (see Sect. 3.2). Since it can be expected that more massive systems are also characterized by a higher hot halo temperature, the results shown in Fig. 3.10 may be a result of the subgrid model calibration. Moreover, even though the scatter around this correlation is very similar between simulations and observations (0.23 and 0.25 respectively), the slope in simulations is shallower than in observations (1.34 ± 0.03 and 2.14 ± 0.13 respectively). This last feature, together with the smaller scatter around the Magorrian relation with respect to observations highlighted in Sect. 3.2.2, hint that there is space for improvement in the current implementation of the subgrid model for AGN feedback. Nonetheless, it is still interesting to see that simulations predict a correlation also for non-central and less massive systems. Clearly, this result comes in contrast with the observations by Lakhchaura et al. (2019) which show a much weaker correlation for non-central elliptical galaxies and lenticulars.

Even though the results shown in Fig. 3.10 suggest that the correlations are not a consequence of mergers, since they hold at both mass ends for both central and satellite galaxies, the dependence of the results on the employed subgrid model prevent us from drawing general conclusions. Therefore, to constrain the origin of the observed correlation it is useful to study the two channels responsible for the SMBH mass growth. As before, first I focus on the SMBH at the center of BCG (next section), while I will explore the number of mergers for SMBHs within all simulated galaxies in Sect. 3.4.8.

3.4.5 Evolution of SMBH mass

To better understand how the black hole mass of *central* SMBHs evolves with time I separately study the two mechanisms that contribute to the growth of the SMBH mass: the accretion of the diffuse gas, $M_{\text{BH}}^{\text{acc}}$, and the merger with other SMBHs, $M_{\text{BH}}^{\text{mer}}$. First, I analyze how the mass of single SMBH evolves with time via the two separate channels. As an example in Fig. 3.11 I plot the evolution of the three SMBHs shown in Fig. 3.7. As already noted before, the evolution is characterized by an initial phase of intense gas accretion

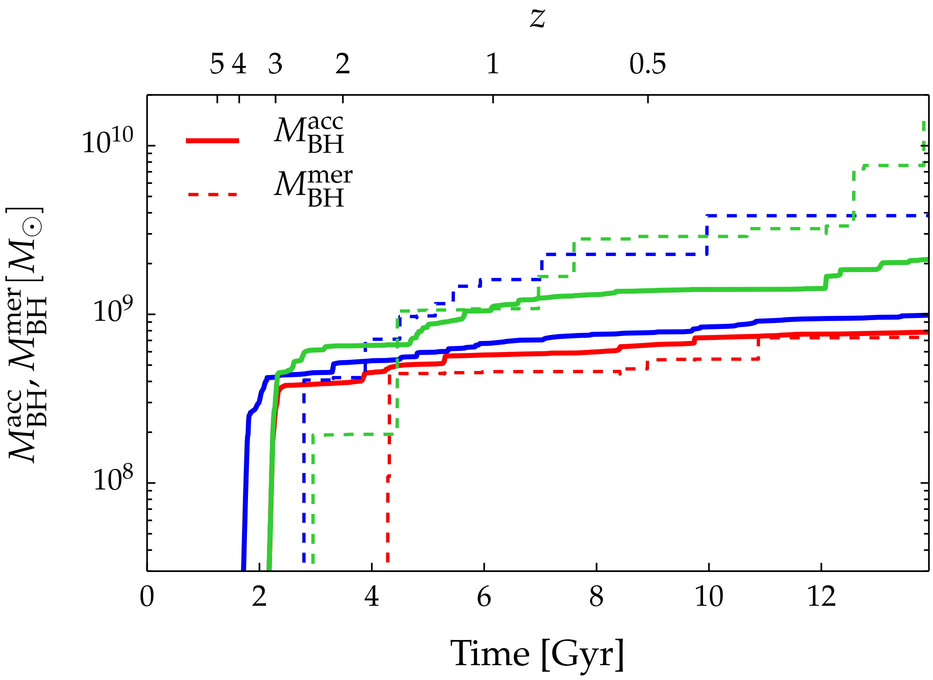

Fig. 3.11: Evolution of the mass of black holes showed in Fig. 3.7. The solid lines represent the mass of the black holes due to gas accretion. Dashed lines represent mass gained via BH-BH mergers.

that for these three systems is approximately between $z = 5$ and $z = 3$. After that, SMBHs still grow by gas accretion but at a much smaller rate. On the contrary the increase of the SMBH mass due to BH-BH mergers becomes more important and it is the main channel of the SMBH mass growth at lower redshifts, that is $z \leq 1$ for the two most massive SMBHs and $z \leq 0.5$ for the smallest one.

In Fig. 3.12 I show the evolution of the complete sample. I plot the median behaviors with a solid line and the 68 per cent of the total sample distributions (from the $16^{\rm th}$ to the $84^{\rm th}$ percentiles) with the shaded regions. The total SMBH mass and the masses gained from the two channels are normalized with respect to the total SMBH mass at $z = 0$. Finally, the dashed vertical lines help to identify three significant times: $z = 0.5$, 1, and 2.

From the SMBH seeding up to $z \approx 2$ the total mass of the SMBH grows almost entirely by gas accretion. Half of the final mass gained through gas accretion is, indeed, accumulated before $z = 2$. Then from $z \sim 2$ to $z \sim 1$ the mass growth due to BH-BH merger becomes more relevant increasing

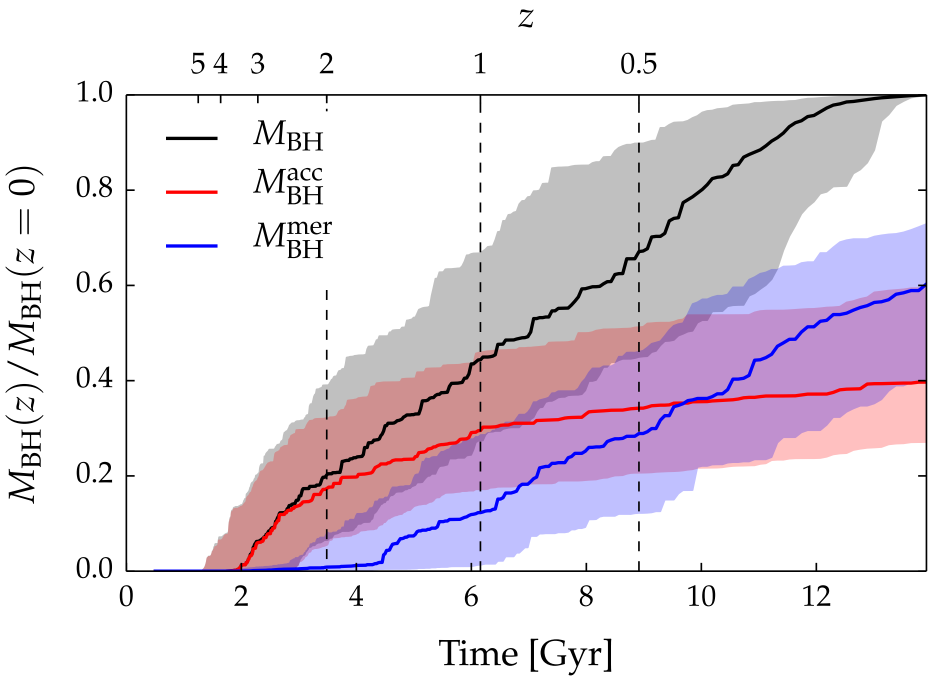

Fig. 3.12: Evolution of SMBH mass divided into two growth channels (gas accretion in red and BH-BH mergers in blue) considering the complete sample. In black we also plotted the total SMBH mass. Solid lines represent median values of our sample and shadowed regions represent 16 and 84 percentiles.

at a rate comparable to the growth rate of $M_{\rm BH}^{\rm acc}$. By $z = 1$ $M_{\rm BH}^{\rm mer}$ makes up on average 25 per cent of the total mass at that redshift. At lower redshift, $z < 0.5$, BH-BH mergers provide the main channel for SMBH mass growth, and eventually $M_{\rm BH}^{\rm mer}$ represents the main component of mass gained by $z = 0$, in line with some previous results (e.g., Volonteri & Ciotti 2013; Dubois et al. 2014; Weinberger et al. 2018). Indeed, the mass accumulated by gas accretion from $z = 1$ to $z = 0$ accounts only for 10 per cent of the total final mass, while during the same period the SMBH gains 50 per cent of its final mass via mergers.

The relative importance of the two channels shown in the figure is, however, characterized by a large scatter. I, therefore, explored whether this is due to the broad mass range investigated and, thus, whether the described behavior depends on the mass of the systems. I divided the sample in three

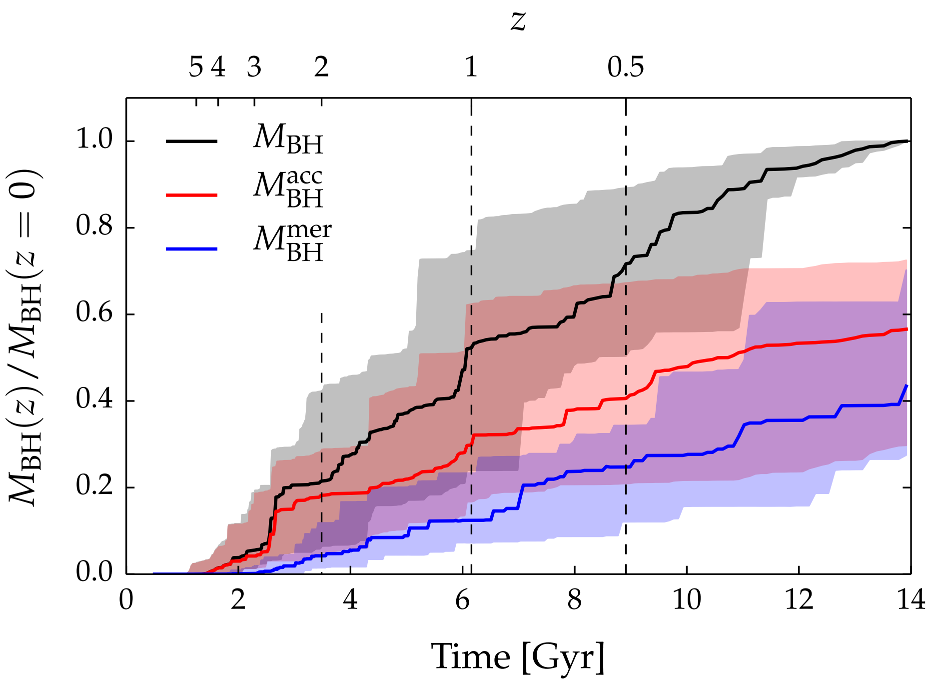

Fig. 3.13: Same as Fig. 3.12 but considering only clusters with $M_{500} > 10^{15} M_{\odot}$ at $z = 0$.

mass bins: at $z = 0$ the least massive objects have M_{500} below $10^{14}\ M_{\odot}$, the most massive above $10^{15}\ M_{\odot}$, and the intermediate in between these two thresholds. The results show that the trends of the relative ratio of the two SMBH growth channels are extremely similar to Fig. 3.12 for the samples of the smallest and intermediate objects. This result is expected for the first mass bin since it is the most numerous, containing 84 objects, but it was not guaranteed for the intermediate sample with only 31 systems. The most massive sample, however, is on average characterized by a continuous and equivalent growth of both channels after $z = 2$ (see Fig. 3.13). As a result, at $z = 0$ $M_{\rm BH}^{\rm acc}$ accounts for ≈ 60 per cent of $M_{\rm BH}$. That said, it has to be noticed that the scatter remains very large and the distributions related to the two channels show a large intersecting area. Therefore, it can be concluded that the scatter shown in Fig. 3.12 is not related to the total mass of the systems.

The stronger relative influence by the SMBH accretion with respect to the BH-BH merger in most massive clusters can be due to two different factors: on the one hand AGN feedback is not able to completely balance gas cooling, on the other hand BH-BH mergers could be less frequent. In the following I show some evidence that both phenomena are actually in place.

To demonstrate that the AGNs are less efficient in regulating the gas cooling in the cores of massive clusters I computed the total energy released by AGN feedback at $z < 1$ and related it to the gas mass within $0.1 \times R_{500}$. I find that the ratio of the two quantities is a strongly decreasing function of M_{500} and that it changes by more than a factor of 10 from the least massive to the most massive systems. This suggests that the heating provided by the AGN feedback is relatively smaller for large objects where, therefore, the gas cooling is less contrasted. The central SMBH has therefore more cold gas at its disposal.

To test the reduced frequency of BH-BH merger, I computed at $z = 0$ the number and mass of SMBHs which are inside $0.1 \times R_{500}$ and are not bound to any substructure. I find that 80 per cent of the most massive systems (16 objects over 20) have several SMBHs in that central regions with a total mass greater than 10 percent of the mass of the central SMBH. Analysing the first mass bin ($M_{500} < 10^{14} M_{\odot}$), instead, only 10 per cent of clusters have enough SMBHs able to account, all together, for at least 10 per cent of the mass of the central SMBH. This is mostly due to the fact that more massive clusters host more massive and extended BCGs. When the substructures interact with these well-established BCGs they are more easily disrupted (see Sect. 3.4.6 for further details) at a larger radii, preventing or delaying mergers between their SMBHs and the central SMBH.

3.4.6 Recent growth of SMBH and stellar component

In our simulations the SMBH mass increases by a factor of ~ 2.5 between $1 > z > 0$. Ragone-Figueroa et al. (2018) found instead, selecting the most massive cluster in each Lagrangian region, that the central stellar component measured within 30 kpc features a significant smaller growth. I checked that the growth factor of central SMBHs remain unchanged also considering this reduced subsample. This difference is due to the fact that in our simulations many substructures colliding with the BCG at $z < 1$ are largely disrupted and their stars quickly become part of the ICL or settle in the outermost radii of the BCG itself. This feature confirms some previous results. For example, Murante et al. (2007) shows that the bulk of the star component of the ICL

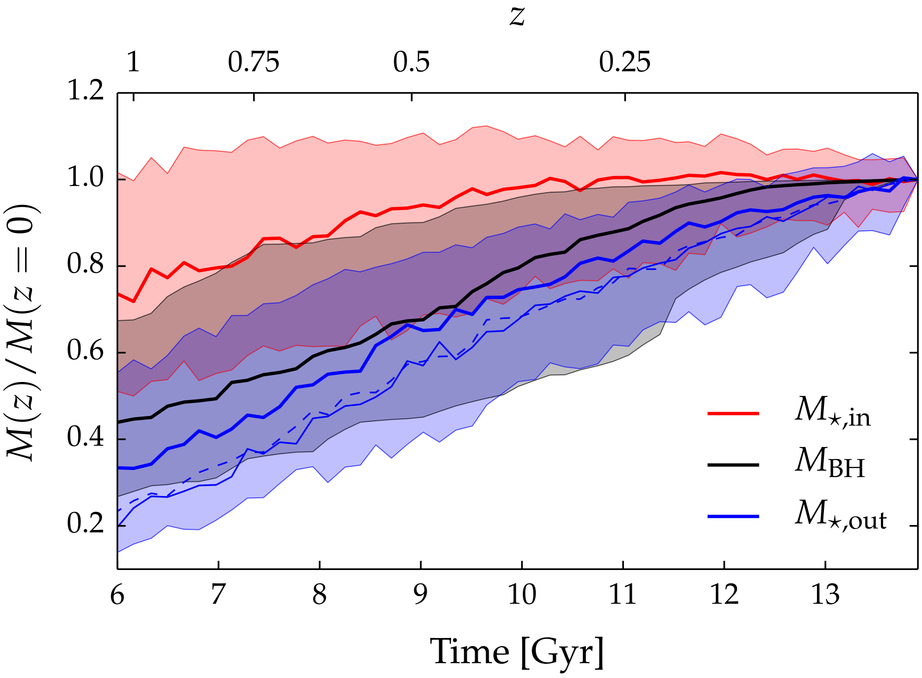

Fig. 3.14: Evolution of $M_{\star,\rm in}$, defined as the stellar mass inside a spherical region of radius 30 kpc, SMBH mass, and $M_{\star,\rm out}$, defined as the total mass of the stars enclosed in a spherical shell with radii 30 kpc and 100 kpc. All the quantities are normalized to their respective values at $z = 0$. Solid lines represent median values and shadowed regions represent 16 and 84 percentiles. The three different blue lines represent three definition of $M_{\star,\rm out}$. In particular the thin blue solid line is the stellar mass in a spherical shell with radii 100 kpc and 200 kpc while the dashed blue line is the stellar mass in a spherical shell with radii 50 kpc and 350 kpc.

originates during the assembly of the most massive galaxies in a cluster (and, in particular, of the BCG) after $z \sim 1$.

To visualize this effect, whose detailed study will require a dedicated analysis, I simply compared the evolution of the SMBH mass and the inner stellar component, defined as $M_{\star,\rm in} = M_\star(r/{\rm kpc} < 30)$. Furthermore, I added a measure of the outer stellar component, defined as $M_{\star,\rm out} = M_{\star,\rm not-bound}(30 < r/{\rm kpc} < 100)$. The "not-bound" identification specifies that all stars which are gravitationally bound to substructures identified by Subfind and different from the BCG have been excluded. $M_{\star,\rm out}$, therefore, comprises both the ICL and the outermost stellar mass of the largest BCG in the sample. The median values of $\Delta M_{\star,\rm in}$, $\Delta M_{\rm BH}$ and $\Delta M_{\star,\rm out}$ are computed

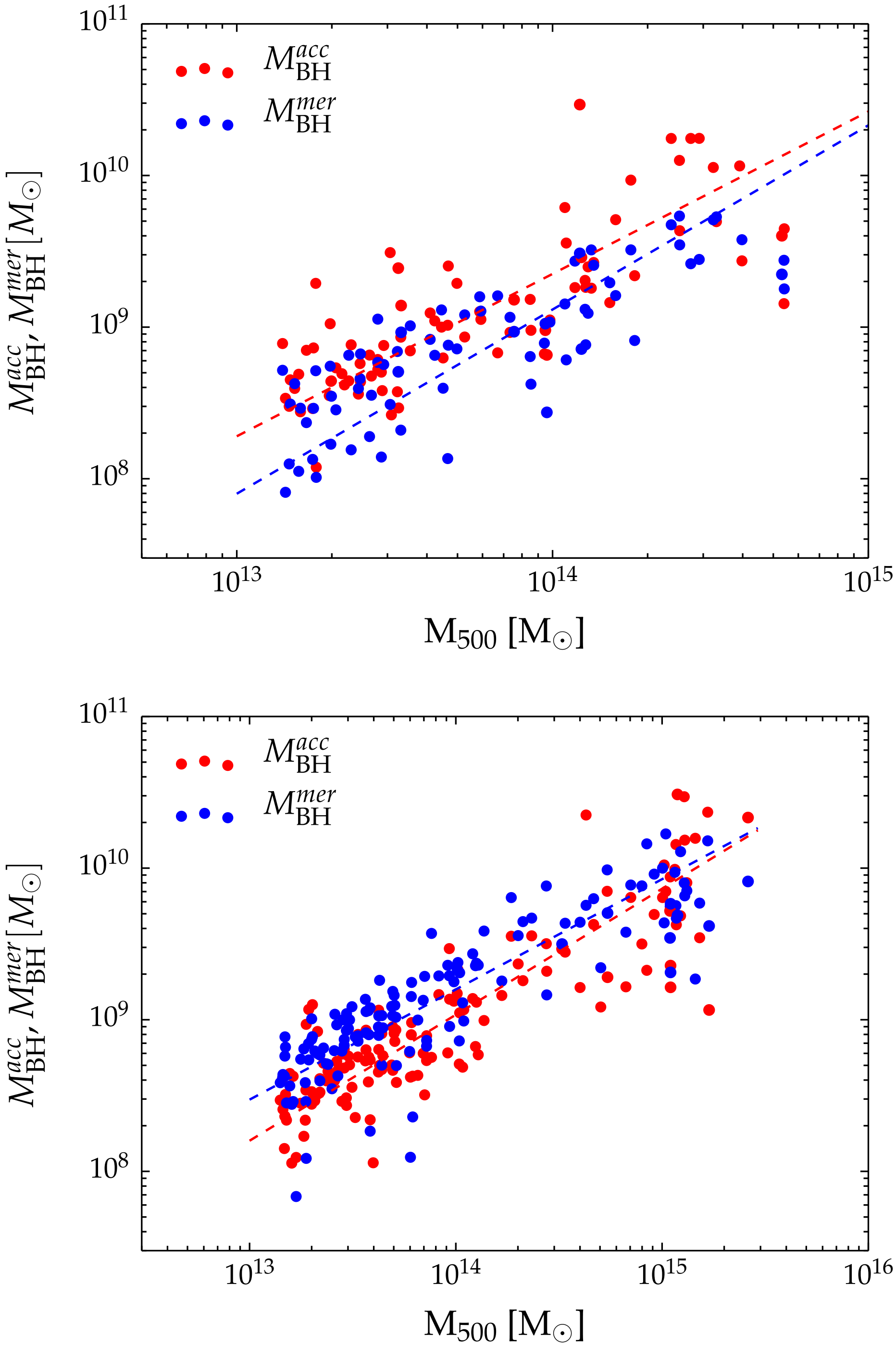

Fig. 3.15: Correlation between SMBH mass and M_{500} at $z = 1.0$ (upper panel) and $z = 0$ (lower panel). Blue points represent the mass gained by mergers while red points represent the mass gained by gas accretion. Dashed lines represent best fitting lines to the data.

after the normalization to their respective mass values at $z = 0$.

I considered 30 kpc for $M_{\star,\rm in}$ because I wanted to evaluate the changes on the stellar component in the immediate surrounding of the SMBH; furthermore, this was used in Ragone-Figueroa et al. (2018) as one of the possible definition of the BCG mass. For the outer component, instead, I also considered the mass of the unbound stars measured in other two spherical shells: between 100 kpc and 200 kpc and between 50 kpc and 350 kpc. As clear from Fig. 3.14, the choice of this region does not substantially change the conclusions: while $M_{\star,\rm in}$ slowly increases from $z = 1$ to $z = 0$, the SMBH mass and $M_{\star,\rm out}$ rapidly increase. At $z = 1$, indeed, the quantities are about 80 percent, 45, and 35 per cent of their final values, respectively. The remarkable agreement between the two extra definitions of the outer stellar component – $M_{\star,\rm not-bound}(100 < r/{\rm kpc} < 200)$ and $M_{\star,\rm not-bound}(50 < r/{\rm kpc} < 350)$, thin blue solid and dashed line in Fig. 3.14 – implies that the growth rate of the ICL is independent on the specific radius used.

The final emerging picture is that many small substructures actually reach the cluster core and merge with the BCG. However, few of their stars remain in the innermost region. The interaction with the BCG causes that most stars of the structures are tidal shocked and stripped. Subsequently, they become gravitationally unbound thereby taking part of the ICL. During the disruption of the substructures, their most massive SMBHs feel the gravitational attraction of the underlying potential and sink towards the minimum of the cluster potential contributing to the growth of the SMBH at the center of the BCG. It has to be noted, however, that the modeling of BH-BH mergers is very simplistic and could overestimate the efficiency of this physical process which take place at a scale well below the gravitational softening of the simulations.

3.4.7 The $M_{\rm BH} - M_{500}$ relation for the two SMBH growth channels

Given that at $z = 1$ and $z = 0$ the SMBHs have grown from both channels (through gas accretion and BH-BH mergers), it is relevant to check whether the SMBH mass of the two channels are separately both related to the total mass or whether only one exhibits a tight correlation while the other mostly contributes to increase the scatter. This possibility is investigated in Fig. 3.15

where both $M_{\rm BH}^{\rm acc}$ and $M_{\rm BH}^{\rm mer}$ as a function of M_{500} have been considered at $z = 1$ (upper panel) and at $z = 0$ (lower panel). As we have seen, at $z = 1$ the gas accretion is the dominant channel. In Sect. 3.4.5, we saw that this channel shows only a slight increment from $z = 1$ to $z = 0$. For this reason, the red points, referring to $M_{\rm BH}^{\rm acc}$ are substantially unchanged in the two panels. Viceversa, $M_{\rm BH}^{\rm mer}$ becomes the dominant component at $z = 0$. The results of the linear fits of the relations are reported in Table 3.2 also for the other redshifts.

From the figure, it is evident that both masses correlate well with M_{500} at both redshifts independent of which one of the two is the dominant channel from the SMBH mass growth. From the table, we notice that the slopes of the two relations are consistent within 1 σ being the $z = 1$ slightly steeper as expected from the Sect. 3.4.3. Most importantly, the two scatters are similar and both slightly higher than the scatter of the relation of the total SMBH mass (see Table 3.2).

Finally, it is important to emphasize that Fig. 3.9 suggests that the $M_{\rm BH} - M_{500}$ relation is already in place at $z = 2$ when the SMBH mass was almost entirely gained only by gas accretion. These results enlighten that, at least in our simulations, mergers are not essential to establish the relation at first.

3.4.8 $M_{\rm BH} - M_{\rm BH}$ mergers in non-central galaxies

In Sect. 3.4.5 we have studied the growth of SMBH at the center of BGGs/BCGs, concluding that it is equally contributed by accretion of gas and BH-BH mergers. Therefore, the latter can play an important role in the evolution of these exceptionally massive objects. However, we can expect the situation to be sensibly different for satellite galaxies, where a much smaller number of BH-BH mergers is expected. To have a qualitative idea on the typical number of mergers experienced by simulated SMBHs of different masses, in Figs. 3.16, 3.17, 3.18, and 3.19 I show the typical merger trees for SMBH whose final masses are $M \sim 10^8$ $\mathrm{M}_\odot$, $M \sim 5 \times 10^8$ $\mathrm{M}_\odot$, $M \sim 5 \times 10^9$ $\mathrm{M}_\odot$, and $M \sim 10^{10}$ $\mathrm{M}_\odot$ respectively. It is clear from the plots that the complexity of the trees increases with the SMBH final mass, as SMBHs of $M \sim 10^8$ $\mathrm{M}_\odot$ experience only few mergers, while SMBH with $M \sim 10^{10}$ $\mathrm{M}_\odot$ are characterized by up to ~ 20 mergers during their evolution.

To study the number of mergers that different SMBH undergoes in our

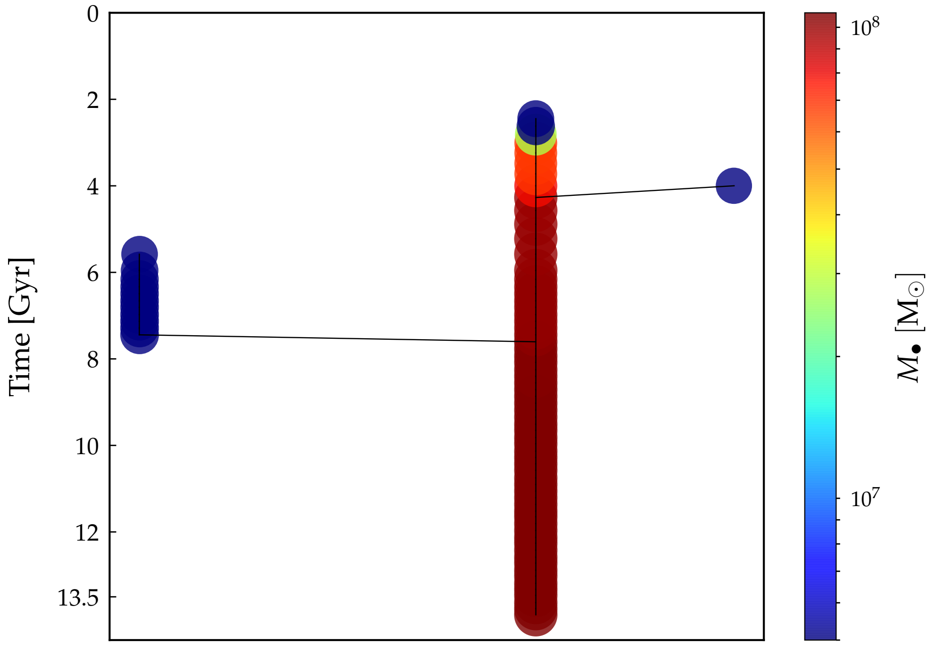

Fig. 3.16: SMBH merger tree for a typical SMBH of $M_{\rm BH} \sim 10^8$ $\mathrm{M}_\odot$ in our simulations. Points are colour-coded according to the mass of the SMBH particle.

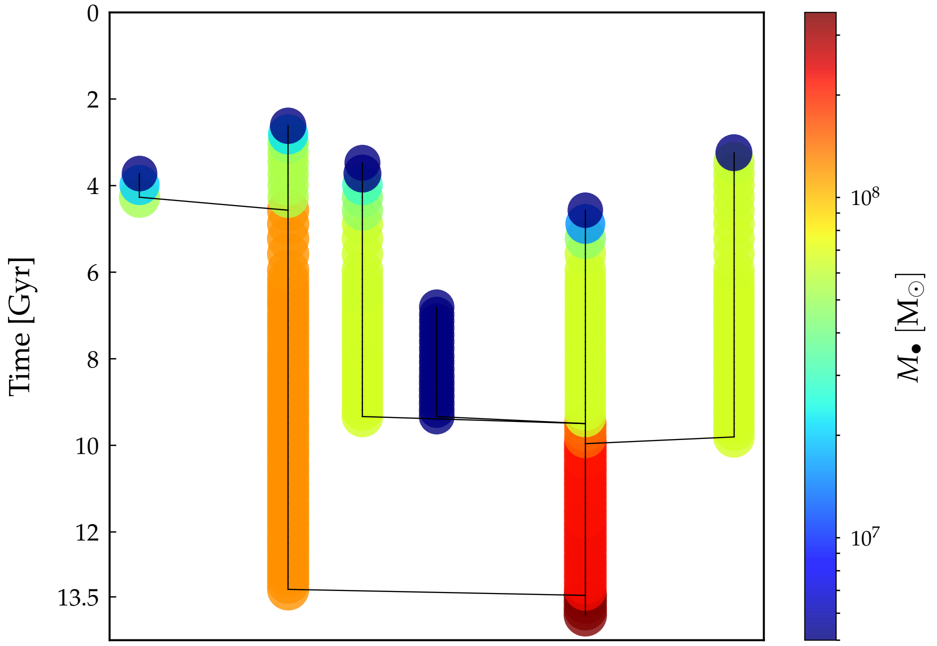

Fig. 3.17: Same as Fig. 3.16, but for a typical SMBH of $M_{\rm BH} \sim 5 \times 10^8$ $\mathrm{M}_\odot$.

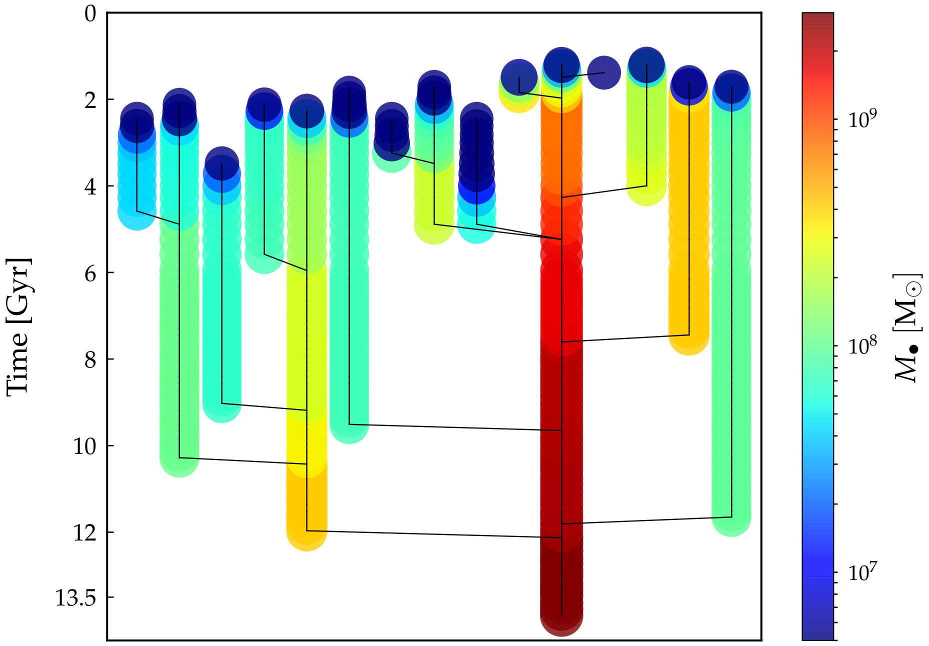

Fig. 3.18: Same as Fig. 3.16, but for a typical SMBH of $M_{\rm BH} \sim 5 \times 10^9$ M$_\odot$.

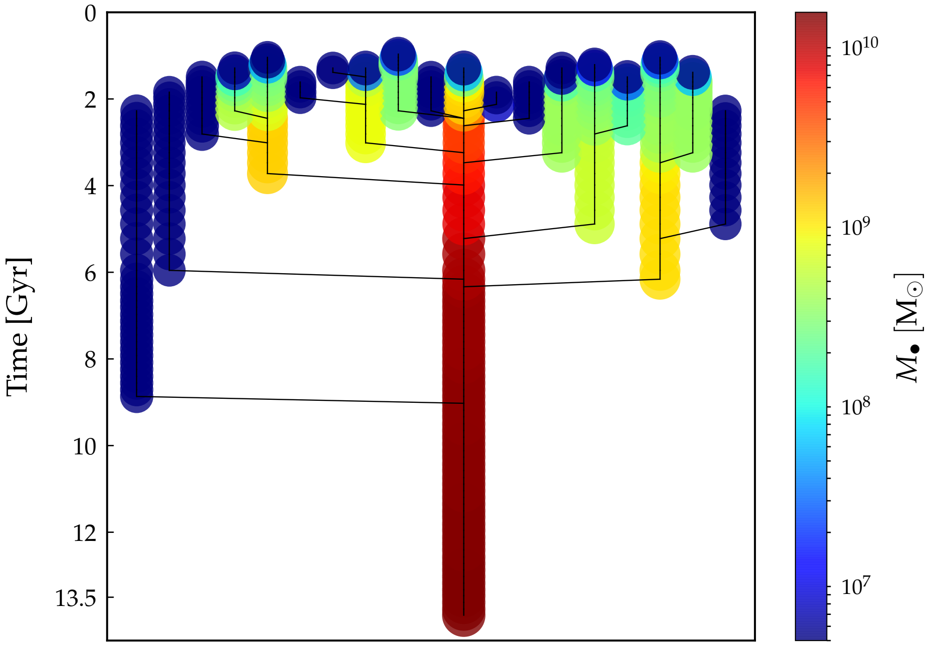

t

Fig. 3.19: Same as Fig. 3.16, but for a typical SMBH of $M_{\rm BH} \sim 10^{10}$ M$_\odot$.

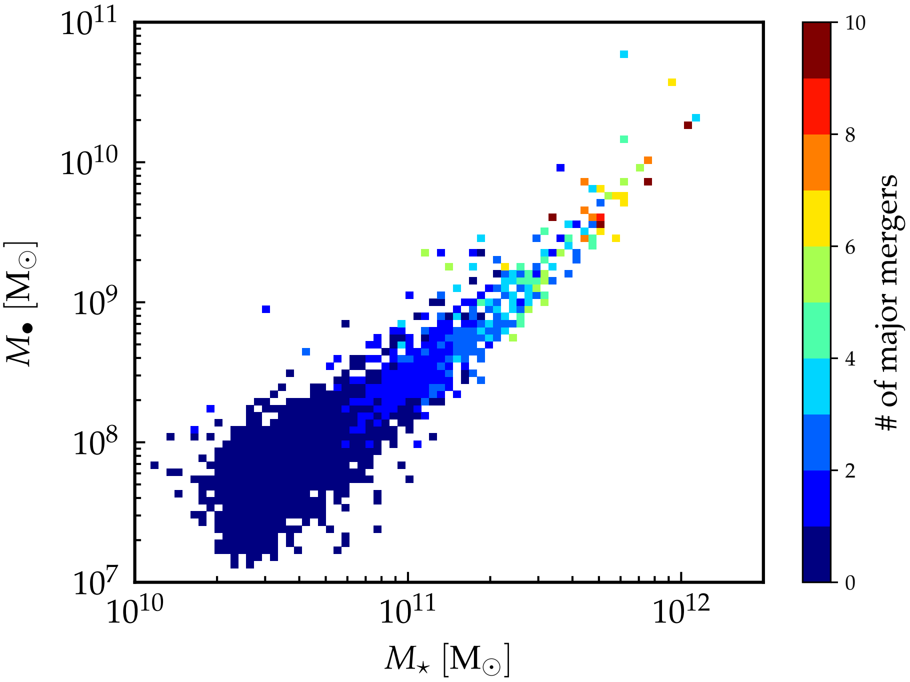

Fig. 3.20: 2D histogram on the $M_{\rm BH} - M_\star$ plane at $z = 0$. Each bin is colour-coded by the median number of major ($M_2/M_1 > 0.25$) BH-BH merger events encountered along the whole merger tree of each $z = 0$ BH particle.

simulations in a more statistical way, in Fig. 3.20 I show a 2D histogram on the $M_{\rm BH} - M_\star$ plane colour-coded by the median number of major mergers experienced by the SMBHs in each bin. In this analysis a major merger is defined considering a ratio > 0.25 between the masses of the merging SMBHs, while the stellar mass of galaxies is computed considering all stellar particles associated to the galaxy by Subfind and within a spherical aperture of 30 pkpc. Moreover, the number of major mergers is computed along all the SMBH merger tree and not only for the main branch. At this point, it is also important to remind that the number of mergers within numerical simulations has to be considered as an upper limit. Indeed, the subgrid prescriptions for BH-BH mergers are quite simplistic and limited by the resolution of the numerical simulations: as described in Sect. 3.2, two BHs particles merge whenever their distance is lower than two softening lengths, i.e. ~ 10 kpc. This roughly means that a BH-BH merger event always happens during a merger between two massive galaxies (massive enough to host a central SMBH).

From Fig. 3.20 we see that most of the simulated SMBHs do not experience more than 2 major mergers, with only the most massive SMBHs ($M_{\rm BH} > 10^9$ $\rm M_\odot$) being characterized by a larger number of merger events, and just a few cases with $N \sim 10$. Since from a theoretical point of view it is expected that the scatter around the $M_{\rm BH} - M_\star$ correlation scales like $\sim 1/\sqrt{N}$, being N the number of major mergers, a non-causal origin to the observed correlation would require $N \approx 30$, hence a drop in the scatter down to $1/\sqrt{30} \simeq 0.18$ (see, e.g., section 4.1.4 by Gaspari et al. 2019). Indeed, in the works by Peng (2007) and Jahnke & Macciò (2011) the proxy for uncorrelated distributions is taken to be a dispersion of 2 dex and 3 dex respectively. In these cases, to reproduce the observed value of the scatter around the $M_{\rm BH} - M_\star$ correlation of 0.40 as reported by Gaspari et al. (2019), the number N of mergers required would be 25 and 56 respectively. Therefore, the result obtained disfavour the non causal origin of the correlation.

Apart from the requirement of a large number of BH-BH mergers, a correlation driven by a non-causal origin would be characterized by two characteristic features: (i) a decreasing scatter toward higher masses, where N is expected to be larger; (ii) a convergence toward a linear relation. However, as I show in Table 3.3, in our simulations the scatter does not show any particular trend with respect to N. Interestingly, we also note that the slope of the relation is steeper at increasing value of N, departing from the linear correlation, in clear contrast with theoretical predictions based on BH-BH mergers. Therefore, even if these arguments can not be considered as conclusive given the uncertainties regarding the employed subgrid models and possible dependence on the numerical resolution of the simulations, which will be investigated in future works, the set of numerical simulations analyzed in this Chapter suggest a causal connection between SMBH and hosting galaxies where the observed correlations are driven by AGN feedback.

Table 3.3: Results of linear regression for the $M_{\rm BH} - M_\star$ correlation in the form $\text{Log}(M_{\rm BH}) = \alpha + \beta\ \text{Log}(M_\star)$. Different rows refer to different samples selected by the numbers of major mergers (first column) that SMBHs undergo along the whole merger tree.

$N_{\rm merger}$	α	β	σ
all	-6.65 ± 0.09	1.37 ± 0.01	0.17
0	-4.61 ± 0.15	1.18 ± 0.01	0.17
$[1,3]$	-7.87 ± 0.23	1.48 ± 0.02	0.18
> 3	-10.2 ± 1.1	1.69 ± 0.09	0.20

3.5 Discussion

As previously remarked the correlation between the BCG mass and the SMBH mass has been diffusely studied and often used to extract the mass of the SMBH knowing the mass of the hosting galaxy. In Bogdán et al. (2018), the authors found in their observed sample that the scatter between the SMBH mass and the global cluster properties is tighter by almost 40 per cent than the scatter of the $M_{\rm BH} - M_{\rm BCG}$ relation. Indeed, in their Table 4 they report $\sigma_{M_{\rm BH}|M_{\rm BCG}} = 0.61$ and $\sigma_{M_{\rm BH}|T} = 0.38$. The values of the scatters increase in the later analysis by Phipps et al. (2019) because of the method used to derive $M_{\rm BH}$, the authors suggest. Despite, also in that case the two intrinsic scatters in $M_{\rm BH}$ are comparable between each other. As a consequence, the global properties of cluster within R_{500} are also suitable to estimate the SMBH mass. I show in Sect. 3.4.1 that the distribution of our simulated data is in reasonable agreement with the observations by Bogdán et al. (2018) and Gaspari et al. (2019), who used dynamical measurements of $M_{\rm BH}$. I demonstrate that for our simulated objects there is a clear correlation between the mass of the SMBHs, located at the minimum of the potential well, and the temperature or total mass of the clusters within R_{500}. In this section I discuss the properties of all the relations related to central SMBHs described in this Chapter and listed in Table 3.2.

To this end I refer to Fig. 3.21 where I show the covariance matrix between the deviations of all the quantities of interest from their best-fitting relations, that are their residual at fixed mass. These are defined as logarithmic differences between the actual value, generically referred as X, and the

Table 3.4: Correlation matrix. Each element represents the Spearman coefficient of the quantities of interest. The three values refer to $z = 0$, $z = 0.5$ and $z = 1$ respectively. The values in bold have probability to be different from 0 below 0.2 per cent.

	$\delta(T_{500})$	$\delta(M_{\rm BCG})$	$\delta(M_{\rm BH})$	$\delta(M_{\rm BH}^{\rm acc})$
$\delta(M_{\rm BCG})$	**0.498**— 0.072 — 0.255			
$\delta(M_{\rm BH})$	0.322 — 0.210 — 0.355	**0.557** — **0.693** — **0.694**		
$\delta(M_{\rm BH}^{\rm acc})$	0.310 — 0.243 — 0.267	0.288 — **0.405** — **0.485**	**0.684** — **0.804** — **0.865**	
$\delta(M_{\rm BH}^{\rm mer})$	0.230 — 0.087 — 0.277	**0.612** — **0.751** — **0.679**	**0.777** — **0.753** — **0.737**	0.190 — **0.304** — **0.384**

expected value, $X_{\rm FIT}$, from the $X - M_{500}$ relations[5] provided in Table 3.2:

$$\delta(X) = \log[X/X_{\rm FIT}]. \tag{3.6}$$

The deviations are computed for each quantity $X = T_{500}$, $M_{\rm BCG}$, $M_{\rm BH}$, $M_{\rm BH}^{\rm mer}$, $M_{\rm BH}^{\rm acc}$. The panels above the diagonal refer to $z = 1$ while those below to $z = 0$. The diagonal panels show the distribution of $\delta(X)$ at $z = 0$. I used the temperature subsample whenever $\delta(T_{500})$ is considered. For each pair of deviations I listed the Spearman correlation coefficients in Table 3.4 computed at $z = 0$, 0.5, 1 and I marked in bold the correlations whose probability to be consistent with zero is less than 2 per thousand and its module is greater than 0.4. A strong correlation between $\delta(M_{\rm BH})$ and $\delta(X)$ is converted into a small scatter in the relation $M_{\rm BH} - X$.

As previously commented, the scatter $\sigma_{M_{\rm BH}|T_{500}}$ is comparable to $\sigma_{M_{\rm BH}|M_{500}}$ (see Table 3.2). As a consequence, the temperature and the total cluster mass are equally good proxy for the SMBH mass. The similarity between these two proxies can be explained by looking at the correlation between $\delta(T_{500})$ and $\delta(M_{\rm BH})$ in Fig. 3.21. The panels for the two considered redshifts, $z = 0$ and $z = 1$, highlight how the variations of cluster temperature are not directly reflected into variations of the SMBH mass. At first sight, this can be surprising as one could expect that both quantities are strongly dependent on the dynamical activities of the cluster core and, especially, sensitive to merger events that impact the innermost region of the clusters. However, the response of the temperature and the SMBH mass to merger is not simultaneous: we saw in Sect 3.4.2 that the typical delay between the increase of the $M_{\rm BH}$ after a merger can be around 1-3 Gyr, while the temperature increase typically occurs in less than 1 Gyr from the merging episode. In addition, the

---

[5] The (M_{500}, T_X) relation has previously been inverted into (T_X, M_{500}).

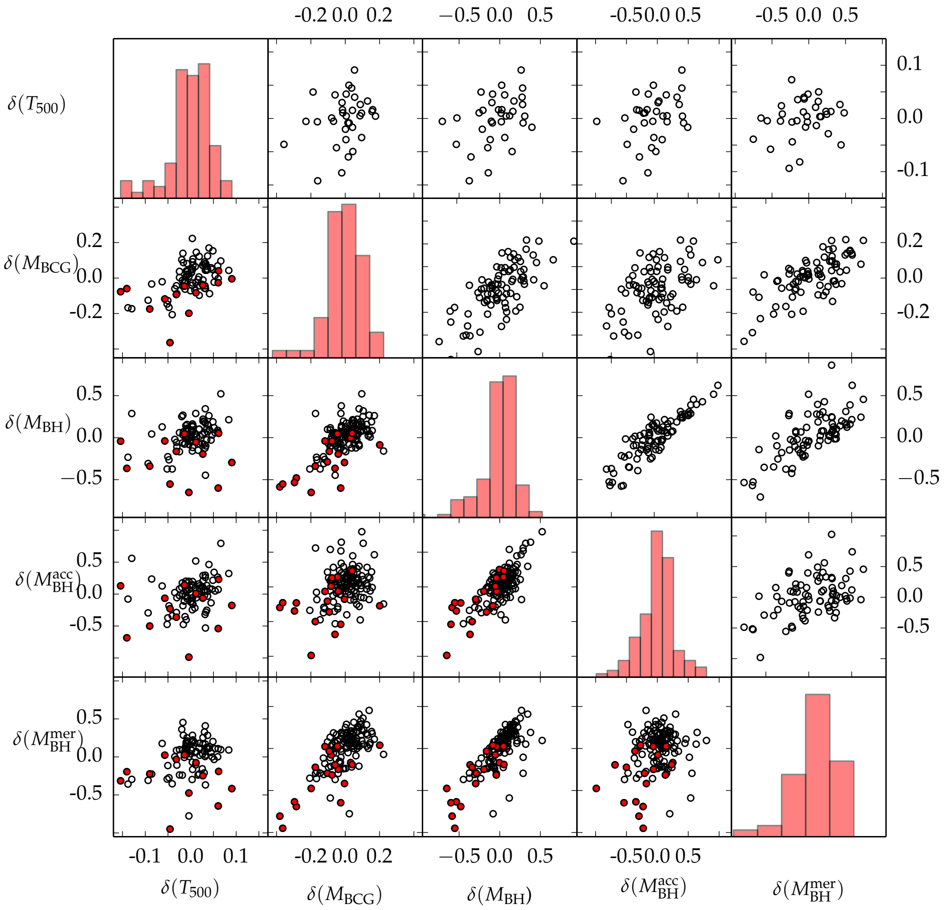

Fig. 3.21: Covariance matrix. Each axis represents the logarithmic difference between the actual value of a quantity X and the expected value from the linear relation (X-M_{500}) at its fixed mass, as defined by Eq. 3.6. Panels above the diagonal refer to $z = 1$ while panels below the diagonal refer to $z = 0$. The diagonal panels show the distribution of $\delta(X)$ at $z = 0$. Red points define clusters which have experienced a mass growth of at least 40% during the last Gyr.

rapid increase of the ICM temperature is followed by a small drop caused by the expansion of the shock towards the more external regions. This temperature oscillation along with the mismatch between the two time-delays explain why the correlation coefficients between $\delta(T_{500})$ and all $M_{\rm BH}$ components are always low and with a high probability to be consistent with zero. These characteristics are also in place when the temperature variations are compared with the variation on the SMBH mass due to BH-BH mergers.

When comparing, instead, the scatter of the relation between the SMBH mass and the cluster properties with the scatter of the $M_{\rm BH}-M_{\rm BCG}$ relation, we find that $\sigma_{M_{\rm BH}|M_{\rm BCG}}$ is smaller at all times. At redshift $z=0$, for example, $\sigma_{M_{\rm BH}|M_{500}}$ is ≈ 25 per cent larger, although the two scatters are in agreement between 2σ. The difference between the scatters is more significant at $z\geq 1$ where typically $\sigma_{M_{\rm BH}|M_{500}}$ is $\approx 1.4\times\sigma_{M_{\rm BH}|M_{\rm BCG}}$. In the covariance matrix formalism this translates into a correlation between $\delta(M_{\rm BCG})$ and $\delta(M_{\rm BH})$. Indeed, at $z\leq 1$ the correlation is $\geq$ 0.55. Moreover, the correlation is stronger if computed with respect to $M_{\rm BH}^{\rm mer}$ when it reaches values around 0.7. As we can see from Fig. 3.21, the correlation at $z=0$ is significant for the presence of situations of either pre-mergers or mergers with a large impact parameter when both $M_{\rm BCG}$ and $M_{\rm BH}$ (and in particular $M_{\rm BH}^{\rm mer}$) are smaller than the average of the sample at fixed total mass (i.e., their δ is negative). At $z=1$, we also notice a correlation between the variations of the two quantities in the other direction (both $\delta(M_{\rm BCG})$ and $\delta(M_{\rm BH}^{\rm mer})$ greater than zero) implying that the SMBHs that gained mass through $z\geq 1$ mergers are hosted in BCG with higher stellar mass with respect to the average of the sample.

In Fig. 3.7, I show that the scatter of the $M_{\rm BH}-M_{500}$ relation is influenced by the presence of the systems that recently experienced a major merger. Indeed, all objects that increased their total mass by at least 40 per cent in the last Gyr are in the bottom part of the overall distribution (see Sect. 3.4.2 and Fig. 3.7). In Fig. 3.21 I identify these objects as red points. In the majority of the cases their variations with respect to the mean are negative. When we exclude these objects and reapply our fitting procedure[6], we find that the scatter of the $M_{\rm BH}-M_{500}$ relation reduces by almost 20 per cent ($\sigma_{M_{\rm BH}|M_{500}}=0.14\pm0.01$), it remains comparable to the re-computed scatter of the $M_{\rm BH}-T_{500}$ relation ($\sigma_{M_{\rm BH}|T_{500}}=0.14\pm0.02$) and consistent with the new $\sigma_{M_{\rm BH}|M_{\rm BCG}}=0.13\pm0.01$. In other words, even if the removal of the dynamically active objects induces a decrease in the scatters of all of the three relations, the most important reduction impacts the scatter at fixed total mass, reducing the gap between $\sigma_{M_{\rm BH}|M_{\rm BCG}}$ and the scatter of the relations involving global cluster properties.

---

[6] The best-fitting relations of the samples derived by excluding the clusters with recent fast accretion are:
$M_{\rm BH}/(10^9{\rm M}_\odot)=10^{0.49\pm0.02}\times(M_{500}/10^{14}{\rm M}_\odot)^{0.77\pm0.03}$;
$M_{\rm BH}/(10^9{\rm M}_\odot)=10^{0.56\pm0.02}\times(T/2{\rm keV})^{1.32\pm0.06}$;
$M_{\rm BH}/(10^9{\rm M}_\odot)=10^{-0.41\pm0.03}\times(M_{\rm BCG}/10^{11}{\rm M}_\odot)^{1.17\pm0.04}$.

In the interpretation of these results from simulations, it is important to remember that the simulated data do not reproduce the observed scatter of the $M_{\rm BH} - M_{\rm BCG}$ relation (Fig. 3.1 and also Ragone-Figueroa et al. 2013; Bogdán et al. 2018). On one hand the growth of simulated SMBHs is regulated by simplistic subgrid models that do not capture all physical processes in place and might lead to a reduced scatter. On the other hand, as explained when discussing Fig. 3.1, a large portion of the observed scatter around the $M_{\rm BH} - M_{\rm BCG}$ relation can be ascribed to observational uncertainties associated either with the quantity definition (e.g., treatment of intra-cluster light, BCG boundary definition) or with the measurement procedures (e.g., not fixed aperture mass for the BCG or application of scaling relation to infer the SMBH mass). In simulations, instead, the BCG and SMBH masses are always known and precisely defined. These arguments not only provide a possible explanation for the difference between the simulated and observed scatters but also underline that the errors on the measures of $M_{\rm BCG}$ derived from observations are not easily reducible. The estimate of the SMBH mass from the BCG mass can always be subject to these uncertainties. The global cluster properties are also subject to systematics, which however can be treated as follows. A systematic bias on the global temperature can be dealt with precise instrument calibration or with multi-temperature fitting. The uncertainties on the total mass are reduced when measurements coming from various wavelengths are combined, such as mass reconstruction from gravitational strong and weak lensing, galaxy dynamics, SZ, and X-ray. These considerations, along with the limited difference in the relation scatters, emphasize how the global cluster properties can be powerful proxies for the SMBH mass. This conclusion is even stronger at high redshift, such as $z = 1$.

As a final comment, we note that in this analysis the correlation between $M_{\rm BH}$ and the stellar velocity dispersion has not been considered. This analysis could add important pieces of information, since a few authors still regard the $M_{\rm BH} - \sigma_e$ as the fundamental one (e.g., Shankar et al. 2016). Unfortunately, the current numerical resolution of the simulations does not allow a reliable estimate of this quantity. Therefore, this analysis is left for future works.

3.6 Summary

In this Chapter I showed that a number of observations found strong correlations between the mass of SMBHs at the center of galaxy clusters and global properties of the cluster itself, like its mass (M_{500}) and its X-ray temperature (T_{500}). Interestingly, the scatter around this correlation was found to be lower than the one around the so called Magorrian correlation, i.e. $M_{\rm BH} - M_{\star}$. Moreover, even though there is a general consensus on the presence of such correlations ($M_{\rm BH} - M_{500}$, $M_{\rm BH} - T_{500}$), their origin is still debated. In the work led by Gaspari we showed that the correlation involving X-ray temperature is not limited to clusters and groups, but is indeed the tightest relation involving all the SMBHs with mass measured by dynamical means (Gaspari et al. 2019). This evidence has been regarded as an indirect proof in favour of a physical connection between SMBHs and hosting galaxy/groups/clusters (Gaspari & Sadowski 2017, Gaspari et al. 2019). On the other hand, Lakhchaura et al. (2019) found that correlations involving X-ray temperature are present only when SMBHs central to groups and clusters are considered, while for non-central galaxies this correlation is absent. This result hints that the observed correlations are driven by mergers.

To discern the physical processes that drive the observed correlations, in this Chapter I studied correlations involving central SMBHs and cluster properties in our cosmological simulations. After showing the agreement between numerical results and the observational data at $z = 0$, I explored how the relation between the SMBH mass and the cluster mass establishes by looking at the co-evolution of these quantities in individual systems. I then looked at the evolution of the entire sample considering four different times ($z = 0.5, 1, 1.5$, and 2). Finally, I characterized the role played by the two channels (accretion of gas and BH-BH merging) for the SMBH growth, for both SMBHs in BCGs and satellite galaxies. The main results can be summarized as follows.

- The $M_{\rm BH} - M_{500}$ relation at $z = 0$ originates from a non-simultaneous growth of the SMBH and of the cluster. In particular, objects evolve on the $M_{\rm BH} - M_{500}$ plane either at almost constant $M_{\rm BH}$ or at almost constant M_{500}. After the seeding, SMBHs immediately gain mass at the Eddington limit by the accretion from the abundant surrounding gas, which is mostly cold and thus efficient at increasing the SMBH mass. This phase typically lasts half Gyr and can lead to the formation of SMBHs with a mass already of the order of $M_{\rm BH} \approx 10^8 - 10^9$ $\rm M_\odot$. The fast SMBH growth ends when the $M_{\rm BH}$ is high enough to cause an intense feedback that leads to the ejection of part of the gas outside the shallow potential wells of the hosting galaxies. After this phase, the systems lie on the $M_{\rm BH} - M_{500}$ relation. Subsequent evolution is driven by the rapid increase of the cluster total mass during cluster mergers. These phases typically last 1 Gyr. After that, the substructures move towards the cluster center and, eventually, reach the core feeding the central SMBH with gas and/or inducing a BH-BH mergers. Clusters that recently experienced major merger events are in general below the mean relation.

- In our simulations, SMBHs grow by two different channels. Gas accretion is the most relevant channel at redshift $z > 2$ and the only player at the earliest times. The accretion is slowed down only when the SMBHs are massive enough to balance gas cooling via AGN feedback. At lower redshift ($z = 1$) one quarter of the SMBH mass is ascribed to mergers. From that time to $z = 0$ the BH-BH merger contribution becomes progressively more important. Indeed, mergers contribute by about 60 percent of the total $z = 0$ SMBH mass on average. Since the contribution to the $z = 0$ $M_{\rm BH}$ is almost equally contributed by gas accretion and BH-BH mergers, the observed correlation is the result of both these two processes that operated at different times. I remark, however, that even though mergers are important for the evolution of these SMBHs, a correlation is already in place at $z = 2$, when gas accretion is the only important contributor to $M_{\rm BH}$.

- The $M_{\rm BH} - M_{500}$ and $M_{\rm BH} - T_{500}$ relations present a similar scatter, meaning that they are equally valid SMBH mass proxy. On the other hand, the scatter of the $M_{\rm BH} - M_{\rm BCG}$ relation, at $z = 0$, is $\approx 25\%$ lower in our simulations, although the two values are in agreement within 2σ. However, it is important to stress that the observed scatter of the $M_{\rm BH} - M_{\rm BCG}$ relation is larger then the simulated one, mainly for two reasons: the numerical limitation of a simplistic description of SMBHs growth and the large uncertainties affecting the observational measurements of both SMBH and BCG masses. That said, when the most dynamically active objects are discarded from the sample, the scatters of all relations ($M_{\rm BH} - M_{\rm BCG}$, $M_{\rm BH} - M_{500}$ and $M_{\rm BH} - T_{500}$) become similar, thus strengthening the predicting power of the cluster global quantities on the mass of the central SMBH.

- Finally, even though BH-BH mergers represent an important channel for central SMBH growth, the same is not true for SMBHs at the center of satellite galaxies. In this case, the typical number of major mergers that SMBHs with $M_{\rm BH} < 10^9$ $\rm M_\odot$ undergo along the whole merger tree is $N_{\rm merg} \lesssim 4$. Since it would require $N_{\rm merg} \approx 30$ (e.g., Gaspari et al. 2019) to completely explain the observed correlations involving $M_{\rm BH}$ by means of BH-BH mergers, our numerical simulations suggest that SMBHs and hosting galaxies are causally connected.

Chapter 4

Star formation rate in Protocluster regions

In this Chapter I study the star formation rate (SFR) in 12 of our cosmological hydrodynamical simulations of galaxy (proto-)clusters in the redshift range $0 < z < 4$, comparing them to recent observational studies; I also investigated the effect of varying the parameters of the star formation model on galaxy properties such as SFR, star-formation efficiency, and gas fraction.

The Chapter is structured as follow: after a brief introduction in Sect. 4.1, in Sect. 4.2 I describe the simulations set up, with particular focus on the AGN feedback implementation and the subgrid star formation model. In addition the BCGs properties and the stellar mass function at $z = 0$ will be compared with observations. In Sect. 4.3 and Sect. 4.4 I compare the predicted SFRs in protocluster regions with the available observations at $z \sim 2$ and $z \sim 4$ respectively, and I analyze the main sequence of star forming galaxies at both redshifts. In Sect. 4.5 I show the evolution of the mass normalized SFR in clusters and protoclusters. In Sect. 4.6 I study gas related properties of our simulated galaxies, in comparison with observations, before concluding with a summary of the results in Sect. 4.7.

The work presented in this Chapter is based on the paper published on Astronomy & Astrophysics:

- **Bassini, L.**; Rasia, E.; Borgani, S.; Granato, G. L.; Ragone-Figueroa, C.; Biffi, V.; Ragagnin, A.; Dolag, K.; Lin, W.; Murante, G.; Napolitano, N. R.; Taffoni, G.; Tornatore, L.; Wang, Y.:

The DIANOGA simulations of galaxy clusters: characterising star formation in protoclusters,
Astronomy & Astrophysics, Volume 642, October 2020, id.A37, 19 pp.

4.1 Scientific context

In Chapter 1 we have seen that today galaxy clusters are populated by massive ellipticals, whose stellar population is typically very old, with stars nearly as old as the Universe. Both observations (see Fig. 1.6) and theoretical models (see Fig 1.7) suggest that these massive galaxies are subject to passive evolution at $z < 1$ and have formation times $z_f \gtrsim 2$. For these reasons, it is expected that protocluster regions at high redshift ($z \gtrsim 2$) are characterized by very high star formations rates.

At these high redshifts, structures lack the presence of a massive virialized halo and often multiple less massive halos are spread over large scales (see Sect. 1.3.1). This is in line with theoretical expectations from numerical simulations, which predict a hierarchical formation of massive clusters formed by the assembling of smaller halos that at $z = 2$ might occupy a region as large as $20 \ \mathrm{cMpc}$ (see Fig. 1.12).

Since at this redshift protoclusters are not virialized, it is difficult to detect them with techniques based on the ICM properties. Hence different methods have been used, such as those based on galaxy over-densities. This approach, however, can bias the results, depending on the galaxy properties used for the selection. In this respect, an important population of galaxies are DSFG. As discussed in Sect. 1.3.1, these galaxies are supposed to be the progenitor of local massive ellipticals, and trace the dusty star-forming phase of protoclusters.

As shown by Granato et al. (2015)[1], numerical simulations have been unable to reproduce the high SFRs observed in protoclusters characterized by overdensities of DSFGs, as simulations lack sufficiently high peaks of star formation activity at early epochs. Indeed, Granato et al. (2015) found that the bulk of star formation in the progenitors of massive galaxy clusters occurred at higher rates and lasted less than in simulations. However, at the

---

[1] In his work, Granato et al. (2015) used the Dianoga set run with the same mass resolution as the simulations presented in Chapter 3, with a slightly different implementations of the hydro-solver and subgrid models. See Granato et al. (2015) for further details.

time only observations accessible with the Herschel satellite were available, with information only on the integrated SFR on the Mpc scale. In the last few years, with instruments like ALMA, it has been possible both to resolve single sources within protoclusters and have information on the galaxy cold gas content (e.g., Wang et al. 2018, Gómez-Guijarro et al. 2019, Hill et al. 2020). On the simulations side, we produced a new run of the Dianoga simulations at a ten times higher mass resolution, needed to resolve higher density peaks and related higher SFRs. Hence, times are ready for a deeper inspection on the simulations capability of reproducing protocluster properties around the time of their formation.

4.2 Simulations

The work presented in this Chapter is based on the 12 zoom-in simulations D1, D2, D3, D4, D5, D6, D7, D9, D10, D18, D22, D25 (i.e., the five smaller clusters and seven massive objects listed in Table 2.1). The masses of the particles in the high resolution region are $m_{\rm DM} = 8.44 \times 10^7 \ h^{-1} M_\odot$ for DM and $m_{\rm gas} = 1.56 \times 10^7 \ h^{-1} M_\odot$ for the initial gas particles. This mass resolution is ten times higher than the one employed for the simulations presented in Chapter 3, to which I will refer as LR simulations. The Plummer equivalent gravitational softening used for DM particles is $4.2 \ h^{-1}$ comoving kpc (ckpc) for $z > 2$ and $1.4 \ h^{-1}$ physical kpc (pkpc) otherwise. The softening lengths for gas, star, and black holes (BHs) particles are $1.4 \ h^{-1}$, $0.35 \ h^{-1}$, and $0.35 \ h^{-1}$ ckpc respectively.

4.2.1 SMBHs positioning and feeding

Similarly to the procedure already described in Sect. 3.2, we define during run time groups of particles using the FoF algorithm. Hence, BHs are spawned at the center of each FoF group with a seed mass of $4 \times 10^5 \ h^{-1} \ M_\odot$. The conditions for the seeding are the same used for the LR simulations (see Sect. 3.2.1), with the exceptions of conditions (i) and (ii), where we decreased the mass thresholds on the conditions due to the improved resolution. In particular, the mass threshold imposed on the FoF group is now $10^{11} \ h^{-1}$ M$_\odot$, and the threshold on stellar mass is $2 \times 10^9 \ h^{-1} \ M_\odot$.

As the simulation evolves, the presence of wandering BHs is avoided by adopting a different strategy with respect to the set of simulations presented in Chapter 3. In the previous implementation we pinned the BHs, meaning that we re-positioned them at each time step at the location of the most bound particle of a halo. Here, instead, we assign to the BH a large dynamical mass and we employ low values of star and BH particles softening lengths. Namely, the BH dynamical mass at seeding is imposed to be equal to the DM particle mass until the actual BH mass outgrows that value and the softening values are four times smaller than before, once re-scaled to the higher resolution. These numerical prescriptions are sufficient to mimic a dynamical friction without the necessity to explicitly include a dynamical friction force (Steinborn et al. 2016). Even though this scheme performs overall well at the current numerical resolution, BH centering remains a major challenge for our numerical simulations, and it still can happen that a BH moves from the center of a structure. This is particularly problematic in cluster simulations, where the spurious removal of the SMBH at the center of the BCG might easily lead to catastrophic cooling, with resulting high BCG mass and SFR of the order of $\sim 10^3\ M_\odot\ \mathrm{yr}^{-1}$ at $z \sim 0$. Indeed, in 1 out of the 12 simulations employed in this Chapter, the proto-BCG looses its central BH at $z \sim 4$, and is characterized by an exceedingly high SFR at $z = 0$. Even though it is not an issue for the conclusions of this analysis (see Sect. 4.6), the problem needs to be addressed in future simulations.

After the BH particles are seeded, they can grow by accretion of the surrounding gas (following Eq. 2.31), and by merger with other BHs. The conditions applied for the mergers of two BHs are the same as the ones described in Sect. 3.2.1, with the addition of the third condition: $|V_{\mathrm{pot,rel}}| + v_{\mathrm{rel}}^2 < 0.5 \times c_s^2$, where v_{rel} is the relative velocity between the two BH particles, c_s is the sound speed and $V_{\mathrm{pot,rel}}$ is the difference between the gravitational potentials computed at the positions of the BH particles.

4.2.2 AGN feedback and model calibration

The AGN feedback is implemented accordingly to the scheme already described in Chapter 3 with two main modifications. First, in this implementation we do not use a temperature threshold to define multiphase gas particles. Second, the energy released by AGN feedback is not used to evaporate the cold phase of gas particles, but it is only coupled to their hot phase. As I will

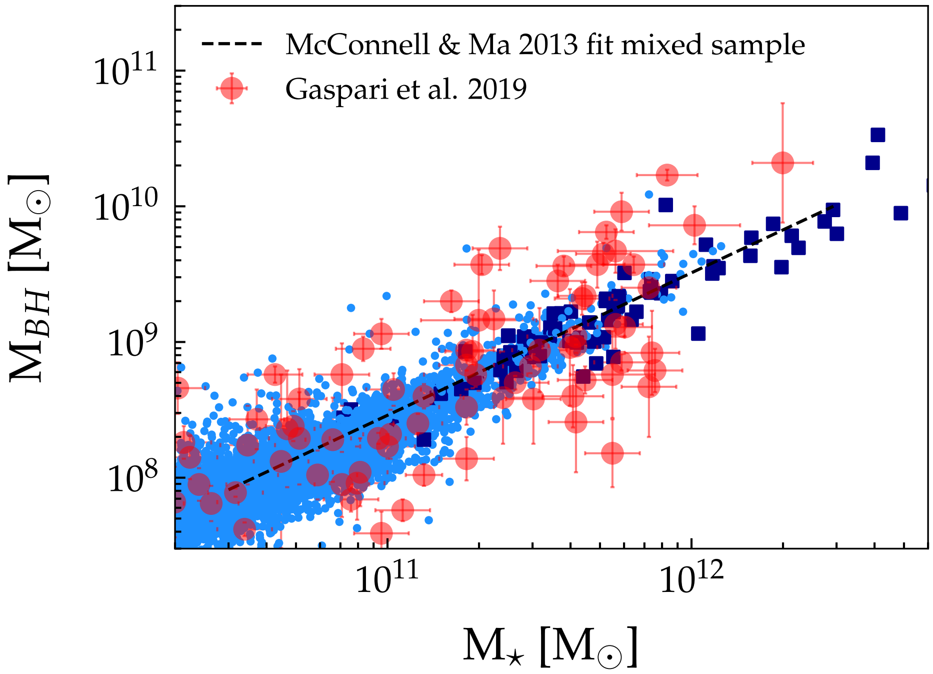

Fig. 4.1: Correlation between the galaxies stellar mass and the central SMBHs mass. Observational data are taken from McConnell & Ma (2013) (dashed black line) and from Gaspari et al. (2019) (red circles). The simulated stellar masses for satellite galaxies (cyan points) are obtained considering the star particles, bound to the substructure (accordingly to Subfind) and within 50 pkpc from its center. The mass of the central galaxies (dark-blue squares) is obtained by summing over all stellar particles within an aperture of $0.15 \times R_{500}$.

show in Sect 4.2.3 these modifications are motivated by the fact that this implementation results in a better agreement between the simulated galaxy stellar mass function and the observed one, with the side effect of producing too massive BCGs at $z = 0$ (see Sect. 4.2.4).

As done for the LR simulations, the values of ϵ_f and ϵ_r of Eq. 2.32 are chosen in order to reproduce the observed normalization of the Magorrian relation (Magorrian et al. 1998). In particular, we aim at reaching agreement with the observational results reported by McConnell & Ma (2013) and more recently by Gaspari et al. (2019). The value chosen for ϵ_r is 0.07 independently of $\dot{M}_{\rm Bondi,\alpha}$, while ϵ_f is lower than 1 and fixed equal to 0.15 only in quasar-mode, when $\dot{M}_{\rm Bondi,\alpha}/\dot{M}_{\rm Eddington} > 0.01$. The values of both parameters are different from the ones chosen for the LR simulations (see

Sect. 3.2.2). This is not surprising, because the two set of simulations differ in the implementation of the AGN feedback, and even more importantly in the numerical resolutions. Indeed, the model for AGN feedback has not reached a strong convergence yet, meaning that each time the resolution of the simulation is changed, the parameters have to be re-calibrated accordingly.

In Fig. 4.1 I show numerical results in comparison with observations. In the plot, dark-blue squares represent central galaxies, defined as galaxies at the centre of groups with at least 100 substructures. All other simulated galaxies are represented by light-blue points. Stellar masses of non-central galaxies are computed considering the star particles associated to the substructures identified by Subfind and within a sphere of 50 pkpc. Stellar masses of central galaxies are computed considering an aperture of $0.15 \times R_{500}$ to match the aperture used by Gaspari et al. (2019). We note that even though simulations correctly reproduce the normalisation of the observed correlation, the scatter is still under-reproduced, especially at the high mass end. Indeed, the intrinsic scatter around the observed correlation of Gaspari et al. (2019) is $\sigma = 0.40 \pm 0.03$, while it is a factor of two lower in our simulations[2] ($\sigma = 0.20$). As discussed in Sect. 3.2.2, even though the observed scatter can be marginally boosted by uncertainties in the assumptions made to obtain these quantities from observational data (e.g. star formation history, IMF, metallicity, etc.), the most probable explanation for this difference is that the subgrid models adopted do not capture the diversity of conditions of BH accretion and AGN feedback at small scales.

4.2.3 Galaxy stellar mass function

Again, since our models have been calibrated only to match the SFE in galaxies and the Magorrian relation, it is interesting to study the prediction of our simulations regarding other galaxy properties. First, I start by comparing the observed and simulated GSMF. Since the observed GSMF is computed in the field, I use the same normalization for the simulated GSMF as discussed in Sect. 3.2.3. The stellar mass of each galaxy is then computed using three different definitions: the sum of all stellar particles that Subfind associates

---

[2] For the linear regression we used the public Python package *linmix* (https://github.com/jmeyers314/linmix), which accounts for measurement errors in both the dependent and independent variables.

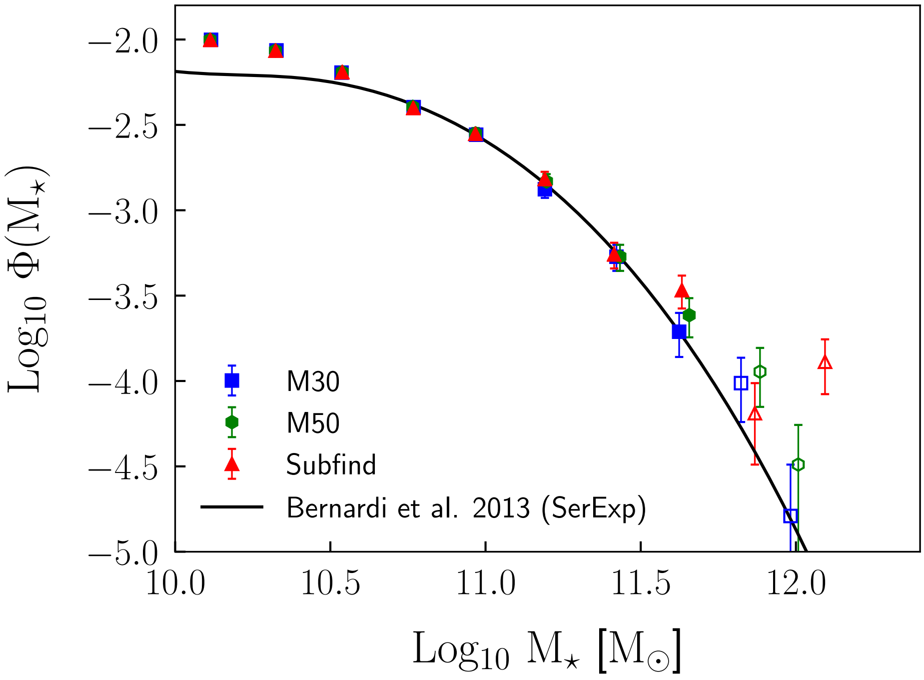

Fig. 4.2: Galaxy stellar mass function (GSMF) at $z = 0$. Observational data are taken from Bernardi et al. (2013) (black solid line). Simulations data are derived considering as stellar mass the sum of all stellar particles bound to the galaxy by Subfind (red triangles), and the same sum restricted to particles within 50 pkpc (green hexagon) and 30 pkpc (blue squares). Error bars are computed assuming Poissonian errors. Filled and empty marks represent the mass bins with respectively more than and less than 10 galaxies.

to a substructure and the same sum limited to stellar particles within 30 pkpc and 50 pkpc from the center. The results are shown in Fig. 4.2, where I plot the GSMF obtained with the three definitions of stellar mass. Results from simulations agree with observations from Bernardi et al. (2013) starting from the stellar mass of galaxies that can be considered as well-resolved in our simulated set ($M_\star > 10^{10}\ M_\odot$). The main difference with respect to observations is around 10^{10} M$_\odot$, where simulations have too many galaxies. As noted by Henden et al. (2019), larger values of the softening length numerically decrease the number of galaxies at these masses. However, an investigation of the stellar feedback will be needed to better describe the GSMF at our low-mass end. In particular, adopting a variable mass loading factor as suggested by Muratov et al. (2015), with larger values at lower stellar masses, will likely help to improve the agreement with observational results. Regarding the different definitions of stellar mass, there is no statistical difference in the results once a fixed aperture is used, as Subfind likely also associates a fraction of the ICL to massive galaxies. The good agreement with observational data is an improvement with respect to the GSMF relative to our LR simulations (see Fig. 3.3). In that case, I showed that the GSMF was a factor of approximately two below the results of Bernardi et al. (2013) at $M_\star \sim 10^{11}\ M_\odot$. This difference, as I discuss in the following subsection, is not due to the increased resolution but to the different implementation of the AGN feedback.

4.2.4 Properties of the BCG

In this section I study the properties of our BCGs at $z = 0$. In particular I study their mass and their SFR.

$M_{\star,\mathbf{BCG}} - M_{500}$ correlation

In Fig. 4.3 I show the correlation between the stellar mass of the BCG and M_{500}. In this plot, $M_{\star,\mathrm{BCG}}$ is defined as the total stellar mass associated to the halo (according to Subfind) and within a $2D$ aperture of 50 pkpc. I checked that using different line-of-sight directions brings no more than 40% difference in the estimated stellar mass, with a median difference of 2% for our sample. In the plot, I also highlight the properties of the BCG that lost its central BH at $z \sim 4$ (see Sect. 4.2.1).

From the figure, we see that this set of simulations tends to have overly massive BCGs with respect to observational data (a factor of two at $M_{500} = 3 \times 10^{14}\ M_\odot$), in line with the findings of other groups (e.g. Bahé et al. 2017, Pillepich et al. 2018, Henden et al. 2019). Moreover, these simulations have more massive BCGs than our LR simulations (orange line in the plot, see also Fig. 3.2), being a factor of 2.3 more massive at $M_{500} = 3 \times 10^{14}\ M_\odot$. A possible explanation could be the different resolution. However, in order to investigate this hypothesis we ran a simulation at a ten-times-lower mass resolution and obtained only a $\sim 12\%$ lower BCG mass. Hence the BCG mass is very stable against the mass resolution of the simulation (see also the discussion in Ragone-Figueroa et al. 2018). To check whether or not the different results with respect to LR simulations are due to the different

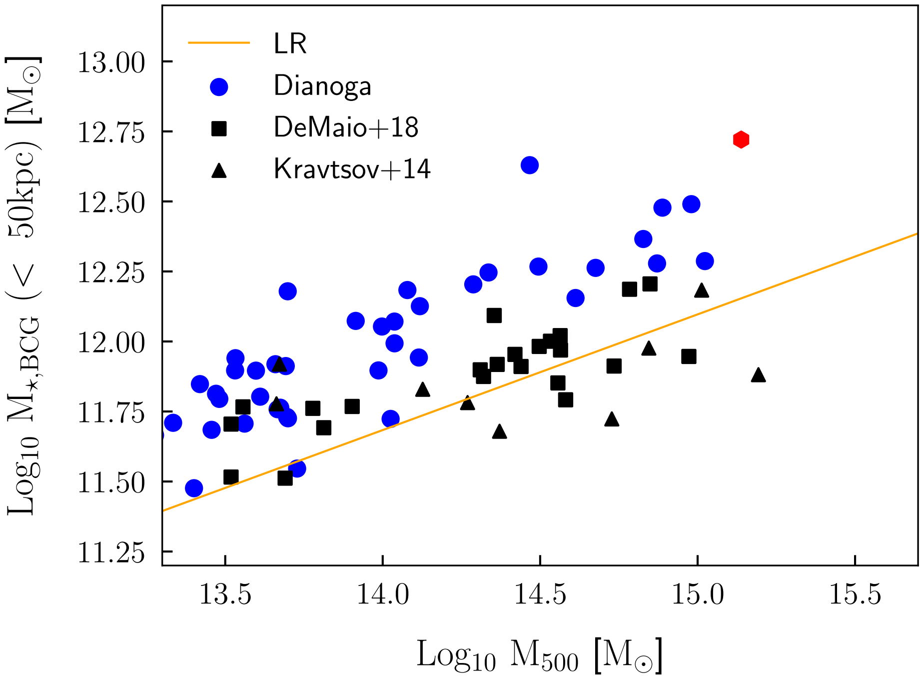

Fig. 4.3: Correlation between BCG stellar mass and M_{500} at $z = 0$. Observations are taken from DeMaio et al. (2018) (blacks quares) and Kravtsov et al. (2018) (black triangles). The simulated values are shown as blue points. The red hexagon refers to the BCG that lost its central BH (see Sect. 4.2.1). The orange line is the fit to LR simulations (Ragone-Figueroa et al. 2018). BCG masses are obtained summing over all stellar particles bound to the main subhalo of a group or cluster by Subfind (BCG+ICL) and within a 2D aperture of 50 pkpc.

implementations of the AGN feedback adopted, we ran two more simulations: one at the current mass resolution and the other with a ten-times-lower resolution, both implementing the same AGN prescription as that in Ragone-Figueroa et al. (2018) (i.e., the same adopted for the simulations presented in Chapter 3). I recall that in this setup, gas particles need to be colder than a fixed temperature threshold to be considered multiphase and the energy released by the AGN feedback is used to evaporate the cold gas (see Sect. 3.2.2). Even in this case, there is no particular trend with resolution, the results being in agreement within 5%. Moreover, the BCG masses obtained in these last two runs are in agreement within 30% the results of our LR simulations (orange line in Fig. 4.3). In addition, with the Ragone-Figueroa et al. (2018) setup, together with a lower BCG mass, we also get a lower normalisation for the GSMF, in line with the results presented in Sect. 3.2.3.

We conclude that the different BCG masses are not due to the increased resolution but to the different prescriptions for the AGN feedback. In particular, not including a temperature threshold for particles to become multiphase reduce the efficiency of AGN feedback. Indeed, after receiving thermal energy and exiting the multiphase stage, particles are still found in very dense regions. Therefore, they rapidly re-become multiphase, losing the energy gained from AGN feedback within the two-phase ISM model of star formation (see also the discussion in Sect. 3.2.2). Finally, with the current implementation of feedback, we conclude that it is difficult to simultaneously reproduce both the observed $M_{\rm BCG} - M_{500}$ relation and the GSMF. In this respect, it is however always important to keep in mind that observational data are affected by different uncertainties. In the context of the stellar mass function, the main source of uncertainty is the algorithm used to assign to each galaxy a value of $M_{\star}/L$ (Bernardi et al. 2017). Apart from the GSMF of Bernardi et al. (2013) that we used in Fig. 3.3, other works based on different values for the stellar to mass ratio report lower normalization for the GSMF, especially at the highest mass end. A lower normalization for the observed GSMF would enable to reach a better agreement between observations and simulations for the BCG stellar masses. However, it is still unclear which method to derive the $M_{\star}/L$ in observations is the more accurate (Bernardi et al. 2017).

Star formation rate of BGCs

In Fig. 4.4 I show the SFR of our simulated BCGs in comparison with observational data. Observations are taken from McDonald et al. (2018) and constitute a subsample of the BCGs used in Fraser-McKelvie et al. (2014). The original selection has been made considering all galaxy clusters in a volume-limited sample, $z < 0.1$, with a measured X-ray luminosity in the *ROSAT* $0.1 - 2.4$ keV band $L_X > 10^{44}$ erg s^{-1}. This luminosity cut ensures a completeness $> 80\%$ for the cluster sample (see Fraser-McKelvie et al. 2014). Moreover, selecting the sample on cluster properties rather than BCG properties enables us to correctly account for low values of SFR and non-detections. However, it has been noted that the SFRs published in Fraser-McKelvie et al. (2014) lack important k-corrections which lead to biased

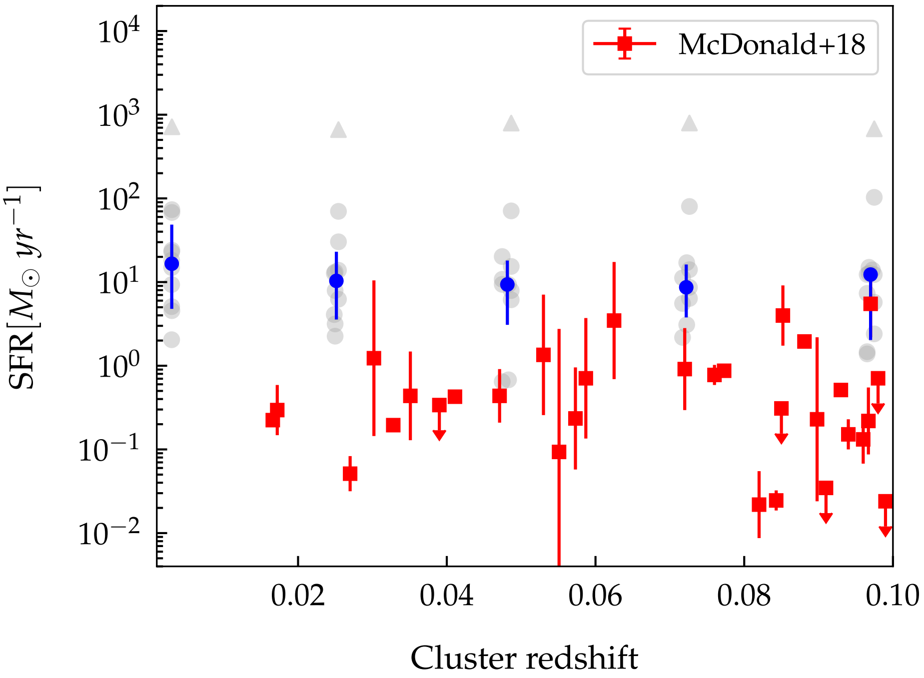

Fig. 4.4: Star formation rate of BCGs in observations and simulations. Grey circles are BCGs of our simulations from different snapshots, while the grey triangle represents the BCG that lost its central BH at $z \sim 4$ (see Sect. 4.2.1). BCGs from the same snapshot are shifted only for visualisation purposes. The median values are shown as blue circles and the vertical bars indicate the range between the 16^{th} and 84^{th} percentiles. A 2D aperture of 30 pkpc is used. Red squares are BCGs from the sample of McDonald et al. (2018) (see text for more details).

results (see Green et al. 2016). McDonald et al. (2018) recomputed the SFRs using $12\ \mu m$ flux following the procedure of Green et al. (2016) for all the clusters with $L_X > 3.3 \times 10^{44}$ erg s^{-1}. The final sample comprises 33 objects and is complete above the cut in X-ray luminosity. In grey I show the results of our simulations. I emphasise that the BCGs are taken from the same simulated regions at different redshifts, and therefore are not independent. In blue I plot the median value with 16^{th} and 84^{th} percentiles. To mimic the selection of McDonald et al. (2018), I considered only the 11 clusters with $M_{500} > 2.8 \times 10^{14}\ M_\odot$ ($M_{200} \gtrsim 4 \times 10^{14}\ M_\odot$), which corresponds to $L_X > 3.3 \times 10^{44}$ erg s^{-1} following the correlation between L_X and M_{500} showed by Truong et al. (2018). The simulations used in the work of Truong et al. (2018) are not the same as those used for this work, but I checked

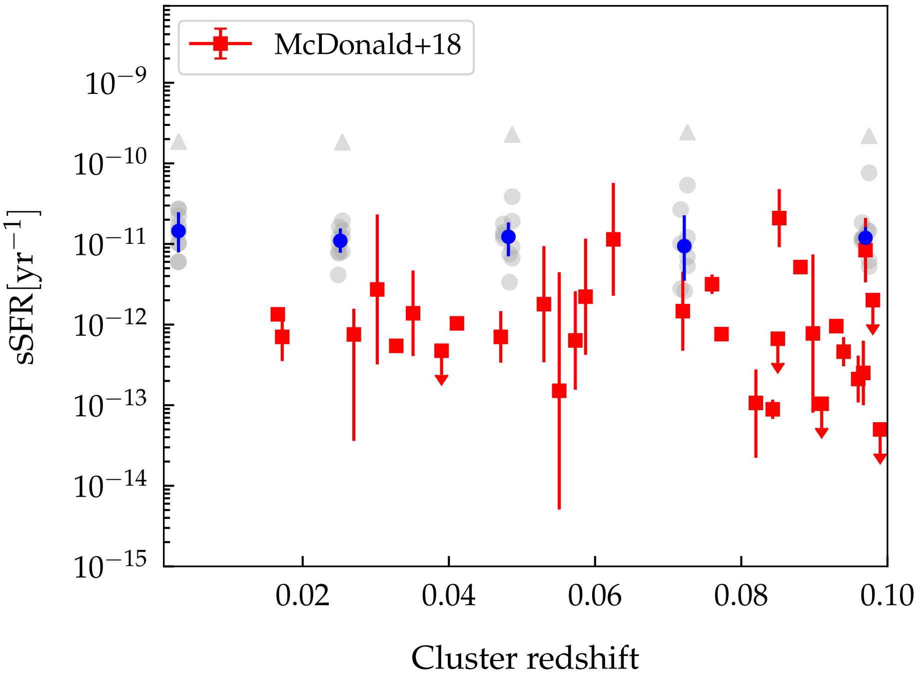

Fig. 4.5: Specific SFR of BCGs in observations and simulations. Grey circles are BCGs of our simulations from different snapshots (blue circles are median values with $16^{\rm th}$ and $84^{\rm th}$ percentiles), while the grey triangle is used for the BCG that lost its central BH at $z \sim 4$ (see Sect. 4.2.1). BCGs from the same snapshot are shifted only for visualisation purposes. A 2D aperture of 30 pkpc is used. Red squares are BCGs from the sample of McDonald et al. (2018) (see text for more details).

that using a relation based on our clusters leads to the same final sample. The SFR in simulations is the instantaneous SFR predicted by the effective model for multiphase particles computed considering all the particles bound to the group by Subfind and within a 2D aperture of 30 pkpc. I employed this aperture to directly compare with other numerical simulations, after checking that the aperture choice does not affect our conclusions. Our simulations present a high residual SFR at these low redshifts ($\sim 10\ \mathrm{M}_\odot\ \mathrm{yr}^{-1}$ against the average observed SFR of $\sim 0.3\ \mathrm{M}_\odot\ \mathrm{yr}^{-1}$). Considering a 3D aperture of 30 pkpc brings us to the same conclusions, as the bulk of SFR is located near the centre of the cluster and the median difference between a 3D and a 2D aperture is 25%. Similar results were also found by other groups. Henden et al. (2019) made a similar analysis considering all the clusters with $M_{200} > 10^{14} M_\odot$ and computed the instantaneous SFR within a spherical aperture of $30\ \mathrm{kpc}$ at $z = 0.2$. Their results show that their BCGs form stars at a rate similar to ours when they do not have a null SFR (see their Fig. 8).

Even though the disagreement between simulations and observations is quite large (a factor of ~ 30 at $z \sim 0$ according to our results), it is important to keep in mind that measuring the SFR of galaxies is always a non-trivial task, especially in the case of BCGs due to their low SFR values and to the crowded environment. In the particular case of the sample used in our comparison, the SFR is obtained from the $12\ \mu m$ luminosity through the relation derived by Cluver et al. (2014). However, this relation is calibrated on star-forming galaxies and flattens at SFR $< 5\ \mathrm{M}_\odot\ \mathrm{yr}^{-1}$. For this reason the values of SFR inferred from observations of BCGs are likely to be underestimated, thus possibly alleviating the tension outlined in Fig. 4.4. The same caution should be exercised when considering the conclusions drawn in the following paragraph.

In Fig. 4.5 I plot the sSFR for our simulations and the McDonald et al. (2018) observations. As I did for the SFR, I checked that the choice of the aperture does not affect our results. Indeed, the results obtained using an aperture of 30 and 50 pkpc are in agreement within 30% at $z = 0$. Also in this case, numerical simulations appear to be an order of magnitude above observations. Similar results were also found by other groups. Davies et al. (2019) showed that Eagle simulation presents a sSFR $\sim 10^{-11}\ \mathrm{yr}^{-1}$ at $M_{200} \sim 10^{14} M_\odot$ and $z = 0$, and that IllustrisTNG BCGs have a sSFR of $\sim 2.5 \times 10^{-12}$ at $M_{200} \sim 10^{14} M_\odot$, which is a factor of three higher than the median value of the McDonald et al. (2018) BCGs. Moreover, considering that the BCG sSFR is an increasing function of mass in IllustrisTNG (see Fig. 12 of Davies et al. 2019) and that the sample of McDonald et al. (2018) is of massive clusters ($L_X > 3.3 \times 10^{44}\ \mathrm{erg\ s}^{-1}$), the factor of approximately three is probably a lower limit.

For our simulations, a possible solution to this mismatch could be a more effective AGN feedback. However, Ragone-Figueroa et al. (2018) found a very similar result (sSFR $\sim 1.5 \times 10^{-11}\ \mathrm{yr}^{-1}$ at $z = 0$) with an implementation of the AGN feedback that is more effective in quenching star formation (see also results in Sect. 4.2.3 and Sect. 4.2.4). Moreover, with the current scheme a more effective feedback could (at least in principle) reduce the gap in the SFR between simulated and observed BCGs, at the cost of an increase in the difference in the GSMF (see Sect. 4.2.3). Therefore, a better solution would be to modify the prescription of the AGN feedback in order to have more efficient quenching only for massive galaxies.

4.3 Protoclusters at $z \sim 2$

In this section I compare our simulations to observational results of protocluster regions of different sizes and identified at $z \sim 2$. As I am interested in comparing values of SFR, I include only protocluster regions with coverage in the FIR and submillimetre wavelengths, because the total star formation budget is mainly contributed by its obscured component. In particular, I compare with the observations of Clements et al. (2014), Dannerbauer et al. (2014), Wang et al. (2016), Kato et al. (2016), Coogan et al. (2018), and Gómez-Guijarro et al. (2019).

4.3.1 Protocluster SFR within ~ 1 pMpc

In Fig. 4.6 I compare the observed star formation rate obtained by Clements et al. (2014), Dannerbauer et al. (2014), and Kato et al. (2016) with the same quantity computed in simulations. With the red bands I show the protocluster regions at $1 \lesssim z \lesssim 3$ identified as clumps in Planck 857 GHz band by Clements et al. (2014). This frequency is suitable for identifying DSFGs, which trace star-bursting phases of protoclusters (e.g. Granato et al. 2004). Clements et al. (2014) retrieve the far-infrared luminosity, $L_{\rm FIR}$, by fitting the spectral energy distribution (SED) with a modified black body formula, and then they compute the SFR using the relation given by Bell (2003), which assumes a Salpeter IMF (Salpeter 1955). In order to compare with our simulations, which instead adopt a Chabrier IMF (Chabrier 2003), I divided the Clements et al. (2014) values of SFR by 1.74. I also include in our comparison the analysis that these latter authors performed on the fields previously introduced by Stevens et al. (2010), who analysed the density flux of submillimetre galaxies (SMGs) obtained at 850 μm in five fields centred on QSOs in the redshift range $1.7 < z < 2.8$. The SFRs for these fields are computed following the procedure already described, with the only difference being that the FIR luminosity is computed from the F_{850} flux using an Arp 220 spectral template. Also in this case I corrected for the choice of the IMF. Among the four clumps and five fields analysed in Clements et al. (2014) I

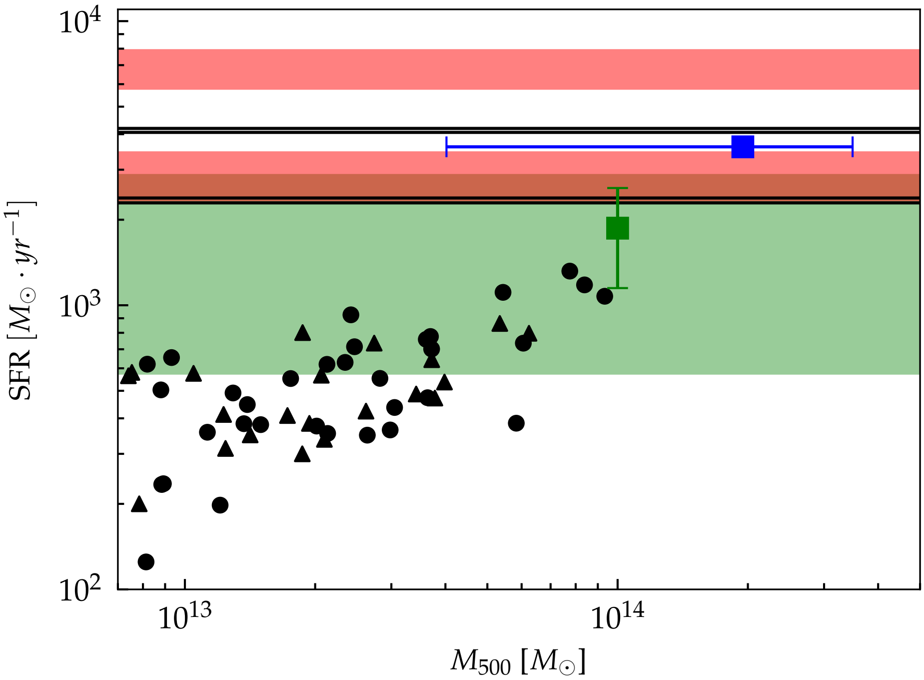

Fig. 4.6: Star formation rate of protocluster regions at $z \sim 2$ in observations and simulations within an aperture of ~ 2 pMpc. Red bands refer to two clumps from Clements et al. (2014), black solid lines refer to four fields from Stevens et al. (2010) and analysed by Clements et al. (2014). The blue square highlights to the Spiderweb structure (Dannerbauer et al. 2014). The green square and green band show the two protoclusters analysed by Kato et al. (2016) (HS1700 and 2QZCluster, respectively). Black circles and triangles refer to numerical simulations, where the SFR is plotted against protocluster mass (see text). We used black circles for groups which end up in the central cluster of the region at $z = 0$, and black triangles otherwise.

include in the comparison the six residing at $1.74 < z < 2.27$ (the values of SFR for the four fields are 2240, 2330, 3966, and 4095 $\mathrm{M}_\odot\ \mathrm{yr}^{-1}$, and thus they overlap in Fig. 4.6). The physical volume used to compute the SFRs in Clements et al. (2014) clumps is $4.2\ \mathrm{Mpc}^3$, equal to a sphere of $1\ \mathrm{Mpc}$ radius, while the fields are characterised by a volume of $1.4\ \mathrm{Mpc}^3$, equivalent to a sphere of $0.7\ \mathrm{Mpc}$ radius.

Dannerbauer et al. (2014) studied the FIR properties of the protocluster associated to the radio-galaxy HzRG MRC1138-262 at $z = 2.16$ (also known as Spiderweb galaxy, Pentericci et al. 2000, Miley et al. 2006). This structure is characterised by an overdensity of Lyman alpha emitters (LAEs), and has been studied at different submillimetre wavelengths (see Dannerbauer et al. 2014 and references there in). Observations in the FIR (100, 160, 250, 350, 500, and 850 μm) were used to fit the SED of detected sources assuming a grey body formula, which was used to compute the total FIR luminosity and the correlated SFR through the relation given by Kennicutt (1998). The resulting SFR computed within a sphere of $1~\mathrm{pMpc}$ radius, corrected to a Chabrier IMF, is $\sim 3600~\mathrm{M_\odot~yr^{-1}}$ and is showed as a blue square in Fig. 4.6. Numerical simulations suggest that this protocluster is the progenitor of a massive $z = 0$ cluster (Saro et al. 2009), with a predicted mass of $M_{200} \sim 10^{15}~\mathrm{M_\odot~yr^{-1}}$. Therefore, this structure is a candidate progenitor of the massive simulated clusters used in this study. Finally, I also show the observations in the FIR of another two known protoclusters: 2QZCluster ($z = 2.23$, Matsuda et al. 2011) and HS1700 ($z = 2.3$, Steidel et al. 2005). Kato et al. (2016) used SPIRE bands (250, 350, and 500 μm) to obtain a colour-selected sample of DSFGs possibly associated to these two protoclusters. In their work, these latter authors found overdensities of DSFGs in both protoclusters regions, even though the redshift of these sources is not yet confirmed. Assuming a grey-body spectrum, these latter authors computed L_{IR} in the $\sim 1~\mathrm{pMpc}$ region containing the highest number of DSFGs, obtaining values very similar to the one reported by Clements et al. (2014). I show Kato et al. (2016) results in Fig. 4.6 as a green square (HS1700) and green band (2QZCluster). In both cases the upper limit on the value of SFR is obtained assuming that all the detected sources are within the protocluster, while the lower limit is obtained subtracting field average values (see Kato et al. 2016 for further details).

Regarding the data from simulations, I considered at $z = 2$ the five most massive groups identified by Subfind in each of the analysed regions. The mass M_{500} of the group is given by Subfind, while the SFR is the sum of the instantaneous SFR of all gas particles within a sphere of $1~\mathrm{Mpc}$ radius from the centre of the group. This aperture matches the volume adopted for Clements et al. (2014) clumps, and is slightly larger than the volume of Stevens et al. (2010) fields. In addition, I adopt another possible definition of the SFR: the SFR averaged over $\sim 100~\mathrm{Myr}$. Although this may be the optimal choice when comparing to DSFGs, it does not quantitatively affect our results as our most highly star forming protocluster region is characterised by a 2% difference in the SFR when the two methods are used. For this reason I only use the instantaneous SFR throughout the paper. In Fig. 4.6 I also differentiate between the progenitors of the most massive cluster at the centre of each region by $z = 0$ and the groups that will form other objects. From the plot it is clear that the simulated protoclusters do not reproduce the high SFR observed, as the difference between the highest value of SFR rate reached within our set of simulated protoclusters ($\sim 1300\ \mathrm{M_\odot\ yr^{-1}}$) is a factor of approximately five lower than the SFR measured in one of the Clements et al. (2014) clumps ($\sim 7000\ \mathrm{M_\odot\ yr^{-1}}$), and a factor of approximately three lower than the SFR measured within the protocluster associated to the Spiderweb galaxy ($\sim 3600\ \mathrm{M_\odot\ yr^{-1}}$). This result is in agreement with the conclusions of Granato et al. (2015), who used a set of simulations with the same initial conditions used here but at ten-times-lower mass resolution and a previous version of our code (the main difference being the prescription for AGN feedback and BH repositioning; see Ragone-Figueroa et al. 2013) together with dust reprocessing and radiative transfer post-processing performed with GRASIL-3D (Domínguez-Tenreiro et al. 2014) to directly compare FIR fluxes with Clements et al. (2014). Granato et al. (2015) concluded that simulations fail to reproduce the observed fluxes at $z = 2$ by a factor $\gtrsim 3 - 4$. Given the results shown in Fig. 4.6, we conclude that the results of Granato et al. (2015) hold at higher resolution and are not dependent on the particular prescription adopted for AGN feedback.

4.3.2 Protocluster SFR within ~ 100 pkpc

In Fig. 4.7 I compare simulations with observations by Wang et al. (2016) (blue square), Coogan et al. (2018) (red square), and Gómez-Guijarro et al. (2019) (green bands). In particular, Wang et al. (2016) recently discovered a cluster (CL J1001+0220) at $z = 2.506$. This structure, detected as an overdensity of distant red galaxies (DRGs), appears as a massive, virialised halo. Through an analysis of the velocity dispersion, stellar mass content, and also the detected X-ray emission, Wang et al. (2016) estimated the cluster mass to be $10^{13.9\pm0.2} M_\odot$. However, differently from local clusters, CL J1001+0220 is characterised by a high fraction of massive ($M_\star > 10^{11} M_\odot$) star forming galaxies. The SFR in the 80 pkpc core region, computed from FIR luminosity and corrected to a Chabrier IMF, is estimated to be $\sim 2000\ M_\odot\ \mathrm{yr}^{-1}$. Moreover, the fraction of starbursting galaxies is $\sim 25\%$, much higher than the

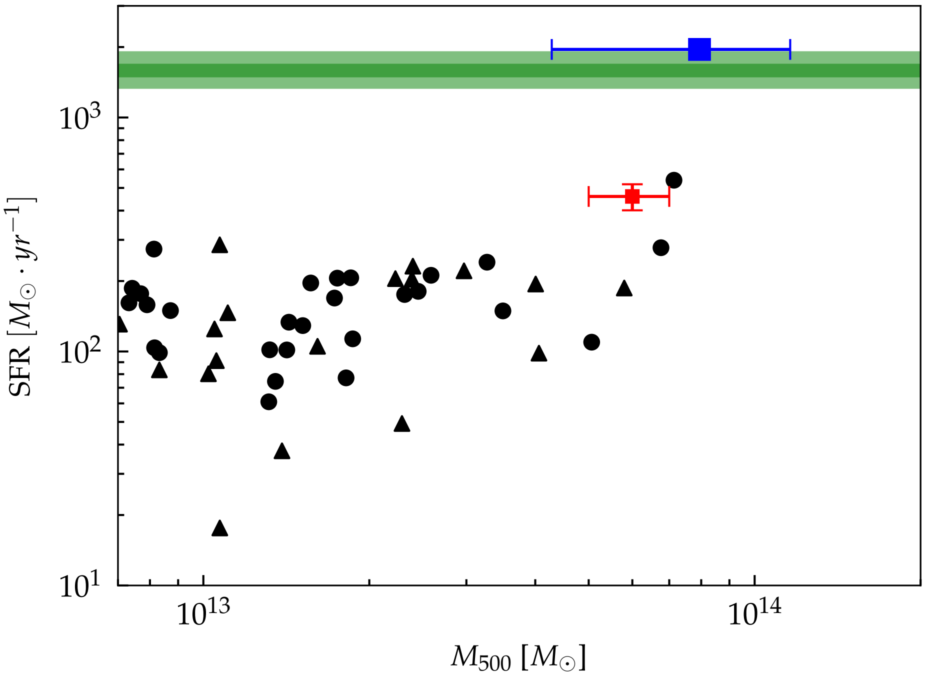

Fig. 4.7: Star formation rate of protocluster regions at $2 < z < 2.6$ in observations and simulations within an aperture of $\sim$ 100 pkpc. Green bands refer to two protoclusters from Gómez-Guijarro et al. (2019), the blue square refers to Wang et al. (2016), and the red square refers to Coogan et al. (2018). Black circles and triangles refer to numerical simulations, where the SFR is plotted against protocluster core mass. We used black circles for groups which end up in the central cluster of the region at $z = 0$, and black triangles otherwise.

value in the field which is about 3% accordingly to Schreiber et al. (2015). Gómez-Guijarro et al. (2019) spectroscopically confirmed two protoclusters through CO emission lines (a third one was analysed in the same work, but it was associated with the well-known CL J1001+0220 cluster in the COSMOS field; see Wang et al. 2016, Wang et al. 2018). These objects were previously recognised as separate sources by Bussmann et al. (2015) who observed with ALMA 29 bright DSFGs taken from the Hermes Survey (Oliver et al. 2012). The two new protoclusters are composed of four and five gas rich DSFGs over a region of 125 pkpc and 64 pkpc at $z = 2.171$ and $z = 2.602$, respectively. The $L_{\rm IR}$ used to compute the SFRs of single sources following Kennicutt (1998) are computed integrating the SED fitted from the available IR flux measurements at 24, 250, 350, 500 μm, and 3 mm.

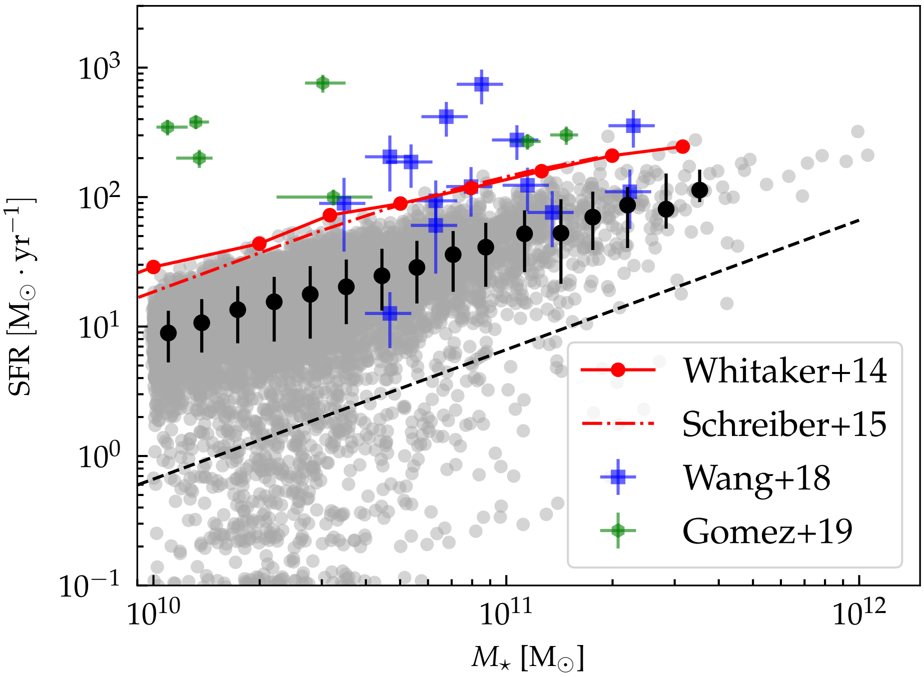

Fig. 4.8: Star formation rate as a function of galaxy stellar mass at $z \sim 2.3$. Red solid and dashed lines are observational data from Whitaker et al. (2014) and Schreiber et al. (2015), respectively. Green hexagons and blue squares are galaxies from the protoclusters of Gómez-Guijarro et al. (2019) and the cluster of Wang et al. (2018), respectively. Grey points are galaxies in our simulations. Black dashed line fix the distinction between active and passive galaxies (Pacifici et al. 2016). Black points represent median values of star forming galaxies with 16th and 84th percentiles. Both SFRs and stellar masses are computed considering a 3D aperture of $30\ \mathrm{pkpc}$.

Finally, I also include in the comparison the observations by Coogan et al. (2018) of the protocluster Cl J1449+0856, identified by Gobat et al. (2011) as an overdensity of IRAC colour-selected galaxies. The protocluster has also been detected from the X-ray emission, from which a mass has been estimated in the range $[4-6] \times 10^{13}\ \mathrm{M}_\odot$ (Valentino et al. 2016). Coogan et al. (2018) employed ALMA observations of $870\ \mu m$ continuum and the CO(4-3) emission line to compute the SFR within the $\sim 0.08\ \mathrm{pMpc}^2$ cluster central region (see Coogan et al. 2018 or Strazzullo et al. 2018 for more details on the computation of the SFR). The value of SFR reported in Fig. 4.7 is the sum of the SFR obtained for obscured ($\sim 400\ \mathrm{M}_\odot\ \mathrm{yr}^{-1}$) and unobscured ($\sim 60\ \mathrm{M}_\odot\ \mathrm{yr}^{-1}$) star formation. As a final remark, we note that the values

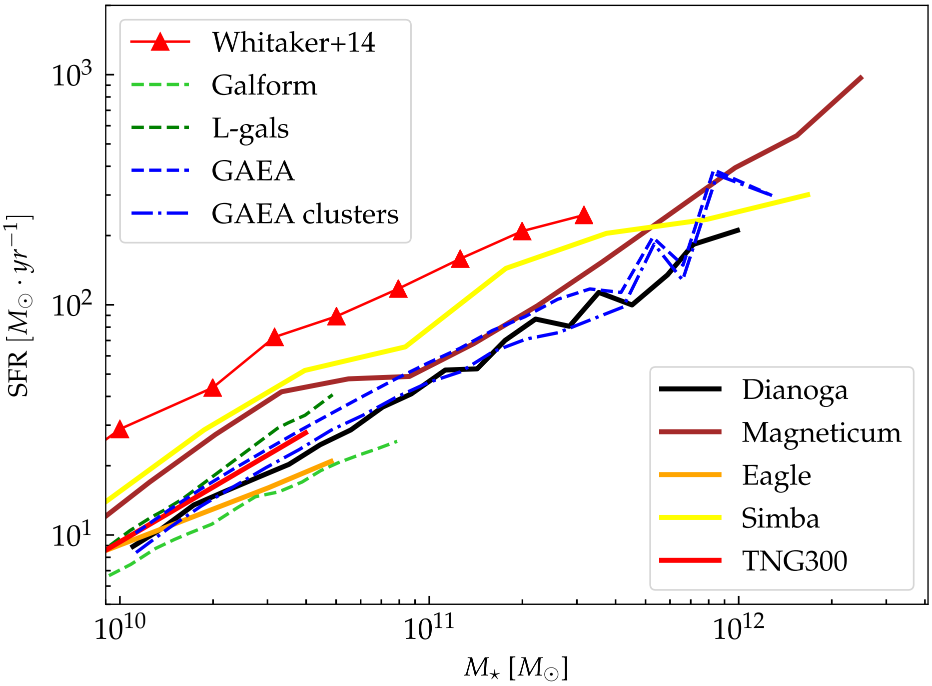

Fig. 4.9: Main sequence of star forming galaxies at $z \sim 2$. Red triangles are observational data from Whitaker et al. (2014). The black line shows median values for our simulations. Coloured solid and dashed lines are data from other cosmological simulations and semi-analytical models respectively. In particular: Eagle (orange solid line, Guo et al. 2016), TNG300 (red solid line, Donnari et al. 2019), Simba (yellow solid line, Davé et al. 2019), Galform (green dashed line, Guo et al. 2016), L-galaxies (dark green dashed line, Guo et al. 2016), and GAEA (blue dashed line, Hirschmann et al. 2016). For the GAEA model we also show the results obtained considering only galaxies that at $z = 0$ are within galaxy clusters with mass $> 10^{14.25}\mathrm{M}_\odot$ (see text for more details).

of SFR computed through the $870\ \mu m$ continuum rely on the assumed SED template. The values reported in Fig. 4.7 are obtained considering a template for MS galaxies. Considering a template typical of starburst galaxies, the value of SFR would be twice as high (e.g. Strazzullo et al. 2018).

In numerical simulations I computed the instantaneous SFR considering a 2D aperture of $90\ \mathrm{pkpc}$ (around the mean value of the four observed protoclusters that I use as comparison) and integrating $1\ \mathrm{pMpc}$ along the line of sight. The choice of the projected distance does not affect our results as most of the stars are produced at the centre of the protoclusters. Indeed, I verified that the results are quantitatively the same integrating up to $3\ \mathrm{pMpc}$ along the line of sight. Similarly to previous results, the most highly star forming region within our set of simulations (SFR $\sim 500\ M_{\odot}\ \mathrm{yr}^{-1}$) underpredicts the highest observed SFR (SFR $\sim 2000\ M_{\odot}\ \mathrm{yr}^{-1}$) by a factor of approximately four.

4.3.3 Main sequence of star forming galaxies

To explore a possible origin for the difference between SFRs in simulations and observations, in Fig. 4.8 I show the observed and simulated correlation between stellar mass and SFR in galaxies. In particular, I compare with the MS of star forming field galaxies as derived by Whitaker et al. (2014), obtained considering star forming galaxies selected in UVJ colours in the redshift range $2 < z < 2.5$, and with the MS at $z \sim 2.3$ from Schreiber et al. (2015), who used a similar approach but considered only photometry at rest-frame wavelengths larger than $30\ \mu\mathrm{m}$ to avoid pollution from AGNs. To compare these latter results with our simulations and the results of Whitaker et al. (2014) I corrected the Schreiber et al. (2015) MS to a Chabrier IMF. In the plot I also include single galaxies from the protoclusters of Gómez-Guijarro et al. (2019) and the cluster of Wang et al. (2018). For our simulations, I use the redshift-dependent threshold in sSFR of Pacifici et al. (2016), which mimics the selection in UVJ colours, to distinguish quiescent from star forming galaxies.

As we can see from the plot, the SFRs of simulated galaxies are below the observed relation by a factor of approximately three. This is a known discrepancy between simulations (and also semi-analytical models) and observations (see, e.g. Davé et al. 2016 and Xie et al. 2017). Indeed, around the peak of the cosmic SFR density, simulations show a normalisation for MS of star forming galaxies that is a factor of approximately two to three lower than observations. In Fig. 4.9 I show the results from different numerical simulations and semi-analytical models. All but our simulations refer to cosmological boxes, meaning that a possible bias in our results toward a lower MS normalisation can be expected when comparing with other simulations. However, observational works do not find differences between the MS computed in different environments at this redshift (e.g. Koyama et al. 2013). This result is also in line with the predictions of the GAEA semi-analytical model (Hirschmann et al. 2016). In particular, I computed the MS of star forming galaxies considering only the main progenitors of the galaxies that are found in a cluster with mass $M_{\rm vir} > 10^{14.25}$ $\rm M_\odot$ at $z = 0$ (GAEA clusters in the plot), finding no more than a 30% difference with respect to the MS obtained considering all active galaxies in the simulation.

The discrepancy outlined in Fig. 4.9 is an interesting feature given the fact that this difference persists also in numerical simulations which reproduce the GSMF at every redshift (e.g. Davé et al. 2019). A systematic factor of approximately three in the galaxy SFR at $z \sim 2$, which naturally arises in cases where the observed normalisation of the MS is matched, could alleviate the discrepancy between the SFR in simulated and observed protoclusters (see Fig. 4.6 and Fig. 4.7). Moreover, looking at individual galaxies in observed protocluster regions in Fig. 4.8, we see that most of them are above the MS with also a few galaxies classified as starburst. In this respect it is interesting to note that galaxies within the cluster identified by Wang et al. (2016), detected also in X-ray and hence probably in a more mature evolutionary stage with respect to the structures identified by Gómez-Guijarro et al. (2019), are characterised by higher masses and are scattered around the observed MS. On the contrary, galaxies within Gómez-Guijarro et al. (2019) structures have lower masses and very high SFRs, all above the MS. The level of SFR of these galaxies is not reproduced by simulations that, besides underpredicting the normalisation of the MS, do not exhibit strong starbursts (see Sect. 4.6.1).

4.4 Protocluster at $z \sim 4$

In this section I compare our simulations to observational results of protocluster regions identified at $z \sim 4$. In particular I compare with the observations by Oteo et al. (2018) and Miller et al. (2018). Before discussing our results, it is important to make a few considerations. First, the protoclusters studied at $z \sim 2$ in the previous section come from relatively small surveys, the largest being the one analysed by Clements et al. (2014). This survey encompasses 90 deg^2, that in the redshift range $0.76 < z < 2.3$ corresponds to $\sim 0.6\ h^{-3}$ $\rm cGpc^3$ in our cosmology, and thus is smaller than the cosmological box from which the simulated clusters are extracted (see also Granato et al. 2015). This is not true for the protoclusters studied by Oteo et al. (2018) and Miller et al. (2018). The first has been identified within the H-ATLAS fields, corresponding to a total sky area of $\sim 600\ \mathrm{deg}^2$ (Ivison et al. 2016), while the second comes from a catalogue from $\sim 770\ \mathrm{deg}^2$ of the South Pole Telescope Sunyaev-Zel'dovich (SPT-SZ) survey (Mocanu et al. 2013). The comoving volume corresponding to the H-ATLAS fields in the redshift range $2.7 < z < 6.4$, corresponding to the redshift spanned by the ultra-red galaxies selected with Herschel by Ivison et al. (2016), is $\sim 10\ h^{-3}\ \mathrm{cGpc}^3$, about ten times larger than the box from which the simulated clusters are extracted. Therefore, Oteo et al. (2018) and Miller et al. (2018) structures could be sufficiently rare not to be sampled by our simulations. Moreover, the protoclusters analysed at $z \sim 2$ include a few bona fide $z = 0$ massive clusters (Dannerbauer et al. 2014, Wang et al. 2016, Coogan et al. 2018). However, this may not be the case for the ones observed by Oteo et al. (2018) and Miller et al. (2018), as it is not guaranteed that a halo of $M_{\mathrm{halo}} \sim 10^{13}\ M_{\odot}$ at $z \sim 4$ will eventually evolve to a Coma-like structure at $z = 0$. Indeed, numerical simulations suggest that the value of the mass of the most massive halo in a protocluster region at $z \sim 4$ is not enough to safely predict the cluster mass by $z = 0$. An analysis of the large-scale structure, such as the galaxy overdensity over a scale of $\sim 5\ \mathrm{pMpc}$, would be needed to place better constraints on the final cluster mass (see Chiang et al. 2013 and Chapter 1). It is important to keep this in mind when comparing observations and simulations.

The observations by Oteo et al. (2018) and Miller et al. (2018) of two highly star forming protocluster cores at $z \sim 4$ and $z \sim 4.3$ are shown in Fig. 4.10 with a green line and blue squares respectively. The protocluster core presented by Oteo et al. (2018) was firstly detected as part of an overdensity of DSFGs in the wide-field LABOCA (a low-resolution bolometer camera on the APEX telescope) map at $870\ \mu\mathrm{m}$. Subsequent observations with ALMA at $2\ \mathrm{mm}$ and $3\ \mathrm{mm}$ revealed that the most luminous source consists of at least 11 separate sources, of which ten were spectroscopically confirmed to be at $z = 4.002$ and are therefore part of the same structure. The L_{IR} for the ALMA resolved sources are computed considering the flux density at $2\ \mathrm{mm}$ ($\sim 400\ \mu\mathrm{m}$ at rest frame) and assuming an ALESS template for the SED. The resulting SFR (corrected to a Chabrier IMF) in the $260\ \mathrm{pkpc} \times 310\ \mathrm{pkpc}$ central region is $\sim 3700\ \mathrm{M}_{\odot}\ \mathrm{yr}^{-1}$. It has to be noted that this value is highly uncertain as it depends on the assumed SED template. However, Oteo et al. (2018) showed that within a large range of

SED templates, only the one reported by Pearson et al. (2013) yields a lower SFR than the one obtained with ALESS (by a factor of 0.66). The protocluster from Miller et al. (2018), SPT2349-56, was first detected by the South Pole Telescope (SPT). Subsequent follow up observations with LABOCA and ALMA led to the identification of 14 sources in an extremely small area (~ 130 kpc diameter) at $z = 4.3$. Star formation rates were derived from 870 μm flux density ($S_{870\ \mu m}$) assuming a SFR-to-$S_{870\ \mu m}$ ratio of $150 \pm 50\ \mathrm{M_\odot\ yr^{-1}/mJy}$, which is typical for SMGs. The gas mass of all 14 galaxies was computed from CO(4-3) line luminosity (converted to CO(1-0) line luminosity through the ratio $r_{4,1} = 0.41 \pm 0.07$) assuming a $\mathrm{CO/H_2}$ conversion factor of $\alpha_{\mathrm{CO}} = 0.8 \frac{\mathrm{M_\odot}}{\mathrm{K\ km\ s^{-2}\ pc^2}}$ and through the relation:

$$M_{\mathrm{gas}} = \alpha_{\mathrm{CO}} L'_{\mathrm{CO(1-0)}}. \tag{4.1}$$

When the CO(4-3) line is not detected, [CII] line luminosity is converted to CO(4-3) using the average CO(4-3)/[CII] ratio for their detected sample (Miller et al. 2018).

The SFR in simulations is computed considering a 2D aperture of 130 pkpc and integrating 1 pMpc along the line of sight. I also verified that the choice of the length of the cylinder does not quantitatively affect our results. In particular, integrating over the whole box along the line of sight and using different orientations for the cylinder axis induce differences in the measured SFR not higher than 50% at SFR $> 400\ \mathrm{M_\odot\ yr^{-1}}$. This suggests that at this redshift, the star formation takes place only in the densest simulated regions. As I did at $z \sim 2$, for each of our regions I selected the five most massive groups at $z = 4.3$. Also in this case, the most star forming group within our simulations differs from observations by a factor of approximately four.

However, it is important to remember that both SPT2349-56 and the protocluster observed by Oteo et al. (2018) represent very rare objects. In fact, none of our simulated protoclusters at $z \sim 4$ has more than seven star forming galaxies with a mass higher than $10^{10}\ \mathrm{M_\odot}$, while Oteo et al. (2018) and Miller et al. (2018) spectroscopically confirmed 10 and 14 sources, respectively. Thus, we conclude that among the main progenitors of our 12 clusters (7 of which very massive), we do not have a structure with the same number of star forming galaxies as these observed protoclusters. Even though this could certainly be due to the limited statistics of the simulated volumes, it

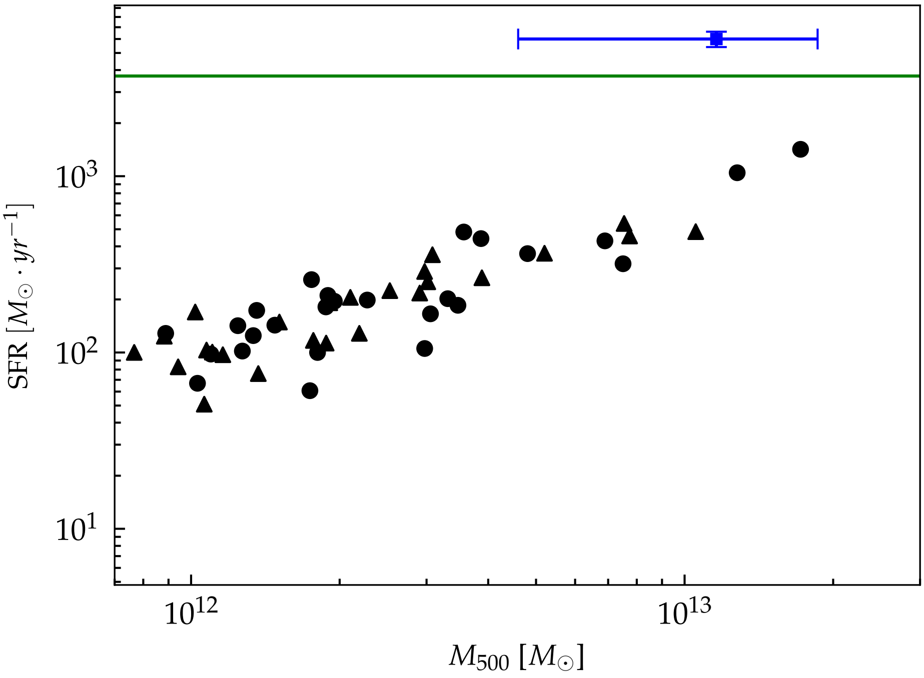

Fig. 4.10: Star formation rate as a function of M_{500} at $z \sim 4.3$. The blue square and green line are the observed values of Miller et al. (2018) and Oteo et al. (2018) protoclusters respectively. Black symbols refer to the SFR computed in a cylinder 1 pMpc long and within a circular aperture of 130 pkpc in our simulations. The five most massive groups of each region are shown. We used black circles for groups which end up in the central cluster of the region at $z = 0$, and black triangles otherwise.

could also be related to the star formation subgrid model, which does not correctly describe galaxy properties at this redshift, or both. Nevertheless, assuming that doubling the number of star forming galaxies within a protocluster to match the observed number within SPT2349-56 would also double the total SFR, the SFR of the 'boosted' simulated protoclusters would still be a factor of approximately two lower than the observed SFR.

In Fig. 4.11 I show the MS of star forming galaxies at $4 < z < 4.8$. In particular I compare our simulations with the MS for the field as observed by Steinhardt et al. (2014), together with detected galaxies in SPT2349-56 as reported by Hill et al. (2020), who updated the values of SFR of Miller et al. (2018) and estimated the mass of single galaxies by dynamical methods (through their measured line widths). As we can see from the plot, simulations show relatively good agreement with observations with no statistical

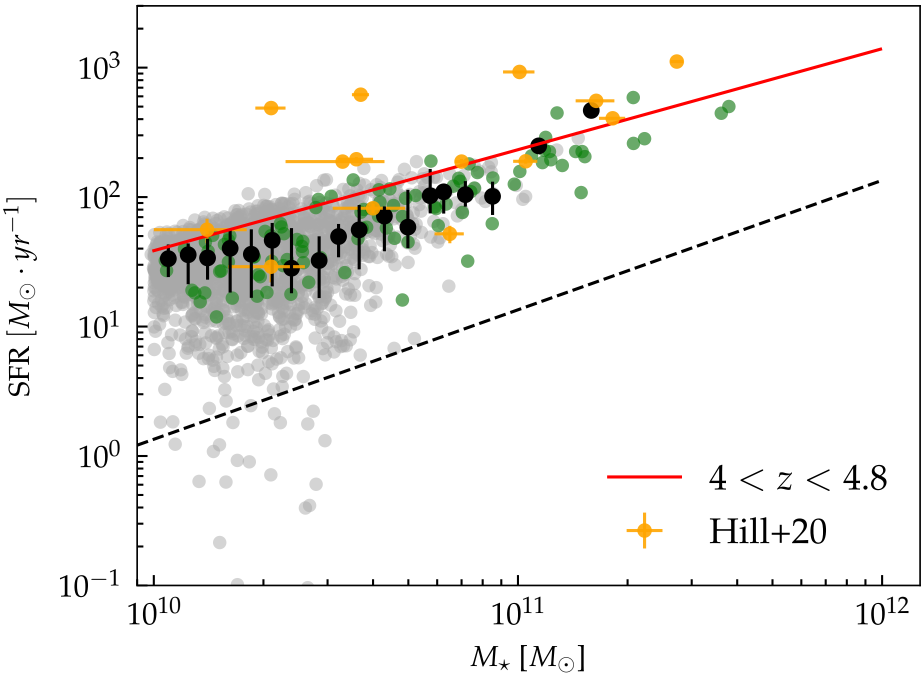

Fig. 4.11: Star formation rate as a function of galaxy stellar mass at $z \sim 4.3$. The red line shows observational data from Steinhardt et al. (2014). Orange dots represent galaxies of SPT2349-56 as analysed in Hill et al. (2020). Grey points are galaxies in our simulations. The black dashed line fixes the distinction between quiescent and star forming galaxies (Pacifici et al. 2016). Black points represent median values with 16th and 84th percentiles for star forming galaxies. Green circles are galaxies from the simulated protoclusters shown in Fig. 4.10.

difference in the normalisation of the MS. Therefore, we cannot explain the difference we observe in terms of SFR as being due to a systematic offset on the SFR-$M_\star$ plane. However, if we look at the galaxies in SPT2349-56, we see that they are scattered around the MS with also a few strong starbursts. On the contrary, galaxies in our simulated protoclusters are mainly MS galaxies with a very small scatter. Therefore, we conclude that at $z \sim 4$ our simulations fail to reproduce the high SFR observed because they are unable to produce strong starbursts lying well above the MS.

4.5 Redshift evolution of mass normalized SFR

In this section I show the evolution of the SFR once normalised by the cluster mass, $\Sigma(\mathrm{SFR})/\mathrm{M_{cl}}$. The results are shown in Fig. 4.12.

$\Sigma(\mathrm{SFR})/\mathrm{M_{cl}}$ is an increasing function of redshift with an observationally driven empirical parametrisation of $(1+z)^n$ (e.g. Cowie et al. 2004, Geach et al. 2006). Popesso et al. (2012) used a sample of nine groups in the redshift range $0.1 < z < 1.6$ and nine clusters in the redshift range $0.1 < z < 0.85$ and derived the best fit to be $(213 \pm 44) \times z^{1.33 \pm 0.34}$ and $(66 \pm 23) \times z^{1.77 \pm 0.36}$ for groups and clusters, respectively. Popesso et al. (2012) also showed that there is no evidence for a significant $\Sigma(\mathrm{SFR})/\mathrm{M_{cl}} - \mathrm{M_{cl}}$ or $\mathrm{M_{cl}} - z$ correlation, concluding that $\Sigma(\mathrm{SFR})/\mathrm{M_{cl}} - \mathrm{z}$ is a genuine correlation (not driven by a decreasing mass evolution with redshift within their sample). Recent observations of highly star forming protocluster regions suggest a stronger evolution with redshift, $\propto (1+z)^7$ (e.g. Smail et al. 2014, Ma et al. 2015, Santos et al. 2015, Smith et al. 2019), in line with the trend found by Cowie et al. (2004) for the number of star-forming ultraluminous infrared galaxies (ULIRGs) in the redshift range $0 < z < 1.5$. In Fig. 4.12 I add the previously cited protocluster regions at high redshift. We note that for these protoclusters the SFR is computed within an aperture of ~ 1 pMpc, with two exceptions: Miller et al. (2018) computed the SFR within a 2D aperture of ~ 130 pkpc and Wang et al. (2016) computed the SFR in a 2D aperture of ~ 80 pkpc. All the SFRs derived assuming the Salpeter IMF are converted to a Chabrier IMF.

To build the comparison I considered clusters and groups in our simulations with a mass threshold varying with redshift. In particular, the minimum mass considered is $M_{200} > 10^{14}$ at $z = 0$, decreasing linearly with redshift up to $M_{200} > 10^{13}$ at $z = 4.3$. I made this choice to mimic as close as possible the minimum mass of the protoclusters and clusters in Fig. 4.12 at all redshifts. To mark a few examples, Popesso et al. (2012) clusters are in the mass range $[3.9, 27.6] \times 10^{14}\ \mathrm{M_\odot}$; the cluster by Smith et al. (2019) at $z \sim 2$ has an estimated mass of $0.5 \times 10^{14}\ \mathrm{M_\odot}$; and the protocluster by Miller et al. (2018) at $z \sim 4.3$ has an estimated mass of $1.16 \pm 0.70 \times 10^{13}\ \mathrm{M_\odot}$. I use M_{200} (like Popesso et al. 2012) as an estimate of the cluster mass and I compute the instantaneous SFR considering all gas particles within R_{200}. This choice confers the advantage that it matches the aperture used by Wang et al.

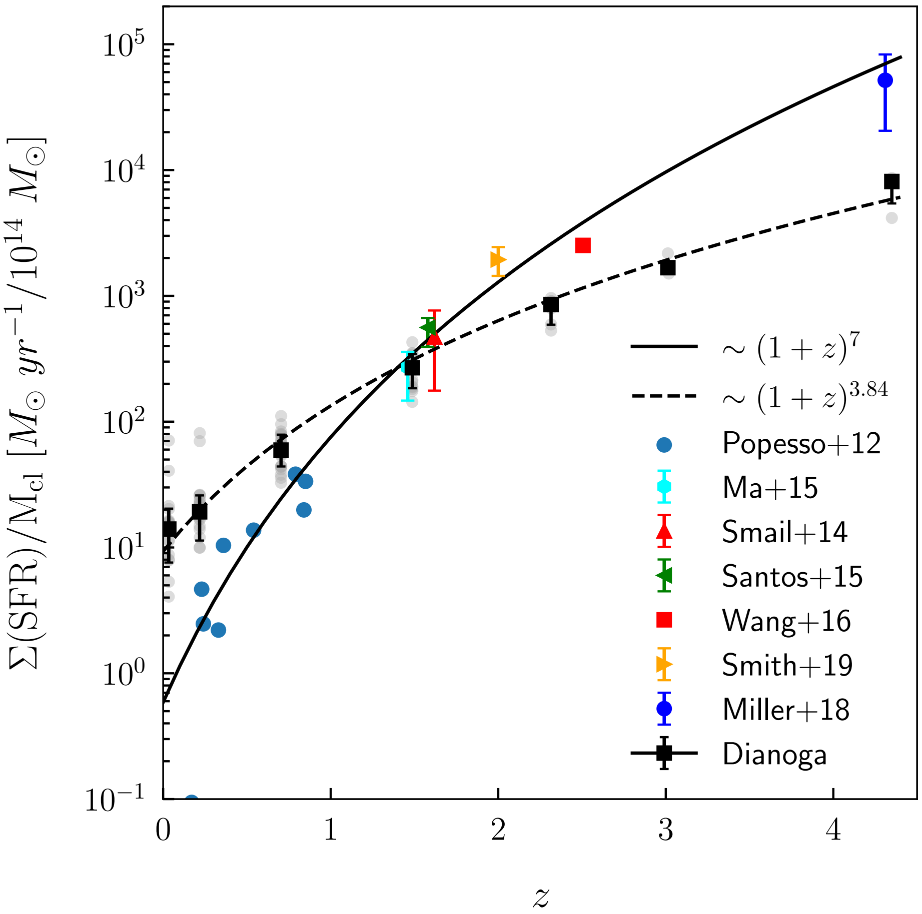

Fig. 4.12: Star formation rate normalised by cluster mass as a function of redshift. Black squares represent median values from Dianoga simulations (grey points). See the text for a complete explanation of sample selection. The dashed black line is the best fit to simulations. Coloured points are observational data from Popesso et al. (2012), Ma et al. (2015), Smail et al. (2014), Santos et al. (2015), Wang et al. (2016), Miller et al. (2018), and Smith et al. (2019). The solid black line $\sim (1+z)^7$ shows an empirical fit to data suggested by Cowie et al. (2004) and Geach et al. (2006).

(2016) and Miller et al. (2018), the two observations at the highest redshifts ($R_{200} \sim 300$ pkpc and $R_{200} \sim 150$ pkpc at $z = 3$ and $z = 4$ respectively).

Simulated clusters show a clear evolution with redshift; however, the trend is shallower than in observations and is better described by $\propto (1+z)^{3.84\pm0.15}$. In particular, simulations predict a higher SFR at low redshift, reflecting the results already discussed in Fig. 4.4. At redshift $z > 2$, the

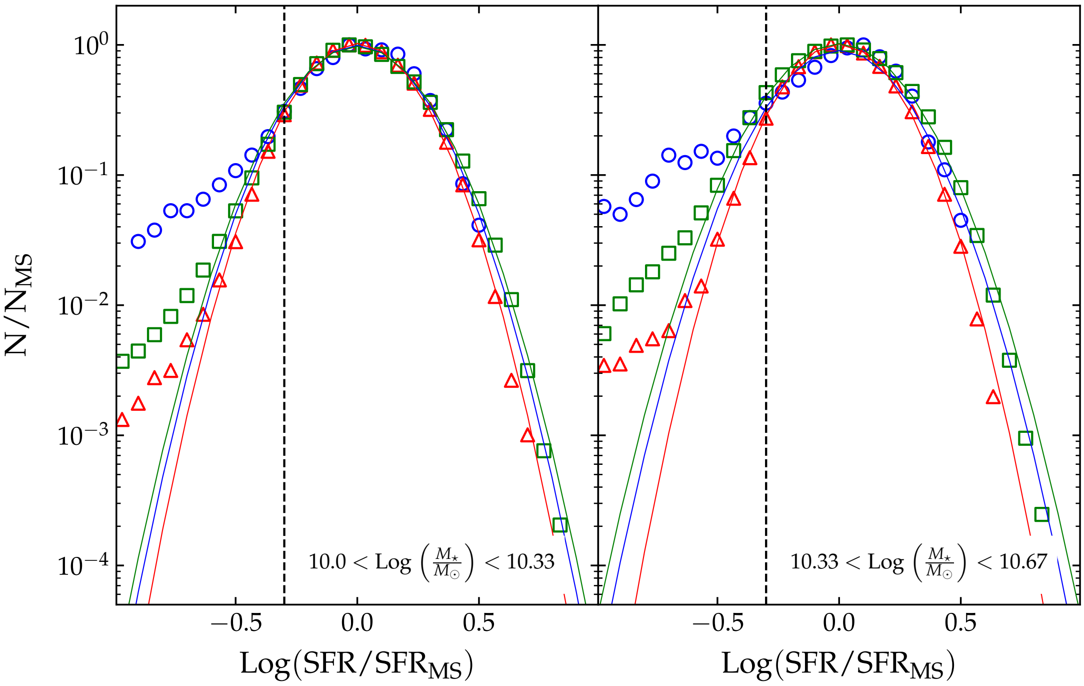

Fig. 4.13: Star formation rate distribution of star forming galaxies at fixed stellar mass at $z = 2$. Blue points refer to Dianoga simulations, green squares to Magneticum Box2b, and red triangles to Magneticum Box2. $\mathrm{SFR_{MS}}$ is computed independently for every simulation. $\mathrm{N_{MS}}$ is the number of galaxies within the bin corresponding to SFR=$\mathrm{SFR_{MS}}$. Only bins with at least ten galaxies are shown. Coloured solid lines are Gaussian fits to simulations. Vertical black dashed line define the threshold above which data are used to estimate the fit.

predicted SFR is much lower, mirroring the outcome of the discussion of the previous sections. A similar mismatch with respect to observations has also been pointed out by Ragone-Figueroa et al. (2018) for the sSFR of BCGs of our lower resolution simulations.

4.6 Discussion

In recent years, a good number of observational studies have confirmed the detection of protocluster regions characterised by SFRs from several hundreds to several thousands of $\mathrm{M_\odot\ yr^{-1}}$ (Clements et al. 2014, Dannerbauer et al. 2014, Umehata et al. 2015, Wang et al. 2016, Oteo et al. 2018, Coogan et al. 2018, Miller et al. 2018, Gómez-Guijarro et al. 2019, Smith et al. 2019, Lacaille et al. 2019). These high values of SFR are often dominated by DSFGs, with typical SFRs from $\sim 100\ \mathrm{M_\odot\ yr^{-1}}$ to $\sim 1000\ \mathrm{M_\odot\ yr^{-1}}$. The physical reason of these high values of SFR is debated. Some observations suggest that starburst galaxies and SMGs are characterised by a high star formation efficiency (e.g. Daddi et al. 2010). Other recent observations suggest that the starbursting phase of galaxies is related to high gas fractions (e.g. Scoville et al. 2016, Gómez-Guijarro et al. 2019). Finally, some observations suggest that starburst galaxies are characterised by both high star formation efficiency and high gas fraction (Genzel et al. 2015, Béthermin et al. 2015).

In this section I focus on starburst galaxies in our simulations and the differences in terms of star formation efficiency and gas fraction with respect to galaxies in the observed protoclusters used as references in Sects. 4.3 and 4.4. I also investigate the implications for the subresolution model of star formation adopted in our simulations.

4.6.1 Starburst galaxies in numerical simulations

Galaxies are usually defined as starburst depending on how much their SFR is above the SFR of MS galaxies with the same mass and at the same redshift. Here, following Schreiber et al. (2015), I consider the threshold $\mathrm{SFR/SFR_{MS}} > 4$. In the $M_\star$–SFR plane, starburst galaxies do not only represent the tail of the MS distribution. Indeed several studies have shown that at fixed stellar mass and redshift, the distribution of galaxies around the MS is better described by a double Gaussian (Sargent et al. 2012, Schreiber et al. 2015), where the second component describes the population of starburst galaxies. This population is estimated to comprise 3% of star forming galaxies without significant redshift dependence (Schreiber et al. 2015).

Following the works mentioned above I study the starburst population in our simulations by plotting the distribution of galaxies around the MS in two mass bins at $z = 2$; see Fig. 4.13. Since in principle it is not guaranteed that the most star forming galaxies will be within protocluster regions, I also plot the results from the Magneticum simulations[3]. The Magneticum simulations are a set of hydrodynamical simulations of different cosmological volumes

---

[3] http://www.magneticum.org/

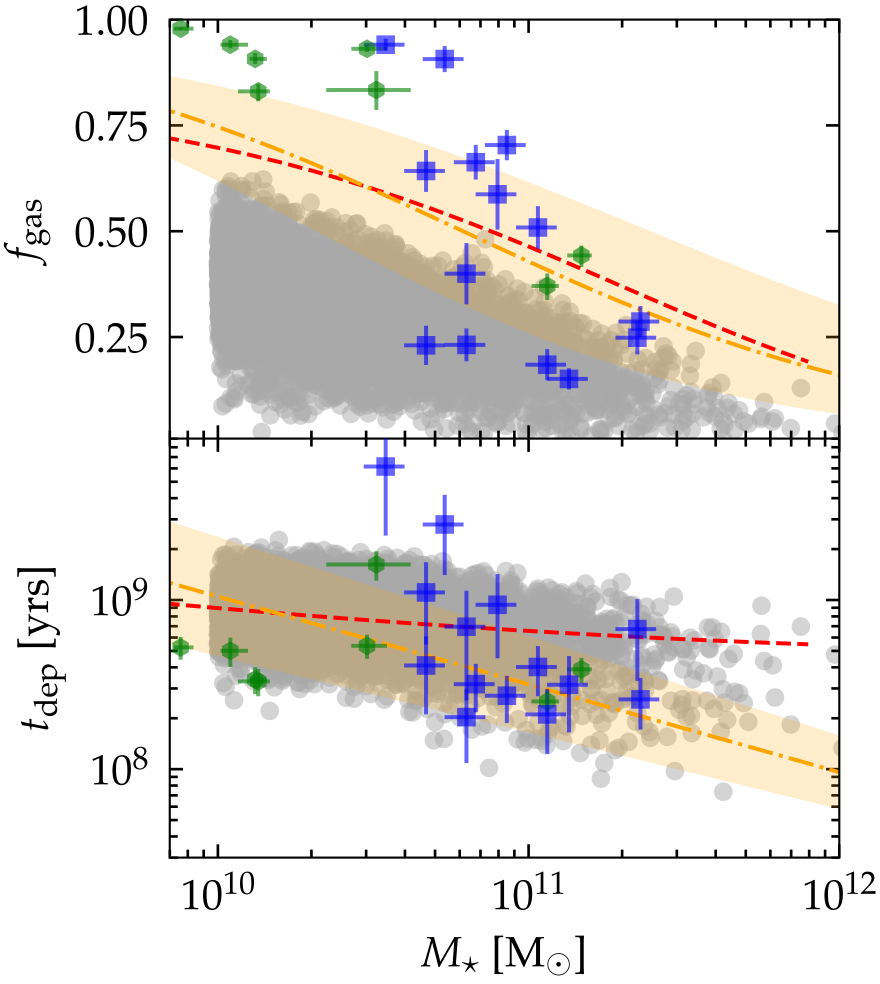

Fig. 4.14: Galaxy correlations at $z = 2.3$. *Top panel:* Gas fraction as a function of stellar mass. *Bottom panel:* Depletion time as a function of stellar mass. Grey circles refer to Dianoga simulations at z=2.3. Green hexagons and blue squares are data from Gómez-Guijarro et al. (2019) and Wang et al. (2018) respectively. The orange dashed line is the functional form of Liu et al. (2019) for MS galaxies at $z = 2.3$, while the shaded region encompasses galaxies with an SFR that is four times lower and higher than MS galaxies. Red dashed lines are obtained combining the MS by Whitaker et al. (2014) and the integrated Kennicutt-Schmidt law from Sargent et al. (2014, orange line in the plot).

(Hirschmann et al. 2014, Ragagnin et al. 2017) performed with the same GADGET-3 code used in our simulations (see Hirschmann et al. 2014 for the differences in the AGN feedback implementation). From the Magneticum set, I consider the Box2 and Box2b (352 and 640 h^{-1} Mpc respectively). The mass resolution is $m_{\mathrm{DM}} = 6.9 \times 10^8\ h^{-1}\ M_{\odot}$, a factor of ten lower than the one used for this work.

In Fig. 4.13 the value of $\mathrm{SFR}_{\mathrm{MS}}$ is computed for each simulation considering only active galaxies (see Sect. 4.3, Fig. 4.8). The two mass bins analysed are chosen following Sargent et al. (2012). I analysed only the two lower mass bins as at higher masses the number of galaxies in the Dianoga simulations is too low for a statistical analysis. Blue points are Dianoga simulations, red triangles are results for Box2, and green squares are results for Box2b. Only bins with at least ten galaxies are plotted. Solid lines are Gaussian fits to the data, which were obtained considering only galaxies with $\mathrm{SFR} > 0.5 \times \mathrm{SFR}_{\mathrm{MS}}$. This cut, marked as a vertical black dashed line in the plot, is needed to avoid considering galaxies on their way to being quenched (but still selected as active by our cut in sSFR) in the Gaussian fit. The three simulations are in very good agreement in both mass bins, despite the different box sizes and environment, and can all be fitted with a single Gaussian with a standard deviation estimated to be $0.19 < \sigma < 0.21$. This value is in agreement with the results of Sargent et al. (2012) ($\sigma = 0.188$), but is lower than the estimate of Schreiber et al. (2015) ($\sigma = 0.31$). Finally, the fraction of starburst galaxies (i.e. SFR/$\mathrm{SFR}_{\mathrm{MS}} > 4$) is $0.03\% < f_{\mathrm{SB}} < 0.2\%$, at least one order of magnitude lower than what was estimated by Schreiber et al. (2015).

As a final warning, it is also important to keep in mind that the observational estimates of the values of SFR, in particular for starburst galaxies, are affected by a number of uncertainties. A relevant role is played by the assumption of the IMF, as studies on the chemical abundances and abundance ratios suggest that starburst galaxies are characterised by a top-heavy stellar IMF (e.g. Romano et al. 2017, Romano et al. 2019). If this proves to be correct, it could have important implications for the estimated values of SFR, affecting as a consequence also the conclusions reached in this section. Indeed, a more top-heavy IMF would lower the SFR values obtained through observations, while affecting numerical predictions to a much lesser extent (see also the discussion by Granato et al. 2015).

4.6.2 Star formation efficiency and gas fraction

In this section I study the cold gas and SFR properties of our simulated galaxies to determine which variable is more related to the underestimated normalisation of the MS at $z \sim 2$ (see Sect. 4.3) and to the absence of starburst galaxies.

In Fig. 4.14 and Fig. 4.15 I study the gas fraction and the depletion time in simulations and observations at $z \sim 2$ and $z \sim 4$ respectively. The two are defined as

$$f_{\rm gas} = \frac{M_{\rm gas}}{M_{\rm gas} + M_\star}, \tag{4.2}$$

where $M_{\rm gas}$ is the cold gas mass that in simulations is computed considering only the cold phase of SPH particles, and

$$t_{\rm dep} = \frac{M_{\rm gas}}{\rm SFR}. \tag{4.3}$$

I plot at $z \sim 2$ and at $z \sim 4$ all the galaxies in the observed protoclusters used in Sects. 4.3 and 4.4, respectively. Moreover, I add the functional forms of $f_{\rm gas}$ and $t_{\rm dep}$ from Liu et al. (2019), which depend on redshift, stellar mass, and relative distance from the MS ($\rm SFR/SFR_{MS}$). The red dashed line in Fig. 4.14 was computed as follows: given a galaxy stellar mass, I assume that the expected SFR for a MS galaxy is given by the MS relation of Whitaker et al. (2014). Given the SFR, I assume that the mass of molecular gas is given by Eq. 4 of Sargent et al. (2014) for normal galaxies. Combining $M_\star$, $M_{\rm gas}$, and SFR I obtain the expected values of $f_{\rm gas}$ and $t_{\rm dep}$ for normal star forming galaxies. This procedure is supported also by recent observations with ALMA, which show that massive ($M_\star > 10^{10}\ M_\odot$) MS galaxies obey the star formation law for star-forming galaxies (Liu et al. 2019). From Figs. 4.14 and 4.15 we see that observational data are not in agreement among each other. In particular, data from Hill et al. (2020) at $z \sim 4$ suggest that starburst galaxies are characterised by a shorter depletion time (and thus a high star formation efficiency) than normal star forming galaxies. This is supported by other observations (i.e. Daddi et al. 2010, Sargent et al. 2014, Liu et al. 2019). On the other hand, data from Gómez-Guijarro et al. (2019) and Wang et al. (2018) at $z \sim 2.4$ are characterised by a high gas fraction but a star formation efficiency (or depletion time) that is consistent with the integrated Kennicutt-Schmidt law for normal star forming galaxies.

This is also consistent with numerical simulations, where the position on the MS depends on the gas fraction (see Fig. 8 of Davé et al. 2019). The difference among the observational results is largely due to the different values of the parameter $\alpha_{\rm CO}$ used to derive the molecular gas mass from the CO line luminosity $L'_{CO(1-0)}$ through Eq. 4.1. Gómez-Guijarro et al. (2019) used $\alpha_{\rm CO} = 3.5$, typical for normal star forming galaxies at solar metallicity. Wang et al. (2018) adopted the mass–metallicity relation by Genzel et al. (2015) to retrieve the galaxy metallicity for the members of their cluster, and then computed the metalicity-dependent value of $\alpha_{\rm CO}$ following Genzel et al. (2015) and Tacconi et al. (2018). The values reported for the $\alpha_{\rm CO}$ are in the range $[4.06, 4.12]$, again consistent with normal star forming galaxies at solar metallicity. Hill et al. (2020), on the other hand, used $\alpha_{\rm CO} = 1$, typical for high-redshift SMGs. Due to these arguments, it remains unclear whether starburst galaxies in protocluster environments are mainly driven by a high gas fraction or a high star formation efficiency, as the results strongly depend on the assumptions needed to derive gas-related quantities.

If we look at the population of normal star forming galaxies at $z \sim 2$ (red and orange dashed lines in Fig. 4.14) we see that our simulations match the observed star formation efficiency. This is expected, since the star formation efficiency of our model is tuned in order to reproduce the Kennicutt-Schmidt relation. On the other hand, the simulated gas fractions are consistently lower than observations. In particular, at $M_\star = 10^{10}\ M_\odot$, observations show a $M_{\rm gas}$ that is higher by a factor of ~ 3.5. This factor is very similar to the difference in the observed and simulated MS (see Fig. 4.8). Thus, the lower normalisation in the simulated MS seems to be driven by an underestimated gas fraction.

It is also interesting to study the correlation between the MS galaxies and gas-related properties in simulations. In Fig. 4.16 I show the MS colour-coded with respect to $f_{\rm gas}$ (upper panel) and $t_{\rm dep}$ (lower panel). At fixed stellar mass, galaxies below the MS are characterised by both a long depletion time and low gas fraction. Vice versa, galaxies above the MS have both short depletion times and high gas fraction. This visual impression is also confirmed by the computation of the Pearson's correlation coefficient for the two relations: $\rm Log(SFR/SFR_{MS}) - Log(f_{gas})$ and $\rm Log(SFR/SFR_{MS}) - Log(t_{dep})$. The results are $r = 0.62$ and $r = -0.63$ for the two relations respectively. Moreover, results of the two linear regressions suggest that in our simulations the position on the MS scales with $f_{\rm gas}$ and $t_{\rm dep}$ with similar slopes: SFR/SFR$_{\rm MS} \propto f_{\rm gas}^{0.85}$ and SFR/SFR$_{\rm MS} \propto t_{\rm dep}^{-1}$.

4.6.3 Simulation tests

In the previous sections I showed that our simulations underestimate the normalisation of the MS relation at $z \sim 2$ by a factor of approximately three. Moreover, we have seen that the star formation model (Springel & Hernquist 2003) implemented in our code, with the current choice for the model parameters set to reproduce quiescent mode of star formation, does not reproduce the observed population of starburst galaxies at $z > 2$. While the normalisation of the MS seems to be mainly related to the gas fraction, it remains unclear whether we miss starburst galaxies because we do not correctly sample the star formation efficiency, the gas fraction, or both. Therefore, we performed a set of simulations aiming at checking whether the fraction of starburst galaxies and MS normalisation are sensitive to the choice of the parameters of the subgrid model. All the following simulations are performed for only one of our regions, a cluster with $M_{200} = 5.4 \times 10^{14}\ M_\odot$ at $z = 0$. In Figs. 4.17, 4.18, and 4.19 I show the results for the MS, SFE, and gas fraction at $z \sim 3$, respectively. The choice of the redshift is somewhat arbitrary, as I do not aim to compare simulations with particular observational data but to study the effect of different parameters on our results. Each panel refers to a different simulation, while I plot with grey circles the results for the reference simulation used in the previous sections. In the following I briefly discuss the specific changes for each simulation and the effects on the results.

Increasing the star formation efficiency (t_0 0.3x)

I recall that in the Springel & Hernquist (2003) model, the characteristic time for star formation, $t_\star$, is $t_\star \propto t_0^\star\ t_{\rm dyn}$, where $t_0^\star$ is a parameter usually tuned to reproduce the Kennicutt relation (see Chapter 2). Here I increase the efficiency to match the observed SFE of Hill et al. (2020) (see Fig. 4.15) by lowering $t_0^\star$ by a factor of three. The results of this test are shown in the top-left panel of the figures. From Fig. 4.18 we see that indeed the SFE is higher, but there is little difference in the MS (see Fig. 4.17). Moreover, there is no difference in the fraction of starburst galaxies. In fact, the model is so tightly self-regulated that in response to a high SFE we have a lower gas fraction (see Fig. 4.19), resulting in similar SFRs.

Increasing the star formation threshold ($\mathrm{SFTh}\ 10\mathrm{x}$ and $\mathrm{SFTh}\ \mathrm{t}_0$)

In the $\mathrm{SFTh}\ 10\mathrm{x}$ simulation I increased the density threshold, $\rho_{\rm thr}$, by a factor of ten; this threshold is used to decide whether or not a gas particle becomes multiphase (only multiphase particles can form stars; see Chapter 3 and Springel & Hernquist 2003). Increasing this threshold should allow a larger reservoir of gas to accumulate and reach higher densities before starting to produce stars, increasing the gas fraction and the overall SFR. However, from the top-right panel of Figs. 4.17, 4.18, and 4.19 we see that we do not have major differences in terms of MS normalisation, SFE, and gas fraction. The only appreciable difference is the reduction of the most massive galaxies and the increase of passive galaxies. Indeed, higher densities at the centre of galaxies also means more gas accretion onto the central BH and consequently a stronger AGN feedback.

In the $\mathrm{SFTh}\ \mathrm{t}_0$ run (central-left panel) I increased both the density threshold for multiphase particles by a factor of ten and the SFE by a factor of three. Again, the self-regulation of the star formation model and the AGN feedback prevent any appreciable difference with respect to our fiducial run.

Increasing timescale for cold gas evaporation ($A_0\ 0.1\mathrm{x}$)

Following Springel & Hernquist (2003), even if the subgrid model is explicitly constructed to reproduce quiescent star formation, starburst should arise whenever the timescale for star formation is shorter than the timescale for the evaporation of cold gas. In fact, in this regime self-regulation is expected to break down with cold gas transformed into stars before it can be evaporated by stellar feedback. In practice, the relation that should be satisfied is:

$$\frac{t_c}{t_\star} = \left(\frac{\rho}{\rho_{\rm thr}}\right)^{4/5} \frac{1}{\beta A_0} > 1, \tag{4.4}$$

where $\rho_{\rm thr}$ is the density threshold for a particle to become multiphase, β is the fraction of stars that instantly die as supernovae, and A_0 is a parameter of the model that defines the energy of supernovae used to evaporate cold gas. In this test we reduced the value of A_0 by a factor of ten. From the results shown in the central-right panels we see no improvement in terms of starburst galaxies. Thus, even if I checked that single gas particles satisfy Eq. 4.4, this is not sufficient to have a high-enough integrated value of SFR.

Varying AGN feedback implementation (Tthr)

To quantify the effect of a specific aspect of the AGN feedback implementation on our results I also ran a simulation with the same AGN feedback prescription as that of Ragone-Figueroa et al. (2018). I recall that in that setup there is an extra condition on the temperature ($T<T_{\mathrm{thr}}$) to consider a particle as multiphase and that the energy released by AGN feedback is used to evaporate molecular clouds, while in the current implementation the energy is coupled only to the hot phase of multiphase particles. From the bottom-left panels of Figs. 4.17, 4.18, and 4.19 we can see that the only difference with respect to our fiducial run is that in this case we have less massive galaxies. This is expected from the results shown in Sects. 4.2.3 and 4.2.4, where it is clear that the feedback implementation of Ragone-Figueroa et al. (2018) is more effective in quenching star formation.

No AGN feedback (No-AGN)

Finally, I also performed a simulation without AGN feedback (bottom-right panels). This is of course to test an extreme scenario, as the absence of AGN feedback would result in GSMF, BCG masses, and SFR inconsistent with low-redshift observations. From Fig. 4.17, we see that in this run we have fewer galaxies on their way to becoming passive, and more massive galaxies, as expected. However, the MS retain the same normalisation and there is no sign of an increased fraction of starburst galaxies. Moreover, it is interesting to note that in the *No-AGN* run the SFE is higher in the low-mass regime (see Fig. 4.18). This difference is due to the fact that without AGN feedback the gas reaches higher density, especially in the low-mass regime where the feedback is more efficient in expelling gas outside the shallow potential wells of galaxies.

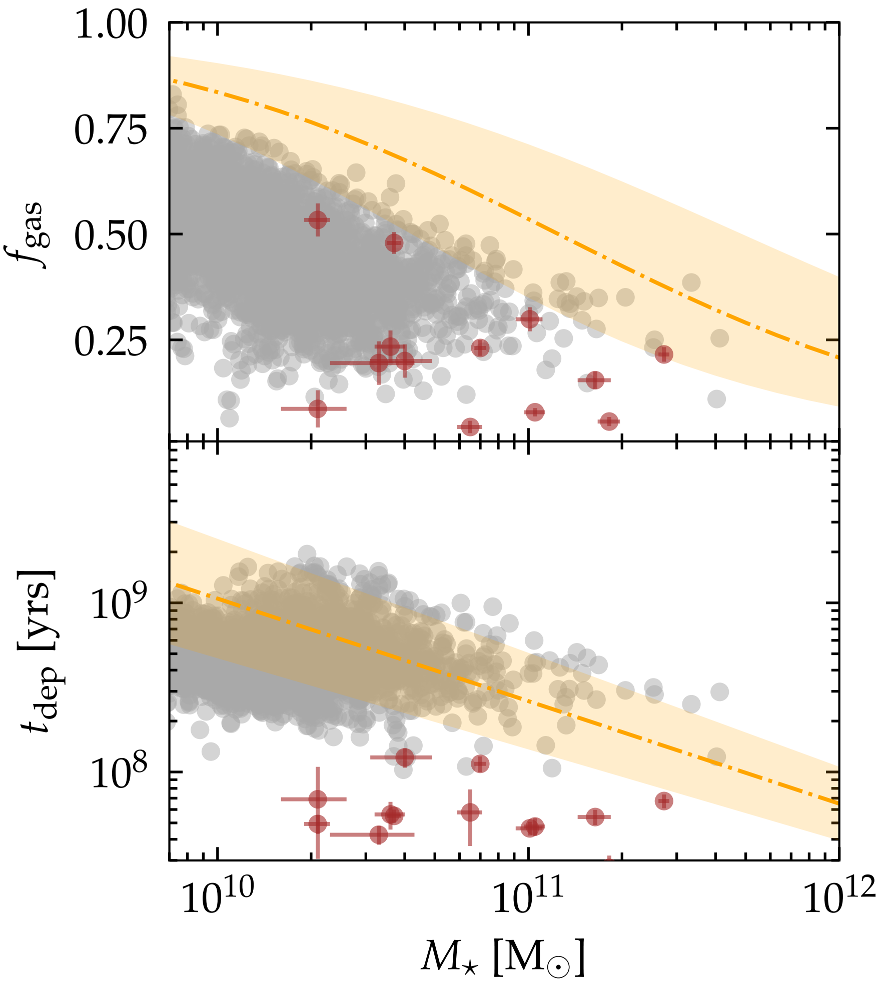

Fig. 4.15: Galaxy correlations at $z = 4.3$. *Top panel:* Gas fraction as a function of stellar mass. *Bottom panel:* Depletion time as a function of stellar mass. Grey circles refer to Dianoga simulations at z=4.3. Brown circles are data from Hill et al. (2020). The orange dashed line is the functional form of Liu et al. (2019) for MS galaxies at $z = 4.3$, while the shaded region encompass galaxies with an SFR that is four times lower and higher than MS galaxies.

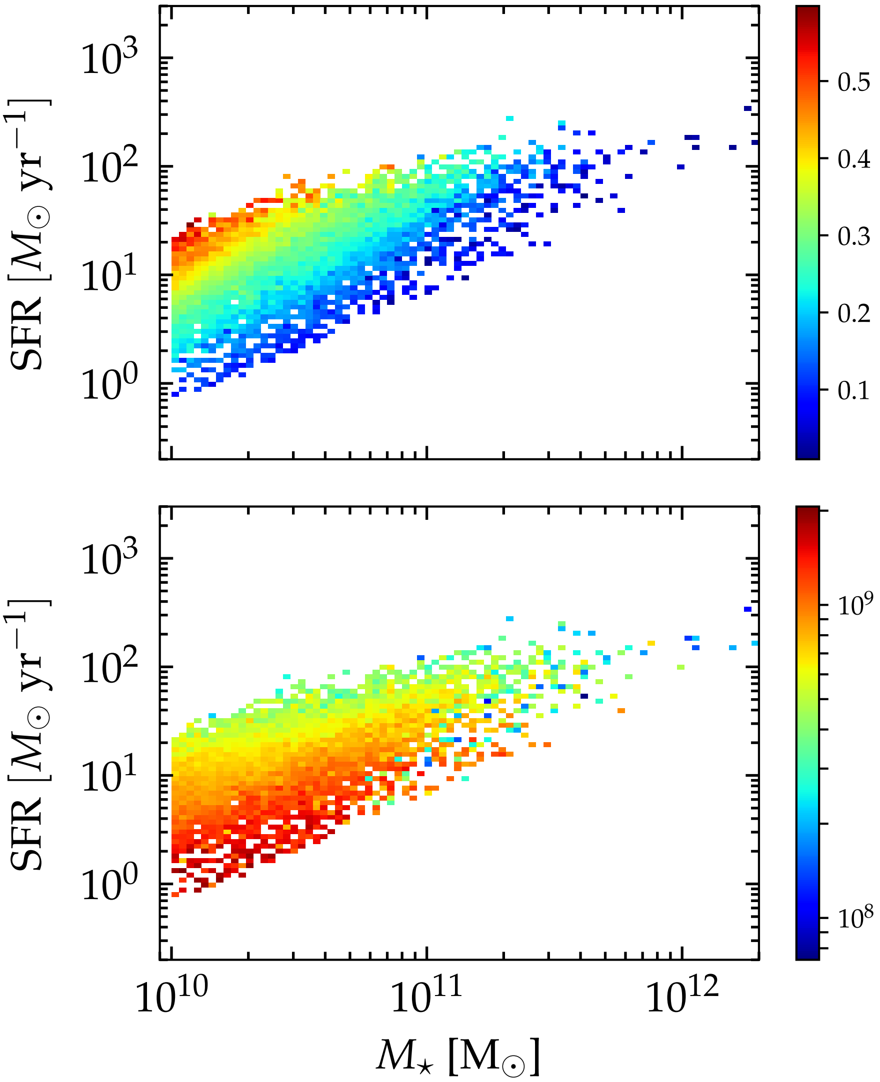

Fig. 4.16: *Top panel:* 2D histogram of MS star forming galaxies in simulations at $z = 2.3$. Each bin is colour-coded with the respective median value of f_{gas} *Bottom panel:* Same as upper panel, colour-coded with respect to t_{dep}

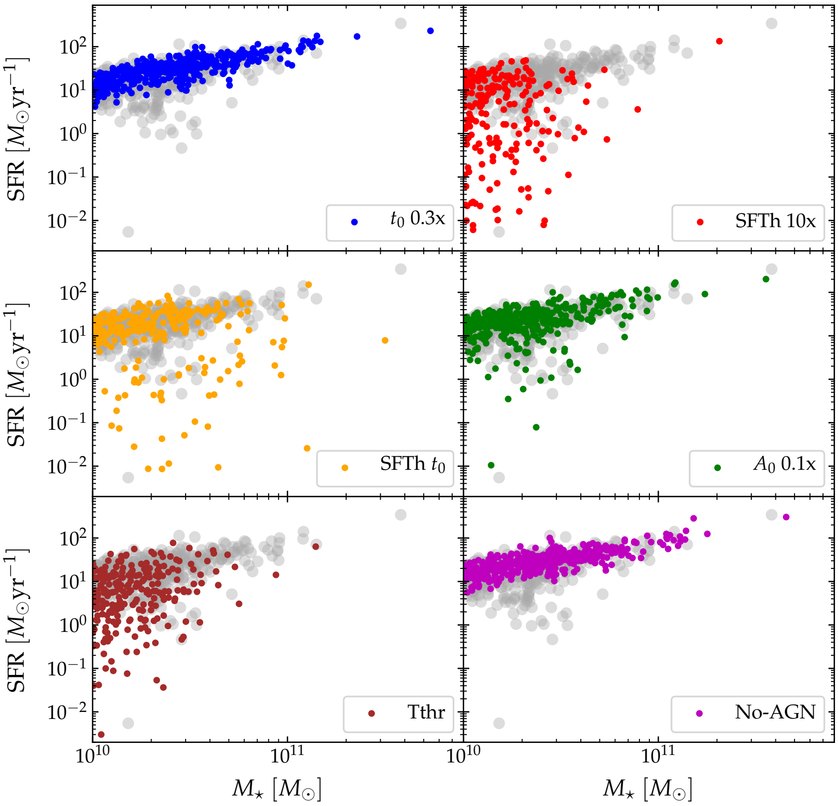

Fig. 4.17: Main sequence of star forming galaxies at $z = 3$ for different simulations. Grey points refer to the results relative to the same region used for the tests with the set up used for this work. Different panels refer to: t_0 $0.3x$: shorter timescale for star formation; *SFTh* $10x$: increased density threshold for star formation; *SFTh* t_0: increased density threshold for star formation and shorter star formation timescale; A_0 $0.1x$: reduced supernova thermal feedback; *Tthr*: AGN feedback implementation as in Ragone-Figueroa et al. (2018); *No-AGN*: no AGN feedback.

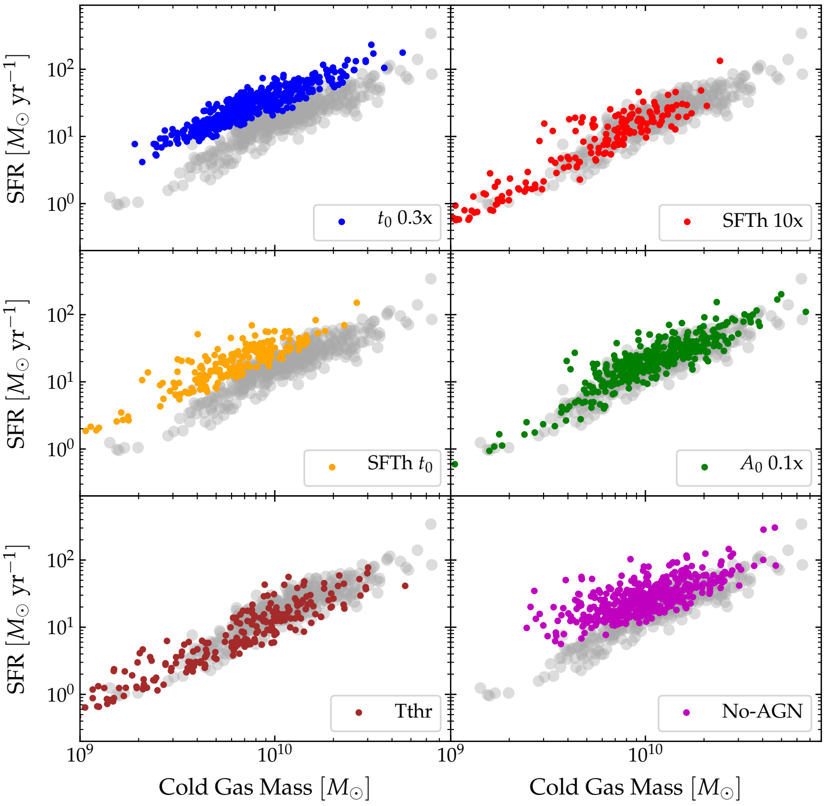

Fig. 4.18: Correlation between cold gas mass and SFR at $z = 3$ for different simulations. Grey points refer to the results relative to the same region used for the tests with the set up used for this work. Different panels refer to: t_0 $0.3x$: shorter timescale for star formation; *SFTh* $10x$: increased density threshold for star formation; *SFTh* t_0: increased density threshold for star formation and shorter star formation timescale; A_0 $0.1x$: reduced supernova thermal feedback; *Tthr*: AGN feedback implementation as in Ragone-Figueroa et al. (2018); *No-AGN*: no AGN feedback.

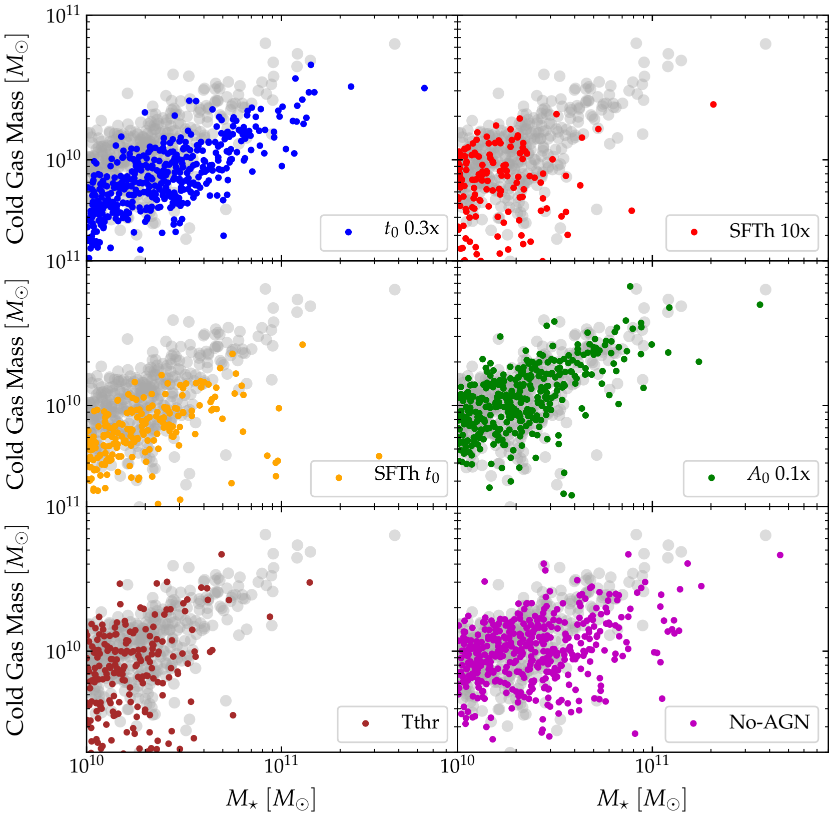

Fig. 4.19: Correlation between stellar mass and cold gas mass at $z = 3$ for different simulations. Grey points refer to the results relative to the same region used for the tests with the set up used for this work. Different panels refer to: t_0 $0.3x$: shorter timescale for star formation; *SFTh* $10x$: increased density threshold for star formation; *SFTh* t_0: increased density threshold for star formation and shorter star formation timescale; A_0 $0.1x$: reduced supernova thermal feedback; *Tthr*: AGN feedback implementation as in Ragone-Figueroa et al. (2018); *No-AGN*: no AGN feedback.

4.7 Summary

In Chapter 1 we have seen that most of the stars within galaxy clusters are produced during burst of star formation at redshift $z \gtrsim 2$. These events take place within the large number of halos which compose a protocluster region, that in turn is spread over tens of Mpc. The number of detected protocluster regions is rapidly increasing in the recent years, even though these observations largely come from highly biased detection techniques. A powerful tool to meaningfully interpret these observational data are cosmological simulations. However, before to use cosmological simulations as a predictive tool, it is important to test them against the available observational data.

For these reasons, in this Chapter I studied the SFR of simulated (proto)cluster regions and the gas properties of (proto)clusters galaxies in the redshift range $0 < z < 4$, in comparison to the available observations. The main results of this analysis can be summarized as follow:

- At $z \sim 0$ the SFR within simulated galaxy clusters is higher than observations. This is mainly driven by higher residual values of SFR within the BCGs, as the current AGN feedback model does not provide enough quenching in the highest galaxy mass regime. The parameters of the AGN feedback can be calibrated in order to obtain BCG masses that are consistent with observations. However, this result come at the price of an under-predicted normalization of the GSMF. These results highlight that with the current model of AGN feedback (Springel et al. 2005, Ragone-Figueroa et al. 2013) it is not possible to reproduce both the GSMF and $z = 0$ BCG masses.

- At $z \sim 2$ simulations under-predict the SFR of highly star forming protocluster regions by a factor of 4 or even larger, in line with the results presented in Granato et al. (2015), which were based on a larger set of lower resolution simulations. This result is indeed stable against numerical resolution and is the combination of two effects: (i) simulations under-predict the normalization of the main sequence at $2 < z < 2.5$ by a factor of 3; (ii) simulations predict a fraction of starburst galaxies (defined as galaxies with a SFR at least four times higher than main sequence galaxies) of $[0.2\% - 0.03\%]$, at least a factor of ten lower than what is found in recent observations (e.g., Schreiber et al.

2015). I verified that this result is independent from the enviroment by studying the Magneticum cosmological boxes of sizes 352 and 640 h^{-1} Mpc. The paucity of starburst galaxies is also found at $z \sim 4$. As a consequence, simulations under-predict the SFR of highly star forming protocluster regions by a factor of 4 also at this higher redshift.

- Comparison with observations suggest that simulations under-predict the gas fraction in galaxies at the peak of the cosmic star formation rate density and consequently the normalization of the main sequence. However, observations of galaxy properties in dense enviroment are not in agreement among each other and strongly depend on the assumptions made to derive the molecular gas mass. Hence, it is not clear whether simulations under reproduce starburst galaxy population because of a low gas fraction or low star formation efficiency.
- The results obtained in this Chapter indicate that the Springel & Hernquist (2003) model is suitable to reproduce the self-regulated evolution of quiescent-low redshift star formation but not violent events like high redshift starbursts. Indeed, I verified that the same results hold within a wide range of values for the model parameters and does not depend on the implementation of the AGN feedback.

Before concluding, it is important to remark that all the observations used through this Chapter can be affected by systematic errors. This is true for both the stellar mass, whose estimate relies on a number of assumptions like star formation history, the IMF, the metallicity, and the optical depth, but also for the SFR, which is usually obtained by converting the FIR and UV luminosities assuming some conversion factor which does not include any additional information about the composition of the underlying stellar populations. These assumptions limit the accuracy of stellar masses and SFRs measurements, with typical errors of ~ 0.3 dex. Moreover, fixing some of the physical parameters that are needed to derive the stellar mass and the SFR from the SED, can lead to systematic errors (e.g., Leja et al. 2019a). One example is the tension between the local cosmic stellar mass density derived from the local GSMF and the one obtained by integrating the cosmic star formation rate density, the latter being higher by ~ 0.3 dex. In this respect, Leja et al. (2019b) showed that this tension can be solved by employing a non-parametric estimate for the star formation history, which brings contemporarely to higher stellar masses and lower SFRs. If this method will be proved to be reliable, it will obviously reduce also the tension between theory and observations highlighted in Fig. 4.9, although enhancing the tensions described in Figs 4.4 and 4.3. However, systematic differences in the measured stellar masses will also affect the normalization of the GSMF (see Leja et al. 2020), on which most of the models used in cosmological simulations are tuned. Therefore, to correctly establish the effects that such systematics have on the simulated MS, it will be necessary to re-calibrate the parameters of the star formation and AGN models, which will also affect the normalization of the MS. This will need to be addressed in future works.

Chapter 5

Conclusions

This PhD thesis addresses the evolution of SMBHs and of the star formation rate within clusters of galaxies from a theoretical perspective. SMBHs at the center of galaxy clusters recently became the subject of an intense research interest, since their mass has been found to strongly correlate with a number of properties of the hosting clusters, like their mass and X-ray temperature. At the same time, the physical processes that drive these correlations are still debated. On the one side, being galaxy clusters very dynamical systems, the observed correlations can be driven by the relatively large number of mergers that are expected within these high density environments (e.g., Lakhchaura et al. 2019). On the other side, the connection can be causal, with AGN feedback playing a key role (e.g., Gaspari et al. 2019). The work presented in this thesis aim at constraining the relative importance of these processes in the growth of central SMBHs and their role in building the observed correlations. By all means, a number of circumstantial evidences point toward AGN feedback as the leading mechanism in regulating the star formation rate at least within local galaxy clusters, as a feedback process is needed to avoid strong cooling flows within clusters cores. At the same time, recent observations targeted on high redshift galaxy protoclusters, i.e. the infancy stages of cluster formation, highlight the presence of exceptionally high values of SFRs within these regions, with values reaching thousands of $M_{\odot}\ \mathrm{yr}^{-1}$, suggesting that feedback processes at high redshift have still to come into play in quenching star formation. These events might be ubiquitous in protocluster history and are currently associated with the formation time of the massive ellipticals which are observed in local galaxy clusters. A theoretical description of these bursts of star formation would be extremely important in order to predict the incidence of these events and to characterize the star formation history of galaxy clusters. Therefore, in this Thesis I also compare the prediction of theoretical models regarding the star formation rate in protocluster regions in the redshift range $2 < z < 4$, comparing them with recent observational results.

The most advanced theoretical tool to tackle the aforementioned problems are cosmological hydrodynamical simulations. In particular, in this thesis I used a set of 29 zoom-in cosmological simulations centred on the 24 most massive clusters extracted from a cosmological box of 1 Gpc side, together with 5 randomly chosen smaller objects (see Sect. 2.5). The simulations are run with the GADGET3 code, a developer version of the public code GADGET2, and include a set of sub-resolution models to effectively describe baryonic physics. These models include metal-dependent radiative cooling, star formation and associated feedback, metal enrichment and chemical evolution, and AGN feedback.

The possible symbiotic growth of central SMBHs and hosting clusters has been studied through the evolution of single systems upon the $M_{\rm BH} - M_{500}$ plane. This analysis, summarized in Fig. 3.7, showed that the evolution of the systems can be divided into two phases. At $z \gtrsim 2$ the SMBHs growth is dominated by the rapid accretion of cold gas, which eventually leads to a strong AGN feedback and consequent expulsion of the remaining gas from the shallow potential well of the proto-cluster. At the end of this phase, the systems already lie upon the $M_{\rm BH} - M_{500}$ relation. Subsequent evolution is then driven by cluster mergers, which cause an increment of the cluster mass, and feed the central SMBHs by inducing BH-BH mergers. This is clear from Fig. 3.12, which shows the evolution of SMBH mass divided into the two growth channels: gas accretion and BH-BH mergers. From this figure it is evident that at $z < 1$ gas accretion proceeds in a more gentle and self-regulated fashion and the mass growth is largely dominated by BH-BH mergers, which at $z = 0$ comprise $\sim 60\%$ of the total SMBHs mass. Given the results obtained, and in particular considering that the correlations are already in place when the mass gained through mergers is negligible, our simulations suggest a causal origin to the correlations between SMBHs and hosting clusters, mediated through AGN feedback.

At the same time, caution has to be applied in interpreting these results, since simulations are affected by limitations. For what concern the physics related to SMBHs, and similarly to all other physical processes not resolved by cosmological simulations, we have to remind that their description is not numerically described and resolved from first principles, but relies on phenomenological sub-resolution models, which are usually described through a suitable parametrization of such processes. As such, these models depend on parameters which are generally tuned to reproduce low redshift observational constraints. Even though low redshift results agree well with observations, this does not necessarily imply that the time evolution is realistically described. Finally, it is also important to keep in mind that the large majority of the sub-resolution models used in cosmological simulations by definition do not provide numerically converged results. This means that as resolution increases, models parameters need to be re-tuned. Again, this does not directly imply that the full evolutionary history will be the same, and some resolution-related differences might be expected.

As for the effects of the resolution on the AGN feedback model implemented in GADGET3, I recall that with the current sub-resolution model implementation both the feeding and feedback processes are related to the distribution of gas particles within a region of tens of kpc, e.g. on galactic scales. This is likely the reason why the scatter around the Magorrian correlation is under-reproduced within our simulations (see Figs. 3.1 and 4.1). Increasing the resolution will affect the region of space at which both the feeding and feedback processes operate, likely affecting the actual level and timing of gas accretion. Future studies, based on higher numerical resolutions, will help to quantify these effects. Moreover, I also showed that with the current implementation of the AGN feedback we can not reproduce the low values of SFR which are observed in local massive BCGs ($\sim 0.1\ \mathrm{M}_\odot\ \mathrm{yr}^{-1}$), which in simulations are over-predicted by a factor of ~ 30 (see Figs. 4.4 and 4.5). Similarly, we have also seen that in this framework it seems unfeasible to reproduce both the correct normalization of the galaxy stellar mass function and realistic BCG masses (see discussion in Sect. 4.2.4). Therefore, a theoretical effort to produce a better modelization for AGN feedback is needed. This result will be likely possible by exploiting the capability of zoom-in simulations on galactic scales, suited to resolve the multiphase structure of the interstellar medium and the related physical processes operating on pc scales. These simulations can then be used to develop effective models for lower-resolution cosmological simulations (e.g., Gaspari & Sadowski 2017).

Constraints on the origin of the observed correlations can also be placed by quantifying the number of mergers that simulated SMBHs undergo during cosmic time. This analysis, presented in Sect. 3.4.8, highlighted that only SMBHs with $M_{\rm BH} > 10^9~{\rm M}_\odot$ undergo more that 3 major mergers, thus disfavouring once again a non-causal origin to the observed correlations. This result is strengthen by the necessarely simplified description of BH-BH mergers adopted in our simulations, since the results obtained has to be considered as upper-limits. Indeed, I recall that in our simulations two SMBHs are forced to merge whenever their distance is $\lesssim 10$ kpc, thus whenever a merger between galaxies occurs. At the same time, the results might depend on the timing of the seeding, which is in turn determined by the resolution of the simulation. For the simulations used for this analysis, a seed of $\sim 10^5~{\rm M}_\odot$ is spawned at the center of each FoF group having a mass $\gtrsim 10^{12}~{\rm M}_\odot$. This threshold scales with the mass resolution of the simulation, meaning that at higher resolution BH seeds are spawned at higher redshift within lower massive halos, likely enhancing the number of mergers that BH particles experience at high redshift. Finally, it is important to remark that modern cosmological simulations do not have reached a high enough resolution to resolve the processes of dynamical friction that enables merging SMBHs to approach each other from $\sim {\rm kpc}$ to $\sim {\rm pc}$ scales. This process, which in simulations is instantaneous, can take several Gyrs. At pc scales, other processes take place, like stellar hardening, e.g. three body encounters between SMBH binary and individual stars. If this process is efficient enough to bring SMBHs at a distance of $\sim 10^{-2} - 10^{-3}~{\rm pc}$, the emission of gravitational waves will eventually enable the merger between the two SMBHs. As such, the theoretical predictions on the number of mergers experienced by SMBHs are very uncertain, depending on a number of physical processes operating at different scales. Eventually, it will be possible to place constraints on the merger rates between SMBHs by exploiting the emission of gravitational waves. This observational probe will be only possible with instruments like LISA, whose launch is planned in 2034. The merger rates measured by LISA will place constraints on the mechanism of formation of the first intermediate-mass BHs, and on the dynamical and environmental processes which determine their coalescence.

Even though the sSFR within simulated central galaxies at $z = 0$ exceeds the values derived from observations, the situation is reversed at $z > 2$ (see Fig. 4.12). In particular, in Chapter 4 I showed how numerical simulations struggle to reproduce the high values of SFR which are observed within protocluster regions at $z \gtrsim 2$ (see Figs 4.6, 4.7, 4.10). Interestingly, these differences are related to a general difficulty for theoretical models to reproduce star formation properties of galaxies at these redshifts, regardless of their environment. Indeed, in Fig. 4.16 I showed how most (if not all) cosmological simulations under-predict the normalization of the main sequence at $z \sim 2$. Furthermore, the distribution of SFR values at fixed stellar mass around the main sequence is well fitted by a single Gaussian, meaning that in cosmological simulations the population of starburst galaxies is largely missed. Interestingly, these results do not depend on the particular implementation of the AGN model, nor on the star formation sub-resolution model parameters, hinting that these limits are intrinsic of the sub-resolution model for star formation (i.e., Springel & Hernquist 2003). The capability to reproduce these high values of star formation rates will be an important task for future developments of the sub-resolution models for star formation implemented in cosmological simulations.

In this respect, future surveys will be extremely valuable to better understand the physical properties of highly star forming galaxies (and of high redshift galaxies in general). For example, observations at radio wavelength with instruments like SKA (and its precursors) will enable to obtain information on the atomic gas content of high redshift galaxies through observations of the 21-centimetre radiation. Moreover, the future installation of ALMA bands 1 and 2 will enable to observe the CO(1-0) line transition at high redshift, needed to limit the uncertainties affecting the measures of molecular gas masses. Indeed, the currently implemented ALMA bands can only target higher-J transition lines, inevitably introducing uncertainty on the derived molecular gas mass due to unknown gas excitation. The information gathered with these instruments will enable to place better constraints on gas-related properties of high redshift galaxies, such as gas fractions, star formation efficiencies, and atomic and molecular mass functions. These observables will be of key importance in constraining feedback processes in current theoretical models.

In the framework of galaxy clusters, during the last years an increasing number of observations shed light on the relationship between over-densities of dusty star forming galaxies and sub-millimetre galaxies to protocluster regions. At the same time, these results have been mostly obtained from observations targeted in the FIR and sub-millimetre wavelengths, and thus are biased toward the highest values of SFRs. In this respect, a better modelization of high redshift galaxy star formation properties would greatly improve the predictive power of cosmological hydrodynamical simulations, enabling to predict the incidence of these bursts of star formation within protocluster regions and to realistically describe the star formation history of protoclusters in general. Concurrently, a better understanding of the evolution of galaxy clusters will also come from future observations, as missions like Euclid will open up the discovery space, finding a large number of high-redshift clusters and proto-clusters. Subsequent followup with instruments aimed at different wavelengths toward this large and homogeneous sample of systems will realistically enable to draw the evolutionary pattern of the most massive objects in the universe.

Appendices

Appendix A

ΛCDM cosmological model

I this Appendix I review the main equations of the standard model of cosmology that have been used in this thesis.

A.1 Space-time metric

Observations of the CMB tell us that the early universe was nearly isotropic. Assuming that we do not occupy any particular place in the universe, this isotropy also imply homogeneity. These properties are also valid in the local universe, if the density field is smoothed over scales larger than $\sim 100\ \mathrm{Mpc}$. This evidence is known as the cosmological principle, stating that the universe is isotropic and homogeneous if observed over scales large enough. Starting from these symmetries, it is possible to write the metric that describes space-time as

$$ds^2 = c^2 dt^2 - a(t)^2 \left[\frac{dr^2}{1 - kr^2} + r^2 (d\theta^2 + \sin^2\theta d\phi^2) \right] , \tag{A.1}$$

where t is the temporal coordinate, and r, θ, and ϕ are the radial and angular coordinates. The constant k defines the geometry of the spacetime, with observations suggesting $k = 0$, i.e. a flat geometry (e.g., Planck Collaboration et al. 2018b). The factor $a(t)$ is commonly defined as the scale factor and determines how the proper (or physical) distance between two cosmological objects changes with time. From the expression of the metric it easy to recover few important results. Let's consider, for example, the proper distance between two galaxies at fixed time t in a flat geometry: $d_{\rm prop} = a(t)r$. Differentiating with respect to time brings:

$$\frac{{\rm d}d_{\rm prop}}{{\rm d}t} = v_{\rm prop} = \dot{a}(t)r = \frac{\dot{a}(t)}{a(t)}a(t)r = H(t)d_{\rm prop}. \tag{A.2}$$

$H(t)$ is the Hubble parameter and Eq. A.2 is now referred as the Hubble-Lemaitre law (Hubble, 1929). The latest data released by Planck (Planck Collaboration et al., 2018b) fixes $H(t=0) = H_0 = 67.4 \pm 0.5$ km/s/Mpc. It is also useful to express the Hubble parameter by means of a dimensionless parameter, h, such that different values of H_0 for different cosmological models will be encodend in h: $H_0 = 100\ h$ km/s/Mpc. The second result that can be recovered regards electromagnetic radiation. Given that the scale factor evolves with time, the wavelength of a given radiation will evolve with it. In particular, if the universe expands the wavelength will increase as a consequence of the expansion, following the relation: $\lambda_e/\lambda_o = a(t_e)/a(t_o)$, where t_e and t_o are the emission and observation times and λ_e and λ_o the relative wavelengths at the respective times. Hence it is possible to define a cosmological redshift as:

$$z = \frac{\lambda_o - \lambda_e}{\lambda_e} = \frac{1-a}{a}, \tag{A.3}$$

where $t_o = t_0 =$ present time and the normalization $a(t_0) = 1$ is assumed. Therefore, in an expanding universe, radiation will be stretched to longer wavelengths as the universe evolves.

Given the metric Eq. A.1, the evolution of the universe is determined by the evolution of the parameter $a(t)$. To describe its dynamics, it is necessary to define an underlying theory of gravity. Using the Einstein's equations of general relativity, the expressions which describe the time evolution of the scale factor are the Friedmann equations, that can be written in the form:

$$\left(\frac{\dot{a}}{a}\right)^2 = H^2 = \frac{8\pi G}{3}\rho - \frac{kc^2}{a^2} + \frac{\Lambda c^2}{3}, \tag{A.4}$$

$$\frac{\ddot{a}}{a} = -\frac{4\pi G}{3}\left(\rho + \frac{3p}{c^2}\right) + \frac{\Lambda c^2}{3}, \tag{A.5}$$

where ρc^2 is the mean energy density of the universe, p its pressure, and Λ the so called cosmological constant. From Eq. A.5 it is clear the effect of the presence of a positive cosmological constant, which leads to an acceleration of the expansion of the universe. Indeed, the effect of the cosmological constant can be accounted defining an effective density, $\tilde{\rho} = \rho + \Lambda c^2/8\pi G$ and an associated effective pressure, $\tilde{p} = p - \Lambda c^2/8\pi G$. The pressure associated to the cosmological constant is negative, as acting to accelerate the expansion of the universe. Another useful parameter that can be derived directly for Eq. A.4 is the critical density, i.e. the density at which the curvature of the universe is 0:

$$\tilde{\rho}_{\rm cri} = \frac{3H^2}{8\pi G}. \tag{A.6}$$

This definition is a useful metric of comparison, and often used to define the mass of galaxy clusters (see Sect. A.3).

From Eq. A.4 and Eq. A.5 it is clear that the evolution of the scale parameter is driven by the energy content of the universe. As this is contributed by matter (ρ_M), radiation (ρ_γ), and by the cosmological constant (ρ_Λ), it is essential to derive the time evolution of all these components. Assuming mass conservation, the matter density will evolve as an inverse of a volume. Given that the volume scales as $V \propto a^3$, the matter density will scale as $\rho_M = \rho_{M,0} a^{-3}$, where $\rho_{M,0}$ is the matter density as measured today. To compute the evolution of the radiation energy density, it has to be taken into account that beside the volume evolution, all wavelengths are stretched by a factor a in an expanding universe (see Eq. A.3). Therefore, $\rho_\gamma = \rho_{\gamma,0} a^{-4}$. Finally, the energy density related to the cosmological constant does not depends on the scale factor. Defining, as it is usually done, $\Omega_X = \rho_{X,0}/\rho_{\rm crit,0}$, the evolution of the Hubble parameter in a flat universe will be given by:

$$H^2 = H_0^2 \left[\Omega_M (1+z)^3 + \Omega_\gamma (1+z)^4 + \Omega_\Lambda\right] = H_0^2 E(z)^2, \tag{A.7}$$

where H_0 is the Hubble constant today.

A.2 Linear evolution theory

If the universe was fully described by the metric defined in Eq. A.1 there would not be galaxies or galaxy clusters, being the universe homogeneous at every scale. However, on small scales, the early universe was characterized by small fluctuations in the density field, as observations of the CMB show. Perturbations in the density field can be described by the density contrast, defined as $\delta\rho(\bar{x}) = (\rho(\bar{x}) - \bar{\rho}_m)/\bar{\rho}_m$, where $\bar{\rho}_m$ is the mean matter density at a given time. In general, it is easier to define quantities in the momentum space and consider the Fourier transform of $\delta\rho(\bar{x})$: $\delta(\bar{k})$. Assuming that the density contrast is an isotropic and homogeneous Gaussian random field, its statistic is fully described by its second moment, the power spectrum $P(k)$. The probability distribution for a given $\delta(\bar{k})$ is given by:

$$\mathrm{Prob}\left[\delta(\bar{k})\right] = \frac{1}{\sqrt{2\pi}P(k)}\exp\left(-\frac{\delta^2(\bar{k})}{2P(k)}\right), \tag{A.8}$$

where the interpretation of the power spectrum as the variance of the density contrast distribution is explicit. Therefore, to fully describe the statistical properties of the density field at each time it is necessary to define the initial power spectrum at early times, right after the inflationary stage, and its evolution. The initial conditions are usually considered to be a power law:

$$P(k) = A_s k^{n_s}, \tag{A.9}$$

while its evolution at each scale can be only computed by means of numerical methods, like cosmological simulations. However, a linear approximation can be used to derive the main results. In the linear regime, each $\delta(\bar{k})$ evolves independently from the other wave vectors as

$$\delta(\bar{k}, t_0) = D_+(t) \times T(k) \times \delta(\bar{k}, t_i), \tag{A.10}$$

where T(k) is the so called transfer function

$$T(k) = \text{constant} \times \begin{cases} 1, & k < k_{\text{eq}} \\ k^{-2}, & k > k_{\text{eq}} \end{cases} \tag{A.11}$$

being k_{eq} the wave vector corresponding to the size of the horizon at matter-radiation equality. This factor takes in consideration that perturbations of different sizes evolve differently in the range of time between the end of inflation and recombination, depending if they enter the horizon before or after matter-radiation equality. $D_+(a)$ is the linear growth factor, normalized to 1 at $a = 1$, and is given by

$$D_+(a) = \frac{5\Omega_M}{2}E(a)\int_0^a \frac{da'}{[a'E(a')]^3}. \tag{A.12}$$

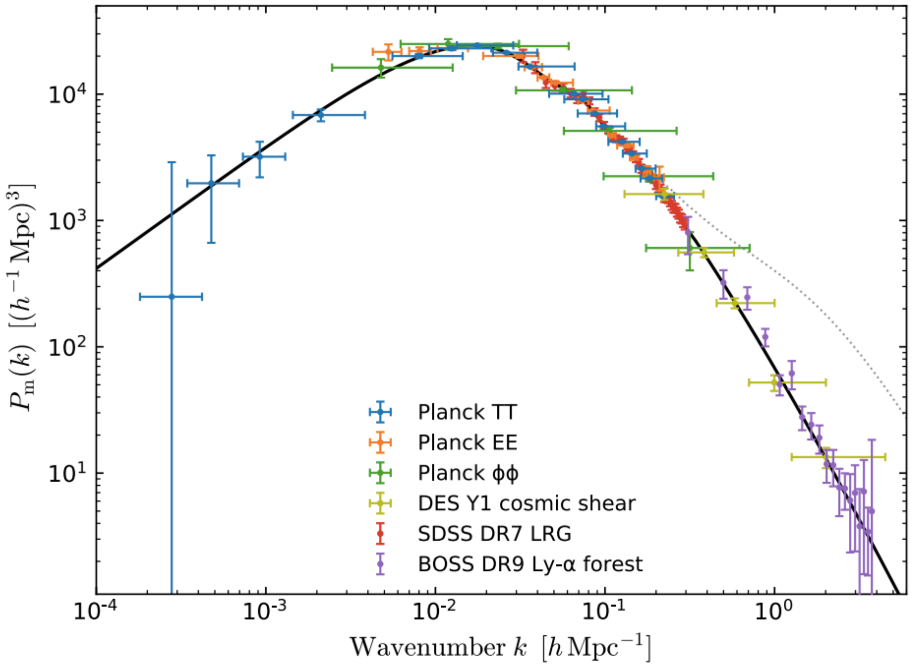

Fig. A.1: The observed matter power spectrum. Black line is the theoretical prediction, while colored points are data from different cosmological probes. Dashed line is deviation from the linear evolution from non linear clustering at small scales. Credits: Planck Collaboration et al. (2018a).

Therefore, the power spectrum at any time can be written as

$$P(k, t_0) = D_+(t)^2 T^2(k) P(k, t_i), \tag{A.13}$$

and $P(k, t_i)$ can be taken in the form given by Eq. A.9. The resulting power spectrum today will be then

$$P(k) \sim \begin{cases} k^{n_s}, & k < k_{\rm eq} \\ k^{n_s - 4}, & k > k_{\rm eq} \end{cases}, \tag{A.14}$$

with the turnover near $k = k_{\rm eq} \approx 0.01\ {\rm Mpc}^{-1}$. In Fig. A.1 it is shown the matter power spectrum as measured by different probes. The agreement between the model (black line) and the data is evident, and the two power-laws are clearly visible with a turnover around $k \sim 10^{-2} h\ {\rm Mpc}^{-1}$. From CMB data it is also possible to measure the value of the spectral index n_s, which recent data fix to $n_s = 0.965 \pm 0.004$ (Planck Collaboration et al., 2018b).

Another important quantity related to the density contrast is the density contrast smoothed over some scale R, $\delta(\bar{x}, R) = \int d^3x' W(\bar{x} - \bar{x}', R)\delta(\bar{x}')$. This is important, as the density contrast can be easily defined mathematically in each point of space, but from an observational point of view it is necessary to smooth over a given volume. $W(\bar{x}, R)$ is called window function and can be chosen in a somewhat arbitrarily way as a spherical top-hat, Gaussian, or related functions. To a given scale R it is always possible to associate a mass M, and the two will be interchangeable. Indeed, using a top hat window function it is possible to define

$$\bar{M}(R) = \int d^3x \; W(\bar{x}, R)\bar{\rho}_m = \frac{4\pi R^3}{3}\bar{\rho}_m, \tag{A.15}$$

where $\bar{\rho}_m$ is the average matter density. The smoothed mass distribution is then related to the smoothed density contrast by

$$M(\bar{x}, R) = \bar{M}(R)(1 + \delta(\bar{x}, R)), \tag{A.16}$$

and it is possible to interpret the smoothed density contrast as

$$\delta(\bar{x}, R) = \delta M(\bar{x}, R). \tag{A.17}$$

Finally the smoothed mass distribution can be espressed as a function of the power spectrum as

$$\sigma^2(M) = \langle \delta^2(\bar{x}, R) \rangle = \frac{1}{(2\pi)^3} \int d^3k \; \tilde{W}^2(kR)P(k), \tag{A.18}$$

where $\tilde{W}(kR)$ is the Fourier transform of the window function. Assuming again a power spectrum as defined in Eq. A.9, it is possible to derive

$$\sigma^2(M) \sim \frac{1}{M^{(n_s+3)/3}}. \tag{A.19}$$

Therefore, the variance is larger at smaller masses, leading to the expectation of a hierarchical universe where smaller structures are expected to collapse earlier on average. A parameter of the standard ΛCDM cosmology is the variance $\sigma^2(R)$ computed considering a top hat window function and a scale radius $R = 8h^{-1}$ Mpc, usually defined as σ_8. High value of σ_8 means high variance and thus structures begin to collapse earlier. Recent observations fix the value of this parameter to $\sigma_8 = 0.811 \pm 0.006$ (Planck Collaboration et al., 2018b).

Even though the linear approximation leads to important results, it cannot be used to derive the clustering properties that we observe in the local universe. In fact, when the amplitude of density contrast fluctuations reach unity, i.e. $\sigma^2(M) \sim 1$, the linear approximation breaks down. Further evolution must be studied by means of more sophisticated (but still approximated) theoretical models, or by means of numerical simulations. In the following section I describe the spherical collapse model, one of the simplest, and yet very instructive, model for non linear evolution.

A.3 Spherical collapse model

The simplest scenario is described by a spherically simmetric perturbation with constant density evolved in an Einstein-De Sitter universe with $\Omega_\Lambda = 0$. The dynamics of the problem is fully described by the evolution of the radius of the over-density, R, and thus it reduces to a $1D$ problem. The dynamics is characterized by a first phase of expansion, where $R(t)$ increases at a smaller rate than the cosmic expansion, causing an increasing of the initial over-density as predicted from Eq.A.12. At the turnaround time, t_{ta}, the evolution of the over-density detaches from the cosmic flow, and $R(t)$ decreases until virialization is reached at t_{coll}. The solution is described by means of the virial theorem, and here I just highlight the main results.

First, we notice that at t_{ta} the total energy is equal to the gravitational energy $E = -3GM^2/(5R_{ta})$. At the time of collapse, assuming that the system is virialized, it follows from the virial theorem that $E = E_p/2 = -3GM^2/(10R_{coll})$. From energy conservation it then follows that $R_{ta} = 2 \times R_{coll}$. Moreover, the ratio between the density of the collapsed object and the average cosmic density can be computed considering that the time interval $t_{coll} - t_{\mathrm{ta}} = t_{\mathrm{ta}}$ is equal to the free-fall time $t_{ff} = \sqrt{3\pi/(32G\rho_{ta})}$. This last relation can be inverted to derive the density at the time of the turn-around $\rho_{ta} = 3\pi/(32Gt_{ta}^2)$. Given that $R_{ta} = 2 \times R_{coll}$, it is also possible to compute the density at the time of collapse $\rho_{coll} = 8\rho_{ta} = 3\pi/(4Gt_{ta}^2) = 3\pi/(Gt_{coll}^2)$. In an Einstein-de-Sitter universe with $\Omega_\Lambda = 0$ the background density evolves as $\bar{\rho}_m = 1/(6\pi Gt^2)$. The density contrast at the time of virialization will then be:

$$\Delta = \frac{\rho_{coll}}{\bar{\rho}} = 18\pi^2 = 177.653. \tag{A.20}$$

The density contrast at the time of virialization for different cosmologies can be computed by estimating ρ_{coll} and $\bar{\rho}(t_{coll})$. For the particular case of the cosmological model used for our cosmological simulations (Komatsu et al. 2011), $\Delta = 98$.

This is an important and usefull quantity. Indeed, both in observations and theorical works, such as numerical simulations, cluster of galaxies are defined as regions of space with an average density Δ times the average (or sometimes critical) density of the universe.

Acknowledgements

Il primo sentito ringraziamento va verso i miei supervisors, Stefano ed Elena. Mi avete guidato durante questo dottorato, insegnandomi il mestiere del ricercatore. Siete stati tutto ciò che uno studente possa chiedere, e avete avuto l'incredibile capacità di farmi credere in quello che stavo facendo, quando ero io il primo a dubitarne.

Grazie a tutti i ragazzi della villa, con cui ho condiviso la vita accademica. Grazie ai cavalieri dell'ufficio rotondo. Avete reso l'ufficio un posto piacevole in cui passare le mie giornate. Grazie a voi passerò il resto della mia vita incapace di mantenere un briciolo di serietà ad ogni pubblicità di Giorgio Mastrota, o a qualunque sugo a base di acciughe (preferibilmente salate).

Grazie a tutti i Gufi. Grazie per tutte le giornate insieme. Se di questi tre anni porto via innumerevoli ricordi felici, è soprattutto grazie a voi. Un grazie particolare lo dedico a Melun Cobo. Oltre alle uscite, alle arate a Fifa, le partite a burraco, IMGU (e chissà quant'altro), le discussioni di astro(fisica?) con te hanno riacceso l'entusiasmo per la scienza che avevo perso per strada, e di questo non potrò mai ringraziarti abbastanza.

Ringrazio la mia famiglia. Grazie al vostro supporto incondizionato, la vostra fiducia nelle mie capacità mi ha sempre sostenuto in tutti i momenti in cui non mi sono sentito all'altezza della situazione.

And last, but not least, Lauras! Tra una ciambella a Toronto e una fetta biscottata a colazione con i Pinguini di sottofondo, in questi tre anni sei sempre stata al mio fianco. Con i tuoi piedoni da Hobbit ben piantati a terra, sei stata la colonna che mi ha sostenuto in tutti i momenti difficili. Per quanto questa avventura sia giunta al termine, la nostra è soltanto all'inizio, no mqyestion about it!

List of Figures

References

Allen S. W., Fabian A. C., Johnstone R. M., Arnaud K. A., Nulsen P. E. J., 2001, MNRAS, 322, 589

Allen S. W., Evrard A. E., Mantz A. B., 2011, ARA&A, 49, 409

Andreon S., Newman A. B., Trinchieri G., Raichoor A., Ellis R. S., Treu T., 2014, A&A, 565, A120

Ansarifard S., et al., 2020, A&A, 634, A113

Bahé Y. M., et al., 2017, MNRAS, 470, 4186

Balogh M. L., Baldry I. K., Nichol R., Miller C., Bower R., Glazebrook K., 2004, ApJ, 615, L101

Barnes J., Hut P., 1986, Nature, 324, 446

Bassini L., et al., 2019, A&A, 630, A144

Bassini L., et al., 2020, arXiv e-prints, p. arXiv:2006.13951

Beck A. M., et al., 2016, MNRAS, 455, 2110

Bell E. F., 2003, ApJ, 586, 794

Bell E. F., McIntosh D. H., Katz N., Weinberg M. D., 2003, ApJS, 149, 289

Bell E. F., et al., 2004, ApJ, 608, 752

Bernardeau F., Colombi S., Gaztañaga E., Scoccimarro R., 2002, Phys. Rep., 367, 1

Bernardi M., Meert A., Sheth R. K., Vikram V., Huertas-Company M., Mei S., Shankar F., 2013, MNRAS, 436, 697

Bernardi M., Meert A., Sheth R. K., Fischer J. L., Huertas-Company M., Maraston C., Shankar F., Vikram V., 2017, MNRAS, 467, 2217

Best P. N., Longair M. S., Roettgering H. J. A., 1998, MNRAS, 295, 549

Best P. N., von der Linden A., Kauffmann G., Heckman T. M., Kaiser C. R., 2007, MNRAS, 379, 894

Béthermin M., et al., 2015, A&A, 573, A113

Biffi V., et al., 2017, MNRAS, 468, 531

Biffi V., Planelles S., Borgani S., Rasia E., Murante G., Fabjan D., Gaspari M., 2018, MNRAS, 476, 2689

Birkinshaw M., 1999, Phys. Rep., 310, 97

Birkinshaw M., Gull S. F., Hardebeck H., 1984, Nature, 309, 34

Bîrzan L., Rafferty D. A., Nulsen P. E. J., McNamara B. R., Röttgering H. J. A., Wise M. W., Mittal R., 2012, MNRAS, 427, 3468

Bleem L. E., et al., 2015, ApJS, 216, 27

Bogdán Á., Lovisari L., Volonteri M., Dubois Y., 2018, ApJ, 852, 131

Boldt E., McDonald F. B., Riegler G., Serlemitsos P., 1966, Phys. Rev. Lett., 17, 447

Bonafede A., Dolag K., Stasyszyn F., Murante G., Borgani S., 2011, MNRAS, 418, 2234

Bondi H., 1952, MNRAS, 112, 195

Bouchet F. R., Colombi S., Hivon E., Juszkiewicz R., 1995, A&A, 296, 575

Brodwin M., et al., 2013, ApJ, 779, 138

Brough S., Couch W. J., Collins C. A., Jarrett T., Burke D. J., Mann R. G., 2008, MNRAS, 385, L103

Bryan G. L., et al., 2014, ApJS, 211, 19

Bussmann R. S., et al., 2015, ApJ, 812, 43

Carlstrom J. E., Holder G. P., Reese E. D., 2002, ARA&A, 40, 643

Casey C. M., Narayanan D., Cooray A., 2014, Phys. Rep., 541, 45

Chabrier G., 2003, PASP, 115, 763

Chapman S. C., Casey C. M., 2009, MNRAS, 398, 1615

Chiang Y.-K., Overzier R., Gebhardt K., 2013, ApJ, 779, 127

Chiang Y.-K., Overzier R. A., Gebhardt K., Henriques B., 2017, ApJ, 844, L23

Churazov E., Sazonov S., Sunyaev R., Forman W., Jones C., Böhringer H., 2005, MNRAS, 363, L91

Cimatti A., et al., 2008, A&A, 482, 21

Clements D. L., et al., 2014, MNRAS, 439, 1193

Cluver M. E., et al., 2014, ApJ, 782, 90

Collet C., et al., 2015, A&A, 579, A89

Conroy C., Graves G. J., van Dokkum P. G., 2014, ApJ, 780, 33

Contini E., De Lucia G., Villalobos Á., Borgani S., 2014, MNRAS, 437, 3787

Contini E., De Lucia G., Hatch N., Borgani S., Kang X., 2016, MNRAS, 456, 1924

Coogan R. T., et al., 2018, MNRAS, 479, 703

Cooke E. A., et al., 2016, ApJ, 816, 83

Cooke E. A., Smail I., Stach S. M., Swinbank A. M., Bower R. G., Chen C.-C., Koyama Y., Thomson A. P., 2019, MNRAS, 486, 3047

Couchman H. M. P., 1991, ApJ, 368, L23

Cowie L. L., Barger A. J., Fomalont E. B., Capak P., 2004, ApJ, 603, L69

Daddi E., et al., 2010, ApJ, 714, L118

Dannerbauer H., et al., 2014, A&A, 570, A55

Davé R., Thompson R., Hopkins P. F., 2016, MNRAS, 462, 3265

Davé R., Anglés-Alcázar D., Narayanan D., Li Q., Rafieferantsoa M. H., Appleby S., 2019, MNRAS, 486, 2827

Davies J. J., Crain R. A., Oppenheimer B. D., Schaye J., 2019, MNRAS, p. 2797

De Lucia G., Blaizot J., 2007, MNRAS, 375, 2

DeMaio T., Gonzalez A. H., Zabludoff A., Zaritsky D., Connor T., Donahue M., Mulchaey J. S., 2018, MNRAS, 474, 3009

Dolag K., Borgani S., Schindler S., Diaferio A., Bykov A. M., 2008, Space Sci. Rev., 134, 229

Dolag K., Borgani S., Murante G., Springel V., 2009, MNRAS, 399, 497

Dolag K., Murante G., Borgani S., 2010, MNRAS, 405, 1544

Domínguez-Tenreiro R., Obreja A., Granato G. L., Schurer A., Alpresa P., Silva L., Brook C. B., Serna A., 2014, MNRAS, 439, 3868

Donnari M., et al., 2019, MNRAS, 489, 3036

Dubois Y., Volonteri M., Silk J., 2014, MNRAS, 440, 1590

Eckert D., et al., 2016, A&A, 592, A12

Fabian A. C., 2012, ARA&A, 50, 455

Felten J. E., Gould R. J., Stein W. A., Woolf N. J., 1966, ApJ, 146, 955

Ferrarese L., 2002, ApJ, 578, 90

Ferrarese L., Ford H., 2005, Space Sci. Rev., 116, 523

Ferrarese L., Merritt D., 2000, ApJ, 539, L9

Fraser-McKelvie A., Brown M. J. I., Pimbblet K. A., 2014, MNRAS, 444, L63

Frenk C. S., et al., 1999, ApJ, 525, 554

Fu H., et al., 2013, Nature, 498, 338

Gaspari M., Sadowski A., 2017, ApJ, 837, 149

Gaspari M., Ruszkowski M., Oh S. P., 2013, MNRAS, 432, 3401

Gaspari M., et al., 2019, arXiv e-prints,

Geach J. E., et al., 2006, ApJ, 649, 661

Gebhardt K., et al., 2000, ApJ, 539, L13

Gebhardt K., Adams J., Richstone D., Lauer T. R., Faber S. M., Gültekin K., Murphy J., Tremaine S., 2011, ApJ, 729, 119

Genel S., et al., 2014, MNRAS, 445, 175

Genzel R., et al., 2015, ApJ, 800, 20

Gilbank D. G., Gladders M. D., Yee H. K. C., Hsieh B. C., 2011, AJ, 141, 94

Gladders M. D., Yee H. K. C., 2000, AJ, 120, 2148

Gladders M. D., Yee H. K. C., 2005, ApJS, 157, 1

Gobat R., et al., 2011, A&A, 526, A133

Gobat R., et al., 2013, ApJ, 776, 9

Gómez-Guijarro C., et al., 2018, ApJ, 856, 121

Gómez-Guijarro C., et al., 2019, ApJ, 872, 117

Gonzalez A. H., Sivanandam S., Zabludoff A. I., Zaritsky D., 2013, ApJ, 778, 14

Graham A. W., 2007, MNRAS, 379, 711

Graham A. W., Scott N., 2013, ApJ, 764, 151

Granato G. L., De Zotti G., Silva L., Bressan A., Danese L., 2004, ApJ, 600, 580

Granato G. L., Ragone-Figueroa C., Domínguez-Tenreiro R., Obreja A., Borgani S., De Lucia G., Murante G., 2015, MNRAS, 450, 1320

Green T. S., et al., 2016, MNRAS, 461, 560

Gültekin K., et al., 2009, ApJ, 698, 198

Guo Q., et al., 2016, MNRAS, 461, 3457

Gursky H., Kellogg E., Murray S., Leong C., Tananbaum H., Giacconi R., 1971, ApJ, 167, L81

Häring N., Rix H.-W., 2004, ApJ, 604, L89

Hatch N. A., Cooke E. A., Muldrew S. I., Hartley W. G., Almaini O., Conselice C. J., Simpson C. J., 2017, MNRAS, 464, 876

Hayward C. C., et al., 2020, arXiv e-prints, p. arXiv:2007.01885

Heitmann K., et al., 2008, Computational Science and Discovery, 1, 015003

Henden N. A., Puchwein E., Shen S., Sijacki D., 2018, MNRAS, 479, 5385

Henden N. A., Puchwein E., Sijacki D., 2019, arXiv e-prints, p. arXiv:1911.12367

Henriques B. M. B., White S. D. M., Thomas P. A., Angulo R., Guo Q., Lemson G., Springel V., Overzier R., 2015, MNRAS, 451, 2663

Hill R., et al., 2020, arXiv e-prints, p. arXiv:2002.11600

Hirschmann M., Dolag K., Saro A., Bachmann L., Borgani S., Burkert A., 2014, MNRAS, 442, 2304

Hirschmann M., De Lucia G., Fontanot F., 2016, MNRAS, 461, 1760

Hlavacek-Larrondo J., Fabian A. C., Edge A. C., Hogan M. T., 2012, MNRAS, 424, 224

Hlavacek-Larrondo J., et al., 2015, ApJ, 805, 35

Ho L., 1999, Supermassive Black Holes in Galactic Nuclei: Observational Evidence and Astrophysical Consequences. p. 157, doi:10.1007/978-94-011-4750-7˙11

Hoekstra H., Bartelmann M., Dahle H., Israel H., Limousin M., Meneghetti M., 2013, Space Sci. Rev., 177, 75

Hopkins P. F., 2015, MNRAS, 450, 53

Hopkins P. F., et al., 2018, MNRAS, 480, 800

Hubble E., 1929, Proceedings of the National Academy of Science, 15, 168

Huchra J. P., Geller M. J., 1982, ApJ, 257, 423

Hudson D. S., Mittal R., Reiprich T. H., Nulsen P. E. J., Andernach H., Sarazin C. L., 2010, A&A, 513, A37

Hwang H. S., Shin J., Song H., 2019, MNRAS, 489, 339

Ivison R. J., et al., 2013, ApJ, 772, 137

Ivison R. J., et al., 2016, ApJ, 832, 78

Jahnke K., Macciò A. V., 2011, ApJ, 734, 92

Kaiser N., 1986, MNRAS, 222, 323

Karakas A. I., 2010, MNRAS, 403, 1413

Kato Y., et al., 2016, MNRAS, 460, 3861

Kennicutt Robert C. J., 1998, ApJ, 498, 541

Komatsu E., et al., 2011, ApJS, 192, 18

Kormendy J., Bender R., 2011, Nature, 469, 377

Kormendy J., Gebhardt K., 2001, in Wheeler J. C., Martel H., eds, American Institute of Physics Conference Series Vol. 586, 20th Texas Symposium on relativistic astrophysics. pp 363–381 (`arXiv:astro-ph/0105230`), doi:10.1063/1.1419581

Kormendy J., Ho L. C., 2013, ARA&A, 51, 511

Koyama Y., et al., 2013, MNRAS, 434, 423

Kravtsov A. V., Borgani S., 2012, ARA&A, 50, 353

Kravtsov A. V., Vikhlinin A. A., Meshcheryakov A. V., 2018, Astronomy Letters, 44, 8

Lacaille K. M., et al., 2019, MNRAS, 488, 1790

Lakhchaura K., Truong N., Werner N., 2019, MNRAS, p. L117

Laor A., 2001, ApJ, 553, 677

Leja J., Carnall A. C., Johnson B. D., Conroy C., Speagle J. S., 2019a, ApJ, 876, 3

Leja J., et al., 2019b, ApJ, 877, 140

Leja J., Speagle J. S., Johnson B. D., Conroy C., van Dokkum P., Franx M., 2020, ApJ, 893, 111

Limber D. N., 1959, ApJ, 130, 414

Lin Y.-T., Mohr J. J., 2004, ApJ, 617, 879

Liu D., et al., 2019, ApJ, 887, 235

Lovell C. C., Geach J. E., Davé R., Narayanan D., Li Q., 2020, arXiv e-prints, p. arXiv:2006.15156

Lovisari L., Reiprich T. H., Schellenberger G., 2015, A&A, 573, A118

Ma C. J., et al., 2015, ApJ, 806, 257

Madau P., Dickinson M., 2014, ARA&A, 52, 415

Magorrian J., et al., 1998, AJ, 115, 2285

Main R. A., McNamara B. R., Nulsen P. E. J., Russell H. R., Vantyghem A. N., 2017, MNRAS, 464, 4360

Marconi A., Hunt L. K., 2003, ApJ, 589, L21

Markevitch M., 1998, ApJ, 504, 27

Martizzi D., Teyssier R., Moore B., 2012, MNRAS, 420, 2859

Matsuda Y., et al., 2011, MNRAS, 416, 2041

Matteucci F., Vettolani G., 1988, A&A, 202, 21

Mazzotta P., Rasia E., Moscardini L., Tormen G., 2004, MNRAS, 354, 10

McAlpine S., Bower R. G., Rosario D. J., Crain R. A., Schaye J., Theuns T., 2018, MNRAS, 481, 3118

McCarthy I. G., Schaye J., Bird S., Le Brun A. M. C., 2017, MNRAS, 465, 2936

McConnell N. J., Ma C.-P., 2013, ApJ, 764, 184

McDonald M., Gaspari M., McNamara B. R., Tremblay G. R., 2018, ApJ, 858, 45

McLure R. J., Dunlop J. S., 2002, MNRAS, 331, 795

McNamara B. R., Nulsen P. E. J., 2007, ARA&A, 45, 117

McNamara B. R., Kazemzadeh F., Rafferty D. A., Bîrzan L., Nulsen P. E. J., Kirkpatrick C. C., Wise M. W., 2009, ApJ, 698, 594

Meece G. R., O'Shea B. W., Voit G. M., 2015, ApJ, 808, 43

Meekins J. F., Fritz G., Chubb T. A., Friedman H., 1971, Nature, 231, 107

Merritt D., Ferrarese L., 2001, ApJ, 547, 140

Miley G., De Breuck C., 2008, A&A Rev., 15, 67

Miley G. K., et al., 2006, ApJ, 650, L29

Miller T. B., et al., 2018, Nature, 556, 469

Mittal R., Hudson D. S., Reiprich T. H., Clarke T., 2009, A&A, 501, 835

Mocanu L. M., et al., 2013, ApJ, 779, 61

Monaco P., Theuns T., Taffoni G., 2002, MNRAS, 331, 587

Muldrew S. I., Hatch N. A., Cooke E. A., 2015, MNRAS, 452, 2528

Muldrew S. I., Hatch N. A., Cooke E. A., 2018, MNRAS, 473, 2335

Mullis C. R., Rosati P., Lamer G., Böhringer H., Schwope A., Schuecker P., Fassbender R., 2005, ApJ, 623, L85

Murante G., Giovalli M., Gerhard O., Arnaboldi M., Borgani S., Dolag K., 2007, MNRAS, 377, 2

Muratov A. L., Kereš D., Faucher-Giguère C.-A., Hopkins P. F., Quataert E., Murray N., 2015, MNRAS, 454, 2691

Nagai D., Vikhlinin A., Kravtsov A. V., 2007, ApJ, 655, 98

Newman A. B., Ellis R. S., Andreon S., Treu T., Raichoor A., Trinchieri G., 2014, ApJ, 788, 51

O'Shea B. W., Nagamine K., Springel V., Hernquist L., Norman M. L., 2005, ApJS, 160, 1

Oliver S. J., et al., 2012, MNRAS, 424, 1614

Oteo I., et al., 2018, ApJ, 856, 72

Overzier R. A., 2016, A&A Rev., 24, 14

Pacifici C., et al., 2016, ApJ, 832, 79

Padovani P., Matteucci F., 1993, ApJ, 416, 26

Papovich C., et al., 2010, ApJ, 716, 1503

Pearson E. A., et al., 2013, MNRAS, 435, 2753

Peng C. Y., 2007, ApJ, 671, 1098

Pentericci L., et al., 2000, A&A, 361, L25

Peres C. B., Fabian A. C., Edge A. C., Allen S. W., Johnstone R. M., White D. A., 1998, MNRAS, 298, 416

Phipps F., Bogdán Á., Lovisari L., Kovács O. E., Volonteri M., Dubois Y., 2019, ApJ, 875, 141

Pillepich A., et al., 2018, MNRAS, 475, 648

Planck Collaboration et al., 2013, A&A, 550, A131

Planck Collaboration et al., 2018a, arXiv e-prints, p. arXiv:1807.06205

Planck Collaboration et al., 2018b, arXiv e-prints, p. arXiv:1807.06209

Popesso P., et al., 2012, A&A, 537, A58

Pratt G. W., Arnaud M., Biviano A., Eckert D., Ettori S., Nagai D., Okabe N., Reiprich T. H., 2019, Space Sci. Rev., 215, 25

Price D. J., 2008, Journal of Computational Physics, 227, 10040

Price D. J., 2012, Journal of Computational Physics, 231, 759

Puchwein E., Sijacki D., Springel V., 2008, ApJ, 687, L53

Ragagnin A., Dolag K., Biffi V., Cadolle Bel M., Hammer N. J., Krukau A., Petkova M., Steinborn D., 2017, Astronomy and Computing, 20, 52

Ragone-Figueroa C., Granato G. L., Murante G., Borgani S., Cui W., 2013, MNRAS, 436, 1750

Ragone-Figueroa C., Granato G. L., Ferraro M. E., Murante G., Biffi V., Borgani S., Planelles S., Rasia E., 2018, MNRAS, 479, 1125

Rasia E., et al., 2006, MNRAS, 369, 2013

Rasia E., et al., 2012, New Journal of Physics, 14, 055018

Ricciardelli E., Trujillo I., Buitrago F., Conselice C. J., 2010, MNRAS, 406, 230

Romano D., Karakas A. I., Tosi M., Matteucci F., 2010, A&A, 522, A32

Romano D., Matteucci F., Zhang Z. Y., Papadopoulos P. P., Ivison R. J., 2017, MNRAS, 470, 401

Romano D., Matteucci F., Zhang Z.-Y., Ivison R. J., Ventura P., 2019, MNRAS, 490, 2838

Rosati P., et al., 2002, ApJ, 566, 667

Sabra B. M., Saliba C., Abi Akl M., Chahine G., 2015, ApJ, 803, 5

Sadowski A., Gaspari M., 2017, MNRAS, 468, 1398

Salpeter E. E., 1955, ApJ, 121, 161

Sani E., Marconi A., Hunt L. K., Risaliti G., 2011, MNRAS, 413, 1479

Santos J. S., et al., 2014, MNRAS, 438, 2565

Santos J. S., et al., 2015, MNRAS, 447, L65

Sarazin C. L., 1988, X-ray emission from clusters of galaxies

Sargent M. T., Béthermin M., Daddi E., Elbaz D., 2012, ApJ, 747, L31

Sargent M. T., et al., 2014, ApJ, 793, 19

Saro A., Borgani S., Tornatore L., De Lucia G., Dolag K., Murante G., 2009, MNRAS, 392, 795

Sato T., Matsushita K., Ota N., Sato K., Nakazawa K., Sarazin C. L., 2011, PASJ, 63, S991

Savorgnan G. A. D., Graham A. W., Marconi A., Sani E., 2016, ApJ, 817, 21

Schaye J., et al., 2015, MNRAS, 446, 521

Schechter P., 1976, ApJ, 203, 297

Schreiber C., et al., 2015, A&A, 575, A74

Scoville N., et al., 2016, ApJ, 820, 83

Sembolini F., et al., 2016, MNRAS, 457, 4063

Shankar F., et al., 2016, MNRAS, 460, 3119

Smail I., et al., 2014, ApJ, 782, 19

Smith C. M. A., Gear W. K., Smith M. W. L., Papageorgiou A., Eales S. A., 2019, MNRAS, 486, 4304

Springel V., 2005, MNRAS, 364, 1105

Springel V., 2010a, ARA&A, 48, 391

Springel V., 2010b, MNRAS, 401, 791

Springel V., 2016, Saas-Fee Advanced Course, 43, 251

Springel V., Hernquist L., 2003, MNRAS, 339, 289

Springel V., Yoshida N., White S. D. M., 2001a, New A, 6, 79

Springel V., White S. D. M., Tormen G., Kauffmann G., 2001b, MNRAS, 328, 726

Springel V., Di Matteo T., Hernquist L., 2005, MNRAS, 361, 776

Stanford S. A., et al., 2006, ApJ, 646, L13

Steidel C. C., Adelberger K. L., Shapley A. E., Erb D. K., Reddy N. A., Pettini M., 2005, ApJ, 626, 44

Steinborn L. K., Dolag K., Hirschmann M., Prieto M. A., Remus R.-S., 2015, MNRAS, 448, 1504

Steinborn L. K., Dolag K., Comerford J. M., Hirschmann M., Remus R.-S., Teklu A. F., 2016, MNRAS, 458, 1013

Steinhardt C. L., et al., 2014, ApJ, 791, L25

Stevens J. A., Jarvis M. J., Coppin K. E. K., Page M. J., Greve T. R., Carrera F. J., Ivison R. J., 2010, MNRAS, 405, 2623

Stone J. M., Gardiner T. A., Teuben P., Hawley J. F., Simon J. B., 2008, ApJS, 178, 137

Strazzullo V., et al., 2010, A&A, 524, A17

Strazzullo V., et al., 2013, ApJ, 772, 118

Strazzullo V., et al., 2016, ApJ, 833, L20

Strazzullo V., et al., 2018, ApJ, 862, 64

Sunyaev R. A., Zeldovich Y. B., 1972, Comments on Astrophysics and Space Physics, 4, 173

Tacconi L. J., et al., 2018, ApJ, 853, 179

Tanaka M., et al., 2013a, PASJ, 65, 17

Tanaka M., et al., 2013b, ApJ, 772, 113

Teyssier R., 2002, A&A, 385, 337

Thielemann F. K., et al., 2003, in Hillebrandt W., Leibundgut B., eds, From Twilight to Highlight: The Physics of Supernovae. p. 331, doi:10.1007/10828549˙46

Thomas D., Maraston C., Schawinski K., Sarzi M., Silk J., 2010, MNRAS, 404, 1775

Thomas J., Ma C.-P., McConnell N. J., Greene J. E., Blakeslee J. P., Janish R., 2016, Nature, 532, 340

Toft S., et al., 2014, ApJ, 782, 68

Tonry J. L., 1987, in de Zeeuw P. T., ed., IAU Symposium Vol. 127, Structure and Dynamics of Elliptical Galaxies. pp 89–98, doi:10.1007/978-94-009-3971-4˙7

Tormen G., Bouchet F. R., White S. D. M., 1997, MNRAS, 286, 865

Tornatore L., Borgani S., Matteucci F., Recchi S., Tozzi P., 2004, MNRAS, 349, L19

Tornatore L., Borgani S., Dolag K., Matteucci F., 2007, MNRAS, 382, 1050

Toro E., 2009, Riemann Solvers and Numerical Methods for Fluid Dynamics

Tozzi P., Norman C., 2001, ApJ, 546, 63

Tran K.-V. H., et al., 2010, ApJ, 719, L126

Tremmel M., Karcher M., Governato F., Volonteri M., Quinn T. R., Pontzen A., Anderson L., Bellovary J., 2017, MNRAS, 470, 1121

Truong N., et al., 2018, MNRAS, 474, 4089

Umehata H., et al., 2015, ApJ, 815, L8

Valentino F., et al., 2016, ApJ, 829, 53

Vogelsberger M., Marinacci F., Torrey P., Puchwein E., 2020, Nature Reviews Physics, 2, 42

Volonteri M., Ciotti L., 2013, ApJ, 768, 29

Von Der Linden A., Best P. N., Kauffmann G., White S. D. M., 2007, MNRAS, 379, 867

Vulcani B., De Lucia G., Poggianti B. M., Bundy K., More S., Calvi R., 2014, ApJ, 788, 57

Wang T., et al., 2016, ApJ, 828, 56

Wang T., et al., 2018, ApJ, 867, L29

Weinberger R., et al., 2018, MNRAS, 479, 4056

Whitaker K. E., et al., 2014, ApJ, 795, 104

White D. A., Jones C., Forman W., 1997, MNRAS, 292, 419

Woosley S. E., Weaver T. A., 1995, ApJS, 101, 181

Xie L., De Lucia G., Hirschmann M., Fontanot F., Zoldan A., 2017, MNRAS, 469, 968

Xue Y.-J., Wu X.-P., 2000, ApJ, 538, 65

Zwicky F., 1933, Helvetica Physica Acta, 6, 110